Study of the vibrational dynamics of glasses

Andrea Monaco

THESE DE DOCTORAT DE L'UNIVERSITE
JOSEPH FOURIER

Spécialité

PHYSIQUE

présentée par

M. Andrea Monaco

Pour obtenir le grade de

DOCTEUR de l'UNIVERSITE JOSEPH FOURIER

Etude de la dynamique vibrationelle des verres

soutenue le 12 Decembre 2006

devant le jury composé de:

H. Renevier	Président
C. Alba-Simionesco, S. R. Elliott	Rapporteurs
H. Schober, U. van Bürck	Examinateurs
A.I. Chumakov, G. Monaco	Directeurs de thèse

THESE PREPAREE AU SEIN DU LABORATOIRE:
EUROPEAN SYNCHROTRON RADIATION FACILITY - GRENOBLE

Etude de la dynamique vibrationelle des verres

Andrea Monaco

The beauty of discovery in science:
to transform, at the same time,
our image of the world and that of ourself.

Contents

Introduction

Il est une expérience commune qu'en utilisant juste le sens de l'audition il est possible de récupérer beaucoup d'informations sur le monde qui nous entoure. Par exemple, nous pouvons comprendre si nous sommes dans un endroit surpeuplé ou isolé, si une rue est proche de nous, si nous sommes entourés par des personnes et même nous essayons de prévoir le temps juste avec le bruit du vent.

Cependant, si nous voulions savoir plus au sujet des objets autour de nous, en utilisant seulement notre sens de l'audition, nous serions déus; la matière reste silencieuse si elle n'est pas interrogée. Même dans ce cas-ci, sans bonnes questions, elle n'a pas beaucoup dire. Du bruit qu'un objet produit par le coup d'un marteau nous pouvons faire des hypothèses sur sa composition mais nous ne pouvons rien dire au sujet de sa nature microscopique. Il semble alors qu'onde acoustique ne soit pas les meilleurs moyens d'indiquer les secrets de la matière. L'information sur la nature de la matière condensée devrait être récupérée des modes vibratoires qui montent spontanément (par exemple en raison des mouvements thermiques) sur une échelle de longueur microscopique. Malheureusement, de telles vibrations ne peuvent pas produire un bruit comme celui employé pour entendre.

Si nous imaginons pour améliorer nos facultés sensorielles dans la région des fréquences o de telles vibrations sont présentes, nous découvririons que chaque système a ses propres " son " et, d'ailleurs, nous serions étonnés de découvrir qu'il y a également un " son caractéristique du désordre ". Ceci signifie qu'un " bruit " peut nous dire si la structure du système est amorphe ou cristalline. Cette étonnante découverte n'est pas si lointaine, elle est de Zeller et de Pohl. En 1971, ils ont observé que la capacité de chaleur et la conductivité thermique présentent de différents comportements de la température si mesuré d'un cristallin ou d'un amorphe. Les études successives ont prouvé qu'un tel comportement marque réellement une différence universelle entre la densité des états vibratoires (DOS) d'un verre et de celui d'un cristal. Une telle différence apparat comme une augmentation du nombre de vibrations [1] dans la phase vitreuse au-del de ceux de ses contre-parties cristallines. Cette augmentation des états vibratoires s'appelle le " Boson Peak "(BP) : le " son caractéristique du désordre ".

On n'a jamais proposé l'idée que le désordre topologique pourrait avoir une signature dans les propriétés vibratoires de basse température du système avant l'expérience sur SiO_2 de Zeller et de Pohl en 1971. Depuis cette première expérience, les études de BP ont montré un intérêt croissant, devenant le sujet de nombreuses études théoriques et expérimentales. Étant donné que la présence de BP dans les verres est liée aux pro-

[1] la région de la fréquence o un tel phénomène a lieu est de THz.

priétés vibratoires de cet état, la recherche sur BP peut être placée dans le contexte plus large de l'étude de la dynamique dans les systèmes désordonnés. Les principaux taches de ce sujet de recherche ont été de comprendre l'effet général du désordre sur la dynamique vibratoire des verres. En outre, l'étude de la dynamique des verres permet de rechercher les mécanismes microscopiques sur lesquels les propriétés macroscopiques de ces systèmes sont basées, ainsi certaines de ces études ont des applications potentielles dans la science des matériaux.

En verres, la dynamique vibratoire a été explorée sur un éventail d'échelles de longueurs et de temps de la limite macroscopique, o le système devrait, en principe, apparatre comme continuum, la limite microscopique, o seulement le comportement de chaque atome est pris en considération.

Récemment, ces études expérimentales ont tiré bénéfice de l'arrivée de basé sur de nouvelles techniques spectroscopiques basé sur les rayons X. L'avantage de ces techniques est de fournir des informations précises sur la dynamique vibratoire microscopique et de donner l'accès la recherche sur une large classe des systèmes. Par exemple, les rayons X sondent facilement des échantillons de petites dimensions et dans des conditions extrêmes. L'étude présente dans cette thèse a employé, en tant que méthodes expérimentales principales, deux techniques spectroscopiques de rayons X : Dispersion non élastique nucléaire (NIS) et dispersion non élastique de rayon X (IXS). Utilisant ces technique, nous pouvons mesurer la densité des états vibratoires de différents verres et de sonder les excitations vibratoires des verres une échelle microscopique. Le but final de notre étude est d'étudier les mécanismes responsables de la présence de BP dans les systèmes vitreux.

Trente ans après la première observation de BP, ce dispositif est encore en grande partie discuté dans la communauté scientifique et jusqu'ici son origine n'a pas été complètement comprise. En fait, quoiqu'une grande variété de modèles puissent reproduire le BP dans le DOS des verres ont été proposés, le nombre d'expériences capables de le distinguer est très limité.

Dans ce travail nous avons entrepris une recherche sur la dynamique vibratoire d'une classe des systèmes o la phénoménologie de BP est fortement discutée : verres " hyperquenched et densified ". Grce une caractérisation étendue de nos échantillons, nous avons étudié leur dynamique et les propriétés structurales sur une gamme d'échelle de longueur allant du macroscopique la limite du microscopique. Nous avons observé cela, en changeant la pression appliquée sur le verre, ou en changeant la température de l'échantillon. La modification de la faible part de l'énergie du DOS est strictement corrélée avec les changements de la réponse élastique de continuum du verre. C'est vrai moins qu'une transformation structurale soit induite. La recherche sur le DOS des verres a été enrichie par l'étude de la nature des excitations vibratoires aux énergies comparables celles de BP. Ceci a été fait par des mesures de la dépendance de pression des vibrations haute fréquence d'un verre.

La thèse a été présentée en accord avec les principes suivant :

- Dans le premier chapitre les aspects généraux de l'état vitreux sont présentés en se référant plus particulièrement au comportement particulier des propriétés thermo-dynamiques et au transport de cet état. Ici nous discutons comment

le comportement thermo-dynamique anormal des verres peut être associé la présence du Boson Peak dans la densité des état vibratoires du verre. Enfin une brève vue d'ensemble sur les différents modèles actuels en littérature pour expliquer la pésence du BP.

- Dans le deuxième chapitre, nous discuterons les principales techniques spectroscopiques utilisées dans cette étude: Diffusion non élastique nucléaire (NIS) et la diffusion non élastique de rayon X (IXS). Les principes de base et les aspects techniques du NIS et de l'IXS seront évoquées.

- Dans le troisième chapitre, nous présentons l'étude du verre hyperquenched. Dans ce chapitre, les effets de l'histoire thermique sur les propriétés dynamiques et structurales des verres seront étudiés. Une attention particulière sera consacrée l'analyse de BP.

- Le quatrième chapitre est consacré l'étude de l'effet de la pression et de la densité sur le DOS d'un verre. Les changements que les expériences de DOS sont corrélées une fois de plus avec les changements macroscopiques, moins qu'une transformation structurale ait lieu. Les pricipales implications de ces corrélations sur la phénoménologie de BP sont discutées.

- Dans le cinquième chapitre, nous présenterons une étude sur la dynamique haute fréquence (dans la région de fréquence de THz) d'ortho-terphénylique vitreux, et l'effet de la pression sur cette dynamique sera discuté. En comparant nos résultats aux données disponibles dans la littérature, il a été possible de déduire quelques conclusions sur la nature des modes acoustiques aux énergies comparables celle de BP. Enfin nous présenterons le tableau d'ensemble de BP au lequel le travail actuel nous a permis d'obtenir. Nous récapitulons tous les résultats important, et nous donnerons des perspectives sur des études possibles venir.

Introduction

It is common experience that using just the sense of hearing it is possible to recover a lot of information about the world around us. For instance, we can understand if we are in a crowded or lonely place, if a street is close to us, if we are surrounded by people and even try to forecast the weather just from the sound of the wind.

However, if we wanted to know more about the objects around us, using only our sense of hearing, we would be disappointed; matter keeps silent if it is not interrogated. Even in this case, without the right questions, it does not have a lot to say. From the noise that an object produces once hit by a hammer we can make hypotheses on its composition but we cannot say anything about its microscopic nature. It seems then that acoustic waves are not the best means to reveal the secrets of matter. The information on the nature of condensed matter should be recovered from the vibrational modes that spontaneously rise (for instance because of the thermal motions) on a microscopic length-scale. Unfortunately, such vibrations are not able to produce a sound like the ones used to hear.

If we imagine to improve our sensorial faculties in the region of frequencies where such vibrations are present, we would discover that each system has its own "sound" and, moreover, we would be surprised to find out that there is also a characteristic "sound of disorder". This means that a "sound" is able to tell us if the structure of the system is amorphous or crystalline.

Such astonishing discovery is not too far from that of Zeller and Pohl. In 1971 [1] they observed that heat capacity and thermal conductivity show different temperature behaviors if measured for a crystalline or amorphous SiO_2. Successive studies have shown that such a behavior actually marks a universal difference between the density of vibrational states (DOS) of a glass and that of a crystal. Such difference appears as an increase of the number of vibrations[2] in the glassy phase over those of its crystalline counterpart. This increase of vibrational states is called the Boson Peak (BP): the characteristic "sound of disorder".

The idea that topological disorder could have a signature in the low temperature vibrational properties of the system was never proposed before the experiment on SiO_2 of Zeller and Pohl in 1971. Since this first experiment, studies of the BP have shown an increasing interest, becoming the subject of numerous theoretical and experimental studies.

Due to the fact that the presence of the BP in glasses is related to the vibrational properties of this state, the investigation of the BP can be placed in the wider context

[2]The region of frequency where such phenomenon takes place is $\approx$ THz.

of the study of the dynamics in disordered systems. The main tasks of this subject of research have been to understand the general effect of disorder on the vibrational dynamics of glasses.

Furthermore, the study of the dynamics of glasses allows one to look for the microscopic mechanisms on which the macroscopic properties of these systems are based, thus some of these studies have a potential applications in material science.

In glasses, the vibrational dynamics has been explored over a wide range of lengths and times scales from the macroscopic limit, where the system should, in principle, appear as a continuum, to the microscopic limit, where only the behavior of each atom is taken into account.

Recently, these experimental studies have benefitted from the advent of new x-ray based spectroscopic techniques. The advantage of these techniques is to give accurate information on the microscopic vibrational dynamics and to give access to the investigation of a wide class of systems. For example, x-rays can easy probe samples with small dimensions and under extreme conditions. The study presented in this Thesis has used, as main experimental methods, two x-rays spectroscopic techniques: Nuclear Inelastic Scattering (NIS) and Inelastic X-ray Scattering (IXS). Using these technique we can measure the density of vibrational states of different glasses and probe the vibrational excitations in glasses at microscopic length-scales. The ultimate goal of our study is to investigate the mechanisms responsible for the presence of the BP in glassy systems.

Thirty years after the first observation of the BP, this feature is still largely debated in the scientific community and until now its origin has not been completely understood. In fact, even though a wide variety of models are able to reproduce the BP in the DOS of glasses have been proposed, the number of experiments able to discriminate among are than quite limited.

In the present work we undertook an investigation into the vibrational dynamics of a class of systems where the phenomenology of the BP is highly debated: the hyperquenched and densified glasses. Thanks to an extensive characterization of our samples, we studied their dynamical and structural properties over a range of length-scales from the macroscopic to the microscopic limit. We have observed that, varying the pressure applied on a glass, or changing the thermal history of the sample, the modification of the low energy part of the DOS is strictly correlated with the changes of the continuum elastic response of the glass. This is true unless a structural transformation is induced. The investigation of the DOS of glasses has been enriched by the study of the nature of the vibrational excitations at energies comparable to that of the BP. This has been done through measurements of the pressure dependence of the high frequency vibrations of a glass.

The Thesis has been set out according the following scheme:

- In the first chapter the general aspects of the glassy state are introduced with particular attention to the peculiar behavior of the thermodynamic and transport properties of this state. Here we discuss how the anomalous thermodynamic behavior of glasses can be associated to the presence of the Boson Peak in the density of vibrational state of the glass. Finally a short overview on the different models present in literature to explain the BP is presented.

- In the second chapter we discuss the main spectroscopic techniques used in this study: Nuclear Inelastic Scattering (NIS) and the Inelastic X-ray Scattering (IXS). The basic principles and the technical aspects of NIS and IXS are introduced.

- In the third chapter we present the study of a hyperquenched glass. In this chapter the effects of the thermal history on the dynamical and structural properties of glasses are investigated. Particular attention is devoted to the analysis of the BP.

- The fourth chapter is dedicated to the study of the effect of pressure and density on the DOS of a glass. The changes that the DOS experiences are correlated once more to the macroscopic changes, unless a structural transformation takes place. The main implications of these correlations on the phenomenology of the BP are discussed.

- In the fifth chapter we present a study on the high frequency dynamics (in the THz frequency region) of glassy ortho-terphenyl, and the effect of pressure on this dynamics is discussed. From the comparison of our results to others data available in the literature it has been possible to deduce some conclusions on the nature of the acoustic modes at energies comparable to that of the BP.

  Finally we present the general picture of the BP that the present work has allowed us to get to. We summarize all the main results and we offer perspectives for possible futures studies.

Résumé du chapitre 1

Dans ce chapitre on trouve une introduction aux principales caractéristiques de la phase vitreuse en soulignant les particularités de cet état de la matière condensée qui sont à la base de l'intérêt de notre étude. Les propriétés thermodynamiques du verre telles que la capacité thermique, la conductivité et l'expansion thermique sont mentionnées ici; ainsi que l'analyse de leur comportement a basse température. En effet, toutes ces quantités physiques, à basse température se comportent de manière inattendue si on les compare par rapport à celles des cristaux issus de la théorie de Debye. Dans ce même chapitre on traitera le problème de la dynamique du verre en introduisant le concept de phonon et en illustrant les différents modes vibrationnels que peut supporter le verre. On introduit alors la propriété physique de la densité d'états vibrationnels DOS ($g(E)$) en éclaircissant sur cette grandeur qui est liée aux propriétés thermodynamiques du verre. Dans ces paragraphes on montrera que à basse température, le comportement anormal des propriétés thermodynamiques d'un système vitreux révèle une augmentation du nombre d'états vibrationnels. Dans la RDOS ($g(E)/E^2$) à basse énergie cette augmentation a son maximum que l'on appelle Boson Peak (BP). Enfin la dernière partie de ce chapitre est dédiée au BP. On fournira un bref aperçu de quelques modèles qui décrivent cette caractéristique vibrationnelle du verre. On discutera la validité de certains modèles du BP sur le quel sont basés les résultats de cette thèse.

Chapter 1

General aspects of the glassy state

In this chapter the fundamental properties of the glassy state will be reviewed.

1.1 The glassy state

The glassy state is a state of matter that behaves macroscopically as a solid. The peculiar character of this state compared to crystalline state appears evident in its microscopic structure. The structure of a glass is defined as that of an amorphous solid. The term amorphous reflects its Greek root and is descriptive of any condensed phase which lacks long-range order.

In literature concerned with "glass", there is no a unique definition. Several different ways have been proposed to identify the glassy state, each of them focusing on a different aspect of glasses. One of the most used definitions of glass, that we assume in the context of this thesis, is based not only on the microscopic structural properties of the solid but also on the glass forming process, that starting from a liquid gives rise to the glass. Thus, it has been proposed to define a glass as: "*an amorphous solid that exhibits a glass transition*".

Here the glass transition identifies that phenomenon where a liquid experiences on cooling a change of its internal energy with varying temperature. Such change appears as a sudden modification in the derivative, respect to the temperature, of its thermodynamic properties (e.g. heat capacities c_P, etc). This definition of glass, based on the glass forming process, has the advantage of underlining one peculiarity of the glassy state: its non-equilibrium nature.

The glass cannot be described only by the value of the thermodynamic parameters of the system; one has also to specify as well the thermodynamic history of the material and the experimental time scale of observation. In fact, as it will be clarified in the next paragraph, a glass will exhibit liquid-like or solid like behavior depending on the timescale over which the measurements take place.

In order to clarify the process that drives a system to form a glass, we can deal with an ideal experiment where, starting from isolated atoms we build an amorphous material. The actual experiment that most closely corresponds to this process is cooling a vapor until it condenses into the liquid state and then further gradually cooling the liquid until it solidifies. The results of such experiment, for a given quantity of

material, may be represented using volume versus temperature ($V(T)$) plot such as the one represented in fig. 1.1.

A sharp break or bend in $V(T)$ marks a change of state occurring with decreasing temperature. The first occurs when the gas condenses to the liquid phase at the boiling temperature. Continued cooling now decreases the liquid volume continuously. Eventually, when the temperature is low enough, a liquid-solid transition takes place. Such transition can occur in two ways: either discontinuously to a crystalline solid, or continuously to an amorphous solid (glass). The liquid-crystal transition temperature T_m is marked by a discontinuity in $V(T)$, an abrupt contraction to the volume of the crystalline solid. In a quenching experiment carried out at sufficiently low cooling rate this is usually the route taken to get to the solid state. However, at sufficiently high cooling rates most materials alter their behavior, T_m is bypassed and the liquid phase persists until a lower temperature, T_g, is reached: here the second solidification scenario is realized. During the liquid-glass transition no volume discontinuity appears, $V(T)$ bends over to acquire a smaller slope (similar to that of the crystal) characteristic of the low thermal expansion of a solid compared to a liquid (the thermal expansion is defined as $\alpha = (1/V)(\partial V/\partial T)_P$ [2]). Thus the process of glass formation is an alternative route for a liquid to fall into the solid, by-passing the crystallization mechanism. The differences between glass formation and crystallization have a clear image in the microscopic aspect of the crystalline and glassy state.

The higher cooling rate, responsible for the glass formation, produces randomness in the structure of the glassy state. This disorder should be compared to a standard definition of order: that of a perfect crystal. In a crystal the atoms are arranged on a periodic three dimensional array. Conversely, a glass presents no translational periodicity and then shows topological disorder. In addition, different types of disorder can be added. For instance, spin disorder, when each atomic site possesses a spin or magnetic moment randomly oriented or substitutional disorder where one or more types of atoms are randomly substituted for the others in the crystalline lattice.

Actually, the effect of disorder on the microscopic and macroscopic properties of a solid represents the main reason of interest for the study of the glassy state. Such characteristic has been pointed out to be responsible for the properties that are unique to glasses and are not at all shared with crystalline solids. For instance, the heat capacity c_P and the thermal conductibility k of glasses at low temperature present a behavior that is quite far from what found in crystalline materials. Such peculiarities of the glassy state have been called thermodynamic "anomalies" [3].

The first experimental observation of the differences between the thermodynamic properties of glasses and their crystalline counterparts dates to 1971 by Zeller and Pohl [1]. Before this date it was not predicted that c_P or k could exhibit different low temperature behavior for amorphous silica and crystalline quartz. At low temperatures the structural irregularities of glasses become progressively less important for the propagation of vibrational excitations with increasing wavelength.

Since these first observations the interest to study the glassy state is increased, leading to intensive experimental studies of a wide variety of amorphous materials. The results of such experimental efforts have established the universal nature of the low temperature behavior of c_P and k in glasses. Beyond the interest of these anomalies,

the process of glass formation has been the subject of its own active research efforts.

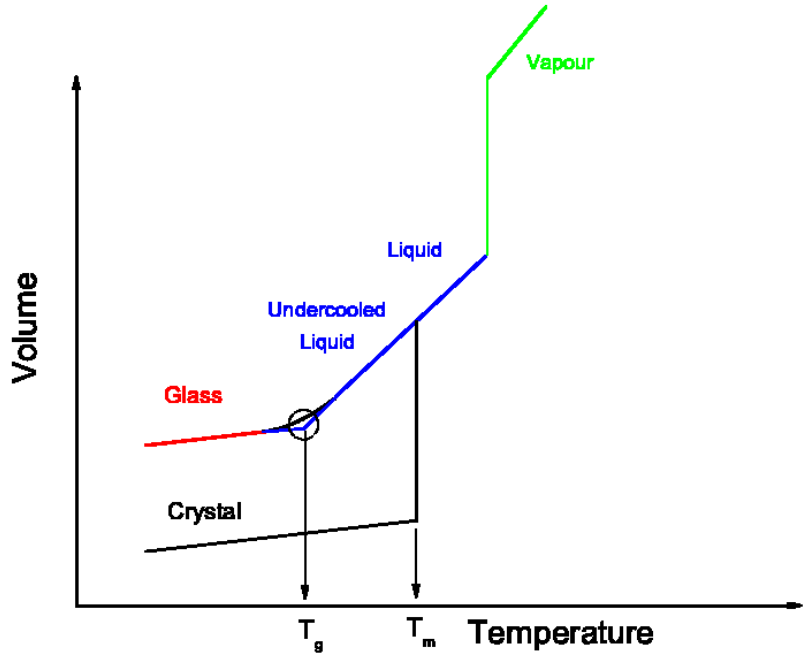

Figure 1.1: *Temperature behavior of the volume of a system through its vapor, liquid, crystalline, and glassy state.*

1.2 The glass transition

The glass transition has been referred to the physical phenomenon that marks the attainment, on cooling, of a state which exhibits the thermodynamic properties of a solid. Such solid has the amorphous structure typical of a glass and it keeps its disordered nature at all temperatures lower than the glass transition temperature (on the time scale of the human experience). The understanding of the nature of the glass transition and its origin is regarded by the scientific community as a central problem in condensed matter physics.

The most general concept of a glass is related to those systems which have some degree of freedom that fluctuate at a rate which depends strongly on temperature (T) or pressure (P) and that become so slow at low T or high P that the fluctuations become frozen. The properties determined by the slow degrees of freedom change value more or less abruptly giving rise to the *glass transition*. The decrease of the degree

of freedom of the system can also be related to the break down of ergodicity [4]. In fact the glass formation process brings the system from an ergodic condition (i.e. the system in equilibrium in the course of spontaneous fluctuations revisits the same state within the experimental observation period) to a non ergodic state. The phenomena associated with the break of the ergodicity condition are macroscopically visible in a sudden change in the derivative of the thermodynamic properties (such as c_P, etc) of the system across the glass transition temperature (T_g). For instance, in glass forming liquids the heat capacity, compressibility and expansivity decrease while the system experience the crossover between the two microscopic dynamical regimes. In a liquid, molecules have extensive translational motions, in contrast atom in glasses can only oscillate around their equilibrium positions since the glass transition marks the freezing of the free diffusion typical of the liquid phase.

In some aspects, the glass transition can be described by monitoring the thermodynamic properties of a system as a function of temperature. Figure 1.2 shows a typical $c_P(T)$ scan ($c_P = (\partial Q/\partial T)_P$, where Q is the heat exchanged by the system) in an amorphous and in a crystalline solid. The glass transition clearly appears as a step in the specific heat on decreasing T. For glassy material, $c_P(T)$ can be followed continuously from low temperature up through T_g and well into the liquid regime and beyond. The curve for the crystal is continuous up to the melting point T_m where c_P diverges because of the heat fusion (finite ΔQ with $\Delta T = 0$, $c_P \to \infty$) associated with the crystal liquid transition. No similar latent heat singularity accompanies the glass-liquid transition.

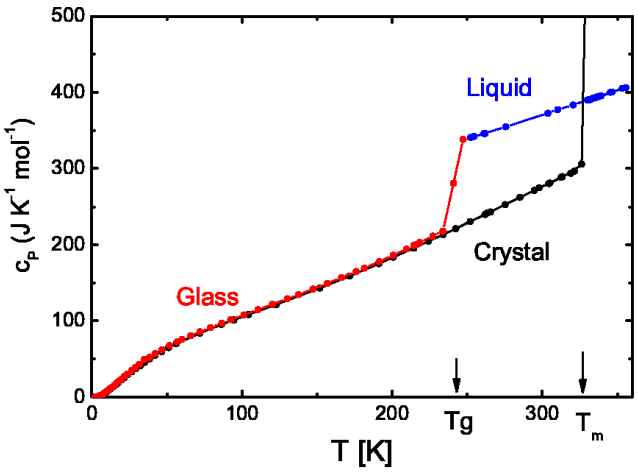

Figure 1.2: *Behaviour of the specific heat of ortho-terphenyl through its liquid-crystal and liquid-glass phase transitions [5].*

The liquid-glass transition can be observed readily through monitoring the change of volume as a function of temperature (as shown in fig. 1.1). The crystallization process

is manifested by an abrupt change in volume at T_m, whereas the glass formation is characterized by a gradual change in the slope of V. The region over which the change of slope occurs, is centered around the glass transition temperature T_g (similar behavior is also exhibited by other extensive thermodynamic variables such as the entropy, S, and enthalpy, H). Since the transition to the glassy state is continuous, it is often used the term "fictive" temperature T_f to mark the transition temperature, which can be defined as that specific temperature where the extrapolated liquid and glass curves intersect (in fig. 1.1 $T_f = T_g$).

The glass transition temperature depends on the rate of cooling of the liquid. The slower the rate of cooling, the larger the region over which the liquid may be supercooled (brought below the melting temperature but still in liquid state), and hence giving a lower T_g. Thus, the glass transition temperature of a particular material depends on its thermal history and is not an intrinsic property.

The reason for the shifting of T_g to lower temperatures when the cooling process is extended over longer times can be described by theories that represent the glass transition in terms of relaxation processes [6]. The typical relaxation time τ of a liquid increases decreasing the temperature. The quantity $1/\tau$ characterizes the rate at which the structure of the system at the atomic scale adapts itself to an external perturbation. This quantity varies enormously during the cooling process. The structural rearrangement response time may increase from 10^{-12}s in the liquid to 10^{10} years at T=$T_g - 50$ K. As T is lowered below T_g, τ becomes much larger than any experimentally accessible time and the material loses its ability to rearrange the atomic configuration, e.g., in response to the imposed decrease of temperature. The system reaches the behavior of a solid with a huge increase of the viscosity and the atoms are frozen into well-defined positions that correspond to the configuration that they had at T_g.

The definition of T_g is always related to the experimental conditions of measurement, in particular to the relation between the characteristic timescale $(1/\omega)$ at which the system is probed, and the time that the system takes to recover its equilibrium after an external perturbation. If the experimental time is short compared to the material relaxation time ($\omega\tau >> 1$), the measured properties are out of equilibrium.

The relation between T_g and the cooling rate at which the experiment is carried out is an indication of the characteristic kinetic nature of the glass transition. The essential requirement for glass formation is that the thermal energy of an ensemble of molecules, ions, etc. can be removed at a rate that, for kinetic reasons, precludes the organization of the particles in a crystal lattice. In fact, the crystalline phase is energetic favorite and crystal growth will always dominate over the formation of the amorphous phase if it is allowed to take place.

The question that then naturally arises is: "Why many systems can get into solid phase by-passing the crystallization and becoming glass?

A connection between the kinetic and thermodynamic nature of the glass transition is provided by the Adam-Gibbs relationship [7]:

$$\tau = \tau_0 exp(\Delta H^*/(TS_c)), \tag{1.1}$$

here τ_0 is a pre-exponential constant, ΔH^* is the activation enthalpy and S_c is the configurational entropy of the system. According to Eq. (1.1), the origin of the increase in

τ approaching T_g, decreasing temperature, is related to the decrease number of configurations that the system is able to sample. In fact, the liquid phase can accommodate a great range of molecular configurations. Conversely, in the crystalline state, translational symmetry places severe restrictions on the relative molecular arrangements. While kinetic effects clearly play a role in the determination of T_g, the Adam-Gibbs formula suggests that the observed liquid-glass transition is a manifestation of an underlying thermodynamic transition. Such thermodynamic transition would correspond to the limit of an infinitely long observation time $t \to \infty$, and of an infinitely low cooling rate ($\partial T/\partial t \to 0$).

The fact that certain extensive thermodynamic variables (e.g. V, S, H) are continuous while the differential quantities α, c_P, k are discontinuous at T_g, might suggest that the glass transition is a second order phase transition [1]. The liquid-crystal transition is an example of the first order transition, since the volume $V = (\partial G/\partial P)_T$ (here G is the Gibbs free energy) changes discontinuously at T_m whereas in a glass $c_P = T(\partial S/\partial T)_P = -T(\partial^2 G/\partial T^2)_P$ is almost discontinuous at T_f (see fig. 1.1 and 1.2).

Unfortunately, this rather simple model of the glass transition fails at several points. A difficulty arises when one examines the predictions made for a second order phase transition. In particular, the Prigogine-Defay ratio, i.e. a ratio of thermodynamic parameters expected to be one for a second order transition, gives a value different from one [8].

The glass transition is not therefore a simple second order phase transition. However, the question remains if the glass formation process can be associated to an ideal glass transition temperature.

Kauzmann [9] answered this question using the argument that the entropy of an undercooled liquid cannot decrease below the value of the crystalline phase. This argument can be understood if we plot S vs T over a large range of temperatures through the liquid, the crystal and the glassy state. Integrating the difference in heat capacity over the temperature interval between the glass transition temperature and the melting point shows that some 60% of the entropy of fusion is lost on the supercooling the liquid before internal equilibrium is lost. In fact we can write:

$$S_{ex} = \Delta S(fusion) - \int_T^{T_m} (c_P(liquid) - c_P(crystal))\ dlogT. \tag{1.2}$$

Here S_{ex} represents the amount by which the entropy of the liquid exceeds that of the crystalline phase at the same temperature and $\Delta S(fusion)$ the change of entropy associated to the fusion of the solid. As the temperature decreases from T_m to T_g, S_{ex} drops sharply as shown in fig. 1.3. The significant feature of fig. 1.3 is the dashed line that extrapolates the behaviour of the liquid below T_g. This part of the curve cannot of course be measured, solidification occurs when the temperature is decreased below T_g. If the glass transition did not intervene, the liquid entropy would equal the crystal's entropy at nonzero temperature T_k (the Kauzmann temperature). At

[1] The definition of the transition order (according the Ehrenfest scheme) is the order of the lowest derivative of the Gibbs free energy which shows a discontinuity at the transition point.

this temperature, which in reality is kinetically unreachable, a thermodynamic phase transition could take place.

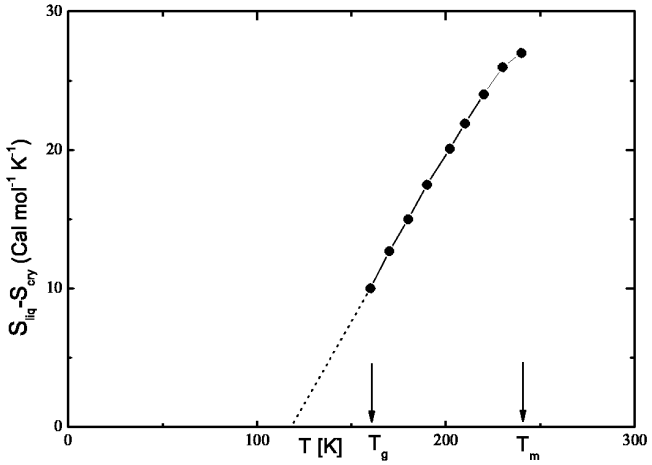

Figure 1.3: *Temperature behavior of the excess of entropy of crystalline* $H_2SO_4 \cdot 3H_2O$ *relative to its liquid phase [11].* $S_{liq} - S_{cry}$ *is equal to zero at* $T=T_k=120$ *K.*

T_k may be regarded as a limiting value that sets a lower bound on T_g. However, the Nature averts the "paradox" of negative entropy and intercedes by solidifying the liquid at T_g.

Different theories invoke other mechanisms to explain glass-transition phenomenology. Despite the variety of arguments used to describe glass forming processes, up to now a theory able to account for all of the phenomena associated with the glass transition is still lacking.

1.3 Fragility of a glass

As we have discussed in the previous paragraph a quantity that can be used to characterize the glass forming process is the structural relaxation time τ. For small departures from equilibrium and over short temperature ranges, the temperature dependence of τ can be approximated by the Adam-Gibbs equation (1.1).

Because the activation enthalpy ΔH^* is positive, a decrease in temperature results in an increases of τ and the rate of structural relaxation decelerates rapidly. The expression 1.1 can be expressed in terms of the Vogel-Fulcher equation [12, 13, 14]:

$$\tau = \tau_0 exp(DT_0/(T - T_0)), \tag{1.3}$$

here T_0 and D are parameters that depend on the system. Starting from the temperature dependence of τ it is possible to classify the systems according their ability to

change structure by varying the temperature around the glass transition temperature T_g. This classification introduces the concept of *fragility* of a glass, m [15, 16].

$$m = \left.\frac{dlog\tau}{d(T_g/T)}\right|_{T=Tg}. \tag{1.4}$$

The same quantity m can also be defined from the temperature behavior of a macroscopic quantity, such as the shear viscosity η. A simple viscoelastic model introduced by Maxwell in 1877 establishes the relationship between τ and η: $\tau = \eta/G_\infty$ (here G_∞ is the shear modulus). The temperature dependence of η and τ are very close, on decreasing the temperature the shear viscosity increases and the value of T where η=10^{12} Pa s defines the glass transition temperature T_g. Moreover, describing the temperature dependence of η by an Arrhenius expression ($\eta = \eta_0 exp(\Delta H^*_\eta/RT)$), it has been found that the structural activation enthalpies ΔH^* and the correspondent shear viscosity enthalpies ΔH^*_η have the same values suggesting that the structural relaxation process and the viscous flow under mechanical stress are controlled by the same mechanisms.

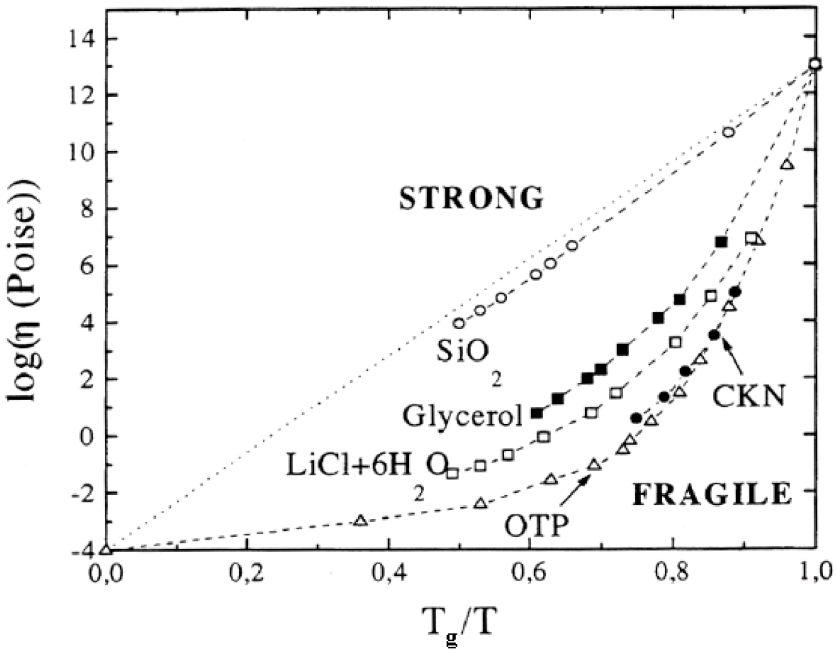

Figure 1.4: *T_g scaled Arrhenius plots for viscosities of different glass forming liquids showing a spread of data between strong and fragile extremes [17].*

Thus, it is possible to define the fragility from the shear viscosity as:

$$m = \left.\frac{dlog\eta}{d(T_g/T)}\right|_{T=Tg}. \tag{1.5}$$

In figure 1.4 we show $log\eta$ versus T_g/T, which shows clearly the difference between a system with a high value of m ("fragile"), and a system with a low value of m ("strong").

Fragile materials (as ortho-terphenyl with m=80 [18]) have a η vs T_g/T behavior that is far from the Arrhenius form of Eq. (1.1), such systems are characterized by simple Coulomb or van der Waals interaction forces. On the other hand, strong materials (e.g. SiO_2 with m=20 [18]) present covalent or directionally oriented bonds and eventually can form networking structures that strongly decrease the ability of the system to rearrange its structure with varying temperature.

1.4 Thermodynamic properties of a glass

1.4.1 General interest

A striking feature of glasses is that they exhibit a behavior markedly different from their crystalline counterpart in some thermodynamic properties such as specific heat (c_P), thermal expansion (α) and thermal conductivity (k). The purpose of this section is to give a short overview of the thermodynamic peculiarities of glasses and to show how the behavior of glasses differs from that of crystals at low temperature.

Since Zeller and Pohl (1971) [1] first found that the thermal conductivity of vitreous silica at low temperature was unexpectedly far from that of crystalline quartz, the study of the thermodynamical properties of glasses has attracted the interest of the scientific community.

Figure 1.5 shows that k has a quite different temperature behavior in crystalline and glassy states, the glass shows a slowly decreasing function in contrast to the peaked behavior characteristic of the crystal. Moreover, the difference between the two behaviors appears much more surprising because it remains at low temperatures. In fact, Debye theory [2] would predict a similar temperature dependence for the thermal properties of the two states (crystalline and glassy) at low temperature.

Debye theory ignores the lattice structure of the system, which is modeled as a continuum elastic medium and predicts a quadratic frequency distribution for the acoustic excitations of the solid. This distribution ($g(\omega)$) has a cut-off at some frequency ω_D (Debye frequency)[2] associated with a characteristic temperature Θ_D (Debye temperature) that represents the temperature needed to efficiently excite all acoustic modes. This simple theory works well for temperature low compared to Θ_D. In fact, at low temperatures the thermally excited acoustic vibrations of the solid have a wavelength much larger than the atomic scale. The continuum approximation is then satisfied.

In amorphous solids, one would expect that the low temperature continuum approximation is valid at least as well as in crystalline solids and that the behavior of the thermal properties should converge to a unique low temperature limit for both: the crystals and glasses. However Zeller and Pohl have shown that this is not the case. The low temperature properties (α, c_P, and k) are so different between a glass and

[2]The Debye frequency ω_D represents the highest frequency of an acoustic vibration that can propagate in the system.

the relative crystal that considerable efforts have been put to attempt to understand them. As a consequence of this, large variety of theories propose different origins for such differences.

1.4.2 Heat capacity

A puzzling behavior of the specific heat c_P of glassy phase has been found. The low temperature value of c_P exceeds the amount predicted by Debye theory. The continuum approximation that underly the Debye model, predicts for the specific heat a T^3 behavior as T tends to zero:

$$c_V = \frac{2\pi^2}{5}\frac{k_B^4 T^3}{\hbar^3 \rho v_D^3}, \qquad \frac{3}{v_D^3} = \frac{1}{v_l^3} + \frac{2}{v_t^3}, \tag{1.6}$$

here ρ is the mass density, and v_D is the Debye sound velocity of the system that is given by a weighted average of longitudinal (v_l) and transverse (v_t) sound velocities.

By analogy to the behavior of thermal conductivity, one would expect that as the structural disorder of a glass becomes unimportant at low temperature (see previous section), c_P should be similar to that of a crystal. Figures 1.5 and 1.6 show that c_P of the glass decreases much more slowly with temperature ($c_P \sim (aT + bT^3)$) than the Debye prediction ($c_P \sim T^3$) valid for a crystal. As a consequence, amorphous materials exhibit an excess of heat capacity at low temperature compared to the Debye limit (see fig.1.6). A bump in c_P/T^3 vs T plot of fig.1.6 is also observed in crystalline materials at higher temperature, such behavior is usually related to the effect of transverse acoustic vibrational excitations near the boundary of the first Brillouin zone.

Despite the fact that the origin of the c_P anomalous behavior of glasses has not found a unique interpretation, it has been recognized that such phenomenon reflects the presence of low frequency modes that are peculiar to the glassy state.

1.4.3 Thermal conductivity

We have an excellent understanding of the fundamental mechanism that control the thermal transport in crystals at low temperature; this contrasts with our understanding of amorphous materials, for which we have a much more primitive level of comprehension.

In a crystal, heat is transported by phonons (i.e. quanta of vibrations) which are the elementary vibrational excitations of the systems. The thermal conductivity can be expressed as [2]:

$$k = \frac{1}{3}\sum_i \int_0^{\omega_M} c_i(\omega) v_i(\omega) l_i(\omega) d\omega. \tag{1.7}$$

In Eq. (1.7) the sum is over all phonon branches (acoustic and optical see section 1.6) v_i and l_i are the phonon velocity and the mean free path. The contribution to the lattice specific heat from phonons of the ith branch and frequency ω is represented by $c_i(\omega)$. The integration in 1.7 is extended from the lowest excited frequency $\omega = 0$ to the highest ω_M excited mode.

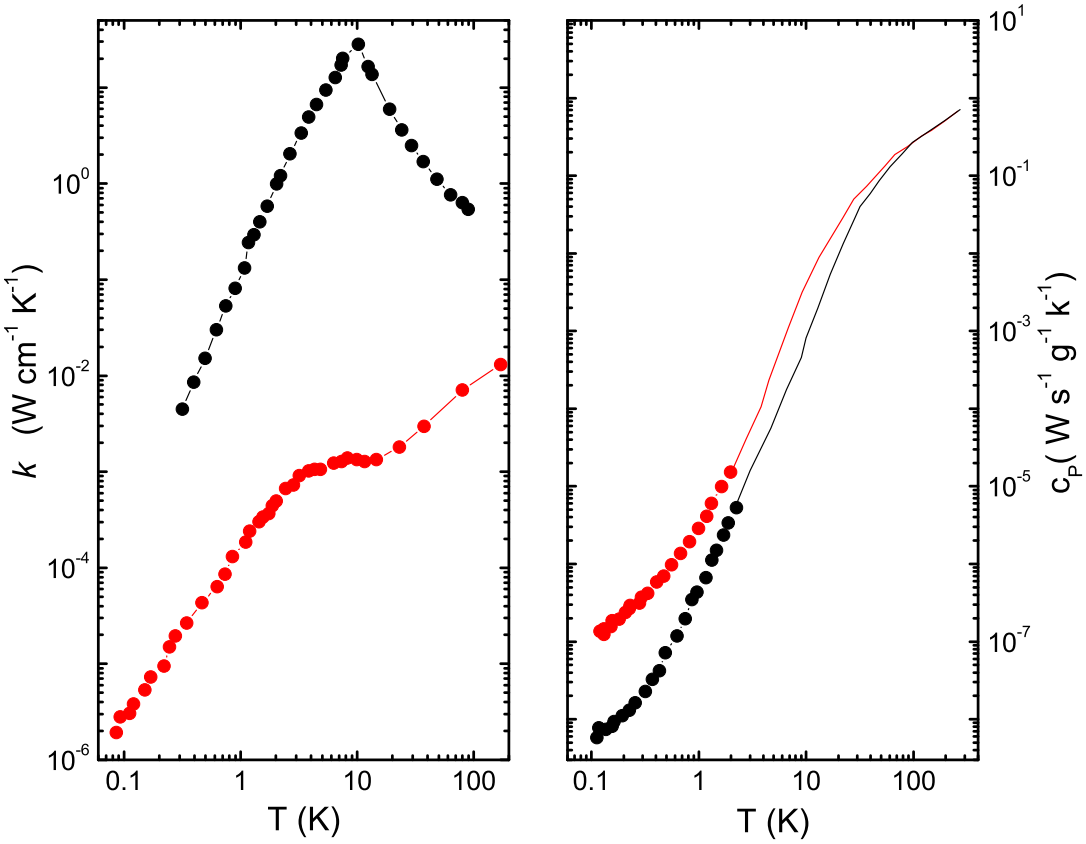

Figure 1.5: *Thermal conductivity and heat capacity measured in amorphous silica (red symbols) and α-quartz (black symbols) by Zeller and Pohl (1971) [1].*

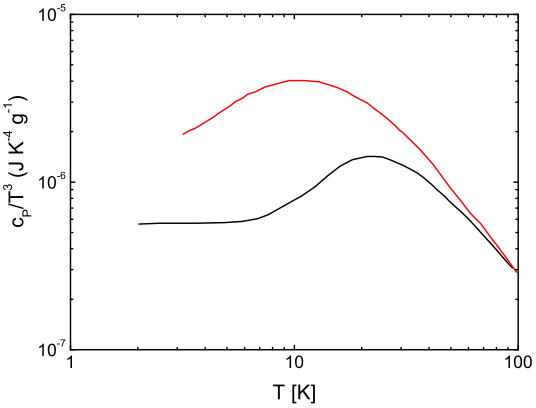

Figure 1.6: *Heat capacity measured in amorphous silica (red line) and α-quartz (black line) by Zeller and Pohl (1971)[1].*

In a crystal the mechanism of thermal conduction is based on phonons that propagate the heat through the system and the ability of this mechanism is related to the efficiency of phonons diffusions through the solid, which is limited by intrinsic scattering processes. At sufficiently low T, l becomes comparable to the size of sample. l is defined only by the dimensions of the crystal and is constant. At low temperature, the Debye approximation is valid (the wavelength of efficiently excited vibrational excitations are much larger than the typical structural inhomogeneities of the system) and k behaves as T^3. At higher temperatures, increasing the phonon population the mean free path becomes reduced by Umklapp processes. The resulting change of regime is marked by the presence of a peak in k (see figure 1.5). Moreover, decreasing the temperature an additional scattering of phonons results from the increase of the anharmonicity of the system.

In contrast, the behavior of amorphous solids is completely different at low temperature. No peak in k is observed, instead a plateau region occurs at 10 K and k behaves approximately as T^2, rather then T^3. The reason for the plateau region of k in glasses is still matter of debate. This behavior can be explained if the phonon free path is highly frequency dependent $l(\omega)$ Each temperature can then be associated to a frequency excitation ω of phonons $\hbar\omega = k_B T$ where k_B is the Boltzmann's constant. The plateau in k would then correspond to a characteristic vibrational frequency (ω_0), and this frequency marks the crossover between two regions with a different behavior of the mean free path: where for $\omega > \omega_0$ l is frequency independent, at $\omega < \omega_0$ l behaves as $\sim 1/\omega^4$. The reasons for such behavior of $l(\omega)$ must be found in a new source of phonon scattering that does not occur in crystalline phase phase.

1.4.4 Thermal expansion

The last thermal property that we discuss as example of the anomalous low temperature behavior of glasses is the thermal expansion coefficient, $\alpha = (\partial lnV/\partial T)_P$ [2].

It has been found that the value of α in glasses is much smaller then that of the crystalline phase. For instance, in vitreous silica at $T = 293$ K $\alpha = 1.4 \cdot 10^{-6}$ K^{-1} [19], smaller than that of quartz and other crystalline forms of silica by a factor 25. The access to the measurement of thermal expansion has been obtained at low temperature only since in the 1960's new reliable techniques as optical levers and capacitance methods became available. The results of these measurements of α have been interpreted in terms of *quasi-harmonic* approximation. In a harmonic model, the potential energy contains no terms beyond the second order term on the expression in the atomic displacement. This limitation inhibits the thermal expansion that can only occurs via the anharmonicity of the system. In the presence of anharmonicity (e.g. the *quasi-harmonic* approximation), the second order coefficients is volume dependent and the atomic vibrations are treated as harmonic but with volume dependent frequencies ($\omega(V)$).

Using the "*quasi-harmonic*" approximation the basic quantity to calculate the thermal expansion is the entropy S, and a change of S resulting from a change of V and T may be written [19]:

$$dS = (\partial S/\partial T)_V dT + (\partial S/\partial V)_T dV = c_V dlnT + \alpha B_T V dlnV. \tag{1.8}$$

Hence, at constant entropy $dS = 0$ we can introduce the Grüneisen parameter γ_{th}

$$\gamma_{th} = \alpha B_T V/c_V = -(\partial lnT/\partial lnV)_S, \tag{1.9}$$

here $B_T = (\partial P/\partial lnV)_T$ represents the isothermal compressibility. According to Eq. (1.9) we observe that γ_{th} is directly proportional to the thermal expansion α. Moreover, γ_{th} is the sum of all Grüneisen parameter of the vibrational modes of the system; $\gamma_{th} = \sum_i \gamma_i c_i / \sum c_i$, here c_i indicates the heat capacity contribution of the i^{th} vibrational mode. It can also be shown that γ may be expressed in terms of the volume dependence of the energy levels of the solid; thus $\gamma_i = (\partial ln\hbar\omega_i/\partial lnV)$.

In order to have a deeper understanding of the mechanisms that control thermal expansion at microscopic levels we can compare γ_{th} predicted by thermodynamics (Eq. 1.9) with the Grüneisen parameter γ_D estimated only from acoustic modes using the Debye approximation:

$$\gamma_D = \left(\frac{\gamma_L}{v_L^3} + \frac{2\gamma_T}{v_T^3}\right)\left(\frac{1}{v_L^3} + \frac{2}{v_T^3}\right)^{-1}, \gamma_{L,T} = \frac{\partial ln\omega_{L,T}}{\partial lnV}, \tag{1.10}$$

here $\omega_{L,T}$ are the corresponding frequencies of the longitudinal and transverse modes of the system. The agreement between the values of γ_{th} and γ_D of course relies on the validity of the Debye approximation and is, in general, fulfilled in crystalline solids at low temperature. In crystals the values of thermal expansion are comparable with that derived from 1.9 replacing γ_{th} with γ_D and α can be calculated directly from the volume derivatives of sound velocities. The agreement between γ_{th} and γ_D is good

in the low temperature limit where the Debye description is adequate. However, as expected, γ_{th} departs significantly from γ_D at higher temperatures.

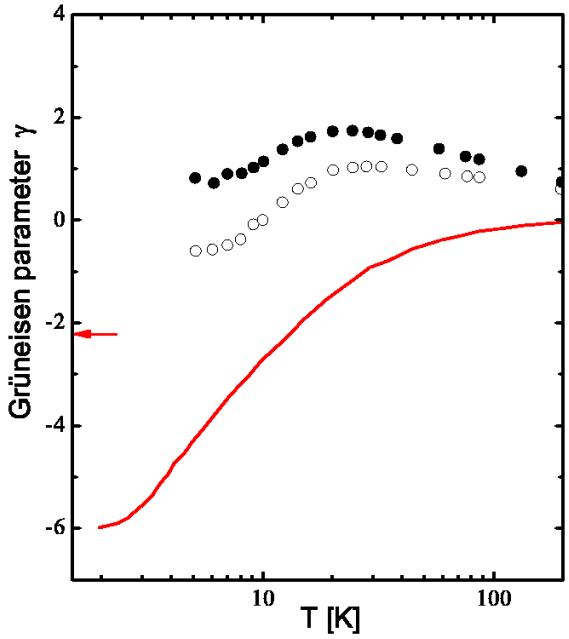

Figure 1.7: *Grüneisen parameter of silica γ_{th} (red line) and α-quartz (circles), the arrow indicates the Debye limit γ_D for the amorphous SiO_2, the full and open symbols are respectively γ_l and γ_T of the quartz [19].*

In most glasses the situation is not this simple, γ_{th} and γ_D are usually markedly different. The magnitude of discrepancy between γ_D and γ_{th} is clearly visible in figure 1.7, where at low temperature γ_{th} clearly departs from the value of γ_D. The comparison between γ_{th} and the value of the Grüneisen parameter obtained by the volume derivative of sound velocities shows that the small value of $|\gamma_{th}|$ in glasses arises from the alternate positive and negative mode Grüneisen parameters of vibrational modes (i.e. alternate sign of γ_i).

Although for practical purposes the thermal expansion is one of the most important properties of a glass, there are no satisfactory descriptions of it at the microscopic level. The study of Grüneisen parameter and then the anharmonicity in glasses will be the subject of the last chapter of this thesis.

1.5 The study of the dynamics of glassy phase

Atomic motions can be described in terms of the field of forces in which the atoms are plunged. This field can be expressed at each point $\bar{r}$ through an interaction potential $V_N(\bar{r})$ that involves all of the N atoms of the system through their positions ($\bar{r}_1$,$\bar{r}_2$,$\bar{r}_3$,.... $\bar{r}_N$). Thus, $V_N(\bar{r})$ reflects the microscopic picture of the glass and can be used to predict the thermodynamic state as well as the other properties of the system.

Atoms in a solid experience spontaneous vibrations, these motions have origin in the thermal excitations of the system. The definition of the temperature T in a solid is associated to the microscopic motions of the atoms about their equilibrium positions, this motion persists even at $T = 0$ where quantum mechanics predicts a kinetic energy different from zero [2]. The existence of thermal vibrations in solids is responsible for the transfer of heat through the system; moreover, the ability of the solid to conduct the heat can be considered as a first characterization of its vibrational properties. Nevertheless, to know more details of the mechanisms that underlie the motions of atoms it is necessary to make a more systematic observation of the microscopic vibrations of the system under controlled thermodynamic conditions. The study of the dynamics in a solid can be approached by perturbing the equilibrium of the system by an external force and recording its reaction (i.e. relaxation to the equilibrium state). Studying systematically the response, and paying attention that the perturbation does not alter too much the equilibrium properties of the system (linear response), it is possible to get information on the field of forces of the system.

The reliability of an experimental technique that follows this procedure to probe the dynamics of a solid is based on the theorem of the "linear response". This theorem sets the equivalence between the response of a system in the regime of small perturbation (linear response) and the spontaneous fluctuations in absence of the perturbation. Considering a dynamical (i.e. dependent on time t) variable of the system $B(t)$, its behavior is controlled by a Hamiltonian of the unperturbed system H_0. When a perturbation is applied to the system through an external field $F(t)$ linearly coupled to the system by another variable $A(t)$, we can write the new Hamiltonian of the system as: $H = H_0 + H'$ where $H' = A(t)F(t)$. Now the value of $B(t)$ out of the equilibrium $< B(t) >_{N.eq.}$ can be written as:

$$< B(t) >_{N.eq.} = \int_{-\infty}^{t} \theta(t-s)F(s)ds, \tag{1.11}$$

$\theta(t)$ is the response function of the unperturbed system. There are several techniques that probe the dynamics of a system in the linear regime ($H' = A(t)F(t)$); they differ in the dynamical variable perturbed, the time and the length-scales explored. In the present study we explore the dynamics of glasses in a time scale of the order of picosecond and in a region of length scale from ≈ 0.1 nm to ≈ 100 nm. In chapter 2 the main features and the interaction processes for the techniques involved in our study will be treated more extensively.

It has been possible to probe the high frequency vibrations of glasses measuring the density of vibrational states DOS using the Nuclear Inelastic Scattering. Moreover, we measured the density fluctuations of the system as function of the probed length

scale and energy using Inelastic X-ray scattering (IXS) and Brillouin Light Scattering (BLS).

The information on the dynamics of a solid collected by these techniques represents the starting point in testing microscopic models for the interpretation of the thermodynamic properties of glasses.

1.6 Vibrational modes in glasses

In the previous section it has been underlined that by studying the dynamics of a system, we have access to basic information on the microscopic mechanisms responsible for the thermodynamic properties of the solid. Nevertheless, in order to establish this link between macroscopic properties and microscopic mechanisms it is necessary to have a theoretical framework, based an assigned interaction potential for the atoms, that is able to predict the vibrational properties of the solid.

The development of such theoretical framework has been carried out since the beginning of the 20^{th} century with the classical paper of Debye (1912) [20] and Born von Karman (1912) [21]. These works were devoted to the study of normal modes and the thermodynamic properties in crystalline solids. A systematic study of the dynamics of disordered systems started in the 50's but it was not until 70's that a formalism was developed that could derive the vibrational spectrum of an amorphous material from a fixed interaction potential. The development of theoretical tools has been followed by the advent of new spectroscopic techniques: Inelastic Neutron Scattering (INS), more recently Inelastic X-ray Scattering (IXS) and Nuclear Inelastic Scattering (NIS) able to experimentally test the reliability of these models.

The difficulty in studying the dynamics of amorphous materials stems from the absence of any real simplifying feature in the geometry of the systems. There is no periodicity in the structures of glasses and then theories applicable to crystalline solids cannot be invoked. Moreover, disordered systems are not sufficiently closely related to any simpler structure that can be used in a perturbative approach to solve the problem. For this reason in amorphous materials we cannot use some of the quite familiar concepts normally associated with crystalline materials.

In a crystal a phonon is wavelike excitation extends spatially through the whole structure. This is not generally true for a disordered system where an excitation of atomic vibrations do not exhibit a well defined wavelength (λ) or wave-vector ($q = 2\pi/\lambda$).

If we consider a crystal with N identical atoms in a volume V, the position of the l-th atom can be specified by the coordinate $\vec{R}_l$: $\vec{R}_l(t) = \vec{x}_l + \vec{u}_l$ where x_l is the equilibrium position of the atom and u_l its displacement about it. The Hamiltonian of the system can written as [2]:

$$H = \frac{1}{2}\sum_{l,\alpha} m\dot{u}^2_{l,\alpha} + \frac{1}{2}\sum_{l,\alpha}\sum_{l',\beta} U_{\alpha\beta}(l,l')u_{\alpha,l}u_{\beta,l'}. \tag{1.12}$$

Here l and l' are the indexes of each particle, α that of the spatial coordinates. m_l is the mass of the particle and the matrix U is the Hessian of the potential energy relative

to the $3N$ variables.

$$U_{\alpha\beta}(l,l') = \left[\frac{\partial^2 U}{\partial u_{\alpha,l}\partial u_{\beta,l'}}\right]. \tag{1.13}$$

The force that a particle feels as effect of the other $N-1$ atoms is:

$$F_\alpha(l) = -\sum_{l',\beta} U_{\alpha\beta}(l,l')u_{\beta,l'}. \tag{1.14}$$

The equation of motion associated with Eq.(1.12) has oscillatory solutions ($u_l = e^{i(qx_l-\omega_l t)}$) in which the $3N$ values for ω can be derived from the secular equation [2]:

$$\left|D_{\alpha\beta}(l,l') - \omega^2\delta_{\alpha\beta}\delta_{ll'}\right| = 0, \tag{1.15}$$

$$D_{\alpha\beta}(l,l') = \frac{U_{\alpha\beta}(l,l')}{m}. \tag{1.16}$$

The amplitudes of the atomic vibrations $e_{\alpha,l}$ satisfy the equation:

$$\omega^2 e_{\alpha,l} = \sum_{l',\beta} D_{\alpha\beta}(l,l')e_{\beta,l'}, \tag{1.17}$$

here $D_{\alpha,\beta}(l,l')$ is called dynamical matrix, it contains all the information on the dynamical quantities of the glass. In the case of a periodic structure, like a crystal, it is convenient to express $D_{\alpha,\beta}(l,l')$ as:

$$D_{\alpha\beta}(l,l') = \frac{1}{m}\sum U_{\alpha,\beta}(l,l')e^{(i\bar{q}(\bar{x}_l-\bar{x}'_l))} \tag{1.18}$$

where $\bar{q}$ is the exchanged wave vector and $\bar{x}_l$ the coordinate of the l-atom.

Introducing the *normal modes* $Q_{q,j}(t)$ we can express the most general solution of the Hamiltonian of a crystal as:

$$\bar{u}_l(t) = \frac{1}{\sqrt{m}}\sum_{q,j} Q_{q,j}(t)\bar{e}(q,j)e^{(i\bar{q}\bar{x}_l)}. \tag{1.19}$$

Here the quantities $u_l(t)$ describe the atomic displacements and Eq. (1.19) expresses each of them as a linear combination of crystalline $Q_{q,j}(t)$. Due to the periodic structure of the crystal the eigenvectors are plane waves and the eigen-frequencies can be labeled with the wave vector and the branch index. Thus, the description of the dynamics of the crystal is reduced to that of the elementary unit cell: for each wave vector q there are $3r$ frequencies where r is the number of atoms in the elementary cell. When $r = 1$ there are only three *branches* called *acoustic* because thy are responsible for the propagation of sound in crystals. If $r > 1$, in addition to the acoustic modes, other $3(r-1)$ modes arise: these are the *optical* modes. The frequencies of these modes tend to a finite value at $q = 0$.

These classical results can be extended to the more general quantum case by replacing Q and P ($P = \dot{Q}$) by the corresponding operators and applying the usual commutation rule valid in quantum mechanics [2]:

$$\left[Q_l^\alpha, P_{l'}^\beta\right] = i\hbar\delta_{ll'}\delta_{\alpha\beta}. \tag{1.20}$$

Q and P can be expressed in terms of particle creation and destruction operators (a^+ and a^-); these particles have fixed energy ($\hbar\omega$) and satisfy the Bose statistics. Thus, the state of the crystal is defined as the state of a gas with N non- interacting particles called "phonons".

In the case of an amorphous material, the presence of the disorder has a consequence that the eigenvectors are no longer plane waves and the concept of "phonon" loses its original meaning.

A wide variety of models have been proposed to describe the effect of disorder in glasses. It has also been claimed that vibrational excitations with different nature can coexist in amorphous materials: propagating, localized and diffusive ones. However, it has been experimentally observed that, at large wavelengths, the vibrational excitations have the same propagating nature as the phonons in crystals. Such results can be confirmed theoretically for a harmonic disordered system. A strategy to solve the equation of motion, when the system lacks translational periodicity, is first to average the equations on the positions of the atoms and then solving it. This average can be expressed in terms of conditional probability for the position of the atoms [22]. Using the harmonic approximation (the potential U is expanded in terms of atomic displacements up to the quadratic term), and a pair-wise spherically symmetric potential U_N

$$U_N(r) = \frac{1}{2}\sum_{m\neq n} U(|r_m - r_n|), \tag{1.21}$$

one can express the values of the dynamical matrix components in terms of the derivatives of the potential:

$$D_{\alpha\beta} = (\rho/m)\int d(r_m - r_n)g(|r_m - r_n|)\nabla_\alpha\nabla_\beta < U(|r_m - r_n|) > [1 - e^{(ik(r_m - r_n))}], \tag{1.22}$$

where $g(r)$ is the pair correlation function that represents the conditional probability to find a particle at r when it is known that another is at $r = 0$. Choosing Cartesian coordinates with the z axis in the direction of the wave vector q, performing the spherical coordinate integration, we obtain [22]:

$$\begin{aligned} D_{xx}(q) &= (\rho/m)4\pi\int dr g(r)[rU'\left(1 - \frac{sin(qr)}{qr}\right) + \\ &\quad (r^2U'' - rU')\left(\frac{1}{3} + \frac{cos(qr)}{(qr)^2} + \frac{sin(qr)}{(qr)^3}\right)], \end{aligned} \tag{1.23}$$

$$\begin{aligned} D_{zz}(q) &= (\rho/m)4\pi\int dr g(r)[rU'(1 - \frac{sin(qr)}{qr}) + \\ &\quad (r^2U'' - rU')\left(\frac{1}{3} + \frac{sin(qr)}{qr} + 2\frac{cos(qr)}{(qr)^2} + 2\frac{sin(qr)}{(qr)^3}\right)], \end{aligned} \tag{1.24}$$

$$D_{xy}(q) = D_{yx}(q) = D_{yz}(q) = D_{zy}(q) = D_{zx}(q) = D_{xz}(q) = 0.$$

Here $U' = \partial U(r)/\partial r$ and $U'' = \partial^2 U(r)/\partial r^2$. The non-diagonal terms of the $D_{\alpha\alpha}$ are 0 due to the use of the spherical pair potential model. The diagonal terms $D_{xx} = D_{yy} = \omega_T^2$ and $D_{zz} = \omega_L^2$ are equal to the squared frequencies of the transverse (ω_T) and longitudinal acoustic excitations (ω_L).

From the asymptotic behavior of Eq. (1.24) at $q = 0$ [22] we obtain ω_L and ω_T that are proportional to q; thus, at $q = 0$ the vibrational excitations have the characteristics of propagating acoustic waves with speeds of sound equal to v_L and v_t:

$$\omega_T = v_T q, \qquad \omega_L = v_L q. \tag{1.25}$$

These results show that systems without translational periodicity can have acoustic modes even if the q wave vector cannot be used as a good quantum number to classify the vibrational modes strictly as "phonons".

It has to be underlined here that the study of the vibrational excitations in solids within the harmonic framework does not allow us to predict the damping of the vibrations. However, a first mechanism responsible for the finite life-time of a density fluctuation in a glass is associated with the disordered nature of the system. An acoustic plane wave cannot be an eigenstate of a system with non periodic structure.

In order to take into account the damping of acoustic waves related to the anharmonicity of the system we need to calculate the terms beyond the second order in the series expansion of $U(r)$. The anharmonicity is in fact responsible for a direct interaction of sound waves with other thermal vibrations.

When a sound wave passes through a solid it can be attenuated by different processes. A first source of absorption arises from the irreversible heat exchange between the compressed and the rarefied regions of the wave. Attenuation of sound wave can also occur in absence of temperature gradient according to the Akhiezer mechanism [24]. In this case the acoustic excitations, that propagate in the solid can cause a disturbance of the distribution of all phonon efficiently excited at a given temperature bringing them out of equilibrium. The thermally excited modes are driven back to thermal equilibrium with a mean thermal lifetime τ_{th}, subtracting energy from the acoustic waves and giving rise to the damping. Such mechanism in a crystal can be described as the collision between the acoustic phonons and the thermal phonons, where τ_{th} is the characteristic time between two collisions. The coupling between thermal phonon and lattice vibrations is determined by the Grüneisen parameter γ and the mean phonon lifetime τ_{th}.

In glasses in addition to the Akhiezer process, other mechanisms have been found to be relevant for the attenuation of vibrational modes. The presence of defects can produce relaxation processes in which unstable structures relax in the strain field of the sound waves. Another possible damping mechanism is the scattering of the sound wave by the static density of elastic constant distribution; a mechanism introduced for the first time by Rayleigh [25]. Finally, the tunneling model has been used to describe the energy dissipation associated with the anharmonic processes at low temperature.

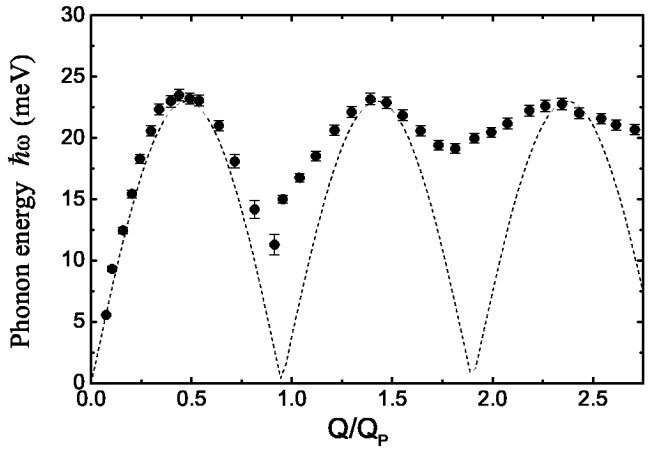

Figure 1.8: *The dots are the phonon energies measured in a metallic glass [23], the dashed line represents what expected for the respective crystal.* $Q_P/2$ *is the boundary of the pseudo-Brillouin zone of the glass.*

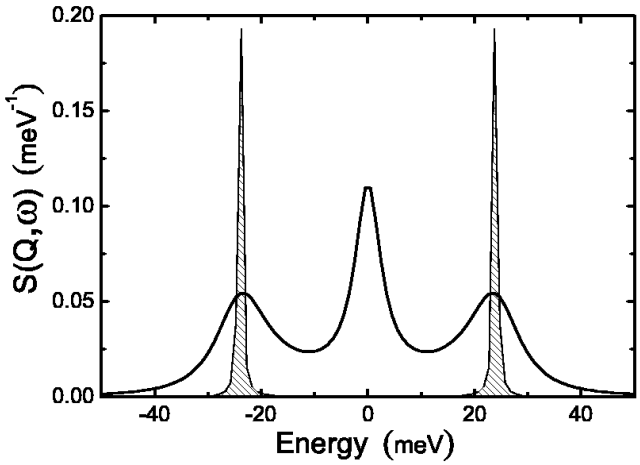

Figure 1.9: *Sketch of the typical dynamic structure factor S(Q,*ω*) of a glass (thick line) and of a crystal (dashed line) measured in the in the energy and wave-vectors regions of meV and* nm^{-1}.

In this model an energy barrier separates two energy levels of the system [26]. If the tunneling occurs, the barrier is overcame and the transition takes place. In this case as well, the coupling of the tunneling systems to the strain field is described by the Grüneisen parameter.

However, it has to be emphasized that the phenomenon of sound attenuation is still not fully understood. The presence of many competing factors that control the energy dissipations of sound waves is the origin of a vivid debate.

1.6.1 Density of vibrational States

In the previous section it has been shown that at low Q values in amorphous systems acoustic phonons can be excited.

At low frequency-i.e. in the long wavelength limit- the precise arrangement of the atoms is of little relevance, the amorphous solid appears homogeneous. The vibrational excitations at the low Q limit can therefore be properly described as acoustic modes. At higher frequencies and lower wavelengths, the modes in general are no longer plane waves. Therefore, the ω vs Q dispersion relationship loses its original meaning that is valid for crystalline systems.

It has also been pointed out in the previous section that structural disorder modifies the nature of vibrational excitations in glasses. Different mechanisms are responsible for the damping of vibrational excitations in glasses compared to those in crystals. Such differences between atomic vibrations in glasses and in crystals have been suggested from the measurements of the dynamical structure factor $S(Q,\omega)$ that in crystal and glasses show relevant differences Fig.1.91.8. $S(Q,\omega)$ represents a measure of the distribution in Q and frequency ω of vibrational excitations (see section 2.2). The $S(Q,\omega)$ therefore contains all basic information on the dynamical behavior of the system. Figure 1.9 shows that at high values of Q, when the wavelength of the excitation ($\lambda = 2\pi/Q$) is comparable with the inter-atomic distance of the system, the crystalline and glassy $S(Q,\omega)$ look quite different. In particular, phonon excitations are no longer well defined and the $S(Q,\omega)$ spectra assume the aspect of distributions of modes in the glassy systems. Both, long-range periodicity and the concept of Brillouin zone are lost, as a consequence, the frequency distribution of excitations become broader and ill-defined. The acoustic waves are no longer eigenstates of the system.

These differences between the vibrational modes of crystals and glasses lead us to look for a quantity that is able to describe the dynamics of the system and is well defined in both the crystalline and glassy states.

A quantity that fulfils these needs is the density of vibrational states DOS $g(\omega)$. In obtaining $g(\omega)$ one measures the number of modes with frequencies between ω and $\omega + \delta\omega$ [2]. This quantity is always well defined irrespective of whether the vibrational excitations are well defined or appear as distributions. The DOS can be written as:

$$g(\omega) = \frac{1}{3N}\sum_{i}^{3N}\delta(\omega - \omega_i). \tag{1.26}$$

Here the sum is extended over the all 3N possible vibrational modes of the system.

The correspondence between the $\omega - q$ relationship and the DOS in a crystal can be visualized in figure 1.10. The peaks present in the DOS of a crystal are associated with the Van Hove singularities, the region where the dispersion curve is flat with $\partial\omega/\partial q = 0$. In amorphous materials the typical sharpness of the crystalline DOS disappears, the Van Hove singularities are smeared out as a consequence of the finite width of energy distribution of vibrational excitations about a given q value. The relevance of the density of vibrational states lies not only on its definition that is not affected by the disordered nature of the system, but in the fact that it represents the natural link between the microscopic description of the glass and its macroscopic (thermodynamic) properties.

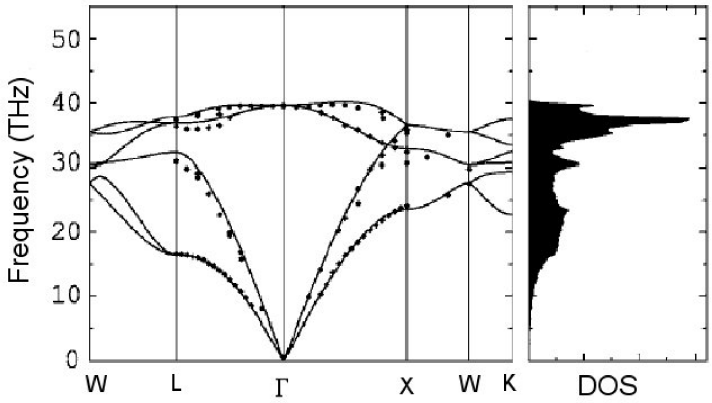

Figure 1.10: *Correspondence between the dispersion curve of a crystalline diamond (left panel) and its DOS (right panel) [27].*

Different thermodynamic quantities can be calculated directly from $g(\omega)$; for example the internal energy (U_I), the heat capacity (c_V) and the vibrational entropy (S_v):

$$U_I = \frac{3}{2}\hbar \int_0^\infty g(\omega)\omega \frac{e^{\beta\omega}+1}{e^{\beta\omega}-1} d\omega, \tag{1.27}$$

$$c_V = 3k_B \int_0^\infty g(\omega)(\beta\omega)^2 \frac{e^{\beta\omega}}{(e^{\beta\omega}-1)^2} d\omega, \tag{1.28}$$

$$S_v = 3k_B \int_0^\infty g(\omega) \left[\frac{\beta\omega}{2} \frac{(e^{\beta\omega}+1)}{(e^{\beta\omega}-1)} - ln(e^{\beta\omega/2} - e^{-\beta\omega/2}) \right] d\omega, \tag{1.29}$$

with $\beta = \hbar/k_B T$.

1.6.2 The excess of vibrational states: the Boson Peak

In the previous section it has been stressed that the density of vibrational states (DOS) $g(\omega)$ is a well defined quantity for both the crystalline and the amorphous materials.

Moreover, it has been shown that $g(\omega)$ is related to the thermodynamic properties of a glass. It is then natural to look at $g(\omega)$ for an answer to the questions concerning the origin of the anomalous low temperature behavior of glasses.

After the first measurements of c_P and k in glasses performed by Zeller and Pohl [1], much more data have been collected fora wide variety of amorphous systems. Researchers have started to attribute the low temperature peculiarities of glasses to an increase of $g(\omega)$ at low energy.

In fact, according to Eq. (1.28) and Eq. (1.7), c_P and k are related to the density of vibrational states. At low temperature, the thermally excited modes of the solid have an energy typical of the acoustic excitations (at 10 K the thermal energy corresponds to ≈ 1 meV), the wavelength of these atomic vibrations is slightly larger than the typical length-scale R of the microscopic inhomogeneities of the solid ($\lambda \geq R$). It is then expected that at low temperature the system appears as a continuum elastic medium for acoustic modes. According to this hypothesis, at low frequency no differences should be present in the $g(\omega)$ of a crystal and of a glass. However, the low-temperature *anomalies* of glasses do not validate to this simple scheme suggesting an excess of vibrational modes compared to the value expected in the continuum approximation.

In order to evaluate the influence of the DOS in the low temperature thermal properties of glasses, we consider the $g(\omega)$ predicted for a continuum medium in the Debye model [2]. Such model approximates a solid as a continuum in which acoustic waves can propagate. Thus the vibrational modes of system are described by the three branches of the acoustic modes, each with the same linear dispersion relation ($\omega = v_D q$). Here v_D is obtained by averaging the longitudinal (v_l) and the transverse (v_t) speeds of sound,

$$\frac{3}{v_D^3} = \left(\frac{1}{v_l^3} + \frac{2}{v_t^3} \right). \tag{1.30}$$

A characteristic wave-vector q_D ($q_D = (2\pi n)^{\frac{1}{3}}$, where n is the number density of the system) is defined as the maximum allowed wave-vector for the acoustic modes. q_D corresponds to the typical inverse inter-particle distance of the system. Consistently, the characteristic Debye frequency $\omega_D = v_D q_D$ and temperature $\Theta_D = (\hbar\omega_D)/k_B$ are defined. ω_D represents the highest frequency of the acoustic waves and the relative Debye temperature Θ_D indicates the temperature above which all modes are efficiently excited.

The DOS predicted by the Debye model has the following form:

$$g(\omega) = \frac{3}{\omega_D^3}\omega^2, \tag{1.31}$$

and the resulting reduced density of vibrational state $g(\omega)/\omega^2$ (RDOS) is a constant equal to $3/\omega_D^3$. The squared behavior of $g(\omega)$ is responsible according Eq. (1.28) and (1.7), for the low temperature behavior T^3 of c_P and k in agreement with the experimental data collected in crystals. In glasses, however, the low temperature anomalies of the thermodynamic properties correspond to an excess of vibrational modes above the Debye level (see figure 1.11); called the "Boson Peak" (BP).

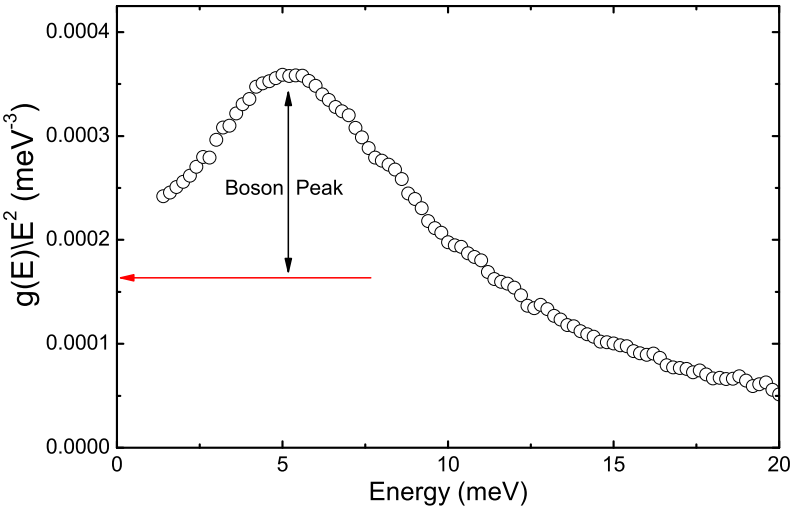

Figure 1.11: *Reduced density of state of a silicate glass (see section 3.8), the red arrow indicates the limit predicted by the Debye model, the black line measures the height of the BP.*

The first measurements of the low energy region of the DOS were performed by inelastic neutron scattering (NIS) techniques in the 60's. These studies have been extended in the last 40 years to a wide variety of materials showing that the BP can be considered as an universal signature of the glassy phase.

Experimental investigations of the behavior of the BP has taken advantage from the use of different spectroscopic techniques; mainly neutron inelastic scattering and Raman spectroscopies. In the recent years Nuclear Inelastic Scattering technique has also been used for these studies.

Due to the universal character of the BP, this feature has recently increased in interest and has been the object of active research in both theoretical and experimental directions. However, debated fundamental questions still exists:

- What is the origin of the universal character of the BP in the glassy phase?
- What is the nature of the vibrational modes in the BP energy region? Are these propagating waves or localized excitations?

In order to answer these questions different and somewhat contrasting models have been proposed in the last 30 years. In roughly chronological order the basic ideas behind these models can be listed as follows: dispersive and damped phonons, tunneling states, cavity models, cellular and microcrystalline effects, scattering from structural inhomogeneities, defects, and effects of the energy landscape of glasses.

Here we briefly discuss only some of these models relevant for the experimental investigations presented in this thesis.

- *Dynamical disorder*

  A first class of models that describes the BP is based on the presence of dynamical disorder in the glass [28, 29].

  The vibrational properties of an amorphous system are described by elastic forces K_{ij} whose strength fluctuates according a distribution density $P(K_{ij})$. Increasing the width of the distribution $P(K_{ij})$ the system becomes unstable, this instability manifests itself by the existence of negative eigenvalues for the vibrational frequencies and by the appearance of the BP. Wider is the distribution stronger the BP will be.

  According to this model the presence of the BP is connected to acoustic modes that, in the low energy region, are strongly affected by the disorder of the elastic constants. The BP is related to the lowest Van Hove singularity of the reference crystalline structure, which is shifted downwards in energy and broadened by disorder. The vibrational states responsible for the BP mainly correspond to the transverse phonon branch [28, 29].

- *Soft modes*

  Another model used to describe the DOS in glasses at low frequencies is based on the presence of *quasi-localized* soft modes [30, 31].

Here the glass is represented as a continuum elastic medium with defects that cause local vibrations with an oscillation frequency ω_0. These modes are *quasi-localized* in the sense that they describe Einstein oscillators, weakly coupled with the continuum medium, with randomly distributed frequency (ω_0). The DOS predicted by this model is able to describes the BP as well as the prevalent acoustic nature of the low frequency modes. The weak coupling between the *quasi-localized* modes and the continuum medium avoids any influence of the localized modes on the acoustic properties of the system. On the other hand the DOS is strongly affected by these *quasi-localized* modes in the energy region of the BP,.

- *Spatial correlated modes*

  The excess of DOS has been suggested to reflect a crossover from long wavelength vibrations propagating in the continuous medium to localized vibrations on a characteristic length scale $R \sim 10\mathring{A}$. R has been interpreted as the correlation length for the disordered structure of the system [32, 33]. The energy of the BP results to be inversely proportional to the size of these spatial correlated regions $\omega_{BP} \sim 1/R$.

  Different studies connect the correlation length R to the middle range order of the glass through the width or position of the first diffraction peak of the glass.

- *Energy landscape*

  Finally, one of the most recent theoretical descriptions of the BP has been built through relating the vibrational properties of glasses to their energy landscape [34]. A solid of N particles has a potential energy that depends on the $3N$ coordinates of the particles; the shape of this energy surface defines the vibrational properties of the system.

  In a glass the energy landscape is characterized by a dominant number of instable energy points (saddle points). In contrast, the crystalline phase presents a large number of stable energy points (minima). The BP is intimately connected to the energetic instability of the glass; the theory states that the height of the BP scales with the number of saddle points in the energy landscape. Such argument allows quantitative predictions about the effect of the thermal history on the height of the BP. Cooling a liquid with a fast rate results in particles becoming trapped in the glassy phase in configurations energetically more unstable compared to those obtained with a slow cooling rate. The faster is the cooling rate, the higher the intensity of the BP will be.

The models that we have briefly introduced here are representative of the wide variety of arguments used to explain the presence of the BP. Such a wide variety of descriptions has encouraged, in these last few years, an intense experimental effort on the topic. However, the comparison between models and experiments, most of the case, does not reach conclusive statements. The main difficulty in combining theoretical models and experimental observations can be summarized by a sentence present in one of the theoretical papers dedicated to the BP.

"It is well known that soluble models are not realistic and realistic models are not soluble" (G. Parisi [35]).

In this sense the simplicity of the models proposed for the BP does not help us in targeting decisive experiments. In order to reveal the details of the mechanisms responsible for the anomalous behavior of glasses one needs to perform an accurate characterization of the system under study. Moreover, the measurement of the basic quantity of these studies, the $g(\omega)$, cannot be always performed in absolute units. Thus, the discussion on the BP does not always stay on safe ground of quantitative analysis.

Résumé du chapitre 2

Ce chapitre est consacré aux deux principales techniques utilisées pour notre étude expérimentale sur la dynamique des verres: " Nuclear Inelastic Scattering " (NIS) and " Inelastic X-ray Scattering " (IXS). Dans les premiers paragraphes de ce chapitre, une brève introduction sera présentée sur l'effet Mössbauer et à son application immédiate en toute que technique spectroscopique. Cet effet permet, en analysant l'énergie des niveaux nucléaires d'un particulier isotope, d'avoir des informations sur les propriétés microscopiques du système quelles la distribution des charges autour du mme isotope. On discute le lien entre les propriétés électriques ou magnétiques d'un système et l'énergie des niveaux nucléaires des isotopes de ce système. Un paragraphe sera dédié à la présentation de la spectroscopie NIS, une technique basée sur l'effet Mössbauer qui exploite les propriétés de la radiation de synchrotron. Cette technique permet de mesurer la DOS d'un système et a été largement utilisée dans le cours de notre étude. Les principales caractéristiques de la spectroscopie utilisée pour nos mesures de NIS seront discutées. Directeur de thèse Dans la seconde partie de ces chapitre la spectroscopie IXS sera présentée, en tant que technique qui permet d'avoir accès au facteur de structure dynamique (S(Q,ω)) d'un système dans une région de moments échangés (Q) et énergies respectivement de nm^{-1} et meV. Il sera ainsi illustré le procès de diffusion inélastique, la section de diffusion et lien avec le S(Q,ω). Enfin les principales caractéristiques techniques de la ligne de diffusion inélastique ID16 a ESRF sont présentées.

Chapter 2

Experimental techniques

2.1 Nuclear resonant scattering

2.1.1 Introduction to the Mössbauer effect

The recoilless resonance absorption of γ rays from nuclei was observed for the first time in 1958 by R. Mössbauer [36]. This effect, thereafter called Mössbauer effect, has found powerful application in the development of new spectroscopic techniques.

A photon emitted in the de-excitation of a nuclear state can be absorbed by another nucleus of the same kind and excite it, the absorption takes place when the energy of the photon emitted by the nucleus matches the energy of the nuclear levels of another nucleus. However, for free nuclei the probability of absorption of photons is very small, such process can only occurs when the nucleus is forced to not recoil.

The energy distribution $N(E)$ of γ ray, emitted by a non-bonded nucleus, has a Lorentian shape with full width at half maximum Γ_0 related to the mean lifetime of the nuclear excited state τ_0 through Heisenberg's uncertainty principle; $\Gamma_0 = \hbar/\tau_0$. The momentum carried by the γ ray is transferred to the emitting free nucleus that recoils with an energy: $E_R \approx E_0^2/(2Mc^2)$, where $E_0 = E_e - E_g$ is the energy difference between excited E_e and ground E_g states and M is the mass of the nucleus. The Lorentian energy distribution of the emitted photons is centered at an energy $E_{em} = E_0 - E_R$ [37] and can be written as:

$$N(E) = N_o \frac{1}{\pi} \frac{(\Gamma_0/2)}{(E - E_{em})^2 + (\Gamma_0/2)^2}. \tag{2.1}$$

Similarly, the absorption cross section $\sigma_a(E)$ is centered at an energy $E_a = E_0 + E_R$:

$$\sigma_a(E) = \sigma_0 \frac{(\Gamma_0/2)^2}{(E - E_a)^2 + (\Gamma_0/2)^2}. \tag{2.2}$$

σ_0 is the maximum of the resonance cross section given by:

$$\sigma_0 = \frac{2\pi c^2 \hbar^2}{E_0^2} \cdot \frac{2I_e + 1}{2I_g + 1} \cdot \frac{1}{1 + \alpha}, \tag{2.3}$$

here I_e and I_g are the spins of the nuclear excited and ground states, respectively, and α the internal conversion coefficient. The factor $1/(1+\alpha)$ originates from the fact that the excited state can have a de-excitation via internal conversion with no γ ray emitted. For ^{57}Fe, α=8.14 and the contribution to the radiative decay is then only 11%.

Thus, according Eq.s (2.1) and (2.2), the emission and the absorption spectra are shifted with respect to each other by $2E_R$ preventing the resonance absorption of the emitted γ rays, due to the negligible overlap of the two distributions in the case of a free nucleus. For a ^{57}Fe atom with E_g=14.4 keV E_R is $2\cdot10^{-3}eV$. Its mean life $\tau = 141$ ns, which in energy corresponds to $\Gamma_0 = 4.7\cdot10^{-9}$eV. Therefore, for a free nucleus of ^{57}Fe $E_R >> \Gamma_0$ and according Eq. 2.1 and Eq. 2.2 the probability of resonance absorption is strongly reduced.

If now we consider nuclei bonded in a solid, there is a finite probability that absorption or emission of the photons can occur without changing the phonon state of the system. In which case, the recoil has to be felt by the solid as whole. The difference in mass between the single nucleus and the solid ($M_{solid} \approx 10^{20}M$) assures that the recoil energy of the nucleus is negligible and the emission is centered at $E = E_0$ [38]. The probability of a nucleus to absorb a γ without changing the phonon state of the system is defined as the Lamb-Mössbauer factor f_{LM}.

It is possible to calculate the probability of the resonant absorption (the magnitude of the f_{LM}) using a classical approach. Considering the nucleus bonded in a solid emitting a γ radiation of energy $E_0 = \hbar\omega_0$, we can write the vector potential as [39]: $\vec{A}(t) = \vec{A}_0 e^{i\omega_0 t}$. At high temperatures, the thermal vibration of the lattice leads to a variation of the emitted frequency via the Doppler shift $\omega(t') = \omega_0(1 + v(t')/c)$ The vector potential then becomes:

$$\vec{A}(t) = \vec{A}_0 exp\left[i\int_0^t \omega(t')dt'\right] = \vec{A}_0 e^{i\omega_0 t} e^{ikx(t)t}, \tag{2.4}$$

where x(t) is the displacement of the nucleus and $k = \omega_0/c$ the wave vector of the emitted radiation. If we apply the Einstein model of the lattice vibrations, we assume the presence of only one vibrational frequency Ω in the lattice, we write $x(t) = x_0 sin(\Omega t)$ obtaining $\vec{A(t)} = \vec{A}_0 e^{i\omega_0 t} e^{ikx_0\ sin(\Omega t)}$.

The frequency distribution of the emitted radiation consist of the frequencies $\omega_0, \omega_0 \pm \Omega$, $\omega_0 \pm 2\Omega$,.... The central line (at $\omega = \omega_0$) corresponds to a transition in which the phonon state of the system is unaltered, its intensity represents the Lamb-Mossbauer factor and is given by:

$$f_{LM} = |A_{n=0}|^2 = J_0^2(kx_0). \tag{2.5}$$

where J_0 represents the Bessel's function.

If we consider a solid with N atoms and we assume $3N$ Einstein modes, the displacement of the emitter $x(t)$ is the sum of different components: $x(t) = \sum_m^{3N} x_m sin(\Omega_m t)$ and f_{LM} can be expressed as:

$$f_{LM} = \prod_{m=1}^{3N} J_0^2(kx_m). \tag{2.6}$$

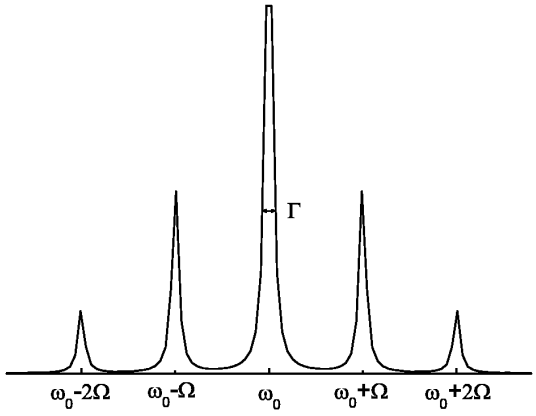

Figure 2.1: *Sketch of the frequency spectrum of a classical electromagnetic wave emitted by the nuclei of a solid according the Einstein model.*

Because f_{LM} cannot exceed 1, and $3N$ is very large, each factor of Eq. (2.6) is close to 1. The amplitude x_m is very small and we can thus expand Eq.(2.6) as a series of x_m. Truncating the series expansion of Eq.(2.6) to the quadratic term we obtain:

$$ln f_{LM} \approx -2 \sum_{m=1}^{3N} \frac{1}{4}(kx_m)^2, \tag{2.7}$$

$$f_{LM} = e^{-k^2<x^2>} = e^{-\frac{E_0^2}{\hbar^2 c^2}<x^2>}. \tag{2.8}$$

Here $< x^2 >$ is the mean square displacement of the nucleus and k the wave vector of the emitted γ-ray. It follows that in order to have a large value of f_{LM}, $k^2 < x^2 >$ should be $\ll 1$. This sets an upper limit to the energy of the emitted γ-ray at about $100 - 150$ keV, above which the resonant absorption cannot be observed. For the same reason the Mössbauer effect is basically zero in gases or liquids, where $< x^2 >$ is extremely large.

2.1.2 Classical Mössbauer spectroscopy

Using Mössbauer spectroscopy one can probe the nuclear energy levels of resonant nuclei present in a system. The nuclear energy levels E_n are influenced by the electronic and magnetic structure of the system and these perturbations are called hyperfine interactions (see following sections). The changes of E_n induced by these interactions can be larger than the natural width Γ_0 of the γ rays emitted by a recoilless nucleus. Thus, by varying continuously the energy of the γ rays emitted by a nucleus and monitoring their absorption in the probed system, is possible to study the hyperfine interactions.

A typical Mössbauer transmission experiment (sketched in fig. 2.2) consists of a γ ray source and of an absorber (i.e. the probed system) at some distance. The energy of

the γ rays emitted by a radioactive source is shifted over an energy range of some μeV via Doppler effect obtained moving the source relative to the absorber with a relative speed v. Thus the energy of the emitted γ ray E_γ can be written as $E_\gamma = E_0\left(1 \pm \frac{v}{c}\right)$, where E_0 is the energy of the γ ray when the source has v=0. From Eq. (2.1) we write the energy distribution of the emitted γ rays $I_s(v, E)$ as:

$$I_s(v, E) = \frac{f_{LM}\Gamma_0/2\pi}{(E - E_0(1 - \frac{v}{c}))^2 + (\Gamma_0/2)^2}. \tag{2.9}$$

Here $I_s(v, E)$ has been normalized to obtain $\int_{-\infty}^{\infty} I_s = f_{LM}$. The number of photons that pass through the absorber and hit the detector on the other side, depends on the number of atoms per unit number (n), thickness (d) and the absorption cross section. An interaction of a γ rays with absorber consists of two contributions: one associated with the electronic absorption σ_e and the other related to the nuclear resonant absorption σ_n. The fraction of radiation transmitted through the sample $T(E)$ can be written as:

$$T(E) = e^{-dn\sigma(E)}, \tag{2.10}$$

$$\sigma(E) = \sigma_{el} + \sigma_n(E), \tag{2.11}$$

$$\sigma_n(E) = \beta f_{LM}\sigma_0 \frac{(\Gamma_0/2)^2}{(E - E_0)^2 + (\Gamma_0/2)^2}. \tag{2.12}$$

In Eq. (2.12), β represents the isotopic enrichment of the sample. The intensity of the radiation arriving on the detector $Z(v)$ can be written as:

$$Z(v) = (1 - f_{LM})e^{-dn\sigma_{el}} + \int_0^{\infty} I_s(v, E)e^{-dn\sigma_{el}}e^{-dn\sigma_r(E)}dE. \tag{2.13}$$

The factor $(1 - f_{LM})e^{-dn\sigma_{el}}$ originates from the non resonant part of the radiation emitted by the source. The transmitted intensity I_e far from the resonance is given by $Z(\infty) = e^{-dn\sigma_{el}}$. For a thin sample ($e^{-dn\sigma_r(E)} \approx 1 - dn\sigma_r(E)$) we obtain:

$$\frac{Z(v)}{Z(\infty)} = 1 - dn\int_0^{\infty} I_s(v, E)e^{-dn\sigma_{el}}e^{-dn\sigma_n(E)}dE, \tag{2.14}$$

$$= 1 - \frac{1}{2}dn\beta f_{LM}^s f_{LM}^a \sigma_0 \frac{(\Gamma_0/E_0)^2}{(v/c)^2 + (\sigma_0/E_0)^2}, \tag{2.15}$$

where f_{LM}^a and f_{LM}^s are respectively the Lamb-Mössbauer factor of the absorber and of the emitter nucleus.

R. Mössbauer, in 1957, was the first to measure the nuclear resonant absorption [36].

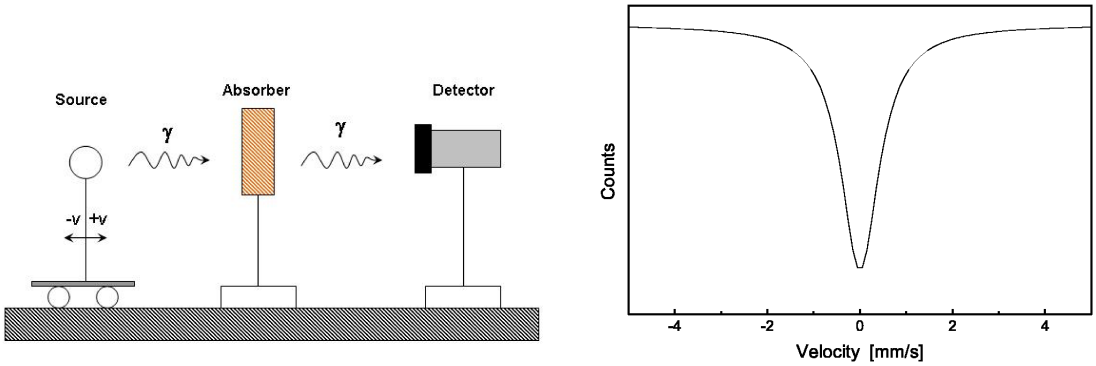

Figure 2.2: *Set-up for a Mössbauer spectroscopy experiment in transmission geometry (left panel). Sketch of the line shape of a Mössbauer spectrum in absence of splitting or shift of the nuclear levels by hyperfine interactions (right panel).*

Perturbation of the energy of nuclear levels: hyperfine interactions

In the previous section we have analyzed the nuclear resonant absorption, here we discuss how the energy of nuclear levels can be altered by the local environment around nucleus.

Nuclei are positively charged and have various kinds of nuclear moments. In addition they are surrounded by electric and magnetic fields that are created mainly by electronic charges and currents present in their own atomic shells. These fields perturb the energy of nuclear levels but their influence is so weak that these perturbations called *hyperfine interactions* [37]. The interaction Hamiltonian $\mathcal{H}$ of a nucleus can be written as [40]:

$$\mathcal{H} = \mathcal{H}_N + \mathcal{H}_C + \mathcal{H}_Q + \mathcal{H}_M = \mathcal{H}_N + \mathcal{H}_{hfs}. \tag{2.16}$$

Here $\mathcal{H}_N$ represents the energy of intranuclear forces and $\mathcal{H}_{hfs}$ is associated with the hyperfine interactions. $\mathcal{H}_C$ refers to the electric monopole interaction that is a result of penetration of electrons into the nuclear volume. $\mathcal{H}_Q$ stands for interaction of the nuclear electric quadrupole moment with the electric field gradient at the nuclear site and $\mathcal{H}_M$ represents the interaction between the nuclear magnetic dipole and the magnetic field.

Electric monopole interaction: the isomer shift

The electric monopole term has its origin in the finite probability of an electron penetrating inside the nucleus volume. The Coulomb interaction between protons and electrons inside the nucleus causes a shift in the nuclear energy levels. Assuming constant electronic charge density, $\rho(0)$, inside the nuclear volume, the energy shift δE can be written as [41]:

$$\delta E = \frac{2\pi}{3} Ze^2\rho(0) < r^2 >, \tag{2.17}$$

where $< r^2 >$ is the mean square nuclear radius. The energy shift is different for the ground and excited state and the energy of a γ ray emitted by source nuclei $(E_\gamma)_s$ is:

$$(E_\gamma)_s = (E_e + \delta E_e)_s - (E_g + \delta E_g)_s = E_0 + \frac{2\pi}{3} Ze^2\rho_s(0)(< r^2 >_e - < r^2 >_g). \tag{2.18}$$

The absorbing and emitting nuclei have different chemical environments; therefore, the absorption and emitter probability has the maximum value at different energies: $(E_\gamma)_s$ and $(E_\gamma)_a$. The energy difference between $(E_\gamma)_s$ and $(E_\gamma)_a$ is called isomer shift δE and is defined as:

$$\delta E = (E_\gamma)_s - (E_\gamma)_a = \frac{2\pi}{3} Ze^2(\rho_s(0) - \rho_a(0))(< r^2 >_e - < r^2 >_g). \tag{2.19}$$

The value of S is due mainly to the ability of electrons of s-shells to penetrate in the nucleus [41]. The total s-electron density at a nucleus is composed of a contribution from filled s-orbital of inner electron shells, as well as those electrons from chemical bonds. The changes in the valence shell (e.g. change of oxidation state, change of spin state or change of bond properties) can therefore influence the s-electron density at the nucleus. The modification may be caused either by direct altering the s-electron population in the valence shell or by shielding the s-electrons by electrons with nonzero angular momentum.

Electric quadrupole interaction: the quadrupole splitting

The electric quadrupole moment of nuclear states with spin $I > 1/2$ interacts with the non spherical symmetric distribution of electronic charges leading to so-called quadrupole splitting. The nuclear charge distribution can be described by the nuclear quadrupole moment eQ_{ij} (a 3×3 tensor of rank 2) [37]. The value of Q_{ij} differs from 0 when the nucleus is not spherically symmetrical. The distribution of the electronic charges can be described by the electric field gradient (EFG) tensor, whose components are defined as second derivatives of the electric potential V produced by extra-nuclear charges at the nuclear site $(\partial^2 V/\partial x_i \partial x_j)$. It is possible to find a principal axis coordinate system where all non diagonal components of V_{ij} vanish. Moreover, Laplace's equation requires that the trace of V_{ij} is zero $(V_{xx} + V_{yy} + V_{zz} = 0)$. The interaction of the electric quadrupole moment of the nucleus with the EFG is described by the Hamiltonian:

$$\mathcal{H}_Q = \frac{e^2 Q V_{zz}}{4I(2I-1)}[3I_z^2 - I^2 + \eta(I_x^2 - I_y^2)]. \tag{2.20}$$

Here eQ represent the nuclear charge and I_x and I_y are the components of the spin on the x and y axes. In Eq. (2.20) z has been chosen as the principal axis, thus the eigenvalues for the Hamiltonian, in the case of $I = 3/2$, are:

$$E_Q = \frac{e^2 Q V_{zz}}{12}\left[3m_I^2 - \frac{15}{4}\right]\sqrt{(1+\eta^2/3)}, \tag{2.21}$$

where η is the asymmetry parameter, $\eta = |(V_{xx} - V_{yy})/V_{zz}|$ and m_I is the magnetic quantum number. The electric quadrupole interaction leads to a splitting of the $(2I+1)$-fold degenerate energy level of a nuclear state into sub-levels characterized by the magnitude of the magnetic quantum number m_I.

As Q is constant for each nuclear level of a given Mössbauer nuclide [41], changes in the quadrupole interaction energy can arise only from changes of EFG at the nucleus. Two sources contribute to the total EFG. The first of them results from charges on distant ions that surround the Mössbauer atom, giving the lattice contribution $(V_{zz})_{lat}$. The other come from anisotropic electron distribution in the valence shell of the Mössbauer atom, the valence electron contribution $(V_{zz})_{val}$. The lattice contribution is still enhanced by the fact that the field gradient from the distant ions polarizes the electron shells of the Mössbauer atom. In contrast, the valence contribution is diminished by shielding of the core electrons. Taken together, the sum of both contributions can be expressed as:

$$V_{zz} = (V_{zz})_{lat}(1-\gamma_\infty) + (V_{zz})_{lat}(1-R), \tag{2.22}$$

whereγ_∞ is the Sternheimer anti-shielding factor that accounts for the fact that $(V_{zz})_{lat}$ induces a polarization of the electronic shell of the Mössbauer nucleus. R is the Sternheimer shielding factor that express the core electrons shielding of $(V_{zz})_{val}$. This shielding is normally much weaker than γ_∞. For ^{57}Fe we have $\gamma_\infty \approx -9$ and R=0.25-0.35 [42].

Magnetic hyperfine splitting

A nucleus with a spin $I > 0$ has a non zero magnetic dipole moment μ_I and interacts with the magnetic field B_{hf} according the Hamiltonian $\mathcal{H}_M$ [41]:

$$\mathcal{H}_M = -\vec{\mu}_I \vec{B}_{hf}. \tag{2.23}$$

The eigenvalues of the Hamiltonian are:

$$E_M = -\frac{\mu_I}{I} m_I B_{hf}, \tag{2.24}$$

where $\mu_I = (1/\hbar) g_I \mu_N I$, g_I is the Landé factor of the nuclear state with spin I and μ_N is the nuclear magneton. According to Eq. (2.24), a nuclear state I splits into an equidistant set of $2I+1$ non degenerate sub-levels characterized by the sign and the magnitude of the magnetic quantum number m_I. The selection rules for possible γ transitions are Δm=-1,0,+1, where Δm is the change of magnetic quantum number between the two nuclear states. In the case of ^{57}Fe the nuclear angular moment are I_g=1/2 and I_e=3/2, the ground state splits into two levels and the excited state into four. Six transitions are allowed.

The magnetic hyperfine field acting on a nucleus is the sum of five main contributions:

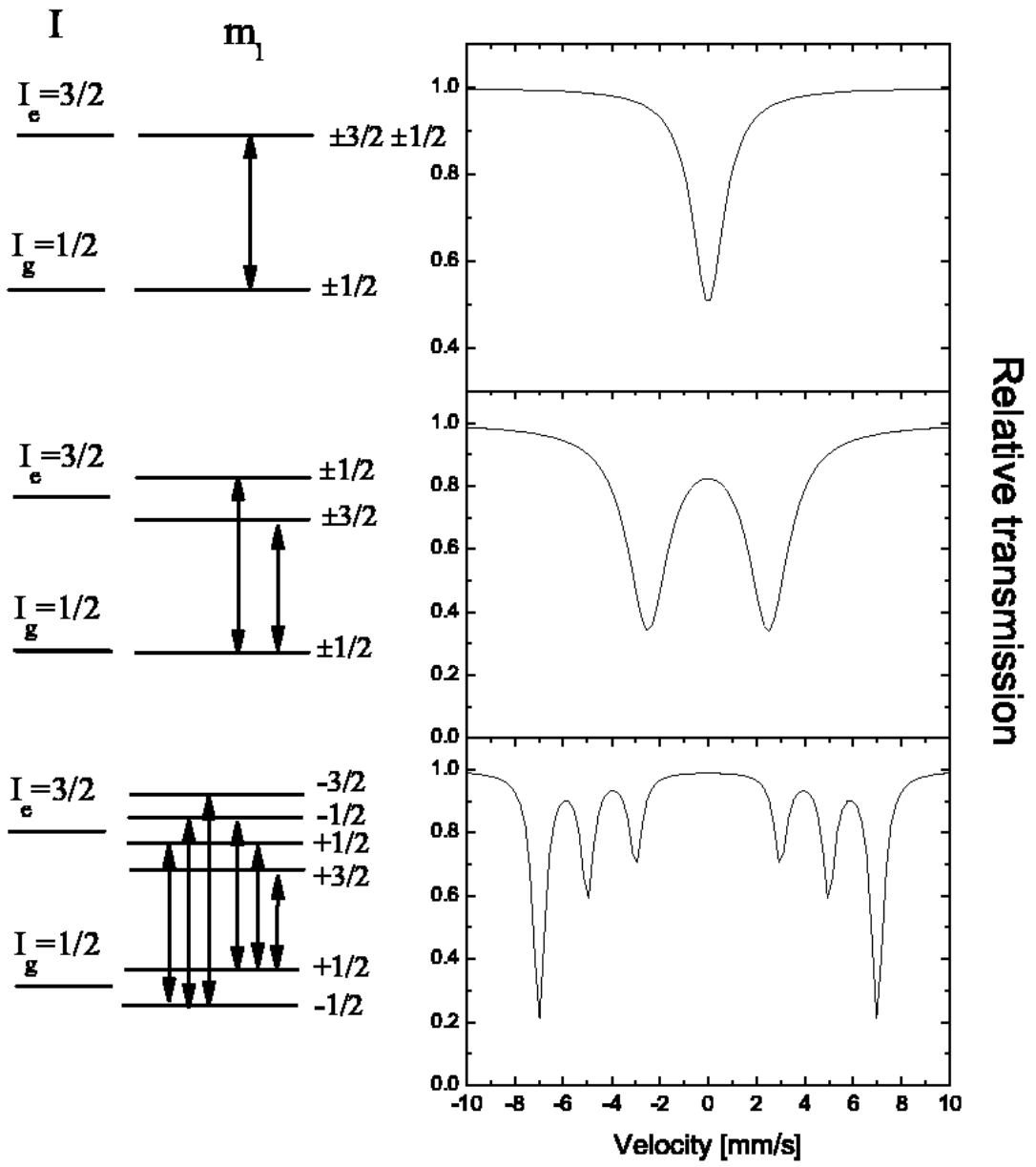

Figure 2.3: *Sketch of nuclear transitions and of the corresponding Mössbauer spectra for I_e=3/2 and I_e=1/2. Unsplit levels in the absence of hyperfine interactions (upper graph), a quadrupole splitting (middle graph) and a magnetic hyperfine splitting (lower graph) are represented.*

$$B_{hf} = B_{core} + B_{cep} + B_{orb} + B_{dip} + B_{thf}. \tag{2.25}$$

The Fermi contact or core polarization field B_{core} is due to the interaction of unpaired spin density of s-electrons at the nuclear site with the nuclear magnetic moment. Even for a closed s-shell, the net spin density is nonzero, as the spin of the s-electrons interact with the total spin of the outer electron shell (p, d and f). The conduction electron polarization field B_{cep} is the contribution from polarization of the conduction electrons by the electrons of the outer shells (like 4 f or 5 f). The conduction electrons have a finite probability to penetrate the nucleus and induce a spin density at nuclear site with a mechanism similar to the that of polarization (previously described). The orbital field B_{orb} come from the interaction of the nucleus with the orbital angular moment of the electrons of open shells. The dipolar field B_{dip} is the coupling between the magnetic moment of the nucleus and the magnetic moment associated to the spin of the electrons. The contribution is zero for s-electrons, closed or half-filled shells and for cubic local symmetry. Finally, the transferred hyperfine field B_{thf} originates from the influence of distant magnetic ions, these can polarize the core electrons or the conduction electrons via magnetic interaction.

2.1.3 Nuclear inelastic scattering

In this section, we will shortly introduce the Nuclear Inelastic Scattering (NIS), the technique that has been intensively used during this thesis work for the measurements of the density of vibrational states of glasses (see chapter three and four). NIS spectroscopy exploits the performance of third generation source of synchrotron radiation and existence of Mössbauer isotopes with resonant energies in the 10-30 keV energy range.

The principle, on which the NIS is based, is the process of nuclear absorption of a photon. NIS allows measurements of the DOS because for a particle energy transfer phonons with any momentum contribute equally to nuclear absorption. Therefore NIS represents an alternative route to access the DOS, compared to the standard experimental method of Inelastic Neutron Scattering (INS) [44]. Despite the fact that first NIS experiment was relatively recent (1995)[45] in comparison to the INS, NIS has already proven to be a very competitive technique. The NIS technique presents some relevant advantages to measure the DOS relatively to INS. In particular, NIS measures the DOS without the use of any model, in absolute scale [46]. Moreover, using x-rays as probe, small beam size can be achieved to investigate systems with small dimensions and under extreme conditions.

Absorption process is by definition specially incoherent over various nuclei, the radiation collected in an experiment of NIS is purely incoherent [43].

Such properties of NIS bypass most of the difficulties related to measurements of the DOS by INS. In fact, in order to derive the DOS of a system one has to have access to the incoherent part of the scattered radiation of the sample. With neutron scattering technique, besides the incoherent scattering, there is also the coherent contribution to the scattering of the sample. Such contribution can be evaluated from models of the probed system or can be reduced in INS experiments by making use of the

incoherent approximation: the scattered radiation with a exchanged momentum $Q \rightarrow \infty$ it is purely incoherent. This approximation can be obtained collecting the radiation scattered at high Q values. However, the price that one has to pay in the high Q region is an increase of the contribution to the total scattering of multi-phonon processes [1](that scales with Q) [44]. A reasonable compromise between the coherent and the incoherent scattering and the multi-phonon contribution is needed. The compromise is obtained considering the average of the scattering over a large range of Q values performing a subsequent evaluation of the multi-phonon contribution.

Another limitation to the accuracy of the DOS measurements performed by INS is the difficulty to obtain the DOS in absolute units. INS data are normalized using an external input parameter, the Debye Waller factor[2].

This parameter is evaluated from a model of the dynamics of the system. The same parameter also has a critical relevance the evaluation of multi-phonon contributions [44]. Conversely, with the NIS technique no theoretical model has to be invoked. Because nuclear absorption is limited to Mössbauer nuclei, it is easy to use the mass of these atoms in order to obtain a normalization constant. Furthermore, the correction for the multi-phonon contribution is straight forward. Contrary to neutrons, using NIS there are no multiple scattering processes.

Finally, we have to recall the different nuclear selectivity of INS and NIS. By definition, NIS is only sensitive to the vibrations of atoms with Mössbauer nuclei. On the other hand, the sensitivity of INS is related to the incoherent cross section of nuclear species. This difference imposes certain limitations on the accessible materials for the two techniques, giving a useful feature of site selectivity that allows considering INS and NIS as two complementary tools for the study of lattice dynamics.

Cross-section of NIS and the DOS

We want to calculate the probability of absorption or emission of a γ ray of momentum $\vec{p}$ by a single nucleus of a sample, so that, the nucleus experiences a transition from a state $|A\rangle$ to a state $|B\rangle$ and, at the same time, the solid in which the nucleus is embedded changes from a lattice state $|n_0\rangle$ to a lattice state $|n\rangle$.

As the interaction of the γ ray with a nucleus is much stronger than the interaction among different nuclei, we can consider the latter as a perturbation. The interaction operator describing the absorption of a γ ray of momentum $\vec{p}$ by a single nucleus a can be written as:

$$H' = \sum_{i=1}^{P} c a_p e^{\frac{i\vec{p}\vec{r}_i}{\hbar}} = e^{\frac{i\vec{p}\vec{R}_a}{\hbar}} \sum_{i=1}^{P} c a_p e^{\frac{i\vec{p}(\vec{r}_i - \vec{R}_a)}{\hbar}}. \tag{2.26}$$

Here $c = c(\vec{p})$ is a constant, a_p is the annihilation operator for a photon with momentum p_i, r_i is the position of the i^{th} nucleon within the nucleus; a, P is the number of nucleons in nucleus a and R_a is the position of nucleus a with respect to the center of mass of

[1] A multi-phonon process involves the creation or the annihilation of more than one phonon.

[2] The Debye-Waller factor parameter is a measure of the ratio between the inelastic and the total scatterd radiation.

the whole system of nuclei. For a transition from the state $|An_0, p\rangle$ to the state $|Bn\rangle$, the transition matrix element is:

$$\langle Bn|H'|An_0p\rangle = \langle B|\sum_{i=1}^{P} ca_p e^{\frac{i\vec{p}(\vec{r}_i-\vec{R}_a)}{\hbar}}|A\rangle\langle n|e^{\frac{i\vec{p}\vec{R}_a}{\hbar}}|n_0p\rangle. \tag{2.27}$$

Here the first term corresponds to the change in the internal state of nucleus a from $|A\rangle$ to $|B\rangle$, whereas the second term corresponds to a change in the state of the nucleus a.

We can now write, from usual dispersion theory [47], the absorption cross section of a γ ray with energy E by a nucleus a:

$$\sigma_a(E) = \frac{\sigma_0\Gamma_0^2}{4}\sum_{n,n_0} g_{n_0}\frac{|\langle n|e^{\frac{i\vec{p}\vec{R}}{\hbar}}|n_0\rangle|^2}{(E_0 - E - \epsilon_n - \epsilon_{n0})^2 + (\Gamma_0/2)^2}. \tag{2.28}$$

Here $E_0 = E_B - E_A$ is the difference between the energy of the final state (E_B) and that of the initial (E_A) of the nucleus a, e_n and e_{n0} are respectively the energies of states $|n\rangle$ and $|n_0\rangle$, of the whole system, Γ_0 is the width of the excited state of the nucleus and g_{n0} is the statistical weight factor for the state $|n_0\rangle$. In Eq. (2.28) the width of the nuclear levels Γ_0 has been assumed to be independent from the state $|n\rangle$, finally σ_0 is the resonant absorption cross section. The absorption cross section can be written in a more useful way, using the definition of the Dirac δ function:

$$\delta(x) = \frac{1}{2\pi}\int e^{itx}dt, \tag{2.29}$$

$$\sigma_a(E) = \frac{\sigma_0\Gamma_0^2}{4}\sum_{n,n_0} g_{n_0}|\langle n|e^{\frac{i\vec{p}\vec{R}}{\hbar}}|n_0\rangle|^2\int_{-\infty}^{\infty} d\rho\frac{\delta(\rho - \frac{\epsilon_n-\epsilon_{n0}}{\hbar})}{(E - E_0 - \hbar\rho)^2 + (\Gamma_0/2)^2}. \tag{2.30}$$

Therefore,

$$\sigma_a(E) = \frac{\sigma_0\Gamma_0^2}{8\pi}\int_{-\infty}^{\infty} dt\left\{\sum_{n,n_0} g_{n0}|\langle n|e^{-\frac{i\vec{p}R(\vec{0})}{\hbar}}e^{\frac{i\vec{p}R(\vec{t})}{\hbar}}|n_0\rangle > |\right\}\times\int_{-\infty}^{\infty} d\rho\frac{e^{-it\rho}}{(E - E_0 - \hbar\rho)^2 + (\Gamma_0/2)^2}. \tag{2.31}$$

Taking into account that $|n\rangle$ is an eigenstate of $\mathcal{H}$ (the Hamiltonian of the interacting system) with eigenvalue ε_n, that $|n_0\rangle$ is eigenstate of $\mathcal{H}$ with eigenvalue ε_{n0} and that the closure relation $\sum_n |n\rangle\langle n| = 1$ is applied to the state $|n\rangle$, we can write the cross section as:

$$\sigma_a(E) = \frac{\sigma_0\Gamma_0^2}{4\hbar}\int_{-\infty}^{\infty} dt e^{-it\frac{E-E_0}{\hbar} - \frac{\Gamma_0}{2\hbar}|t|}\left\{\sum_{n,n_0} g_{n0}|\langle n|e^{-\frac{i\vec{p}R(\vec{0})}{\hbar}}e^{\frac{i\vec{p}R(\vec{t})}{\hbar}}|n_0\rangle|\right\}. \tag{2.32}$$

Here the temporal evolution of operators in Heisenberg notation has been used. The quantity included in curly brackets is, at the same time, the description of the quantum mechanical and the statistical average of the operator $e^{-\frac{i\vec{p}R(\vec{0})}{\hbar}}e^{\frac{i\vec{p}R(\vec{t})}{\hbar}}$ in the state $|n_0\rangle$ at the temperature T. Therefore we write:

$$\sigma_a(E) = \frac{\sigma_0 \Gamma_0^2}{4\hbar} \int_{-\infty}^{\infty} dt e^{-it\frac{E-E_0}{\hbar} - \frac{\Gamma_0}{2\hbar}|t|} \left\langle e^{-\frac{i\vec{p}R(\vec{0})}{\hbar}} e^{\frac{i\vec{p}R(\vec{t})}{\hbar}} \right\rangle_{T,n_0}. \tag{2.33}$$

If we define a function $G_s(r,t)$ such that:

$$\left\langle e^{-\frac{i\vec{p}R(\vec{0})}{\hbar}} e^{\frac{i\vec{p}R(\vec{t})}{\hbar}} \right\rangle_{T,n_0} = \int e^{\frac{i\vec{p}\vec{r}}{\hbar}} G_s(\vec{r},t) d\vec{r}, \tag{2.34}$$

we have:

$$G_s(\vec{r},t) = \frac{1}{(2\pi)^3} \int e^{-\frac{i\vec{p}\vec{r}}{\hbar}} \left\langle e^{-\frac{i\vec{p}R(\vec{0})}{\hbar}} e^{\frac{i\vec{p}R(\vec{t})}{\hbar}} \right\rangle_{T,n_0} d\left(\frac{\vec{p}}{\hbar}\right). \tag{2.35}$$

In general $G_s(r,t)$ describes the correlation between the positions of the same particle at different times. In the classical approximation it gives the probability of finding a particle at time t at position r, if the same particle was the origin at $t = 0$.

We can now substitute the definition Eq. (2.34) into Eq. (2.33), define $E - E_0 = \hbar\omega$ and $p = \hbar k$, obtaining:

$$\sigma_a(E) = \frac{\sigma_0 \Gamma_0^2}{4\hbar} \int_{-\infty}^{\infty} dt \int_0^{\infty} d\vec{r} e^{-i(\vec{k}\vec{r} - \omega t) - \frac{\Gamma_0}{2\hbar}|t|} G_s(\vec{r},t). \tag{2.36}$$

It is worthwhile to mention that the incoherent differential scattering cross section for slow neutrons is proportional to the integral in Eq. (2.36) [48]. In order to calculate $\sigma_a(E)$ one needs an explicit form for $G_s(r,t)$. It can be calculated rigorously only in the case of a Maxwellian gas or for a solid in the harmonic approximation. In these two cases, van Hove has shown [48] that the self-correlation function has the general form.

$$G_s(\vec{r},t) = \frac{1}{[2\pi\gamma(t)]^{\frac{3}{2}}} e^{-\frac{r^2}{2\gamma(t)}}. \tag{2.37}$$

For a monatomic cubic crystal [48] we have:

$$\gamma(t) = \frac{\hbar}{M} \int_0^{\infty} \left[\left(1 - cos\frac{zt}{\hbar}\right) coth\left(\frac{z}{2k_B T}\right) - isin\left(\frac{zt}{\hbar}\right) \right] \frac{g(z)}{z} dz, \tag{2.38}$$

where M is the mass of the nucleus and g(z) is the distribution of energy levels of the phonons (i.e. the phonon density of states) normalized so that $\int_0^{\infty} g(z)dz = 1$ and where g(z)=0 beyond $z = z_{max}$. With some algebra and the definition $2W = (k^2\gamma(\infty))/2$ one can write a new expression for the cross section [49]:

$$\sigma_a(E) = 2\pi \frac{\sigma_0 \Gamma_0}{4\hbar} e^{-2W} \left\{ \frac{\hbar\Gamma_0/2\pi}{(E-E_0)^2 + (\Gamma_0/2)^2} + \sum_{n=1}^{\infty} \frac{(k^2/2)^n}{n!} \frac{1}{2\pi} \int_{-\infty}^{\infty} dt e^{-i(\omega t - \omega t) - \frac{\Gamma_0}{2\hbar}|t|} [\gamma(\infty) - \gamma(t)]^n \right\}. \tag{2.39}$$

We define:

$$\int_0^\infty \frac{g(z)}{z} coth\left(\frac{z}{2K_BT}\right) dz = F(T), \tag{2.40}$$

from which it follows that $2W = \frac{\hbar^2 k^2}{2M} F(T)$. The cross section then becomes:

$$\sigma_a(E) = \frac{\sigma_0 \Gamma_0 \pi}{2\hbar} e^{-2W} \left\{ \frac{\hbar\Gamma_0/2\pi}{(E-E_0)^2 + (\Gamma_0/2)^2} + \sum_{n=1}^{\infty} \frac{(2W)^n}{n!} \frac{1}{2\pi} \frac{1}{F(T)^n} \int_{-\infty}^{\infty} dt e^{-i(\omega t)} \right.$$
$$\left. \times \left[\int_0^\infty \frac{g(z)}{z} coth\left(\frac{z}{2k_BT}\right) cos\left(\frac{zt}{\hbar}\right) dz + \int_0^\infty \frac{g(z)}{z} isin\left(\frac{zt}{\hbar}\right) dz \right]^n \right\}. \tag{2.41}$$

If one chooses $E_0 = 0$, sets $1/(k_BT) = \beta$ and defines the function $S_1(E,T)$ as:

$$S_1(E,T) = \left\{ \frac{g(|E|)}{2F(T)E} \left[coth\left(\frac{\beta E}{2}\right) + 1 \right] \right\} = \frac{g(|E|)E_R}{2WE} \left(\frac{1}{1-e^{-\beta E}} \right), \tag{2.42}$$

the absorption cross section can be written in its final form:

$$\sigma_a(E) = \frac{\sigma_0 \Gamma_0 \pi}{2\hbar} e^{-2W} \left\{ \delta(E) + 2W S_1(E,T) + \sum_{n=2}^{\infty} \frac{(2W)^n}{n!} S_n(E,T) \right\}, \tag{2.43}$$

where:

$$S_n(E,T) = \int_{-\infty}^{\infty} S_1(E-E',T) S_{n-1}(E,T) dE'. \tag{2.44}$$

The first term inside the curly brackets in Eq. (2.43) gives a sharp absorption peak that represents the recoilness absorption of γ-rays and therefore corresponds to an elastic process. The other terms are the inelastic interactions accompanied by phonon exchange: the term containing the $S_1(E,T)$ describes the absorption of a γ ray associated with creation or annihilation of one phonon (single phonon term) while the term containing the $S_n(E,T)$ is the absorption of a γ ray with creation and/or annihilation of n phonons (multi-phonon term).

Thus, according to Eq. (2.43) from the inelastic absorption process, once isolated the one phonon term from the multi-phonon contribution, one can derive the DOS of the resonant nuclei. This procedure can be carried out using the forward and the back Fourier transform of the experimental data. The experimental energy spectrum of NIS is directly proportional to the absorption cross section; the entire spectrum can be written as [50]:

$$I(E,k) = I_0 \int dE' P(E') \sigma_a(E-E') \tag{2.45}$$

where $P(E)$ is the instrumental function. The single-phonon contribution to the cross section can be obtained by dividing the Fourier transformation of the experimental data $\int dE e^{iE\tau} I(E,k)$ by the Fourier transformation $Q(\tau)$ of the experimental function.

The logarithm of this ratio separates the single phonon term from the multi-phonon contribution.

$$J(k,\tau) = \frac{\int dE e^{iE\tau} I(E,k)}{I_0 f_{LM} Q(\tau)}, \tag{2.46}$$

$$M(k,\tau) = ln(1 + J(k,\tau)), \tag{2.47}$$

$$M(k,\tau) = \int dE e^{(iE\tau)} S_1(E). \tag{2.48}$$

Finally, from the reverse Fourier transformation, we can obtain the partial density of phonon states:

$$g(E) = \frac{E}{E_R}(1 - e^{-\beta E}) \int \frac{d\tau}{2\pi} e^{-\imath E\tau} M(k,\tau). \tag{2.49}$$

2.1.4 Experimental set-up

As the intensity of the radiation emitted in the nuclear resonant process is much weaker than that scattered by the electrons of the system, the main problem dealing with nuclear spectroscopy is to separate the two scattering contributions. This task is accomplished using two mechanisms simultaneously. Firstly, the broadband synchrotron radiation is monochromatized to meV, in order to reduce the ratio between electronic scattering and nuclear scattering. Secondly, electronic scattering is much faster than the nuclear scattering ($\approx 10^{-15}$s for electronic scattering as compared to $\approx 10^{-8}$s for nuclear scattering). In order to separate in time the fast electronic scattering from the slow nuclear scattering it is possible to use the pulsed time structure of synchrotron radiation.

If two successive pulses have a time difference comparable or larger than the nuclear lifetime then it is possible to detect the delayed photons of the nuclear deexcitation, in a time window that is completely free from the contribution due to electronic scattering. The electronics used for the data collection allow discriminating the scattering from the electrons, i.e. the signal that arrives at early times after the passage of the bunch of electrons in the undulator. Proper synchronization of the system of data collection with synchrotron radiation pulses allows accepting of only the counts from the delayed nuclear scattering. In the "16-bunch mode" of the synchrotron operation at the ESRF, 16 equally spaced bunches of electrons produce 16 pulses of synchrotron radiation, each with a duration $\approx$ 100 ps and with a separation of 176 ns between two consecutive pulses. This is particularly favorable for ^{57}Fe, which has a lifetime τ_0=141 ns. The scattering from the electrons takes place almost instantaneously (on the time scale of nuclear scattering) when the pulse hits the target, and the products of the nuclear de-excitation can be observed in the time between two pulses.

In a NIS experiment, the delayed nuclear scattering is integrated over the whole available time window, and its energy dependence is studied. It is therefore necessary to have a high resolution monochromator with an energy resolution of $\sim$ meV allowing the study of lattice dynamics. The typical experimental set-up of the nuclear resonance

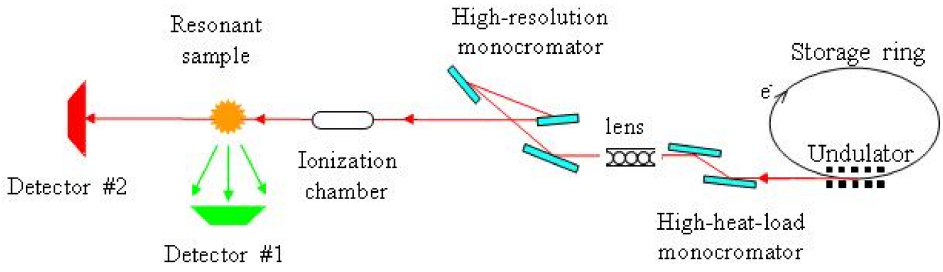

Figure 2.4: *Sketch of the experimental layout of the ID-18 beam-line.*

beam-line ID-18 is shown in figure 2.4. A synchrotron radiation beam is produced by three undulators (1.5 m per segment, minimum gap of 11 mm and a period of 32 mm for two and 20 mm for the third) optimized for the energy of the ^{57}Fe nuclear transition: 14.4 keV. The beam is monochromatised in two stages. In the first stage, the bandwidth is reduced down to few eV by a high-heat-load monochromator.

The high-heat-load monochromator has the task of handling the heat load of the "white" radiation produced by the undulators and reducing the energy bandwidth of the radiation to the eV region ($\Delta E/E \sim 10^{-4}$). This is obtained with two Si (1 1 1) reflections. The crystals are cut slightly asymmetric to match the angular acceptance of the x-ray. The offset between the incoming and the out-coming beam is 25 mm, the monochromator can easily be tuned over the energy interval between 6 and 30 keV. In the second stage, the bandwidth is reduced down to the meV region ($\Delta E/E \sim 10^{-7}$) by a high resolution monochromator HRM. A narrow energy bandpass is achieved with high order reflection, which provides large angle-energy dispersion and has small angular acceptance. A triple set of crystals gives an energy resolution of 0.5 meV at 14.4 keV keeping the flux as high as $5.5{\cdot}10^8$ photons/s (at 90 mA synchrotron current). With this setup of the HRM it is possible to switch among energy resolution of 0.5, 1 and 2 meV. However, the HRM can only be tuned over a limited energy interval, and it is necessary to design a special HRM for each Mössbauer isotope. For better matching the beam divergence to the angular acceptance of the first crystal of the HRM, collimating lens have been installed downstream of the high heat-load monochromator. For example at 14.4 keV, the intrinsic divergence of the x-ray beam of about 14 μrad has been decreased to 1.7 μrad.

After the high-resolution monochromator, the beam passes through ionization chamber, which monitors the flux of incident radiation. As the nuclear scattering has to be separated in time from the electronic one, a fast detector (with ns to sub-ns time resolution) with fast recovery time is mandatory. The detector must survive the intense initial flash and be able to count a single photon event from the delayed nuclear radiation few nanoseconds later. The detectors used for NIS experiments at ID-18 are avalanche photodiodes (APD) characterized by a time resolution between 100 ps and 1 ns.

An APD is placed in forward direction and detects the delayed photons that have

interacted elastically with the target.

In order to collect in the widest possible solid angle the secondary products of nuclear absorption (atomic fluorescence) another APD is placed as close as possible to the target. The products of nuclear deexcitation can be observed within a wide solid angle around the target. The energy transfer from the x-rays to the system are determined as a difference between the energy of the incident radiation and that at the resonance (i.e. 14 keV). In NIS, the narrow width of nuclear levels ($\sim$ neV) makes the nuclear resonance itself an ideal energy reference. At the resonance ($E = E_0$), the APD counts the absorption events after having excited elastically the nuclei of the target, whereas at energies above or below resonance the APD detects the nuclear absorption process after having inelastically excited the nuclei of the target. In this case the nuclear resonance can be excited by creating ($E > E_0$) or annihilating ($E < E_0$) phonons.

2.2 Inelastic X-ray Scattering

In this section the theory of Inelastic X-ray Scattering (IXS) is presented in the first two sections. The basic working principles of an IXS spectrometer are discussed in the last section with reference to beamline ID-16 at the European Synchrotron Radiation Facility.

2.2.1 IXS cross-section

The energy dependence of the Inelastic X-ray Scattering provides a direct determination of the coherent dynamical structure factor, $S(Q, \omega)$, whenever the listed hypotheses hold [51]:

- The scattering process is dominated by the Thomson term and both the resonant and the spin-dependent contributions to the electron-photon interaction can be neglected.
- The center of mass of the electron cloud follows the nuclear motion without delay; i.e. the adiabatic approximation is valid.
- There are no electronic excitations in the considered energy transfer range.

The IXS scattering schematics is illustrated in fig. 2.5. Here, and in the following, the suffixes "i" and "f" refer to the incident and scattered photon, respectively. The incoming photon, characterized by its energy $\hbar\omega_i$, wave-vector $\vec{k}_i$, and polarization $\widehat{\varepsilon}_i$, is scattered by the sample at an angle 2θ within a solid angle $d\Omega$. The energy, wave-vector and polarization vector of the scattered photon are denoted by: $\hbar\omega_f$, $\vec{k}_f$ and $\widehat{\varepsilon}_f$, respectively. According to energy and momentum conservation laws, the momentum and energy transfer to the sample are:

$$\hbar\omega \equiv \hbar(\omega_f - \omega_i) \qquad \text{and} \qquad \hbar\vec{q} \equiv \hbar\left(\vec{k}_f - \vec{k}_i\right). \tag{2.50}$$

In the limit $\omega \ll \omega_i$, which is the case for IXS, the modulus of $\vec{k}_i$ and $\vec{k}_f$ are basically the same, and the modulus of the exchanged momentum is entirely determined by the scattering angle 2θ and the wave vector k_i:

$$q = 2|\vec{k}_i|sin(2\theta/2) \tag{2.51}$$

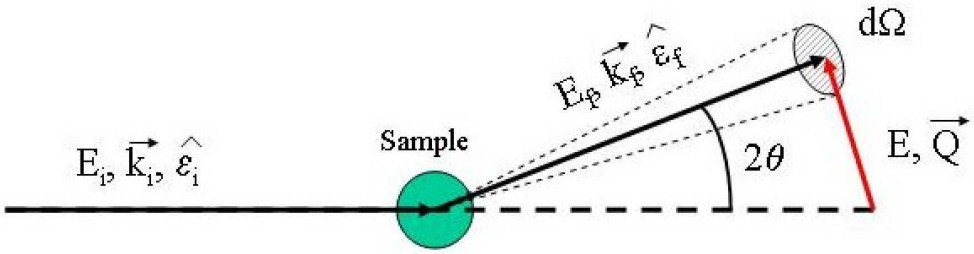

Figure 2.5: *Kinematics of a scattering experiment.*

The double differential cross section, $\partial^2\sigma/\partial\Omega\partial\omega_f$, representing the fraction of photons having frequency $\omega_f \pm d\omega_f$ scattered into a solid angle $d\Omega$ around the direction defined by $\vec{k}_f$, can be calculated within the frame of linear response theory assuming a weak coupling between the probe and the system. In this approximation the double differential cross section can be regarded as an intrinsic property of the unperturbed sample. Neglecting the interaction of the probe (i.e. the incident photons) with the nuclei, in the weak relativistic limit the interaction between probe and system is described by the photon-electron interaction Hamiltonian, $\mathcal{H}_{int}$. It consists of four terms [53]:

$$\mathcal{H}_{int} = \frac{e^2}{2mc^2}\sum_j \vec{A}(\vec{r}_j,t)\cdot\vec{A}^*(\vec{r}_j,t) + \frac{e}{2mc}\sum_j \vec{A}(\vec{r}_j,t)\cdot\vec{p}_j(\vec{r}_j,t) - \\ -\frac{e}{mc}\sum_j \vec{s}_j\cdot\vec{A}(\vec{r}_j,t) - \frac{e^2}{2m^4c^4}\sum_j \vec{s}_j\cdot(\frac{d\vec{A}}{dt}(\vec{r}_j,t)\times\vec{A}(\vec{r}_j,t)). \tag{2.52}$$

The sum extends over all the electrons in the system, the electron positions, momenta and spins are indicated as $\vec{r}_j$, $\vec{p}_j$ and $\vec{s}_j$, respectively. m and e are the electron mass and charge, while c is the speed of light. Finally, $\vec{A}(\vec{r}_j,t)$ is the vector potential of the photon electromagnetic field, which, in the quantum electrodynamic representation with the gauge $\nabla\cdot\vec{A}(\vec{r}_j,t) = 0$, can be written as [54]:

$$\vec{A}(\vec{r}_j,t) = \left(\frac{4\pi c^2}{V}\right)^{1/2}\sum_\lambda [a_\lambda\hat{\epsilon}_\lambda e^{i(\vec{q}_\lambda\cdot\vec{r}_j)} + a^*_\lambda\hat{\epsilon}_\lambda e^{-i(\vec{q}_\lambda\cdot\vec{r}_j)}], \tag{2.53}$$

where a_λ and a^*_λ are the λ-th components of the photon annihilation and creation operator, and $\hat{\epsilon}_\lambda$ is the polarization of the electromagnetic field.

The first term in Eq. (2.52) describes the diamagnetic coupling between electron current and photon electric field (Thomson scattering). The second term accounts

for paramagnetic coupling responsible for the absorption/emission of a photon by the electron system. The last two terms describe respectively the coupling of the electron spins to the photon magnetic field and the spin-orbit interaction.

For photon energies of the order of 20 keV (i.e. energies $\ll mc^2$, where mc^2 is the rest mass energy of the electron) the magnetic terms are smaller than the first two terms by a factor of 10^{-2}, and will be therefore neglected. Furthermore, the paramagnetic contribution can also be neglected if we consider photons with energies away from any absorption resonance. The interaction Hamiltonian therefore simplifies to:

$$\mathcal{H}_{int} = \frac{e^2}{2mc^2} \sum_j \vec{A}(\vec{r}_j, t) \cdot \vec{A}^*(\vec{r}_j, t). \tag{2.54}$$

The double-differential cross-section can be determined in the framework of first order perturbation theory, according to the Fermi golden rule [55]. Considering the initial and final photon states, $|I\rangle$ and $|F\rangle$ as plane waves, the double-differential cross-section can be written as:

$$\frac{\partial^2\sigma}{\partial\Omega\partial\omega_f} = r_0^2 \left(\frac{k_f}{k_i}\right) (\hat{\varepsilon}_f \cdot \hat{\varepsilon}_i)^2 \sum_{I,F} P_I \left| \left\langle F \left| \sum_j e^{i\vec{q}\cdot\vec{r}_j} \right| I \right\rangle \right|^2 \delta(\hbar(\omega - \omega_F + \omega_I)), \tag{2.55}$$

where $r_0 = e^2/mc^2$ is the classical electron radius and P_I is the equilibrium number of initial states of the system over all the possible states.

Within the validity of the adiabatic approximation, the atomic quantum state, $|S\rangle$, can be factorized into its electronic, $|S_e\rangle$, and nuclear, $|S_n\rangle$, part. This approximation is particularly good for exchanged energies that are small compared to the electron excitation energies. In this case, the contribution to the total scattering coming from the valence electrons close to the Fermi level is small compared to the contribution coming from the core electrons [55]. The double differential cross section, under these hypotheses, can be written as:

$$\frac{\partial^2\sigma}{\partial\Omega\partial\omega_f} = r_0^2 \left(\frac{k_f}{k_i}\right) (\hat{\epsilon}_f \cdot \hat{\epsilon}_i)^2 \sum_{I_n,F_n} P_{I_n} \left| \left\langle F_n \left| \sum_j f_j(\vec{q})\, e^{i\vec{q}\cdot\vec{R}_j} \right| I_n \right\rangle \right|^2 \delta(\hbar(\omega - \omega_F + \omega_I)), \tag{2.56}$$

where $f_j(q)$ is the atomic form factor of the j^{th} atom with position vector $\vec{R}_j$, while the suffix "n" refers to the nuclear states. Now the sum extends over all the atoms of the system. Assuming that all the scattering units in the system are equal, this expression can be further simplified by factorization of the form factor. At the $q \to 0$ limit, $f(q)$ is equal to the number of electrons in the atom. For increasing values of q the form factor decays almost exponentially with a decay constant determined by the radial distribution of the electrons in the atomic shells of the considered atom. Using the Van Hove pair correlation function, $S(q, \omega)$ can be formally written as [48]:

$$S(\vec{q}, \omega) = \frac{1}{2\pi\hbar N} \int_{-\infty}^{+\infty} e^{i\omega t} \langle \sum_{jk} e^{i\vec{q}\cdot\vec{R}_j(t)} e^{-i\vec{q}\cdot\vec{R}_k(0)} \rangle dt, \tag{2.57}$$

where N is the number of particles in the system. Combining Eq. (2.57) and (2.56) one obtains:

$$\frac{\partial^2\sigma}{\partial\Omega\partial\omega_f} = r_0^2 \left(\frac{k_f}{k_i}\right) (\hat{\epsilon}_f \cdot \hat{\epsilon}_i)^2 |f(q)|^2 S(q,\omega). \tag{2.58}$$

This derivation is strictly valid for monatomic systems, but it can be easily generalized to molecular systems with several atomic species by replacing the atomic form factor with the molecular one. In the case of non-crystalline samples with different atoms the procedure to determine the scattering cross section is more complicated. The formalism introduced here is still valid if we assume that the cross section splits into two components: a coherent and an incoherent term. The latter is associated with fluctuations of the form factor while the former is proportional, through the mean value of the form factor, to $S(\vec{q},\omega)$ [52]:

$$\frac{\partial^2\sigma}{\partial\Omega\partial\omega_f} = r_0^2 \left(\frac{k_f}{k_i}\right) (\hat{\epsilon}_f \cdot \hat{\epsilon}_i)^2 [\langle f(q)\rangle^2 S(\vec{q},\omega) + \langle \delta f(q)^2\rangle S_s(q,\omega)]. \tag{2.59}$$

Here $\langle f(q)\rangle^2$ is the average value of the form factor over the whole system while $\langle \delta f(q)^2\rangle$ is the average of its fluctuation. The incoherent part of the cross section is given by $S_s(q,\omega)$, which describes the single particle dynamics rather than the collective behavior.

In order to derive the effective intensity of the radiation collected in an IXS experiment, absorption processes have to be considered as well. In fact, the number of photons (N) that, per unit time, are scattered into the solid angle ($d\Omega$) and in the frequency interval ($d\omega$) are given by [52]:

$$N = N_0 \frac{\partial^2\sigma}{\partial\Omega\partial\omega} d\Omega d\omega n L e^{-\mu L}, \tag{2.60}$$

where N_0 is the number of incident photons per seconds, n is the number of an atoms per unit volume, L is its length along the scattering path and μ is the total absorption coefficient. The maximum IXS intensity is achieved for $L = 1/\mu$, and consequently $N \propto 1/\mu$. Considering X-ray energies of ≈ 20 KeV and $Z > 3$, μ is almost completely determined by the photoelectric absorption process. In this process $\mu \propto Z^3$, with important modifications at energies close to the electron absorption edges. Consequently, the scattering volume of high Z materials is very much reduced, while, on the other hand, the cross section increases as Z^2. Fig. 2.6 reports the scattering intensity for an IXS experiment, as a function of Z, in the case of a sample with optimum thickness and an incident photon energy of 17.8 KeV.

2.2.2 Dynamic structure factor and phonons

In this paragraph it is shown how the dynamic structure factor is related to the quanta of vibrational energy of a system: the phonons [52]. The simplest case is represented by an ideal Bravais lattice with only one atom per unit cell. Being $\vec{u}_j(t)$ the atomic displacement of atom j relative to its lattice equilibrium position, $\vec{R}_j$, its instantaneous position, $\vec{R}_j(t)$, can be expressed as follows:

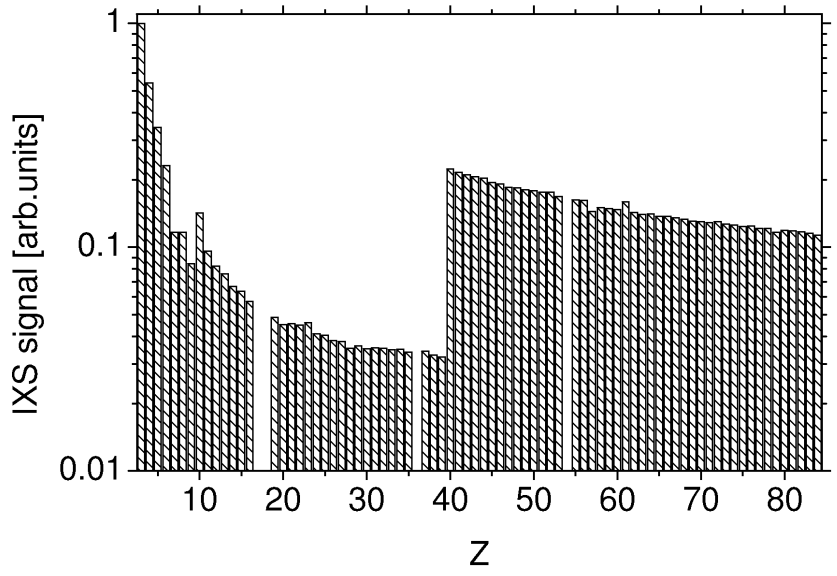

Figure 2.6: *Relative intensity of Inelastic X-ray Scattering, for an optimum sample thickness ($L = 1/\mu$), as a function of the atomic number Z at the photon energy of 17.8 KeV, in the small Q-limit (i.e. $f(Q) = Z$). The large discontinuity between $Z = 39$ and $Z = 40$ is due to the K absorption edge of zirconium.*

$$\vec{R}_j(t) = \vec{R}_j + \vec{u}_j(t) \tag{2.61}$$

The dynamic structure factor (eq.2.57) reads:

$$S(q,\omega) = \frac{1}{2\pi\hbar N}\sum_{j,k} e^{i\vec{q}\cdot(\vec{R}_j-\vec{R}_k)}\int_{-\infty}^{+\infty} e^{i\omega t}\langle e^{-i\vec{q}\cdot\vec{u}_k(0)}e^{i\vec{q}\cdot\vec{u}_j(t)}\rangle dt. \tag{2.62}$$

In the framework of second quantization, the displacement is given by [56]:

$$\vec{u}_j(t) = \sqrt{\frac{\hbar}{2MN}}\sum_{s,\vec{q}}\frac{\hat{\epsilon}_{s,\vec{q}}}{\sqrt{\omega_s(\vec{q})}}[ae^{i(\vec{q}\cdot\vec{R}_j-\omega_s(\vec{q})t)} + a^+e^{-i(\vec{q}\cdot\vec{R}_j-\omega_s(\vec{q})t)}]. \tag{2.63}$$

here the suffix "s" indicates the cartesian indexes and a and a^+ are respectively the annihilation and creation phonon operators. $\vec{q}$ and $\omega_s(\vec{q})$ represent the phonon momentum and frequency, while $\hat{\epsilon}_{s,\vec{q}}$ is the phonon polarization. Exploiting the commutation rules of a and a^+, and some general relations, Eq. (2.62) becomes:

$$S(\vec{q},\omega) = \frac{1}{2\pi\hbar N}\sum_{j} e^{i\vec{q}\cdot\vec{R}_j-2W(q)}\int_{-\infty}^{+\infty} e^{-i\omega t}e^{\langle(\vec{q}\cdot\vec{u}_0(0))(\vec{q}\cdot\vec{u}_j(t))\rangle}dt, \tag{2.64}$$

Where the quantity $e^{-2W(q)} = e^{-\langle(q\cdot u_i(0))^2\rangle}$ is called the Debye-Waller factor. Since we are dealing with small displacements, the argument of the integral can be expanded as:

$$e^{\langle(\vec{q}\cdot\vec{u}_0(0))(\vec{q}\cdot\vec{u}_j(t))\rangle} = 1 + \langle(\vec{q}\cdot\vec{u}_0(0))(\vec{q}\cdot\vec{u}_j(t))\rangle + ... \tag{2.65}$$

The first term leads to elastic scattering, while the second one represents the inelastic scattering with the creation or annihilation of one phonon. Higher order terms can be omitted since only small momentum transfers, compared to the inverse of the typical atomic displacements, are considered. Within this approximation the dynamic structure factor can be expressed as:

$$\begin{aligned} S(q,\omega) &= \frac{1}{4\pi MN} e^{-W(q)} \sum_j e^{i\vec{q}\cdot\vec{R}_j} \frac{(\vec{q}\cdot\hat{\epsilon}_{s,\vec{q}})^2}{\omega_s(\vec{q})} \int_{-\infty}^{+\infty} e^{i\omega t} [e^{-i(\vec{q}\cdot R_j - \omega_s(\vec{q})t)} \langle n_q + 1 \rangle \\ &+ e^{-i(\vec{q}\cdot R_j + \omega_s(\vec{q})t)} \langle n_q \rangle] dt, \end{aligned} \tag{2.66}$$

where $\langle n_q \rangle$ represents the Bose occupation number of the excited phonon mode. For crystals with more than one atom per unit cell, the unit cell form factor has to be taken into account in the calculation of the one phonon process scattering cross section. For disordered systems the lack of translational periodicity makes the treatment more complicated, because the eigenvectors depend also on the equilibrium positions of the atoms [57, 58, 59].

2.2.3 IXS spectrometer: beamline ID-16 at ESRF

The IXS beamline ID-16 at the European Synchrotron Radiation Facility (ESRF) in Grenoble [60] will be briefly described in this section. The instrument layout is reported in fig. 2.7

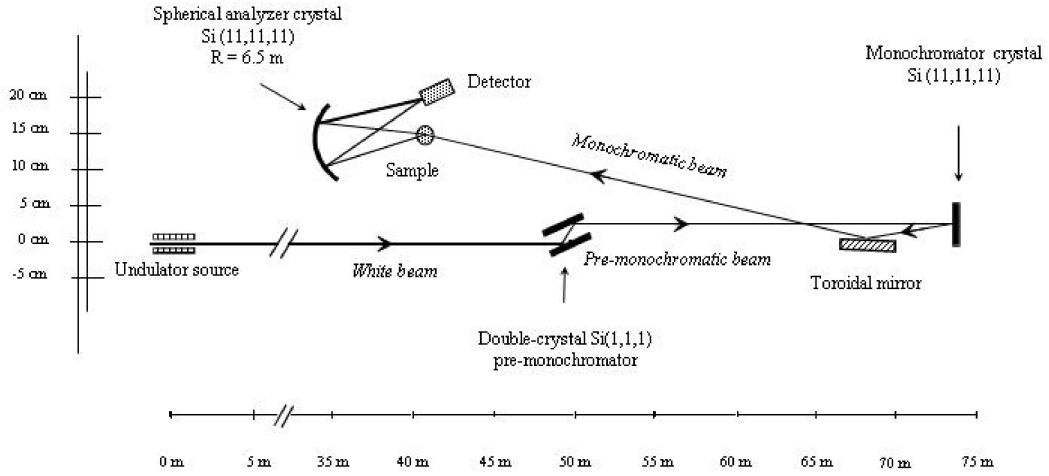

Figure 2.7: *Layout of the IXS beamline ID-16 at the European Synchrotron Radiation Facility.*

The instrumental concept is based on a triple axis spectrometer. The first axis is the one of the monochromator crystal. Its role is to fix the energy, $\hbar\omega_i$, of the

incident photons. The second axis is located at the sample position, and determines the momentum transfer. The third axis is the analyzer crystal, its role is the selection of the scattered photon energy, $\hbar\omega_f$. The ID16 beamline is equipped with a 5 analyzers system that collect 5 different IXS spectra simultaneously. The spectra correspond to 5 different transfer momenta.

The x-ray source consists of three undulators of 35 mm magnetic period, placed in a straight high-β section of the electron storage ring. The x-ray radiation energies used correspond to the 3^{rd} or 5^{th} harmonics of the characteristic undulator emission. The x-ray beam from the undulators odd-harmonics have approximately a 40×15 μRad (horizontal $\times$ vertical) angular divergence (FWHM), a spectral bandwidth $\Delta E/E \approx 10^{-2}$ and an integrated power within this divergence in the order of 200 W.

The x-ray beam from the undulators is pre-monochromatized to give a bandwidth of $\Delta E/E \approx 2 \cdot 10^{-4}$ using in-vacuum nitrogen-cooled channel cut silicon crystal. The main role of the pre-monochromator is to reduce the heat load impinging on the main monochromator. This is mandatory in order to keep the thermal deformation of the silicon crystal below the limits for which the energy resolution is deteriorated.

The x-ray photons from the pre-monochromator impinge onto the high energy resolution backscattering monochromator, consisting of an asymmetrically cut silicon crystal operating at a Bragg angle of 89.98^o. The natural angular acceptance of the crystal, the so-called Darwin width, is larger than the x-ray beam divergence, and, therefore, all the photons within the desired energy bandwidth are transmitted. High order Bragg reflections and perfect crystals are required in order to obtain the necessary energy resolution of $\Delta E/E \approx 10^{-7} \div 10^{-8}$, these reflections are the silicon (h, h, h), with $h = 7, 8, 9, 11, 12, 13$ [61].

The monochromatic beam is focused in the horizontal and vertical plane by a platinum coated toroidal mirror, located at 2 m from the sample.

The scattered radiation is subsequently analyzed in energy. Although problems related to energy resolution are conceptually the same for the monochromator and for the analyzer, the required angular acceptance is very different. The monochromator can be realized using a flat perfect crystal. For the analyzer crystal, the optimal angular acceptance is dictated by the desired momentum resolution. Considering values of Δq in the range of $0.1 \div 0.5$ nm^{-1}, the corresponding angular acceptance of the analyzer crystal must be $\approx$ mrad or higher, a value much larger than the Darwin width. The only way to obtain such a large angular acceptance is the use of a focusing system, which, nevertheless, has to preserve the single crystal perfection necessary to obtain the desired energy resolution. This constraint excludes the possibility to consider elastically bent crystals. A solution consists of gluing a large number of undistorted perfect flat crystals on a spherical surface, on a 1:1 pseudo-Rowland circle geometry with aberrations kept such that the desired energy resolution is not degraded. These analyzers consist of 12000 perfect silicon single crystals of surface size 0.6×0.6 mm^2 and a thickness of 3 mm, glued on a spherical substrate of a radius equal to the length of the spectrometer arm, 6.5 m [62, 63].

The spectrometers are furthermore equipped with an entrance pinhole, motorized slits in front of the analyzer crystal to set the desired momentum resolution, and a detector with its corresponding pinhole. The detectors are Peltier cooled 1.5 mm

thickness silicon diodes with an active area of 2×12 mm^2, inclined at 20^o in order to enhance the x-ray absorption. They have a very low dark count (≈ 1 count in 30 minutes). On ID-16 there are five independent analyzers with a fixed angular offset among them of $\approx 1.5^o$, mounted on a 6.5 m long arm that can rotate around a vertical axis passing through the scattering sample. This allows recording of 5 IXS spectra at the same time, with a nearly constant Q-offset.

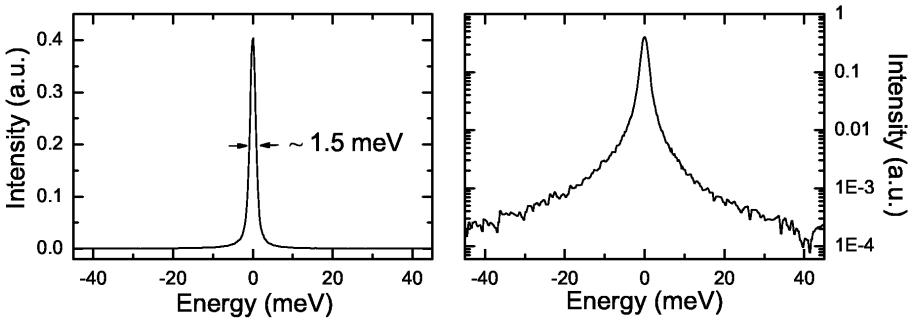

Figure 2.8: *Measured instrumental resolution function, corresponding to the* $Si(11,11,11)$ *configuration of the spectrometer, plotted both in linear and logarithmic scale.*

As a consequence of the extreme backscattering geometry, and in contrast to traditional triple axis spectrometers, the change of energy difference between analyzer and monochromator cannot be performed modifying the Bragg angle of the monochromator or of the analyzer. The energy scans are therefore performed by changing the relative temperature, ΔT, of the monochromator. This induces a relative variation of the lattice parameters, $\Delta d/d = \alpha(T)\Delta T$. Therefore a relative variation of the energy of the diffracted radiation, $\Delta E/E = -\Delta d/d$, is induced as well. Considering that the thermal expansion coefficient of Si α has a value of $\approx 2.58 \cdot 10^{-6}\mathrm{K}^{-1}$ at room temperature, the required energy resolution of $10^{-7} \div 10^{-8}$ implies an accuracy in the temperature control of the monochromator crystal in the mK-range. This task is achieved with a carefully designed temperature bath, controlled by an active feedback system [61], which assures a temperature control with a precision of 0.2 mK in the temperature region around 295 K. In order to convert the temperature scale into the energy scale, the most recent result for $\alpha(T)$ has been considered [64]:

$$\alpha(T) = \alpha_0 + \beta\Delta T, \tag{2.67}$$

where $\alpha_0 = 2.581 \pm 0.002 \cdot 10^{-6}\ K^{-1}$, $\beta = 0.016 \pm 0.004 \cdot 10^{-6}\ K^{-2}$. From Eq. (2.67) one can precisely calculate the variation of lattice constants at the temperature T:

$$\Delta d/d_0 = \int_{T_0}^{T} \alpha_0 + \beta(T' - T_0)dT' = (\alpha_0 - \beta T_0)\Delta T + \frac{1}{2}\beta(T^2 - T_0^2). \tag{2.68}$$

Finally, the variation of the energy of the diffracted radiation, $\Delta E/E = -\Delta d/d$, can easily be found.

Figure 2.8 shows the instrumental function of one of the five analyzers, corresponding to an energy resolution of 1.5 meV, when operating at the Si(11, 11, 11) reflection . It has been recorded by measuring the scattering from a disordered sample (Plexiglas) at a temperature of 10 K and at a q-transfer corresponding to the first maximum of its static structure factor (10 nm^{-1}). In this way the elastic contribution to the scattering is maximized. Table 2.1 summarizes the main characteristics of the spectrometer.

h	Energy [keV]	ΔE [meV]	Q_{max} [nm^{-1}]	ΔQ [nm^{-1}]	Flux [photons/s/200mA]
7	13.839	7.6± 0.2	64	1.89	$1.5 \cdot 10^{11}$
8	15.816	5.5± 0.2	74	2.16	$9.0 \cdot 10^{10}$
9	17.793	3.0± 0.2	83	2.43	$2.7 \cdot 10^{10}$
11	21.747	1.5± 0.1	101	3.00	$6.6 \cdot 10^{9}$
12	23.724	1.3± 0.1	111	3.24	$5.9 \cdot 10^{9}$
13	25.701	1.0± 0.1	120	3.50	$1.5 \cdot 10^{9}$

Table 2.1: *Main characteristics of the ID-16 6.5 m spectrometer for the different $Si(h,h,h)$ reflections. Energy indicates the incident photon energy, ΔE is the total energy resolution, Q_{max} indicates the maximum momentum transfers and ΔQ indicates the Q-spacing between adjacent analyzers. The photon flux values are measured at the sample position.*

Résumé du chapitre 3

Dans ce chapitre on présente une étude sur un verre " hyperquenched ", c'est-à-dire un verre obtenu en refroidissant un liquide en mode extrmement rapide (10^5 K/s). Dans une brève introduction, sera présentée la problématique scientifique qui est objet de notre étude: la dépendance du BP de l'histoire thermique du verre et en particulier de sa température fictive T_f. On discutera des modèle théorique présent en littérature qui permettent d'accomplir des prédictions quantitatives sur l'évolution du BP en fonctionne de T_f. Dans un autre paragraphe, on présente l'objet de les nos études : NaFeCaSiO, et la caractérisation de sa structure et la vitesse du son. En suite, seront discutées les procédures et les résultats des mesures de calorimétrie (DCS scannes), de diffusion de lumière (BLS), de rayon X (XRD) et de spectroscopie Mössbauer. Cette caractérisation de nos échantillons donne évidence à une variation de T_f qui correspond a une diminution de la densité du système avec une correspondant diminution de la vitesse du son. La variation de T_f ne semble pas cependant avoir des effets sur la structure du verre, mme sur une échelle de longueurs plutt petite. Dans une seconde partie de ce chapitre on pressente les mesures NIS de nos échantillons et les relatives DOS. On observe une augmentation de l'intensité du maximum de RDOS en augmentant la T_f du système. Aufin de comprendre l'influence des propriétés macroscopiques du verre sur la variation de DOS obtenue en variant T_f, on a procédé à calculer l'énergie de Debye de chaque échantillon et on a réduit la RDOS en unités d'énergie de Debye. De cette représentation de la RDOS, en unités d'énergie de Debye, on observe que la variation de DOS associée au changement de T_f peut tre complètement décrit par le changement des seules propriétés macroscopiques du système. Dans les conclusions de ce chapitre on reprend les principaux résultats de cette étude sur le verre "hyperquenched" et on le compare avec les prédictions avancées de la théorie.

Chapter 3

Study of a hyperquenched glass

3.1 Scientific Background: the energy landscape approach

One of the peculiarities of the glassy state is represented by the fact that this state is out of thermodynamic equilibrium. A theoretical model to relate the presence of the BP to the non-equilibrium nature of glasses has been developed. As we have already shown in section 1.2, the formation of a glass can be seen as the result of two opposite processes. On the one hand the free energy decreases, favoring the formation of the crystalline phase. On the other hand, the system keeps its disordered structure because the high number of equivalent configurational states augments the value of the entropy. The competition between these two processes leaves the system in a metastable condition, out of thermodynamic equilibrium: the glassy state.

In principle one could quantify the non-equilibrium character of a glass evaluating the free energy that should be subtracted from the system in order to bring it to equilibrium (to obtain the crystalline phase). Equally, one can define the *degree* of non-equilibrium of the system through the difference in energy $\Delta H = H - H_{ref}$, that the system has relative to a reference energy of the glass. It has been observed experimentally that cooling a liquid at different rates leads to the formation of glasses at different temperatures T_f (called fictive temperature). The value of T_f can be used to directly quantify ΔH, defining H_{ref} as the free enthalpy of that glass where $T_f = T_g$ (here T_g is the temperature at which the structural relaxation time τ_α of the glass is equal to 100 s). From the knowledge of the structural relaxation time at T_f: $\tau_\alpha(T_f)$ using the Adam-Gibbs equation (3.1) [7], one can estimate $\Delta H = H(\tau_\alpha(T_f)) - H(\tau_\alpha(T_g))$:

$$\tau_\alpha(T) = \tau_0 exp\left(\frac{\Delta\mu}{TS_c}\right) = \tau_0 exp\left(\frac{\Delta\mu}{H(T)}\right); \tag{3.1}$$

In Eq.(3.1) S_c is the configurational entropy evaluated from the Kauzmann temperature T_K (see section 1.2):

$$S_c = \int_{T_K}^{T} \Delta c_P dlnT, \tag{3.2}$$

$\Delta\mu$ is the free energy barrier for the structural rearrangement. ΔH has been identified in theory as the critical parameter that controls the height and the energy of the BP in glasses. However, the value of ΔH alone is not sufficient to predict the vibrational properties of a glass. In the last few years, a description of the dynamical properties of solids, based on the topological aspect of its energy surface [65], has been developed.

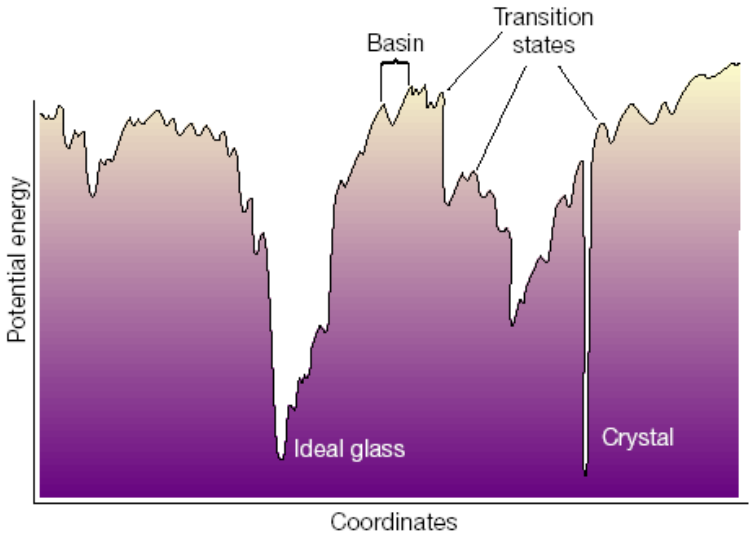

Figure 3.1: *Sketch of the energy landscape.*

Once the interaction potential between the particles is fixed, the potential energy is a function of the spatial coordinates of each particle $H(r_1, r_2...r_{3N})$. Moreover, one can have a *topographic* view of H with a multidimensional map that shows the value of H at any location $\bar{r} = (r_1, r_2....r_{3N})$ of the N particles. In this configurational space (here the number of coordinates is $3N$, associated with the position of all particles) the potential energy of the system is represented by a point that moves on a surface. This surface is characterized by maxima, minima and saddle points. The minima correspond to mechanically stable arrangements of the N particles. The lowest-lying minimum is the configuration where the system is a perfect crystal. In contrast, the higher minima correspond to amorphous packings of the atoms (see figures 3.1 and 3.2). Each minimum is separated from another by a saddle; these energy points characterize metastable phases and play a fundamental role in the transitions of the system. Moreover, indications for a relationship between the distribution of basins and the height of the saddle points have been found [66]. At temperatures higher than the melting point (T_m) the liquid samples the saddles energy points; if the temperature is lowered fast, the system migrates to higher basins. Conversely, upon slow cooling, the system is trapped in one of the lower minima, see 3.2.

The representation of a system through this topographic vision is useful to simplify the description of its collective properties. The manner by which a system samples

its landscape as a function of the temperature provides information on its dynamical behavior. Moreover, from the way in which the system moves over the energy landscape, due to a change in density, we obtain information on the mechanical properties of the system. In recent years, the energy landscape approach has been found to be a powerful tool for the description of the low energy vibrations of glasses, allowing to establish a relationship between the energy landscape and the presence of the BP in the glass [67, 68, 69, 70, 71].

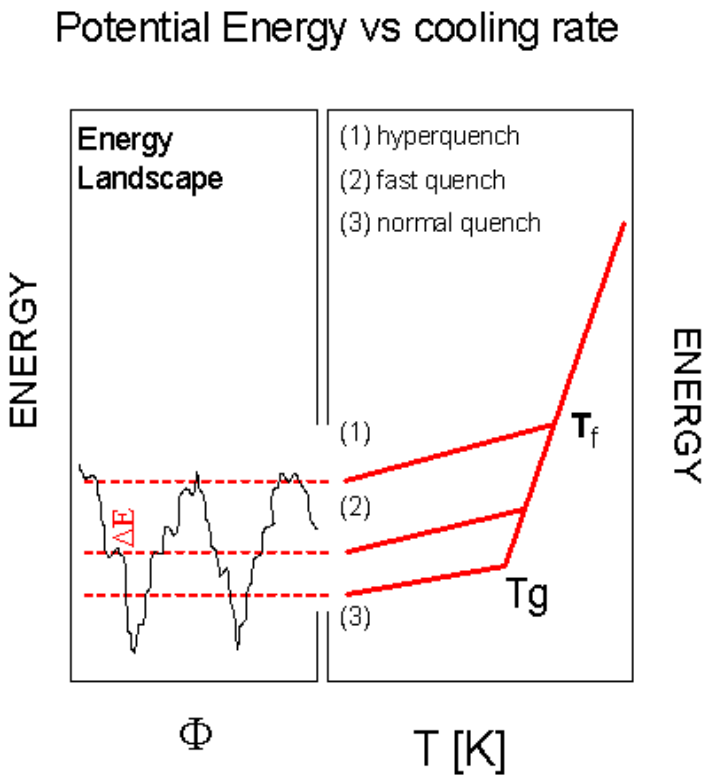

Figure 3.2: *Sketch of the energy landscape of a glass (left panel) corresponding to different cooling processes (right panel).* Φ *is the coordinate of the space of configurations of the system* $\Phi = \Phi(r_1, ..., r_{3N})$.

In order to check the reliability of the description of the dynamics of a glass obtained using the energy landscape approach, hyperquenched glasses have been investigated. These systems are characterized by a high value of T_f obtained by a fast quenching of the liquid, with a cooling rate up to 10^5 K/s. Hyperquenched glasses reveal a non-exponential behavior of the structural relaxation time τ_α. This result has been interpreted considering τ_α as the average of a broad spectrum of relaxation times, suggesting the presence of heterogeneities in the regions where the relaxations take place. Such heterogeneities could be reflected in the energy landscape through the presence of a large number of unstable points. Measurements of DOS in hyperquenched

glasses have revealed an increase of DOS in the BP energy region [68]. The height of the maximum in the reduced density of states (RDOS) $g(E)/E^2$ increases increasing T_f, confirming the connection between the topology of the energy landscape of the glass and the presence of the BP.

In particular the rise in height of the BP can be associated with a transition in the energy landscape between a region dominated by minima to a region dominated by saddle energy points. This transition is controlled by the critical parameter Δ_c ($\Delta_c \propto \Delta H$)[69] that represents the difference between the energy of the glass and that of the same system at the Mode-coupling temperature, T_c [72]. The high number of unstable energy points leads to an increase in the number of low frequency modes in the system that, despite their low energy, have a short wavelength (high value of the corresponding wave vector Q) [70]. The typical linear dependence of the frequency of the vibrational excitations on Q, in the acoustic region (i.e. at low values of Q), would not be influenced by the modes embedded in the BP because of their high Q values. Numerical investigations on the relationship between the energy of the BP and the value of the critical parameter Δ_c [69] allowed the authors to make quantitative predictions of the relation between the height I_{BP} and energy position E_{BP} of the BP with varying T_f. In particular it has been pointed out that: $I_{BP} = g(E_{BP})/E_{BP}^2 \propto E_{BP}^{-1/2}$ because $E_{BP} \propto \Delta_c$, and $I_{BP} = g(E_{BP})/E_{BP}^2 \propto \Delta_c^{-1/2}$.

On the basis of these theoretical predictions, we decided to experimentally investigate the relationship between the DOS and T_f in hyperquenched (high value of T_f) and annealed glasses (samples with low value of T_f obtained by annealing the hyperquenched glasses). Moreover, using different techniques we have probed the effect of the thermal history on both structural and vibrational properties. The results obtained are quite surprising: the increase of DOS at low energy, for increasing values of T_f, is only associated with the change of the *macroscopic* properties of the glass. These conclusions suggest to reconsider some aspects of the previously discussed theory and renew the interest in the experimental investigations on this topic that is still far from being fully understandood.

3.2 The sample

We investigated the effect of the thermal history on the vibrational dynamics of a glass using: 74SiO_2 4CaO 16Na_2O 6FeO (% in weight). The preparation of the samples has been done by Prof. Y. Yue at the Aalborg University, starting from a mixture of raw quartz powder, $CaCO_3$, Na_2CO_3, and Fe_2O_3 added in analytical grades. The mixture has been melted heating the material at high temperature (1500°C); cooling the melt at below 781K a reference glass was obtained.

The choice of a glass with such composition is the result of a compromise between two requirements. On one hand, we would like to have a system representative of a wide variety of glassy materials; like sodium silicates. On the other hand, the system should contain iron atoms that allow using spectroscopic techniques based on the Mössbauer effect. The glass was chosen by starting from a relatively high silica content. In order to introduce iron atoms into the glass, Fe_2O_3 has been added together with Na_2CO_3

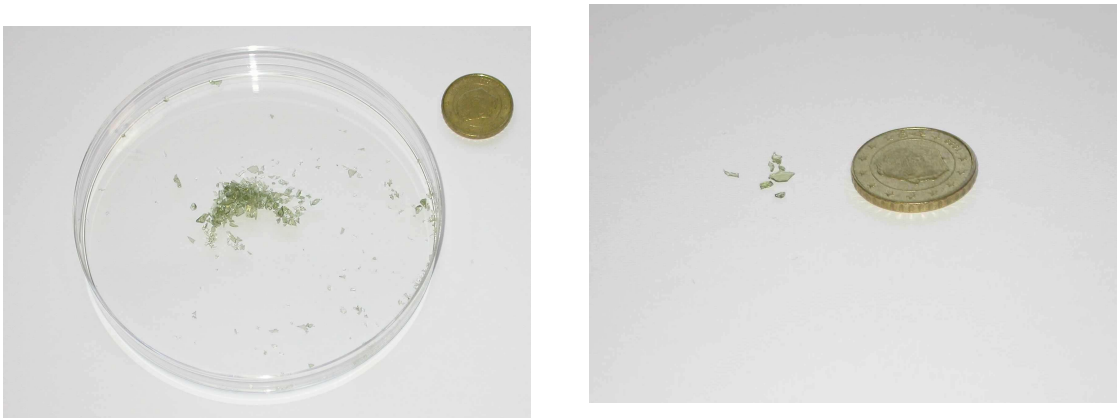

Figure 3.3: *Hyperquenched material (left panel), some pieces of the glass used for the measurements (right panel).*

and $CaCO_3$, these last two components are responsible for the low hygroscopic level of the material and assure the mechanical stability of the system. 30 % of Fe_2O_3 was substituted by the isotopic $^{57}Fe_2O_3$ to increase the cross section of nuclear excitations.

A first characterization of the dynamical properties of the reference glass was provided by viscosity η measurements. In figure 3.4 we report the behavior of η vs T compared with viscosity measurements of other systems. The glass has a "strong" behavior, the index of fragility is m=34, close to other sodium silicate glasses [75]. From differential calorimetric scan measurements (see section 3.3), we determined the glass transition temperature T_g=781 K.

Starting from the reference glass two samples have been prepared: the "hyperquenched" and the "annealed" glass, using different thermal treatments. The final task of this preparation protocol was to have two glasses with different fictive temperature T_f. The "hyperquenched" sample has been obtained by a double-crucible technique to cool the melt at high rates. The raw material was melted in a Pt/Au crucible (80 mm in height and 75 mm in diameter) at 1500°C. After 4-hours of homogenization the crucible has been taken out of the furnace and placed on a porous alumina/silica brick. Then another smaller platinum crucible (72 mm in height and 40 mm in diameter) was immersed upside down into the melt in the larger crucible, was quickly pulled out of the melt, and was quenched into water. By pulling the small crucible from the melt, a thin melt film ($100 - 300$ μm) is generated. The fast quenching of the thin film reduces the material to small pieces: the final hyperquenched sample. To obtain the second sample, the annealed glass, the hyperquenched material was warmed to 785K for 10 minutes and then cooled to room temperature with a rate of 2 K/min.

3.3 Differential scanning calorimetry

As discussed in the first chapter, during heating and subsequent cooling, the temperature T_f is obtained where the structural relaxation time τ_α becomes comparable to

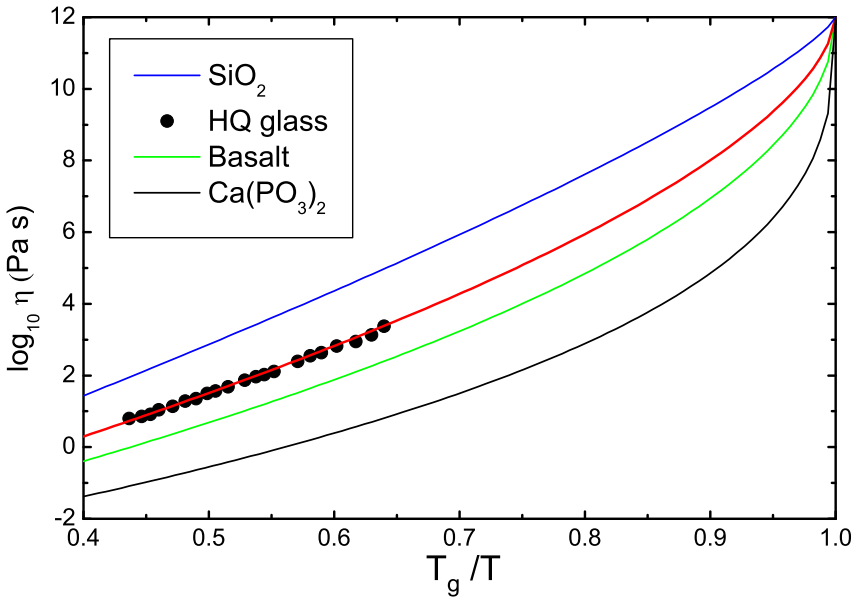

Figure 3.4: *Behavior of viscosity as function of temperature for different compounds, the full circles are the measurements on the hyperquenched glass.*

the characteristic time scale $\Delta t \Delta T / r_c$ ($\Delta t / \tau_\alpha \sim 1$). Where ΔT is the scanned range of temperature and r_c the rate of cooling. Thus, changing the cooling or heating rate r_c, Δt changes ($\Delta t' = \Delta T / r_c'$) and the relaxation time τ_α at T_f will be altered similarly. In fact, because τ_α is temperature dependent, a change in cooling or heating rate changes fictive temperature T_f according to $\Delta t / \tau_\alpha(T_g) = \Delta t' / \tau_\alpha(T_f) \sim 1$.

We have applied high cooling rate and an annealing procedure to get two samples with respectively a higher and a lower T_f relative to the glass transition temperature of a glass (obtained cooling the melt with the reference cooling rate r_c= 10 K/min). The efficiency of the thermal treatments applied to obtain the samples with two different T_f has been evaluated by differential scanning calorimetry scans (DSC). DSC measurements allow us to estimate the potential energy stored in or removed from the sample relative to the value of a reference glass. From this a precise determination of T_f is obtained. The property monitored by DSC scans is the enthalpy (H) and the value measured by the instrument is proportional to the derivative of this function ($c_P = \partial H / \partial T|_P$). If we perform two measurements of c_P varying the temperature from the glass at low temperature T_{cn} up into the melt T_{eq} (c_{P1} scans) and back in the same range of temperature from T_{eq} to T_c (c_{P2} scan) (see figure 3.5 and 3.6), the integrated difference between the two DCS scans gives a measure of the total enthalpy released during the entire heating:

$$\Delta H = \int_{T_c}^{T_{eq}} \frac{\partial \Delta H}{\partial T}\, dT = \int_{T_c}^{T_{eq}} (c_{P2} - c_{P1})\, dT, \tag{3.3}$$

this integral is evaluated between T_c, the temperature where the release of energy starts, and T_{eq}, the temperature where the system returns into equilibrium; i.e. $c_{P2} = c_{P1}$ in the melt. Due to the low compressibility of liquids under ambient pressure, it is possible to neglect the pressure volume work and obtain $\Delta H = \Delta E_T$, where ΔE_T is the total internal energy of the system. ΔE_T is then the sum of two contributions, one from the vibrational energy and one associated with the configurational energy, i.e. $\Delta E_T = \Delta E_v + \Delta E_c$.

ΔE_T represents the variation of energy associated with the shift of the glass formation from T_g to T_f; therefore, we can write:

$$dE_T = (c_{Pl} - c_{Pg})\, dT, \tag{3.4}$$

here c_{Pl} is heat capacity of the liquid and c_{Pg} is the heat capacity of the glass. Combining equation 3.3 and 3.4 one can derive:

$$\int_{T_c}^{T_{eq}} (c_{P2} - c_{P1})\, dT = \int_{T_g}^{T_f} (c_{Pl} - c_{Pg})\, dT. \tag{3.5}$$

From this expression is possible to obtain the T_f of the glass from the energy defined by the two DCS scans (the area between the two curves of figure 3.5) and comparing this energy to that expected from the transition between the liquid and glassy phase (i.e. Eq.(3.5) corresponds to the condition A=B in figure 3.6 (left panel)).

In figure 3.5 we show the up and down DSC scans performed on our samples: the hyperquenched and the annealed glass. The measurements have been performed by Prof. Y. Yue using a differential calorimetric scan model Netzsch STA 449C Jupiter.

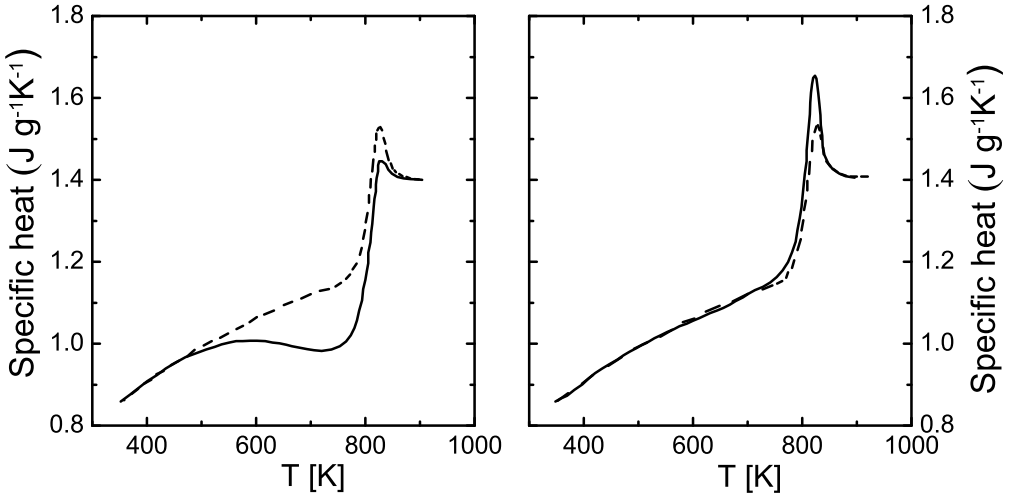

Figure 3.5: *Heat capacity up-scan c_{P1}(continuous line) and down-scan c_{P2}(dashed line) in hyperquenched (left panel)and annealed (right panel) samples.*

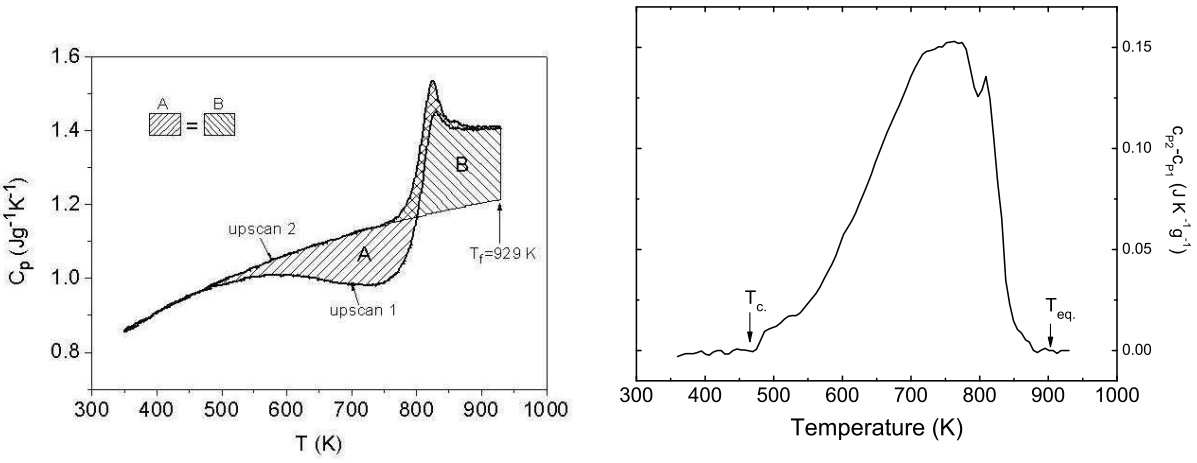

Figure 3.6: *DCS scans (left panel) and corresponding amount of energy released during the heating as function of temperature (right panel).*

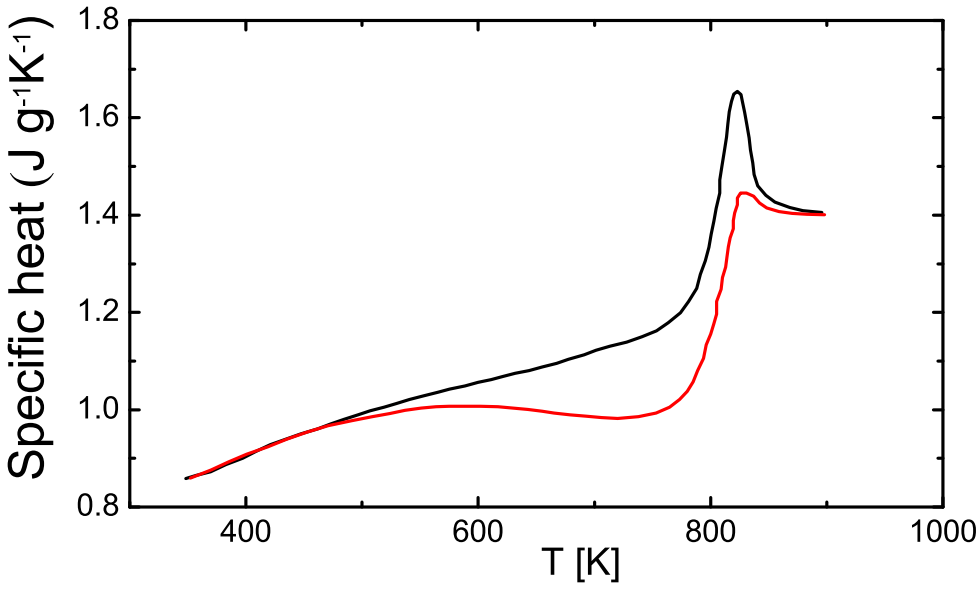

Figure 3.7: *Heat capacity up scans of hyperquenched (red line) and annealed (black-line) glasses.*

For both the cooling and the heating scans a rate equal to 10K/min has been used. The value of T_f according Eq.(3.5) has been found to be 929K and 770K respectively for the hyperquenched and the annealed samples. From the difference between the up DSC scans of the two glasses (see figure 3.7) it was possible to evaluate the excess of internal energy ΔU stored by the hyperquenched glass relative to the annealed one:

$$\Delta U = \int_{T_c}^{T_{eq}} (c_{P1}(Ann.) - c_{P1}(Hq.))\ dT. \tag{3.6}$$

ΔU was found to be 8.0 meV per atom in average.

Furthermore, using the value of T_f we could evaluate, from the measurements of viscosity, the cooling rate r_c at which the hyperquenched glass has been cooled. In silicate systems a simple relationship links the viscosity η_c at $T = T_g$ with r_c [76]:

$$\log\ r_c = A - log\ \eta_c. \tag{3.7}$$

The value of η_c has been derived from viscosity measurements, using the Avramov Eq.(3.8), to extrapolate the experimental data of η_c up to T_f.

$$\log\ \eta = D + B\left(\frac{T_g}{T}\right)^{\alpha}. \tag{3.8}$$

The parameters D, B and α have been fitted to the experimental data (see fig. 3.4). From Eq. (3.7) it was estimated that hyperquenched glass was prepared with the cooling rate of 1500 K/s.

3.4 Density measurements

We characterized macroscopic properties of the samples, in particular their density.

The method that we used for these measurements is historically called Archimedes method, it is in fact an application of the Archimede principle referred as "any body plunged in a liquid experiences a force F_l proportional to the density of the liquid ρ_l and to the volume V of the solid" ($F_l = \rho_l g V$, where g is the gravitational acceleration).

Exploiting such principle the density of a solid can be measured using a liquid with known density ρ_l. Considering the weight of the solid in air W_a and the weight of the solid in the liquid W_l, one can write:

$$W_a = Mg - \rho_a g V \qquad W_l = Mg - \rho_l g V, \tag{3.9}$$

$$\rho = \frac{W_a}{W_a - W_l}(\rho_l - \rho_a) + \rho_a, \tag{3.10}$$

here M is the mass of the solid and ρ_a is the density of the air. The measurement of W_a and W_l of our samples has been performed using a balance (Mettler Toledo AT201) equipped with a sample holder immersed in ethanol (see fig. 3.8). Each sample has been weighed in air and in ethanol, taking into account the F_l acting on the sample holder. The temperature of the liquid was monitored during the measurement. The density of

ethanol depends only slightly on the temperature $\partial\rho/\partial T$=5.5 10^{-4} g/cm^3/K, nevertheless this dependence represents the major source of uncertainty of the measurements. The error in the density using the Archimede's method depends intrinsically on the size of the measured sample. From Eq.(3.10) one recognize that the uncertainty in ρ is inversely proportional to the difference $W_a - W_l$ that is proportional to the volume of the sample V ($W_a - W_l = gV(\rho_l - \rho_a)$). To increase the accuracy of our measurements we weighed (in air and ethanol) all the material obtained from the hyperquenching (or, alternatively from the annealing) processes, then we increased considerably the weight of the measured sample reducing the uncertainty in ρ. Moreover, we repeated the measurements several times, in order to reduce the statistical uncertainty. The value of the density for the hyperquenched was found to be 2.404(1) g/cm^3, and 2.439(5) g/cm^3 for the annealed glass.

Figure 3.8: *Picture of the balance used for the density measurements.*

3.5 The Brillouin light scattering technique

In this section we will briefly consider an application of Brillouin Light Scattering to investigate the macroscopic elastic properties of a solid. The approach that we will fol-

low to describe the capabilities of the BLS technique is based on a classical description of the interaction between matter and radiation. The choice to neglect a more detailed quantum mechanical description of the phenomenon has been motivated not just by reasons of space, but also by the way we used the BLS technique in our studies. We used this spectroscopic technique to characterize the macroscopic dynamical behavior of glasses and, in particular, to measure the longitudinal and transverse speed of sound of the systems. As we will show below, these quantities can be extracted from BLS data using a classical approach to treat the interaction between the probe (i.e. photons) and the system.

If we send a monochromatic radiation on a sample, the spectrum of the scattered radiation contains, in addition to the incident frequency, other components at different frequencies. This phenomenon, is called inelastic scattering and has been observed for the first time in 1928 by C.V. Raman [78]. A possible description of the inelastic scattering can be found within the framework of classical electromagnetism.

A neutral ensemble of charges, as an atom or a molecule, has an instantaneous dipole momentum $\vec{\mu}$:

$$\vec{\mu}(t) = \sum_i q_i \vec{r}_i. \tag{3.11}$$

If now we plunge the charges into an electric field in plane wave form: $\vec{E}_i(r,t) = \hat{\varepsilon}_i E_0 e^{i(\vec{k}_i\vec{r}-\omega_i t)}$ ($\hat{\varepsilon}_i$ is the unit vector in the direction of the radiation of the incident electric field, $\vec{k}_i$ is the wave number and ω_i the frequency of the radiation), the distribution of charges is modified together with the dipole. The induced dipole μ_{in} has to be considered now. This quantity can be written in terms of the applied electric field introducing the molecular polarizability tensor $\bar{\alpha}(t)$ [79]:

$$\vec{\mu}(t)_{in} = \bar{\alpha}(t)[\hat{\varepsilon}_i E_0 e^{i\omega_i t}]. \tag{3.12}$$

Here the possibility for $\alpha(t)$ to depend also on time due to the molecular motion has been included

If we consider a free, isolated atom, α is independent of time, then μ_{in} vibrates with the frequency of the incident electric field and the radiation is scattered elastically (i.e. no change of frequency). At distance $\vec{R}$ from the atom the induced momentum generates a scattered electric field along the direction $\hat{e}_s$ that one can write as [79]:

$$\hat{e}_s \vec{E}_s(R,t) = \frac{\omega_i^2}{\vec{R}c^2} \vec{E}_i e^{i(\vec{k}_i R-\omega_i t)} [\hat{e}_s \hat{e}_i] \alpha e^{i(\vec{q}\vec{r}(t))}. \tag{3.13}$$

Here $\vec{r}$ represents the instantaneous position of the atom with dimensions much smaller than the wavelength of the incident radiation and c is the speed of light. $\vec{Q}$ is the exchanged wave vector defined by the scattering angle θ between the incident ($\vec{k}_i$) and scattered ($\vec{k}_s$) wave vectors whose modulus is respectively equal to $2\pi/\lambda_i$ and $2\pi/\lambda_s$ (λ_i and λ_s are the wavelengths of the incident and scattered radiation). In the hypothesis of quasi-elastic scattering ($\vec{k}_i \approx \vec{k}_s$) Q can be written as:

$$Q = |\vec{k}_i - \vec{k}_s| \sim 2nk_i sin\theta. \tag{3.14}$$

here n is the refractive index.

In the case of a diatomic molecule, the expression of the scattered field can be obtained by taking into account the influence of the intramolecular motion on $\alpha(t)$. The time dependence of the molecular polarizability can be expressed using normal coordinates θ_1 θ_2 (rotational coordinates) and Q (vibrational coordinate) of the molecular modes. Considering only small variations of α compared to the value at equilibrium α_0, we can write α as:

$$\alpha(t) = \alpha_0 + \frac{\partial \alpha}{\partial Q}(Q_0 e^{i\omega_V t}) + \sum_{\theta_1 \theta_2} \frac{\partial \alpha}{\partial \theta_i}(\theta_{0i} e^{i\omega_R t}), \tag{3.15}$$

here ω_V and ω_R are respectively the vibrational and rotational frequencies of the molecule.

In the case of a polyatomic molecule this results is generalized taking into account all normal vibrational modes (that will be 3N-5 or 3N-6 depending if the molecule is linear or not). All normal frequencies of the system will be present in the spectrum of the emitted radiation if the mode is active, i.e.:

$$\left[\frac{\partial \alpha}{\partial Q}\right] \neq 0. \tag{3.16}$$

In addition to the isolated molecule it is also possible to treat the scattering of an ensemble of atoms or molecules. If one sends a monochromatic radiation on a solid, the scattered radiation contains information on the modes involving the entire system. In this experiment the scattered radiation will be the result of the sum of all scattered fields from the induced dipoles of the molecules. In order to treat the interaction of the radiation in a solid we can replace α by the dielectric tensor ε_{ij} [79]:

$$\varepsilon_{ij}(\vec{r}, t) = 1 + 4\pi \alpha_{ij} \rho, \tag{3.17}$$

$$\varepsilon_{ij}(\vec{r}, t) = \varepsilon I + \delta\varepsilon_{ij}(\vec{r}, t), \tag{3.18}$$

here I indicates the unit tensor, ε is the average value of the dielectric constant and $\delta\varepsilon$ represents its fluctuation respect to the mean value. It may be shown [80] that the scattered electric field at a large distance R can be written as:

$$\hat{e}_s E_s(R, t) = \frac{E_0}{4\pi R \epsilon} e^{i\vec{k}_s \vec{R}} \int_V dr^3 e^{i(\vec{q}\vec{r} - \omega_f t)} \hat{e}_s(\vec{k}_s \times (\vec{k}_s \times (\delta\varepsilon(r, t)\hat{e}_s))) \tag{3.19}$$

where $\hat{\varepsilon}_s$ is polarization of the field, k_s the propagation vector and ω_f the frequency of the scattered radiation.

From the expression of the scattered electric field, the information that one can extract on the dynamics of the system is determined by $\delta\varepsilon$. Assuming that the system is locally at equilibrium, the fluctuations of the dielectric constant are associated with density fluctuations. Considering ε as a function of temperature and density we can write:

$$\delta\varepsilon(T,\rho) = \left(\frac{\partial\varepsilon}{\partial T}\right)_\rho \delta T + \left(\frac{\partial\varepsilon}{\partial\rho}\right)_T \delta\rho. \tag{3.20}$$

Experimentally the magnitude of the term $\left(\frac{\partial\varepsilon}{\partial T}\right)_\rho$ is found to be much smaller than $\left(\frac{\partial\varepsilon}{\partial\rho}\right)_T$, so we can neglect it in analysis of the amplitude of the electric field of the scattered radiation. As is shown in Appendix A, in a solid perturbed by an external force, elastic waves (longitudinal and transverse) are generated that locally change the density of the solid. Thus, according to Eq.(3.20) the dielectric constant is modulated by the atomic motions associated with the elastic waves. These modes can be written in terms of normal coordinates as:

$$Q_v(t) = Q_v cos(\omega_v t) \tag{3.21}$$

here ω_v is the frequency of the elastic wave proportional to the speed of sound and wave vector $\omega_v = v_s Q$. Similarly, in the case of $\alpha(t)$ for an isolated molecule, we can write ε in terms of vibrational modes:

$$\delta\varepsilon(t) = \delta\varepsilon_0 + \left(\frac{\partial\delta\varepsilon}{\partial Q_v}\right) Q_v + ..., \tag{3.22}$$

here we have neglected the dependence of ε on the molecular rotations. The first term of the expansion gives rise to an elastic contribution (the frequency of the scattered radiation is the same as that of the incident one) called Rayleigh scattering. The second term is associated with the interaction of the electric field with the elastic waves of the solid and can be written as:

$$\hat{e}_s\vec{E}_s(R,t) \propto \left(\frac{\partial\delta\varepsilon}{\partial Q_v}\right) Q_v cos(\omega_v t) E_i cos(\omega_i t), \tag{3.23}$$

$$\hat{e}_s\vec{E}_s(R,t) \propto \left(\frac{\partial\delta\varepsilon}{\partial Q_v}\right) \frac{Q_v E_i}{2}\{cos[(\omega_i+\omega_v)t] + cos[(\omega_i-\omega_v)t]\}. \tag{3.24}$$

The resulting spectrum of the scattered electric field (E_s) consist of three lines: one located at ω_i, the Rayleigh line, and the others two at frequencies $\omega_s = \omega_i \pm \omega_v$. The frequency ω_v is related to the speed v_s of the elastic wave according the relations: $\omega_v = v_s Q$.

These three characteristic lines are present also into the spectrum of the scattered intensity $I_s(Q,\omega)$: the Brillouin spectrum. The $I_s(Q,\omega)$ is the quantity measured in a light scattering experiment. The theorem of Wiener-Kinchini [80] identify $I_s(Q,\omega)$ with the Fourier transform of the autocorrelation function of the electric field:

$$I_s(q,\omega) = \frac{1}{2\pi}\int \langle\vec{E}_s(0)\vec{E}_s(t)\rangle e^{i\omega t}dt = \frac{k_s^4 E_0^2}{32\pi^3\varepsilon^2 R^2}\int \langle\delta\varepsilon(\vec{q},t)\delta\varepsilon^*(\vec{q},0)\rangle e^{i\omega t}dt. \tag{3.25}$$

Inserting 3.24 into 3.25, it can be shown that $I_s(q,\omega)$ has three characteristic lines (see figure 3.9) located at $\omega_i \pm \omega_s$ and ω_i. To conclude, in this paragraph we have shown that it is possible, by analyzing the spectrum of radiation scattered from a solid, to have access to the characteristic vibrational frequencies of elastic waves propagating in the solid. Moreover, from the knowledge of the momentum transfer in the scattering process we can directly derive the speed of sound of the elastic wave v_s.

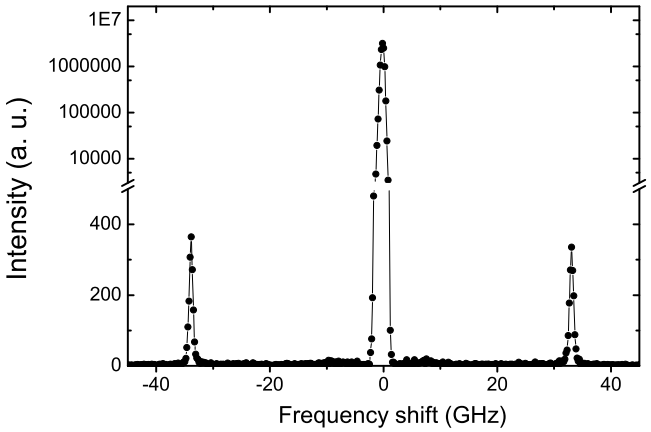

Figure 3.9: *Example of a BLS spectrum.*

3.5.1 The Sandercock interferometer and the experimental setup

The Brillouin Light Sscattering measurements have been performed in collaboration with the group of Prof. D. Fioretto in his laboratory at the Department of Physics of Perugia. The experimental set-up used for the measurements consists of a laser, a Fabry-Perot interferometer and of optical elements used to focus the light on the sample and to collect the scattered radiation.

The laser is the commercial Coherent Inova 300 device at Ar^+ ions with a maximum power of 600 mW on a single mode used at a wavelength of 514.5 nm. The laser beam is focused on the sample by a mirror and a system of lenses that can also be used to collect the radiation scattered from the sample and send it into the interferometer. The interferometer has a variable aperture controlled by a pinhole. The solid angle of the collected scattered radiation, and then the resolution in Q, is defined by a diaphragm located close to the sample.

In figure 3.10 we show the used experimental set-up with two possible scattering geometries. Configuration 1 is the 90° geometry, where 90 stays for the angle θ_{exp} between the direction of the laser incident on the sample and the direction of the collected radiation. Configuration 2 corresponds to the geometry where the laser beam

is focused into the sample using the same lens that collects the scattered radiation, θ_{exp} is now 180° and the geometry is called backscattering. It is possible to change configuration just displacing a mirror.

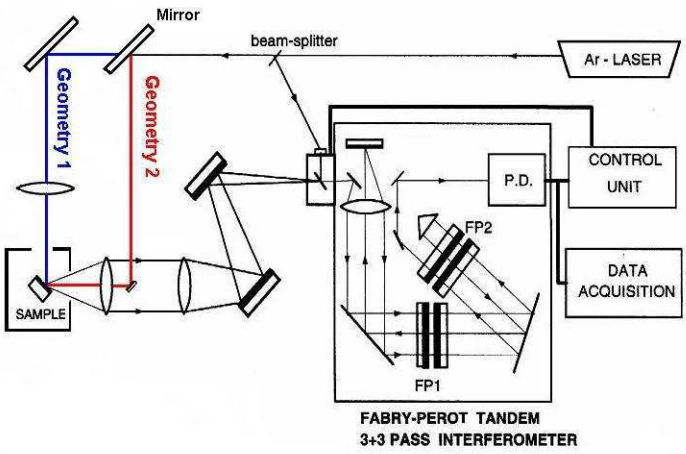

Figure 3.10: *Scheme of the apparatus used for the BLS measurements* .

The interferometer used for the measurements of BLS is a Sandercock Fabry-Perot tandem 3+3 device. This analyzer device consists of two Fabry-Perot interferometers. The scattered radiation is analyzed after three passes through each Fabry-Perot. A Fabry-Perot interferometer is a resonant cavity defined by two mirrors, the cavity works as a filter with a characteristic frequency $\omega_c = \pi c/L$ where L is the distance between the mirrors and c the speed of light. In addition to ω_c the cavity transmits also all the frequencies multiple of ω_c: $\omega_{nc} = n\pi c/L$. Through each cavity the radiation goes three times allowing increasing the filtering power of the device. The two Fabry-Perot interferometers have a slight difference in L and thus also in the characteristic frequencies ($\omega_{nc} = n\pi c/L$, $\omega'_{nc} = n\pi c/L$'). The second Fabry-Perot is tuned on the frequency of the first one changing the relative distance between the mirrors. The condition that allow transmitting through the two Fabry-Perot is: $L - L' = \lambda/2(n - n')$, where λ is the wavelength of the laser. The effect resulting from coupling the two filters (i.e. the tandem effect) is that only one frequency of the first filter is accepted also by the second cavity and the other resonant frequencies ω_{nc} are extinguished. The frequency scan is obtained varying the distance between the mirrors of the cavities with a piezo-electric crystal, thus the transmitted frequency of radiation is modified without destroying the tandem effect.

The characteristic parameters representative for the performance of the spectrometer are:

- The free spectral range defined as $c/(2L)$ that represents the distance in frequency between two modes of the interferometer. In the Sandercock model this parameter can be changed between 3 and 150 GHz by changing L.

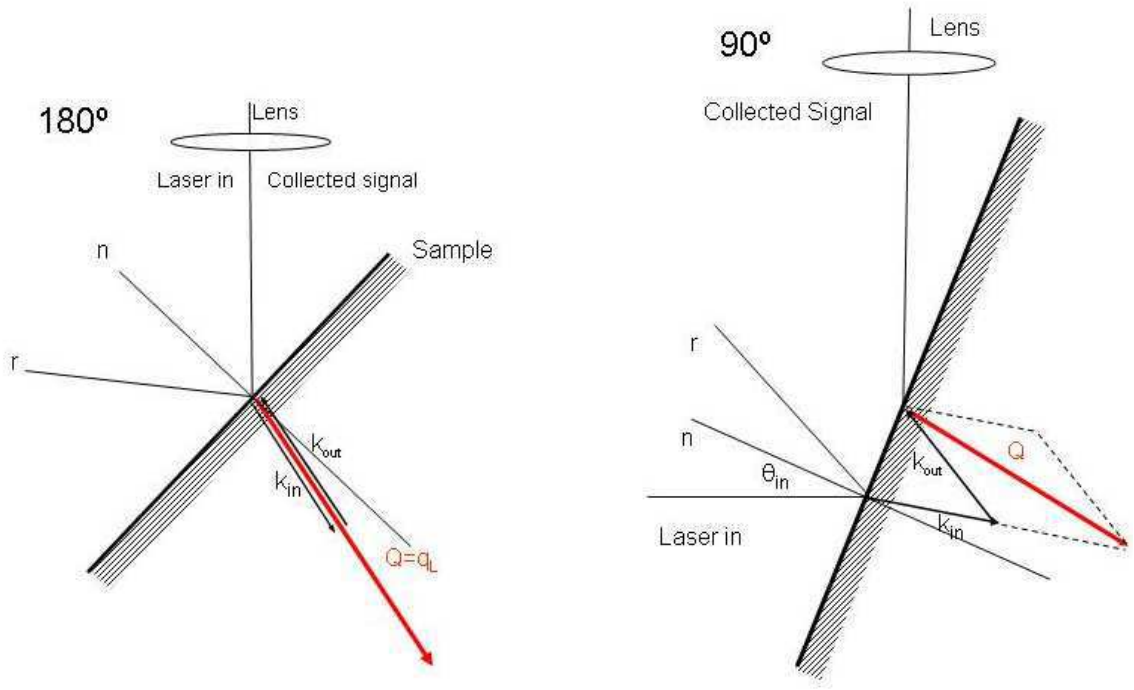

Figure 3.11: *The 90° and the Backscattering (180°) geometries of the BLS measurements.*

- The contrast: the ratio between the maximum and the minimum of the intensity of the radiation transmitted through the interferometer. Thanks to the three passages of the radiation in each cavity the contrast reaches the value of 10^{11}.
- The resolution: the width in frequency of a single mode of the interferometer. This characteristic is determined by the quality of the two cavities, the vibrations of the system and the size of the pinhole. The resolution in our measurements was set to ≈ 0.15 GHz.

Finally the radiation transmitted through the interferometer is collected by a photomultiplier and visualized as a function of the frequency via an acquisition system.

3.5.2 The measured spectra and the speed of sound.

The BLS measurements have been performed using the two different scattering geometries: the 90° and the backscattering ($\theta_{exp} = 180°$) geometry. These two geometries allow us to measure both: the longitudinal and the transverse acoustic modes. In the backscattering geometry the direction of $\vec{k}_{in}$ and $\vec{k}_{out}$ are parallel, the transverse mode cannot be detected in this configuration. In the 90° degree geometry, the spectra show both: the longitudinal and the transverse excitations (see figure 3.12).

We collected 6 different spectra, two in the backscattering geometry and four at 90°. In the 90° geometry, we measured the angle θ_{in} between the direction of the incident laser beam and the vector perpendicular to the surface of the sample $\hat{n}$ (see figure 3.11).

Table 3.1: Here we report: the scattering geometry, the angle θ_i, the exchanged wave vector (Q), the longitudinal (ν_L) and transverse (ν_T) frequencies, and the ratio $R = \nu_L/\nu_T$ for the hyperquenched (Hq.) and annealed (Ann.) glasses.

Sample	Scattering Geometry	θ_i	Q [nm^{-1}]	ω_L [GHz]	ω_T [GHz]	ω_L/ω_T
Hq.	90°	17.5°	0.0318(3)	29.42(3)	17.65(6)	1.67(2)
Hq.	90°	12.5°	0.0321(3)	29.47(2)	17.65(5)	1.67(2)
Hq.	180°	—	0.0356(2)	33.07(2)	—	—
Hq.	180°	—	0.0356(2)	33.18(2)	—	—
Ann.	90°	17.5°	0.0318(3)	30.51(6)	18.14	1.68(2)
Ann.	90°	30°	0.0313(3)	30.61(4)	18.25	1.68(2)
Ann.	180°	—	0.0356(2)	34.10(2)	—	—

The measurement of this angle was possible using the reflection of the laser from the sample, then we determined the angle between the incident and the reflected beam $\hat{r}$. As one can see in figure 3.12, the spectra at 180° have a higher intensity in the inelastic region as compared to the 90° geometry. That difference is caused by the efficiency of the set-up, in the backscattering geometry the same lens is used to focus the laser on the sample and to collect the scattered radiation.

The spectra are cut close to $\omega \approx \omega_i$ (ω_i is the radial frequency of the incident radiation) where the intensity starts to increase because of the elastic scattering, the cut corresponds to the positioning of a filter that reduces the radiation in order to avoid damages to the detector due to the high intensity of the radiation at $\omega \approx \omega_i$.

An accurate measurement of the inelastic features of Fig. 3.12 reveals that the width of the longitudinal peaks measured in the backscattering geometry is smaller of that measured at 90°. This phenomenon is mostly related to the Q distribution of the collected radiation in the 90° scattering geometry [1]. In fact, in the 90° geometry the solid angle for the collection of the scattered radiation increases in comparison to the backscattering geometry: k_{out} varies in an interval and then also Q is not longer defined as a unique value but it is rather the average value of a distribution. The final effect is that each spectrum becomes the superposition of several spectra each

[1] In the 90° geometry the image of the scattering volume is not any longer a point, then the collection optics cannot focus the image in the pin-hole of the spectrometer.

with a different characteristic radial frequency ω_s. Then, an additional broadening of the inelastic features of the spectra $\Delta\omega_s$, is produced. Assuming a linear relationship between ω_s and momentum Q ($\omega_s = vQ$) we obtain $\Delta\omega = v\Delta Q$.

Using a fitting routine we determined the position of each excitation, modeling the peaks as lorentzian functions. The frequencies of the inelastic excitations have been determined averaging the values obtained from the position of the inelastic peaks present on both sides of each spectrum. In table 3.1 we report the measured frequencies ν_L and ν_T. To evaluate the magnitude and direction of Q, we needed to estimate the refractive index n of the sample. In fact, Q is defined by the incident wavelength of the laser λ, the scattering geometry (via the angle θ between the incident radiation and the collected one) and the refractive index: $Q = 4n\pi/\lambda sin(\theta)$.

Passing through the interface between two homogeneous materials, an electromagnetic radiation changes wavelength due to the different values of n. The wave vector inside a material has the value $k_{in} = nk_0$ where $k_0 = 2\pi/\lambda_0$ (λ_0=514.5 nm^{-1}) is the value of the wave vector in the air and n is the refractive index of the material. Moreover, the refraction index changes not just the modulus of the wave vector k_{in}, but also its direction because inside the medium the light is refracted to a new angle $\theta_{r(in)}$. According the Snell's law the direction of k_{in} is closer to the normal to the surface of the sample and similar considerations have to be applied to k_{out} (see figure 3.11). The value of Q in the 90° geometry is defined from the values of n and θ_{in} according to Eq.(3.29).

$$\frac{sin(\theta_{r(out)})}{sin(\theta_{(out)})} = \frac{1}{n} \qquad \frac{sin(\theta_{r(in)})}{sin(\theta_{(in)})} = \frac{1}{n} \tag{3.26}$$

$$\theta_{in} + \theta_{out} = \frac{\pi}{2}, \tag{3.27}$$

$$\theta = \pi - \theta_{r(in)} - \theta_{r(out)}, \tag{3.28}$$

$$Q = 2n|k_0|sin(\theta). \tag{3.29}$$

In the backscattering geometry the orientation of the sample relative to the laser direction does not change the value of Q that is always $2nk_0$ because now $\theta = \pi$. In fact, the same lens is used to focus the incoming laser beam and to collect the scattered radiation (see figure 3.11). The value of n has been determined by comparing the longitudinal excitations measured at 90° and in back scattering geometry. Recalling that $\omega_{L(90°)} = v_L Q_{(90°)}$ and $\omega_{L(180°)} = v_L Q_{(180°)}$ we can write (using Eq.(3.28) and Eq.(3.29)):

$$\frac{\omega_{L(90°)}}{\omega_{L(180°)}} = sin\left[\left(\pi - \arcsin\left(\frac{sin(\theta_{in})}{n}\right) - \arcsin\left(\frac{sin(\theta_{out})}{n}\right)\right)/2\right]. \tag{3.30}$$

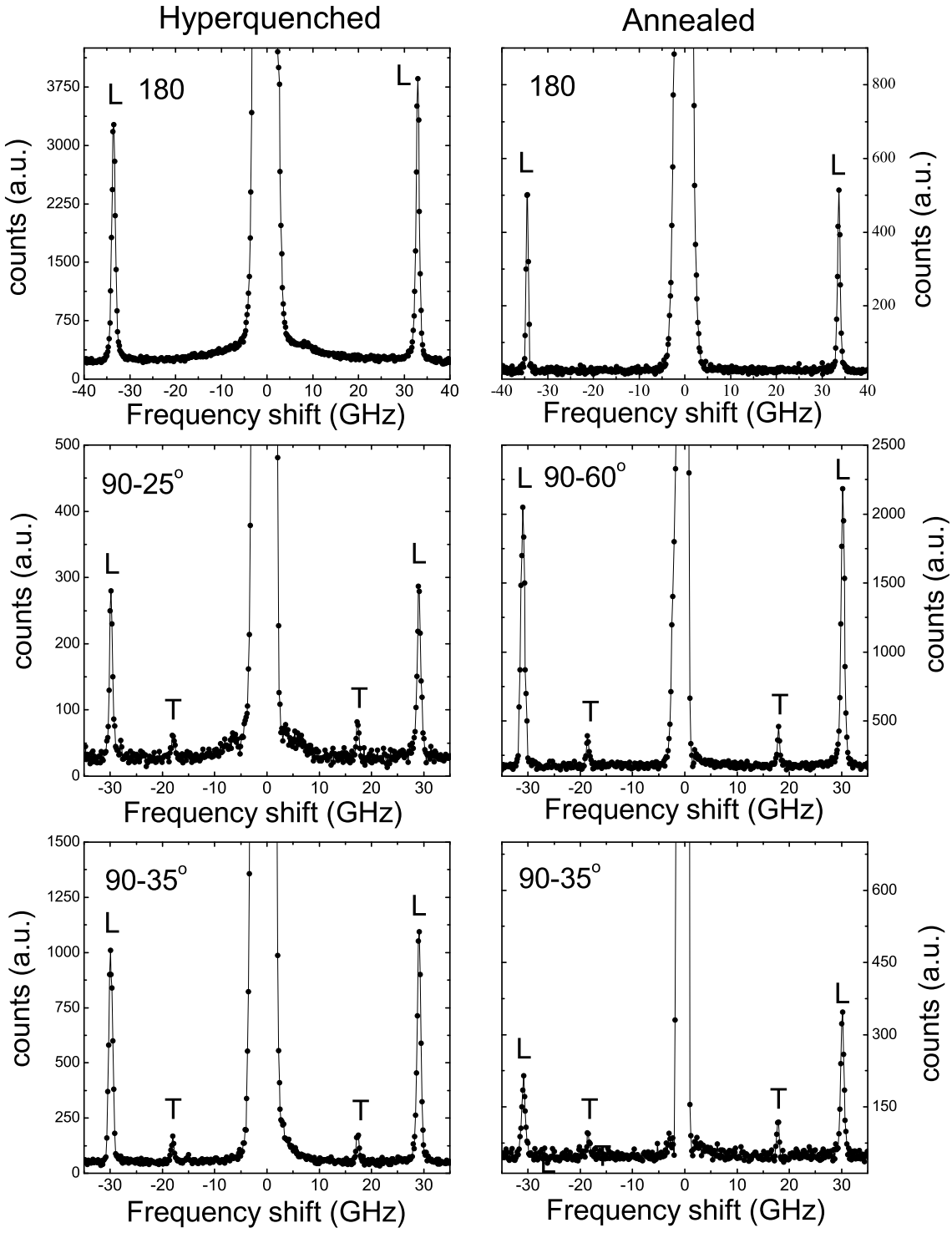

Figure 3.12: *BLS spectra in backscattering and $90^0 - xx^0$ geometry. The xx indicates the values of $2\theta_{in}$, L and T identify respectively the longitudinal and transverse excitations.*

Table 3.2: Here we report the density (ρ), refractive index (n), longitudinal (v_L) and transverse (v_T) sound velocity for the hyper-quenched (Hq.) and annealed (Ann.) glass.

Sample	$\rho\,(\mathrm{g\,cm^{-3}})$	n	$v_L\,(\mathrm{m\,s^{-1}})$	$v_T\,(\mathrm{m\,s^{-1}})$
Hq.	2.404(1)	1.446(2)	5820(20)	3470(20)
Ann.	2.439(5)	1.454(2)	6060(20)	3620(10)

Therefore, using Eq.(3.30) it is possible obtain n from the measurements of $\omega_{L(90^\circ)}$, $\omega_{L(180^\circ)}$ and θ_{in}. Following this procedure we determine the value of n for the hype-quenched sample.

Because of the small dimensions and the quality of the sample, the refractive index for the annealed glass has been estimated using the Clausius-Mossotti equation [2]:

$$\frac{n-1}{n+2} = 4\pi\alpha\rho, \tag{3.31}$$

here α is the polarizability (a parameter related to the chemical composition of the glass). The slight difference in density ($\approx 1.4\%$) according to Eq. (3.31) does not lead to significant changes in n (see Table 3.2). From the value of n we determined the values of the exchanged wave vectors Q and the values of the longitudinal and transverse speed of sound $v_L = \omega_L/Q$, $v_T = \omega_T/Q$. In Table 3.2 we report the measured values of v_L and v_T for both samples, the differences can be observed also from the BLS spectra, see figure 3.13.

Thus we can conclude that the annealed sample has a slightly higher speed of sound ($\approx 4\%$) for both the longitudinal and the transverse waves modes.

3.6 X-ray scattering measurements

In this paragraph we discuss the x-ray scattering measurements performed to investigate the effect of the different thermal history on the microscopic structure of our glasses.

As we have shown in section 2.2, the cross section for the photons scattering process, with energies in the x-ray range, can be written as:

$$\left(\frac{\partial^2\sigma}{\partial\Omega\partial\omega_f}\right) = r_0^2\left(\frac{k_f}{k_i}\right)(\hat{\epsilon}_f\cdot\hat{\epsilon}_i)^2|f(Q)|^2 S(Q,\omega), \tag{3.32}$$

here $\hat{\epsilon}_f$ and $\hat{\epsilon}_i$ are the polarization vectors, k_i and k_f the wave vectors of the photons

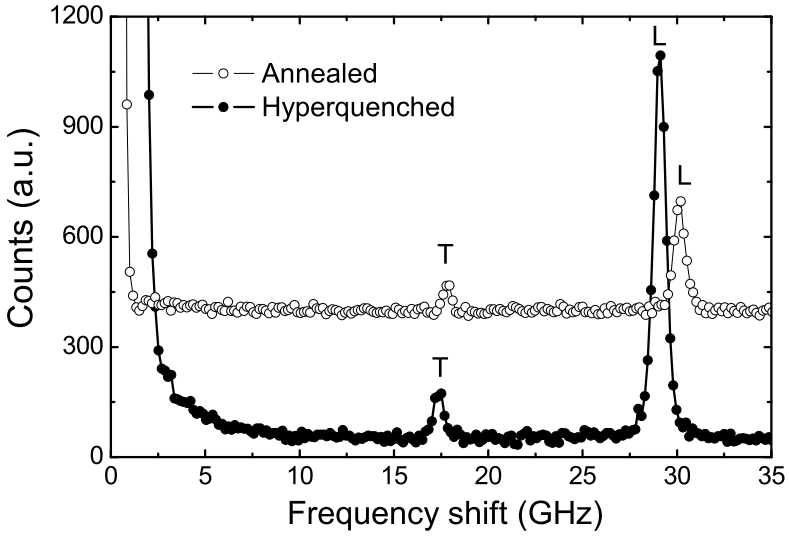

Figure 3.13: *BLS spectra of the annealed and hyperquenched glass collected in the same 90° geometry.*

before and after the scattering process; r_0 is the classical electron radius, $f(Q)$ and $S(Q,\omega)$ are respectively the form factor and the dynamical structure factor of the system. Here, for simplicity, we give the scattering cross section expression valid for a monatomic system. Eq.(3.32) is valid in the following hypothesis [81]:

- The energies of the system in the final state ($\hbar\omega_f$) and the initial state ($\hbar\omega_0$) are comparable $\omega_f/\omega_0 \approx 1$.
- In the probed system the adiabatic approximation can be applied to separate the dynamics of electrons from that of nuclei.

Starting from the expression 3.32 it is possible to extract information on the distribution of nuclei and electrons of a solid through $f(Q)$ and $S(Q,\omega)$. The intensity of the scattered radiation by the sample can be written as:

$$I_{exp} \propto |f(Q)|^2 S(Q,\omega) \tag{3.33}$$

In a system with N different atomic species, we substitute $f(Q)$ and $S(Q,\omega)$ with: $\sum_{i=1}^{N} f_i^2(Q) S_i(Q,\omega)$. If now we consider the integral value of the dynamic structure factor: $\int d\omega S(Q,\omega)$, we probe instead of $S(Q,\omega)$ the static structure factor $S(Q)$. $S(Q)$ represents the Fourier transform of the correlation function of the density fluctuations of the system. From the static structure factor we can have information on the microscopic structure of the system and find what are the typical correlation lengths between the atoms.

The Q dependence of $S(Q)$ has some characteristic features that are strictly associated with the topological aspect of the probed system. For instance, if we consider a crystal (i.e. an ordered system) the $S(Q)$ is composed of Bragg peaks (see figure 3.14 [82] bottom part, here the maxima of the density fluctuations appear as delta functions). The position in Q space of the peaks is related, according to the Bragg law, to the distance between the crystalline planes.

In an amorphous system, the $S(Q)$ loses the well defined structure typical for a crystal and the maxima of $S(Q)$ are not sharply defined (see figure 3.14 [82] upper part). The static structure factor presents pronounced peaks associated with the typical correlation lengths between the atoms, at higher Q values the $S(Q)$ has an oscillating structure.

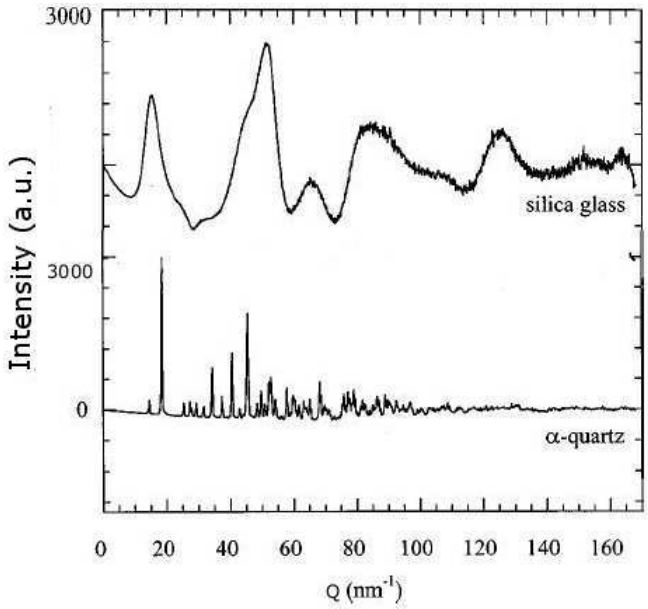

Figure 3.14: *X-ray diffraction data for silica glass and its relative crystalline phase: quartz (from the work of Y. Ding et al. [82]).*

3.6.1 X-ray scattering for hyperquenched samples

The x-ray scattering measurements have been performed at the ID27 beamline [83] at the ESRF. This experimental station is optimized for monochromatic x-ray diffraction on systems at high pressure and high temperature having a high photon flux and high capabilities of focusing the beam. In figure 3.15 we report a sketch of the main elements of the beam line.

The measurements of our samples have been done using an incident beam energy of 33 keV allowing for collecting the scattered radiation over Q values from 5 to 60 nm^{-1}. The geometrical constraints that have limited the probed Q range are: the minimum angle of scattering θ_{min}, defined by the finite size of the beam stop, and the size of

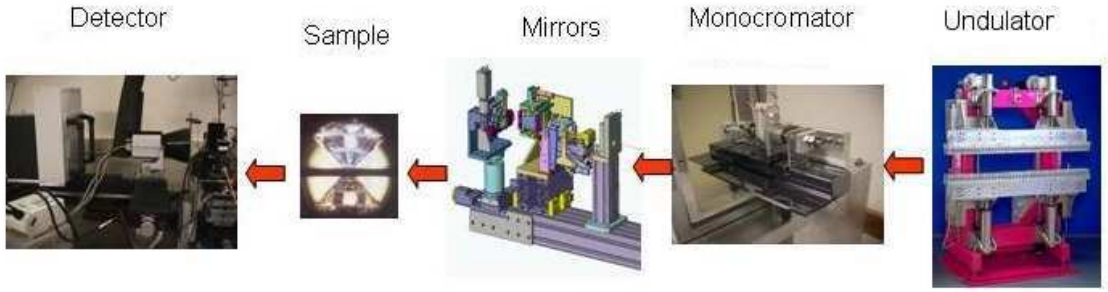

Figure 3.15: *Layout of the ID-27 beamline .*

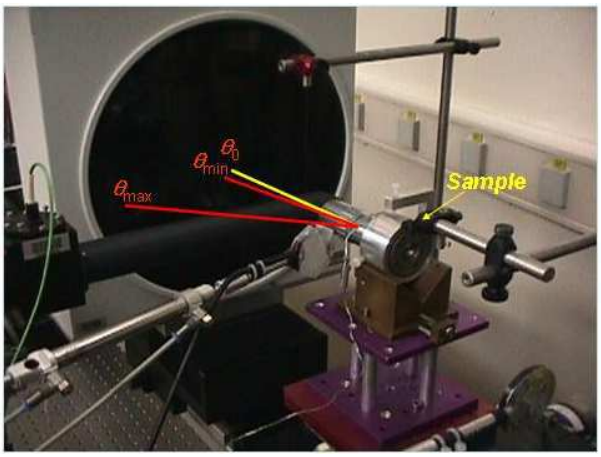

Figure 3.16: *Image plate detector used for the x-ray measurements at the ID-27 beamline.*

the sensitive area of the image plate detector (see figure 3.16). The typical beam size of the sample was about 0.5x0.8 mm^2; the samples have been placed on a needle at 1.5 m far from the detector. In order to have the best efficiency on the detection of the scattered radiation a MAR345 camera has been used. This detector allows for collecting radiation within a surface with a diameter of 150 mm with spatial resolution of 150 μm. The typical acquisition time for each measurement was 1-5 s; the read-out time of the detector was 2 min.

After each measurement of our glasses, the radiation scattered by air has also been measured in absence of sample. In this way the contribution of the scattering from the air I_A has been measured (see figure 3.17). Such contribution is particularly strong at low Q values where it can mask the small features of the static structure factor of the samples. We subtracted I_A from the intensity of the scattered radiation I_{exp} taking into account the absorption of the sample μ:

$$I_c = I_{exp} - I_A e^{-\mu L}. \tag{3.34}$$

Here L represents the length of the sample. The intensity I_c has been normalized in order to have for both the sample the same height of the first diffraction peak located at 17 nm^{-1}. In figure 3.17 we present the scattering intensity for the two samples after normalization and correction for air scattering.

3.6.2 Results

As we have shown in the previous section, the measurements of x-ray scattering allow for having access to the microscopic structure of the system through its static structure factor $S(Q)$. Nevertheless, in a polyatomic system the $S(Q)$ is averaged over different atomic species weighted by the corresponding square form factor $f^2(Q)$. Thus the information coming out from x-ray scattering measurement is not sensitive only to a specific atomic specie. However, this property of x-ray scattering does not represent a problem for the final task of our study: a qualitative understanding of whether there is difference between the microscopic structure of the two glasses.

Due to the identical conditions of measurement, for the two samples we have the identical contributions of other contribution as the Compton scattering. Moreover, the identical composition of the investigated samples (identical $f(Q)$ in Eq. (3.33)) allows us to attribute the differences between the scattered radiation $I(Q)$ for the two samples to the differences in $S(Q)$, and then to the microscopic structure of the samples.

In figure 3.17 we show the x-ray scattering data for both samples: hyperquenched and annealed. The data have been corrected for the air scattering and normalized to have the same height at 60 nm^{-1}. From a first glance at figure 3.17 we cannot recognize any notable difference between the two samples; the two curves follow the same qualitative behavior in the all measured Q range, while at 21 nm^{-1} a small decrease in the intensity of the radiation scattered from the hyperquenched glass can be recognized. Moreover, figure 3.17 shows a slight Q shift between the two curves, in particular the first maximum of the annealed sample moves to higher Q values. This difference is qualitatively consistent with the change in density for the two glasses. In fact, for higher density the average distance between the atoms decreases, and the position of the first maximum at 16.6 nm^{-1} (see figure 3.17) moves to higher Q values.

We can conclude that the different thermal history of the two samples does not have any significant effect in the range of intermediate length scale corresponding to the Q range of 5-20 nm^{-1}.

3.7 Mössbauer measurements

Using Mössbauer spectroscopy we investigated the chemical environment of iron atoms in our samples. Such measurements complete the microscopic characterization of the samples started with the x-ray scattering measurements because they give information on the local structure of iron atoms.

According to the results of x-ray scattering measurements discussed in the previous paragraph, the different thermal history of the two samples does not have a significant effect on the microscopic structure of the glass. However, those results do not exclude

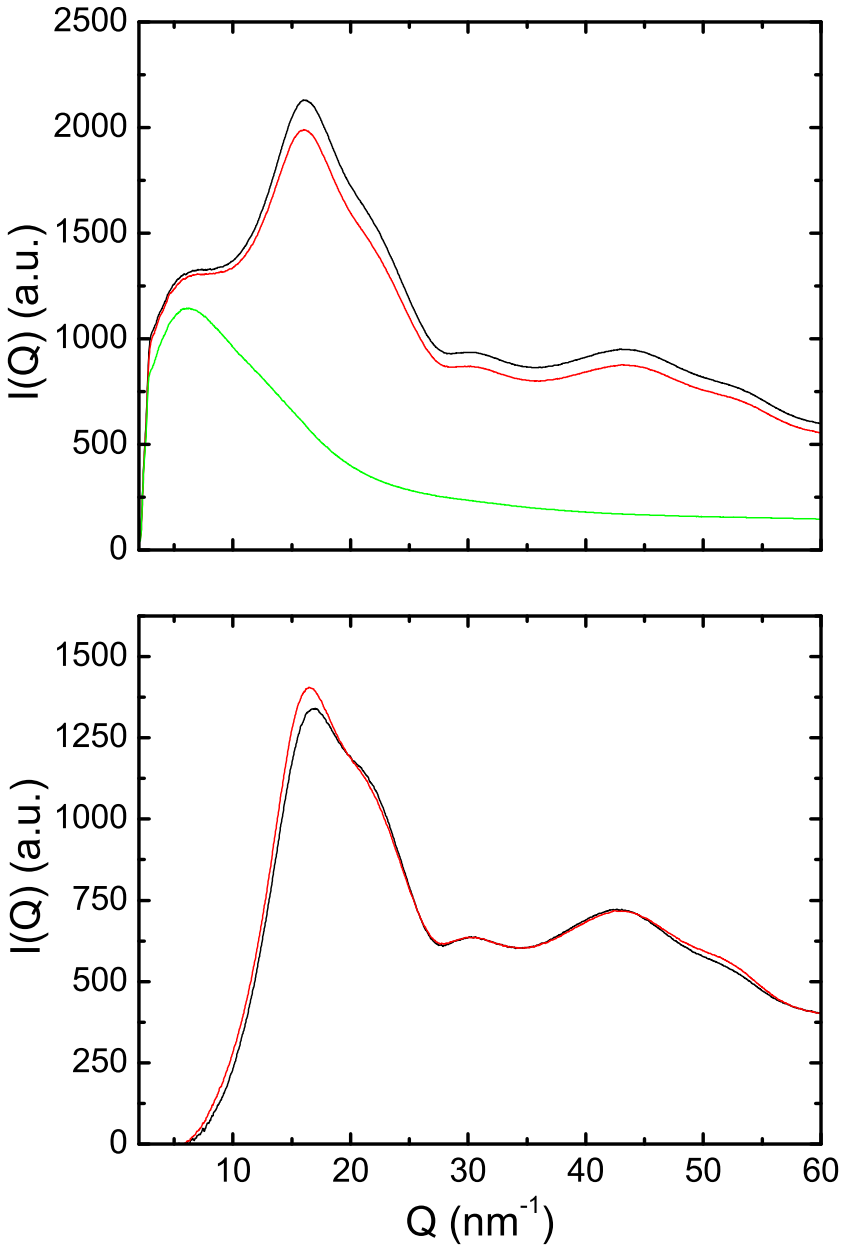

Figure 3.17: *Intensity of the scattered radiation from the hyperquenched (red line) and annealed glass (black line). In the upper panel we show the raw data with the contribution to the scattering from the air (green line). In the bottom panel we show the data corrected for the contribution of air scattering.*

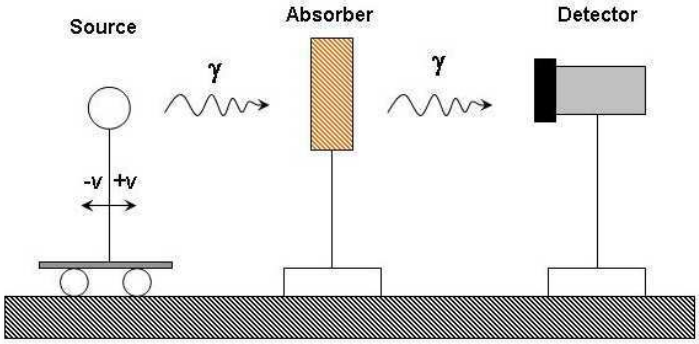

Figure 3.18: *Scheme of the experimental set-up of a Mössbauer measurements.*

completely a slight change of the local structure of the system. The intensity of the scattered radiation is proportional to the static structure factor $S(Q)$ averaged over all atomic species by the corresponding form factor: $f(Q)^2$. Thus a rearrangement of the atomic species with a low number of electrons can be masked by the unchanged structure of heavier atoms.

In order to have a clearer pictures of the local structure of the glasses, we probe our samples by Mössbauer spectroscopy. As we have discussed in paragraph 2.1.2 such technique is chemically selective, allowing the extraction of quantitative information on the distribution of charges around iron atoms. We performed Mössbauer measurements on both samples (annealed and hyperquenched) using a "classical" experimental set-up (sketched in figure 3.18). The measurements have been performed at the ESRF using a transmission geometry. γ rays emitted by the ^{57}Co(Rh) source, that moves with a constant acceleration, go through the sample. When the energies of γ rays matches that of the nuclear levels of iron atoms the probability that the photons are absorbed strongly increases. Detecting the γ rays that pass through the sample we obtain the Mössbauer spectra that correspond to the energy distribution of the absorption cross section of the glass. In figure 3.19 we report the measured spectra. Before the measurement we calibrate the energy scale of the spectrometer by measuring a reference sample of α-iron foil. This sample has a Mössbauer spectrum consisting of 6 characteristic absorption lines allowing calibrating precisely the energy scale of the spectrometer.

Each sample has been measured for 48 hours. The spectra consists of the superposition of two doublets. These two doublets correspond to two different valence states of iron atoms: Fe^{+3} and Fe^{+2}. In order to extract quantitative information on the gradient and magnitude of the electric field acting on the iron atoms we estimate the value of the hyperfine parameters: quadrupole splitting, Δ, and isomer shift, δ (see section 2.1.2). Each spectrum has been compared to the following model function I_M[41]:

$$I_M = B + Ce^{-(A_1Q_1+A_2Q_2)}, \tag{3.35}$$

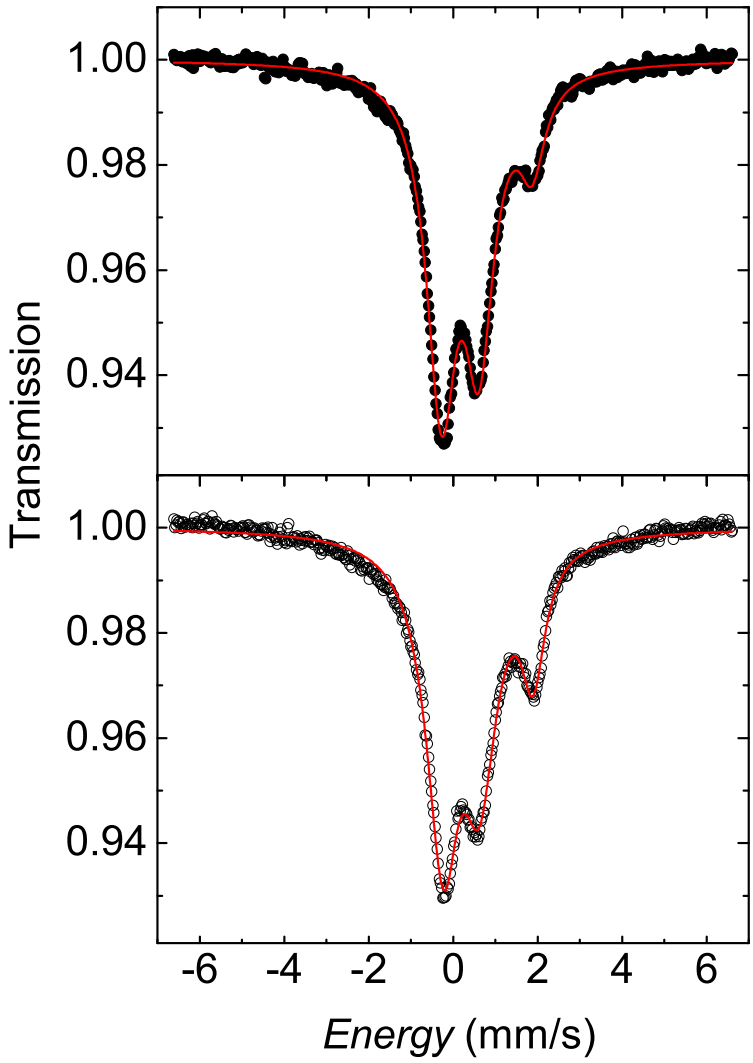

Figure 3.19: *Mössbauer spectra for the hyperquenched (upper panel) and annealed (down panel), the continuous red lines represent the results of the fit.*

Table 3.3: The hyperfine parameters: isomer shift (relative to α-iron) and quadrupole splitting Δ are reported for each sample (Hq. indicates the hyperquenched and Ann. the annealed sample). "Fe state" indicates the state of oxidation of Fe atoms according to the values of the hyperfine parameters. R is the relative weight of the particular excitation state.

Sample	Fe state	δ (mm/s)	Δ (mm/s)	R %
Hq.	3^+	0.24(9)	0.84(7)	81
Hq.	2^+	0.91(1)	2.13(3)	19
Ann.	3^+	0.26(8)	0.82(5)	80
Ann.	2^+	0.94(4)	2.10(0)	20

$$Q_1 = \frac{1}{2}\frac{(\Gamma_1/2)^2}{((x-\delta_1-\Delta_1/2)^2+(\Gamma_1/2)^2)} + \frac{1}{2}\frac{(\Gamma_1/2)^2}{((x-\delta_1+\Delta_1/2)^2+(\Gamma_1/2)^2)},$$

$$Q_2 = \frac{1}{2}\frac{(\Gamma_2/2)^2}{((x-\delta_2-\Delta_2/2)^2+(\Gamma_2/2)^2)} + \frac{1}{2}\frac{(\Gamma_2/2)^2}{((x-\delta_2+\Delta_2/2)^2+(\Gamma_2/2)^2)}.$$

Here δ_i and Δ_i are respectively the chemical shift and the quadrupole splitting, B and C are constants. The parameter Γ_i has been introduced to take into account the broadening of the Mössbauer lines due to the typical distribution of the local environments in glasses [103]. The values of A_i give a measure of the intensity of the Mössbauer lines.

Using a fitting routine we compared the model 3.35 with the experimental data, obtaining the values of $A_i, \Gamma_i, \Delta_i, \delta_i$ that describe the line-shape of each Mössbauer spectrum (see table 3.3). The values of δ_i reported in table 3.3 are given relative to the α-iron absorber. These values have been obtained adding to the measured isomer shift 0.11 mm/s (i.e. the value of δ of the ^{57}Co(Rh) relative to the α-iron).

From the value of A_i we also estimated the relative weight of the particular excitation state $R_i = A_i\Gamma_i/(A_1\Gamma_1 + A_2\Gamma_2)$. This quantity determines the prevalent valence state of iron atoms in the glass. For both samples it has been found that 80% of iron atoms is Fe^{+3} and 20% Fe^{+2}.

The presence in the literature of a study of iron sodium silicates based on Mössbauer and neutron diffraction measurements [84] [85] allows us to use the values of δ to establish the coordination state of the iron atoms. The tetrahedral coordination states for Fe^{+3} and Fe^{+2} state has been found to correspond to values of δ in the range of

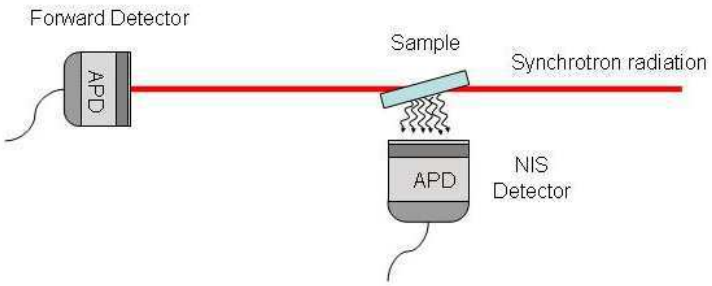

Figure 3.20: *Scheme of the geometry of NIS measurements.*

0.20-0.32 and 0.90-0.95 mm s^{-1}, respectively. Thus the measured values of δ_i 0.24-0.26 for Fe^{+3} and 0.91-0.94 for Fe^{+2} indicate that in our samples most of iron atoms are in the tetrahedral coordination state, the same as silicon atoms. This result suggest that most of iron substitutes for silicon in the glass network.

Both hyperfine parameters (Δ and δ) have been found identical (within the error bars) for the annealed and the hyperquenched glass. Thus the different thermal history and consequently the different T_f of the samples did not produce notable effects on the local environment of the Fe atoms in the glass.

3.8 Nuclear inelastic scattering measurements

In order to probe the effect of the thermal history of our glass on its density of vibrational state (DOS) we performed nuclear inelastic scattering measurements (NIS). The measurements have been performed at the Nuclear Resonance beam line ID18 of the ESRF. We used as hyperquenched material two independent prepared samples: fibers (collected together in a small kapton pocket) and thin plates. All samples have been positioned with an angle below $\sim 10°$ between the surface of the sample and the beam direction. This choice has been motivated by the need to increase the number of photons produced in the nuclear deexcitation that are transmitted through the sample to the detector placed below the sample (see figure 3.20).

The samples have been mounted directly on an avalanche photo diode (APD) detector that collects the secondary products of nuclear deexcitation: Fe-K_α fluorescence radiation. A second APD detector has been placed in the forward direction to measure the instrumental function of the spectrometer (see figure 3.20). In order to have a high energy resolution we used a monochromator with an energy band pass of 0.5 meV.

3.8.1 Energy dependence of NIS

The measurements of the NIS energy dependence have been carried out scanning the incident energy from -120 to +120 meV in steps of 0.2 meV. For each step, the integration time used to collect the secondary products of nuclear deexcitation has been either

5 or 10 s. Thus the typically acquisition time for an entire energy scan was about 1 hour. Several successive scans were added to obtain the raw spectra shown in figure 3.21.

To check the reproducibility of our measurements we performed the NIS measurements for two independently prepared samples for both the annealed and the hyperquenched glass. In order to compare directly the raw spectra they have been normalized to their first moment $< E_1 >_I$. The intensity of the experimental spectrum $I(E)$ is related to the probability of the nuclear absorption of a photon $S(E)$ through the convolution with the instrumental function of the monochromator $P(E)$, see Eq. (3.36). It can be shown [86] that the first moment of the scattering probability $< E_1 >_S$ is equal to the recoil energy of a free ^{57}Fe nucleus: E_R=1.956 meV.

$$I(E) = I_0 \int P(E')S(E - E')\ dE', \tag{3.36}$$

$$< E_1 >_I = \int dEI(E)E =< E_0 >_I < E_1 >_P + I_0 E_R, \tag{3.37}$$

here $< E_0 >_I$ is the zero moment of the spectrum, $< E_1 >_P$ the first moment of the resolution function and I_0 a scaling factor, then combining $< E_1 >_I$, $< E_1 >_P$ and $< E_0 >_I$ we obtain:

$$I_0 = \frac{(< E_1 >_I - < E_0 >_I < E_1 >_P)}{E_R}, \tag{3.38}$$

and if

$$< E_1 >_P = 0, \tag{3.39}$$

$$I_0 =< E_1 >_I / E_R. \tag{3.40}$$

Passing from Eq. (3.38) to Eq. (3.40) we have exploited the symmetry of the instrumental function ($< E_1 >_P = 0$). In order to proceed with a comparison between the collected raw spectra we took into account the different values of I_0 multiplying each set of data by $E_R < E_1 >_{IM} / < E_1 >_I$, where $< E_1 >_{IM}$ is the value of the first moment averaged for all spectra. Figure 3.21 shows that the measurements of both glasses (hyperquenched and annealed) are completely reproducible. The intensity of the experimental spectra of the two samples superimposes on each other. The samples are prepared independently with the same procedure.

Moreover, the NIS data reported in figure 3.21 show a clear difference between the hyperquenched and the annealed glass. At 5 meV, the NIS spectrum of the hyperquenched sample shows an increase of intensity of $\approx 16\%$ compared to the value of the annealed one. The effect cannot be explained by an unlikely normalization error because the effect stays even if the spectra are superimposed on the tails. The difference between the intensity of the NIS spectra of the annealed and hyperquenched samples decreases increasing the energy, at 15 meV the data have already the same value.

Inspecting the NIS data of figure 3.21, the spectra are asymmetric with respect to the zero energy position; the peak at 5 meV is more intense compared to that at -5

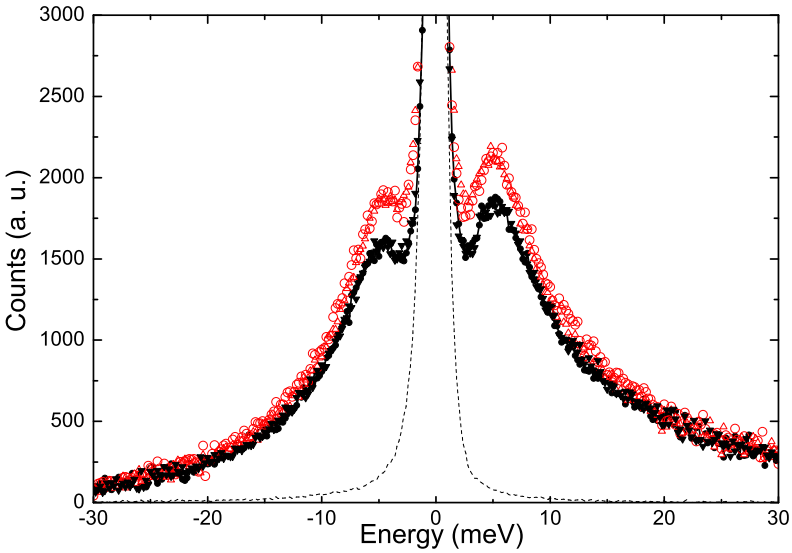

Figure 3.21: *Energy dependence of nuclear inelastic scattering. The circles and triangles show the data for two independently prepared samples. The red color indicate the hyperquenched sample, the black color the annealed sample, and the dashed line is the resolution function.*

meV. Such difference is caused by the processes of creation and annihilation of phonons. In fact, the ratio between the intensities of the positive and negative energy region of the spectra is equal to:

$$\frac{I(E)}{I(-E)} = e^{E/k_B T}, \tag{3.41}$$

where $e^{(+E/(k_B T)}$ is the ratio of the probability to create and annihilate phonons. In equation 3.41 T is the temperature and k_B is the Boltzmann constant.

3.8.2 Density of vibrational States and reduced DOS

From the NIS data showed in figure 3.21 we extracted the DOS using a procedure based on a double Fourier transformation (see section 2.1.3). We first subtracted the elastic scattering contribution from the energy dependence of the NIS data, this has been obtained writing the measured intensity $I(E)$ close to the energy region where $E \simeq 0$ as:

$$I(E) = I_n(E) + \zeta P(E) \tag{3.42}$$

here $\zeta P(E)$ is the elastic contribution, $P(E)$ is the instrumental function and $I_n(E)$ is the intensity of the radiation inelastically scattered. Then, once calculated ζ, from the knowledge of $P(E)$ it is possible to reconstruct $I_n(E)$ from $I(E)$. A raw approximation of $I_n(E)$ at $E \approx 0$ can be obtained by neglecting the contribution of the elastic peak. This first approximation of $I_n(E)$, that we indicate by $I_n^*(E)$, can be obtained by cutting the spectrum of the elastic peak and replacing it by a straight line. Now the value of ζ can be determined minimizing the difference between $I_n(E) = I(E) - \zeta P(E)$ and the value of $I_n^*(E)$. Once subtracted from the spectra the elastic contribution, is possible to evaluate the Lamb-Mössbauer factor starting from the zero moment of the spectrum, according Eq. (3.36) we can write:

$$< E_0 >_{In} = \int dE I_n(E) = I_0(1 - f_{LM}). \tag{3.43}$$

The values of I_0 and f_{LM} (calculated by Eq. (3.43) and Eq. (3.40)) allows us to perform a Fourier transformation procedure able to isolate the one phonon term contribution $S_1(E)$ from the probability of nuclear absorption (see section 2.1.3). $S(E)$ in fact is the sum of different contributions ($S(E) = \sum_i S_i(E)$) that correspond to the processes in which n phonons can be created or annihilated. From $S_1(E)$ it is possible obtain the Fe partial DOS $g(E)$ of the system (see section 2.1.3):

$$g(E) = S_1(E) \frac{E}{E_R} \left(1 - e^{-\beta E}\right). \tag{3.44}$$

From the measured $g(E)$ we can derive different quantities (for instance the f_{LM}) that can be also estimated from the spectral moments of $I(E)$ [46]. The comparison between the two values of the same quantity calculated with the two independent procedures allow us to check the reliability of the measured $g(E)$.

Figure 3.22 shows the measured DOS for the hyperquenched and the annealed sample. The two DOS have a higher statistical quality up to 20 meV, due to the chosen longer acquisition time for this energy range. Looking at the entire measured energy range (figure 3.22) we cannot recognize any significant difference between the two samples; the DOS has the same qualitative behavior for both glasses. Inspecting the measured DOS we observe up to 20 meV the typical monotonic increase of DOS due to the acoustic excitations of the glass (see section 1.6.1). Moreover, a pronounced inelastic feature located between 60 and 70 meV, is evident.

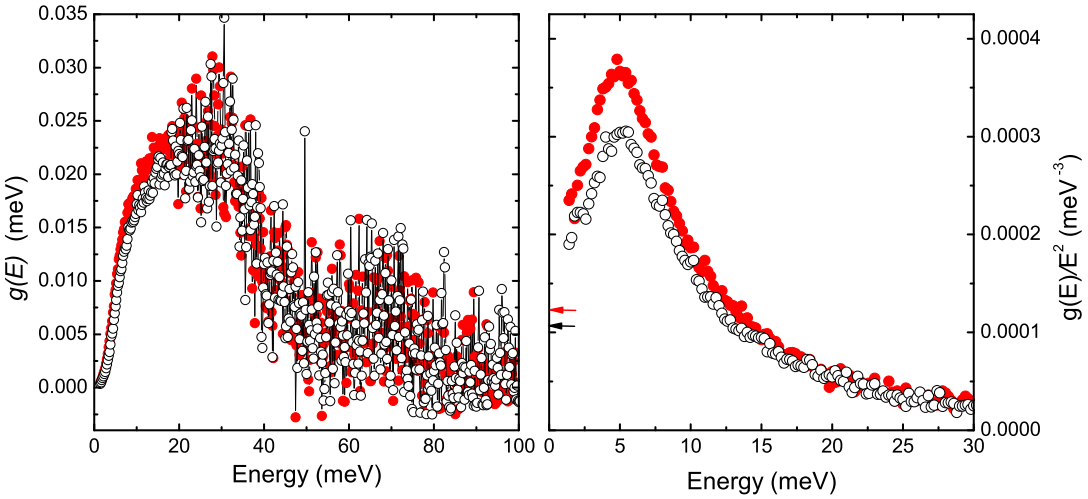

Figure 3.22: *The left panel shows the DOS, the right panel the RDOS. The full red circles represent the hyperquenched glass, the open circles the annealed one. The two arrows on the left panel indicate the zero energy limit of the RDOS estimated by the Debye model.*

In order to investigate the behavior of the DOS at low energy we plot the reduced density of states $g(E)/E^2$. This quantity in fact allows us to make a direct comparison in the low energy region between the data and the behavior predicted by the Debye model. The right panel of that figure shows a large excess of the density of vibrational states over the level defined by the Debye approximation, thus both samples show the BP. The energy position of the BP in our glasses is consistent with the value found in others silicate glasses ($\sim$ 5 meV) [75]. The maximum of the RDOS is $\sim$ 19% higher in the hyperquenched sample compared to that of the annealed one. Moreover, the figure also reveals a slight difference in the energy position of the maximum.

Fitting the energy dependence of the RDOS, for both samples, at energies higher than the BP, we observe that $g(E)/E^2$ has, up to energies of 30 meV, an exponential decay: $g(E)/E^2 \sim exp(-E/E_0)$. As it has been observed as well in others systems [87], increasing the Debye energy of the glass (E_D=28.9 and 30.3 meV, respectively for

the hyperquenched and the annealed glass, see next section) the characteristic energy E_0 increases ($E_0 = 7$ and 7.4 meV, respectively in the hyperquenched and the annealed glass).

Starting from the measured DOS we evaluated the difference in vibrational energy per iron atom between the hyperquenched and the annealed glass $\Delta U = U_{Hq.} - U_{ann}$, where U is determined using the following relation [88]:

$$U = \frac{3}{2}\int_{E_{min}}^{E_{max}} dE g(E) E \frac{e^{\beta E}+1}{e^{\beta E}-1}. \tag{3.45}$$

Integrating the measured density of state in the energy range from E_{min}=2 to E_{max}=20 meV, U has been found equal to 2.0 meV per iron atom, which would correspond to 0.8 meV per atom in average, assuming the same shape of the DOS for all atom species within the considered energy range.

Our NIS measurements reveal that there is a clear difference between the DOS of the hyperquenched and annealed glass. Such difference is evident in the RDOS where it appears as an increase in intensity of the peak at ≈ 5 meV.

3.8.3 RDOS in reduced scales

To evaluate the influence of the modification of the macroscopic properties of the glass to the low energy region of the DOS, we compared the zero energy limits of the RDOS estimated by the NIS measurements, with the corresponding values predicted by the Debye model:

$$\lim_{E\to 0} \frac{g(E)}{E^2} \equiv \frac{m_r}{< m >} \frac{3}{E_D^3}, \tag{3.46}$$

Here we have introduced the factor $\frac{m_r}{<m>}$ because we consider the partial DOS of iron atoms [89], m_r is the mass of the iron atom and $< m >$ is the average atomic mass of the glass. The value of the Debye energy has been calculated from the measured values of density and speed of sound according to the relation:

$$E_D = (6\pi^2 \hbar^3 n \langle v \rangle^3)^{\frac{1}{3}}, \tag{3.47}$$

$$\frac{1}{\langle v \rangle^3} = \frac{1}{3}\left(\frac{1}{v_L^3} + \frac{2}{v_T^3}\right), \tag{3.48}$$

here n is the number of atoms per unit volume, v_L, and v_T are the longitudinal and transverse speed of sound. The values of the Debye energies that we obtain from Eq. (3.47) for the annealed and the hyperquenched sample are respectively: 30.3 ± 0.3 and 28.9 ± 0.3 meV. The corresponding zero energy limit of the RDOSs are shown in the right panel of figure 3.22 as the two arrows at $E = 0$. According to the definition of the BP: the excess of vibrational modes over the Debye level (see section 1.6.2), we have to consider these arrows as reference levels to evaluate the height of the BP.

Figure 3.22 shows that the increase of low energy modes in the hyperquenched glass does not correspond to an increase of the height of the BP with respect to the annealed

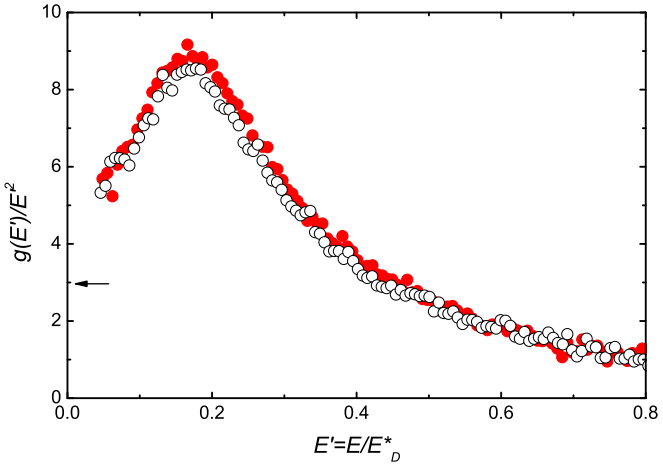

Figure 3.23: *Reduced density of state rescaled in Debye energy units, the red and open circles show respectively the data for the hyperquenched and the annealed glass, the arrow indicate the zero energy limit estimated by the Debye model.*

sample, in fact also the relative Debye level increases. This observation suggests that the differences in RDOS between the two samples can be attributed simply to the different continuum properties of the glass. Plotting the RDOS in dimensionless units $E' = E/E_D$ we remove from the RDOS the effect induced by the transformation of the macroscopic properties of the glass.

Figure 3.23 shows that in the reduced energy units E' the reduced densities of states of the two samples become almost identical. The slight residual difference is comparable to the uncertainty in $3/E_D^3$ and therefore is not significant. Thus, the observed effect of quenching on the density of vibrational states is described entirely by the changes in the macroscopic properties of the glass. In particular this implies that quenching does not affect the height of the BP. The increase of RDOS is compensated by a corresponding increase of the Debye energy and also the position of the BP scales according to the E_D of the glass. The effect of quenching is described by the transformation of a continuum medium.

3.9 Conclusions

The main result of our study is the insensitivity of the BP to the change of fictive temperature of the glass. The different thermal histories of the glass have the effect of transforming its macroscopic properties and then consistently the DOS.

Such results have been obtained combining the measurements of the DOS with those of density and sound velocity in a hyperquenched and an annealed glass (glasses with different T_f). The measured DOS shows a higher level of low-energy vibrational

states for the hyperquenched glass with respect to the annealed one; the difference vanishes after correction for the corresponding Debye energy of the sample.

The measurements of Mössbauer spectra and x-ray diffraction reveal that the different thermal history of the two samples does not have notable effects on the structure of the glass in the intermediate and short length scale range. The changes in DOS between the glasses with different T_f can be associated completely with the transformation of the macroscopic properties of the glass. The increase of the DOS of the hyperqunched glass in the region of the BP is compensated by a lower density and speed of sound that decreases the Debye energy (E_D) of the glass. The energy position of the BP (E_{BP}) scales with E_D. Moreover, the Debye energy of these two glasses correlates with the shape of the RDOS $g(E)/E^2$, which exhibits a characteristic exponential decay: $g(E)/E^2 \sim exp(-E/E_0)$ that is also observed for other systems where the parameter E_0 scales with the Debye energy [90].

This study leads us to reconsider the theoretical arguments that associate the presence of the BP to the peculiar energy landscape of the system and then to the different T_f. We observed that in two glasses, with a significant difference in T_f, the height of the BP is the same and the differences in the DOS are related to changes in the continuum properties of the glass. Conversely, theory predicts [69, 70] that varying, through T_f, the potential energy of the system (H), the BP moves in energy (E_{BP}) and changes in height (I_{BP}) according to the relation: $I_{BP} \propto 1/E_{BP}^{1/2}$ ($E_{BP} \propto \Delta_c$ and $I_{BP} = g(E_{BP})/E_{BP}^2 \propto \Delta_c^{-1/2}$ where $\Delta_c \propto \Delta H$). Moreover, the lack of this effect, in the samples that we have investigated, cannot be associated with the fact that the theory has neglected the effect on T_f of the macroscopic properties of the glass. We found experimentally that the height of the maximum of the RDOS (I^*_{BP}) and its energy position (E^*_{BP}) are correlated differently from what is claimed in theoretical work: $I^*_{BP} \propto 1/E^{3*}_{BP}$ ($I^*_{BP} = g(E_{BP})/E^2_{BP} \propto E_D^{-3}$ and $E^*_{BP} \propto E_D$). A possible explanation for this inconsistency between theory and experiment could be the magnitude of the effect of T_f on the BP. Theory, in fact, points out that this effect is active if the system samples, varying T_f, different energy landscapes. Unfortunately experimentally a relationship between the value of T_f of a glass and its energy landscape cannot be established. However, using annealed and hyperquenched glasses we could relevantly change T_f ($\Delta T_f/T_g$=20%) around T_g (T_f(Ann.)=770 K$< T_g$ and T_f(Hq.)=929 K $> T_g$ where T_g=781 K). According to theory, T_g represents the reference temperature for the system, where it would undergo a transition between an energy landscape characterized by instability configurations of the system ($T_f > T_g$), where the BP clearly appears, and a region of stability ($T_f < T_g$), where the BP progressively decreases. Nevertheless, we observed that while the main effect of varying T_f around T_g is to alter the macroscopic properties of the system, there is no significant effect on the BP of the glass.

Résumé du chapitre 4

Dans ce chapitre, on concentre sur l'étude de la dépendance par la pression et par la densité de la DOS d'un verre, on analysera en particulier la région à basse énergie de la DOS ou est présent le BP. Dans le premier paragraphe, on introduit la thématique scientifique en tant qu'objet de ce chapitre en éclaircissant: soit la pression, soit la densité, pourront tre utilisés comme paramètres pour étude du BP. Il est présenté le verre objet de nos mesures $Na_2FeSi_3O_8$ sous pression et densifié. Le procès de densification est obtenu en appliquant au système original de la pression à haute température. On illustre les résultats de notre mesure de NIS sur le verre sous pression, dans ce cas le verre montre une forte dépendance de la DOS à basse énergie de la pression. Pour approfondir les mécanismes qui contrlent ce phénomène, on analyse les systèmes densifies. On présentera les résultats des mesures de diffusion de rayons X, Mössbauer et BLS, dédiée à caractériser le processus de la densification. Ce processus semble procéder en deux temps, dans un premier temps, il y a un réarrangement de la structure locale du système sans variation de sa vitesse du son ou de la densité. Dans un seconde temps le système augmente sa densité et vitesse du son mais sa structure reste inchangée. Après la caractérisation des échantillons, on illustrera les résultats qui sont obtenus par des mesures NIS. La DOS du système change fortement en augmentant la densification avec une diminution de l'intensité du maximum de la RDOS. Pour chaque échantillon on a procédé à calculer la relative énergie de Debye et à obtenir la RDOS en unités de Debye. Cette procédure nous a permis d'évaluer l'effet du changement des propriétés macroscopiques du système sur la DOS et on à observé l'effet du processus de la densification sur le BP. En conclusion, cette étude révèle que la présence du BP dans les verres dépend fortement de la structure locale du verre.

Chapter 4

Study of a densified glass

4.1 Scientific background

In this chapter we present a study of the effect of pressure and densification on the density of vibrational states DOS of a glass. In particular, we focus our efforts on the investigation of the characteristic excess of low energy modes: the Boson Peak (BP). With an extensive characterization of our samples we evaluate the influence of the changes of the microscopic structure and of the continuum properties of a glass on the DOS. The nature of the mechanisms that control the changes of the BP caused by pressure and densification are discussed.

As we have already showed in section 1.6.2, in glasses the DOS has an excess of states over the value predicted by the Debye model at low energy. This excess of vibrational states is named Boson Peak; because of its universality and lack of full understanding, since many years the Boson Peak is matter of debate in the scientific community. Various experimental works have shown that in the meV energy region the vibrational density of states as well as the BP are strongly influenced by pressure [91, 92, 93, 94]. In particular, increasing the pressure applied to a glass, the BP decreases in intensity and moves to higher energies. For this reason many studies used pressure as a tool to study the nature of the low energy vibrations responsible for the BP. Nevertheless, these studies did not end up with conclusive statements on the origin of the BP supporting different and sometimes not compatibles models. According to these experimental observations the presence of the BP in glasses has been attributed to: *i*) a strong anharmonicity of the glass [92] *ii*) the presence of relaxations modes [93] *iii*) the existence of localized vibrations in the material [95, 96, 97].

The studies of glasses under pressure in the recent past have been complemented by those on densified systems [95, 96, 97, 98, 99]. These materials are obtained with a process of compression of the glass at high temperature: the "densification" process. Once released to ambient condition the samples have a higher density compared to the original glass. Using densified materials it is often simpler to investigate the BP, these samples in fact allow performing *in situ* measurements. The effect of densification on the DOS is similar to that observed in glasses under pressure, increasing densification the BP decreases and moves to higher energies. Nevertheless, different interpretations of the nature of the BP as well as of the effect of densification on the BP have been

reported. In particular, the suppression of the modes induced by the voids present in the glass and the non-reversible change of the structure of the system [96, 99] have been identified as the main mechanisms responsible for the decrease of the BP in densified glasses.

These conclusions contrast with those arising from the studies of glasses under pressure. Despite the universal behavior of the BP as function of pressure and densification a unique common explanation is still lacking. Moreover, in the studies present in literature a precise evaluation of the intensity of the BP is missing due to the difficulties to have access to the macroscopic properties of the samples. According to the definition of the BP (see section 1.6.2) the value of the Debye energy is required to correctly estimate the effect of pressure and densification on the BP. The changes of density and speed of sound, induced by pressure or densification, lead the system to transform its continuum properties and as a consequence the Debye energy of the glass. Heat capacities measurements in glasses under pressure [91, 92] suggest that the change in energy and in intensity of the BP can be described by an increase of the Debye energy of the glass.

In our study we measured the DOS in densified samples as well as in a glass under pressure. Using various techniques we investigated the transformation of the DOS and of the continuum properties of a densified glass. The results obtained with the densified samples allow us to clearly address the responsibility for the change of the BP to a change in the local structure of the glass. We observe that whenever there is no change of the local structure of the sample the effect of densification on the Debye energy of a glass can completely describe the changes of the DOS at low energies.

4.2 The $Na_2FeSi_3O_8$ glass

In order to investigate the effect of pressure and densification in the DOS of glasses we focused our experimental efforts on the study of the $Na_2FeSi_3O_8$ glass. The choice of this glass has been supported by the need to have a system representative of a large class of glasses as silicates. Moreover, we were looking for a glass able to embed iron atoms in its structural network in order to extract from Mössbauer measurements information representative of the dynamics of the entire glass. The $Na_2FeSi_3O_8$ belongs to the class of sodium silicate glasses, these systems have a big relevance in earth science being responsible for many processes of geological interest being the main component of magmas.

The original glass used in our studies has been prepared by the Prof. A. Meyer and F. Kargl at the Technical University of Munich. The $Na_2FeSi_3O_8$ glass has been obtained from a mixture of Na_2CO_3, Fe_2O_3 and SiO_2 oxides powders. The material was melted in an Au/Pt crucible for several hours at 1400° C allowing to evaporate the CO_2 and oxygen. In order to get the melt homogeneous and bubble free it was stirred with a Pt spindle. Finally the glass has been obtained by cooling the sample inside the Pt-crucible, from 1400°C down to room temperature.

Differential scanning calorimetry allowed determination of glass transition temperature of the material $T_g = 744$ K that is almost identical to that of a pure sodium

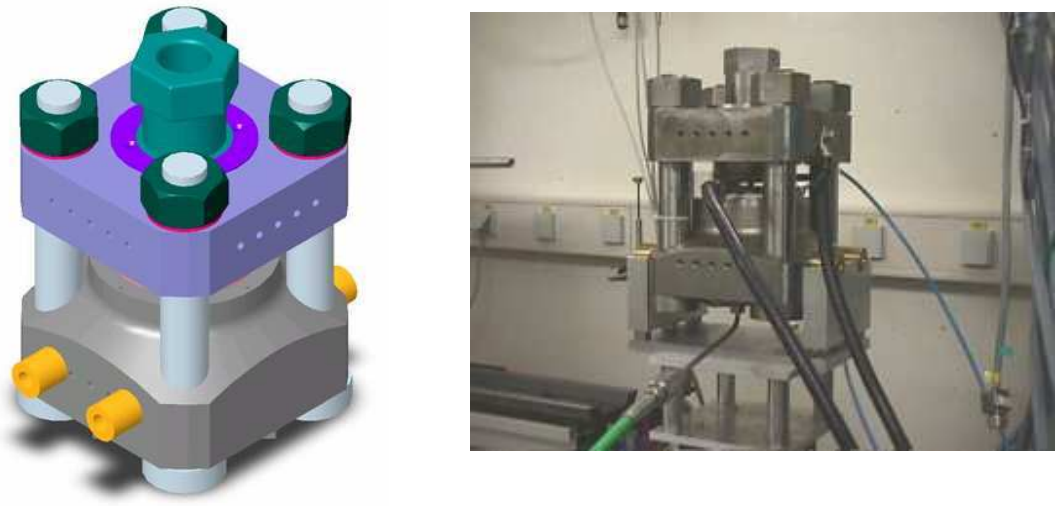

Figure 4.1: *Large volume "Paris-Edinburgh" press used for the densification of $Na_2FeSi_3O_8$ glass.*

silicate glass $Na_2Si_3O_7$ (T_g = 737 K) [75]. The iron atoms present in the glass have been observed (by Mössbauer spectroscopy) to substitute for silicon in the network structure.

The original glass has been used to prepare densified samples. Silicate glasses in fact can experience a densification process; after compressing the systems at high temperature, once that the glass is released to ambient condition its density is higher than that of the original glass. The densified samples have been prepared in the high pressure laboratory of ID27 at the ESRF in collaboration with Dr. W. Crichton. To obtain samples with different densities we compressed the $Na_2FeSi_3O_8$ glass at different pressures, in a Paris-Edinburgh large volume press (see figure 4.1) for 10 minutes at 673 K. The glass has been densified starting from a lump reduced in cylindrical shape to fill the gasket of the press. We prepared according to this procedure four densified samples obtained from a compression of the original glass to $1, 2, 3$ and 7 GPa. Further characterization of the density and structure of the samples reveal the efficiency of the used protocol for densification. In figure 4.2 we show the samples in their final aspect. In the next sections we refer to the samples using the pressure at which they have been prepared, 0 GPa indicates the non-densified glass.

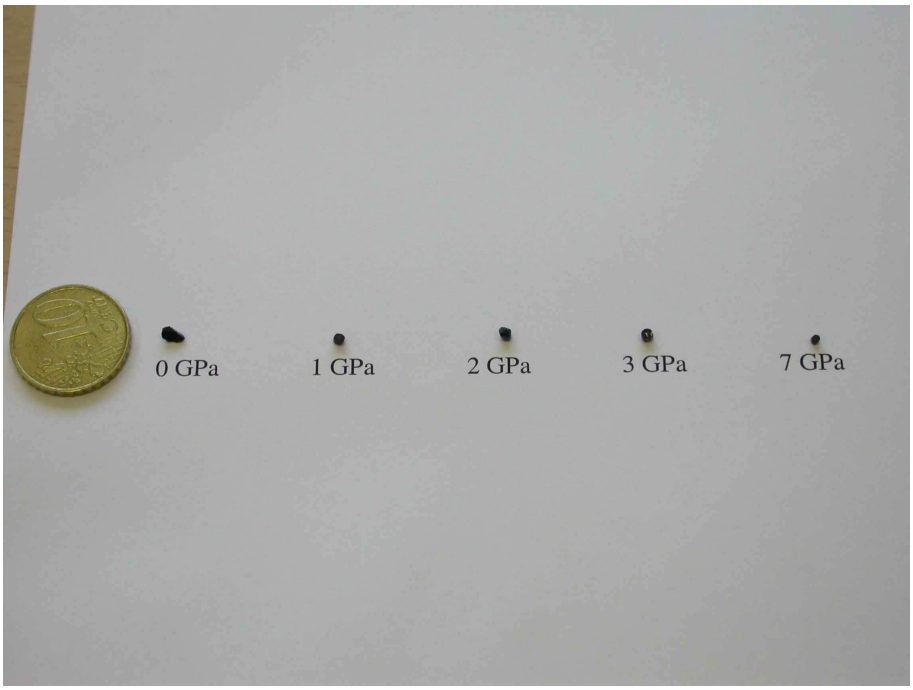

Figure 4.2: *Picture of the densified samples, the labels indicate the pressure at which the glass has been pressurized.*

4.3 $Na_2FeSi_3O_8$ under pressure

We start the study of the $Na_2FeSi_3O_8$ glass investigating the effect of pressure on the density of vibrational state of this glass.

In particular we were interested to probe how the vibrational modes in the low energy part of the DOS are modified by the increase of pressure, what is the influence of pressure on the Boson Peak and whether pressure modifies the DOS of the glass differently in different energy regions.

This study has been performed in collaboration with the group of Prof. G. Wortmann of the University of Paderborn, in particular H. Giefers and U. Ponkratz helped to load the sample in a high pressure cell and to measure the values of pressure.

4.3.1 $Na_2FeSi_3O_8$ in a diamond anvil cell

In order to perform Nuclear Inelastic Scattering measurements on a glass under pressure we used a diamond anvil cell (DAC). This device allows applying pressures exceeding the Mbar.

The cell is essentially made out of a guided piston and a cylinder, which are able to slide one into the other, and of two diamonds mounted with opposed tips that press a Be metallic thin sheet (gasket) of 100 μm thickness. The sample, a powder of $Na_2FeSi_3O_8$, has been placed inside a hole (the diameter of the hole drilled in the gasket was 150 μm) with ethanol used as transmitting medium to ensure hydrostatic

compression. The thickness of the samples is essentially determined by that of the gasket (150 μ m) (see figure 4.3). The relatively small pressure applied mechanically to the piston by a set of screws mounted on the body of the cell allows generating on the sample a much higher pressure ($P_{sample} > 10^3 P_{cell}$). The capability to generate pressure in the GPa range arises from the hardness of the diamond and from the possibility to cut the stones with a surface ratio between the upper face and the culet of $\approx 10^3$. To measure the pressure applied to the sample, a ruby ($\alpha - Al_2O_3 : Cr^{+3}$) of few microns of diameter has been placed in the hole of the gasket. Measuring with a spectrometer the frequency of the ruby luminescence line it was possible to determine the pressure applied to the sample [100]. Using the DAC we applied on the $Na_2FeSi_3O_8$ glass three values of pressure 2.8, 5.6, and 11 GPa.

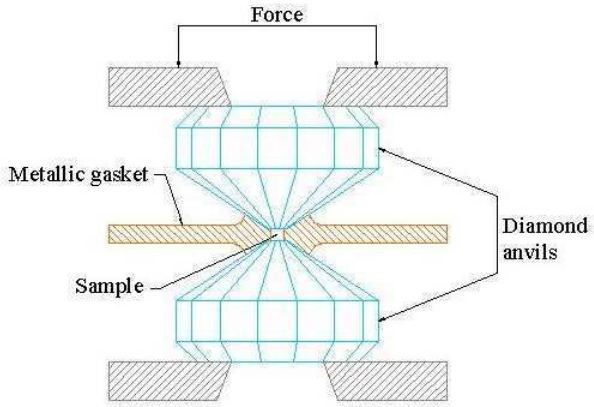

Figure 4.3: *Scheme of a diamond anvil cell (DAC).*

4.3.2 Nuclear inelastic scattering measurements

The Nuclear Inelastic Scattering measurements have been performed at the ID18 beamline at the ESRF. The DAC was placed with the axis aligned on the path of the incident x-ray beam allowing the synchrotron radiation to reach the sample through the two anvils (see figure 4.4). An APD detector close to the cell was used to collect the Fe-K_α fluorescent radiation transmitted through the beryllium gasket. A second APD detector was located in front of the DAC at approximately 2 m. This detector has been used to measure the instrumental function of the spectrometer.

The energy resolution of the spectrometer was 0.5 meV, allowing resolving the inelastic features of the glass also in the BP energy region. Each energy scan has been performed from -70 to +100 meV. We increased, at low energy, the time for collecting the fluorescent radiation in order to have a higher statistics for the spectra. The average acquisition time for each scanned energy point varies from 80 to 130 s. Between 15 and 30 scans were added in order to increase the statistics. The NIS measurements have been done for increasing values of pressure from ambient condition (0 GPa) up to 11 GPa, in figure 4.5 we show the collected NIS data at all pressures.

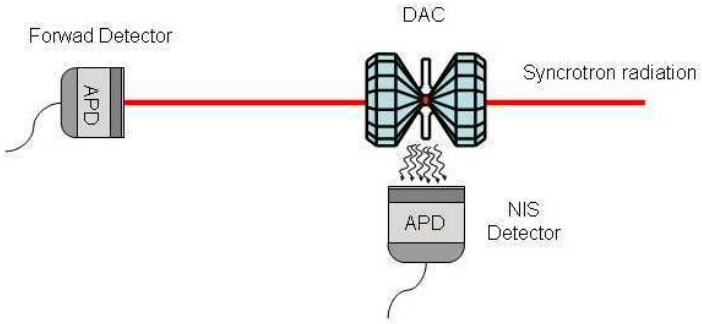

Figure 4.4: *Geometry used for the NIS measurements performed on the sample under pressure.*

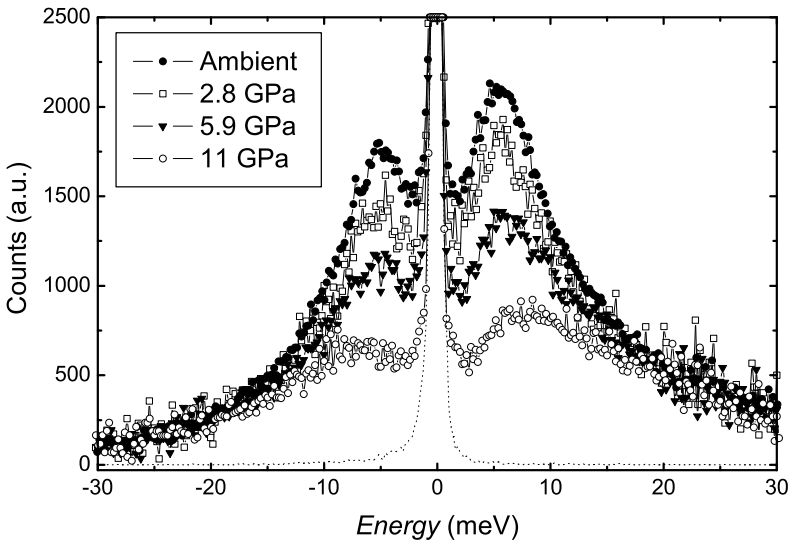

Figure 4.5: *Energy dependence of NIS for $Na_2FeSi_3O_8$ under pressure, the legend shows the different values of pressure, the dotted line is the instrumental function of the spectrometer.*

The energy dependencies present a characteristic peak between 5 and 10 meV, this maximum is the signature of the BP in the DOS of the glass, as we have already discussed in section 3.8.1. The effect of pressure in the low energy region of the spectrum is clearly visible; increasing the applied pressure the maximum decreases in intensity and moves to higher energies.

4.3.3 Effect of pressure on the density of vibrational states

In order to extract from the energy dependence of NIS the density of vibrational state we follow the same procedure discussed in the section 3.8.2. In figures 4.6 and 4.7 we report respectively the value of the DOS and RDOS . The reduced density of states has been plotted to emphasize the presence in the glass of the BP (located at 5÷10 meV) and the effect of pressure in the low energy region of the DOS relative to the E^2 behavior predicted by the Debye model. From figure 4.7 we observe that at higher values of pressure a smaller height of the peak in the RDOS can be observed, its intensity reduces up to $\approx$ 60 % while its position moves toward higher energies by $\approx$ 25 %. However, the effect of pressure on the RDOS is less pronounced at higher energy. All curves corresponding to different pressures merge at 15 meV, beyond this energy it is not possible to distinguish between the RDOS associated to different pressures.

Nevertheless, only from the measurements of NIS we cannot infer about the reason of such behavior, neither we have a quantitative estimation of the effect of pressure on the BP. The magnitude of the BP is defined with respect to the zero energy limit of the RDOS as predicted by the Debye model (see section 1.6.2). We do not have any information on the transformation of the macroscopic and microscopic properties of the glass induced by the changes of pressure. Unfortunately, obtaining such information for a sample loaded in a DAC is not an easy task because of the small dimensions of the samples and of the difficulties arising from the *in situ* measurements.

4.4 Study of densified $Na_2FeSi_3O_8$

In order to perform a more extensive study on the effect of pressure and density on the low energy region of the DOS of $Na_2FeSi_3O_8$, we decided to densify the glass. Applying to $Na_2FeSi_3O_8$ pressure at high temperature (T=$0.9T_g$) (see section 4.2), once released to ambient condition the glass has a higher density. These samples, called densified glasses allow probing the effect of density on the DOS without any constraint associated with the presence of a DAC.

4.5 Density measurements

The method and the instrument used to determine the density (ρ) of our samples are the same used for the hyperquenched glasses and have been already discussed in section 3.4.

Because of the small dimensions of the densified samples the error in the density $\Delta\rho$ has been found larger than we hoped. In fact, as explained in section 3.4 $\Delta\rho$ is inversely

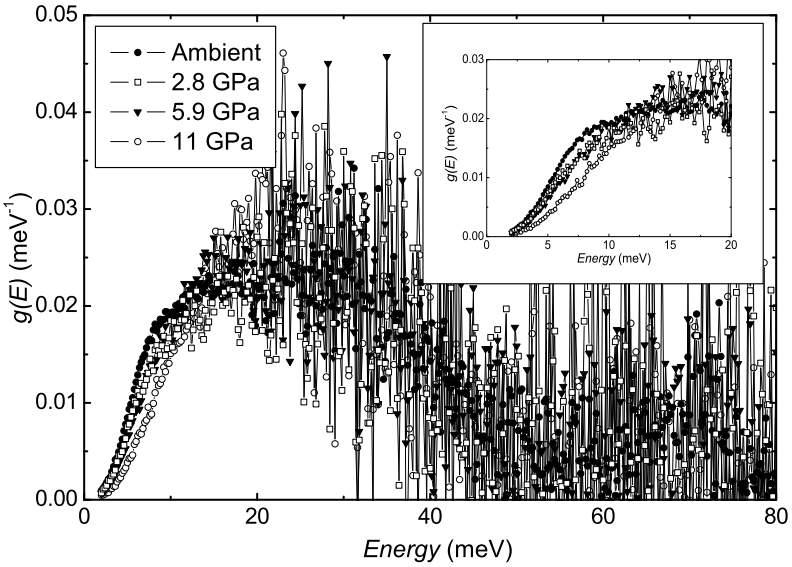

Figure 4.6: *Density of vibrational states (DOS) of $Na_2FeSi_3O_8$ glass under pressure, the inset shows the low energy part of the DOS.*

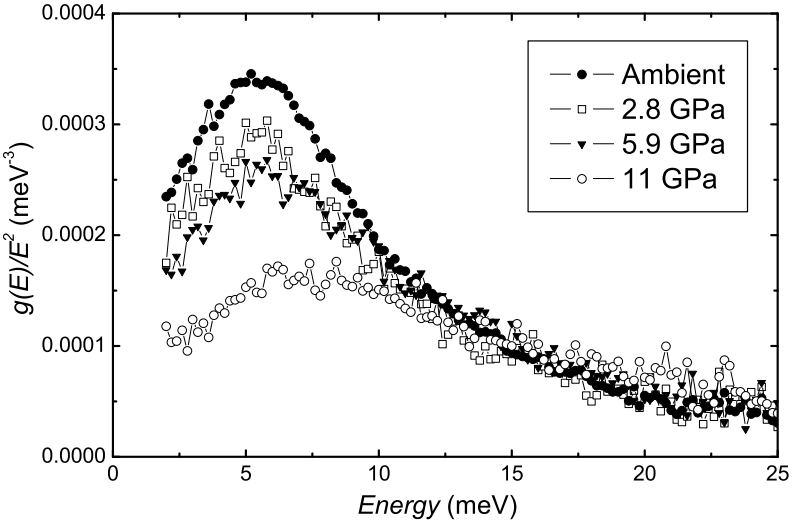

Figure 4.7: *Reduced density of vibrational states (RDOS) of the $Na_2FeSi_3O_8$ glass under pressure.*

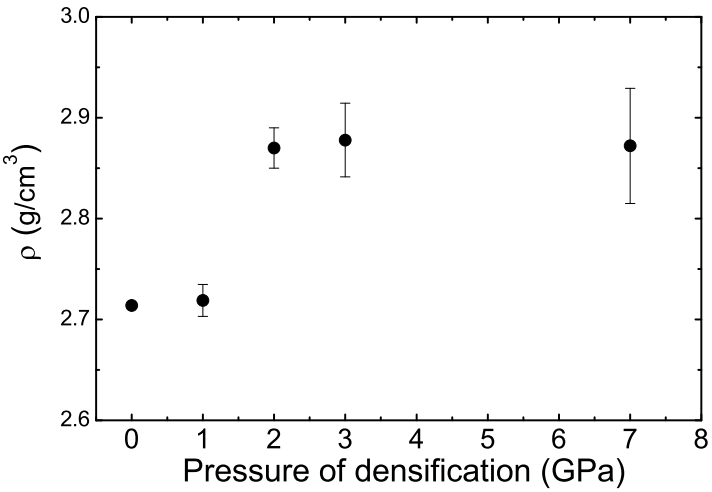

Sample	$\rho\,(\mathrm{g\,cm^{-3}})$
0 GPa	2.714(3)
1 GPa	2.72(2)
2 GPa	2.87(2)
3 GPa	2.88(4)
7 GPa	2.87(6)

Figure 4.8: *Density of the original (0 GPa) and densified (1-7 GPa)* $Na_2FeSi_3O_8$ *glasses.*

proportional to the volume of the sample. In order to reduce $\Delta\rho$ we exploited the high accuracy of the used experimental method, repeating the measurements for each sample 10 times, and considering the variance and the mean value of these measurements we obtain $\Delta\rho/\rho$ in the range of $0.001 \div 0.03$.

In figure 4.8 we show the results of the density measurements of our sample. From a first glance we can conclude that the effect of densification on the density does not proceeds linearly and saturates above 3 GPa. In an initial stage the compression does not alter significantly the density of the glass: the samples 0 and 1 GPa present only a small difference in density. Above 1 GPa, the increase of pressure is followed by an important increase of the density, the 3 GPa sample have a density 6% higher than the initial glass. Above 3 GPa the densification does not change the density significantly.

4.6 Microscopic characterization of samples

In this section we discuss the microscopic characterization of the densification process for the $Na_2FeSi_3O_7$ glass. We present the results of x-ray scattering and Mössbauer measurements showing how the densification modifies the middle range as well as the local structure of the glass. The technical details and the principles on these two techniques are discussed elsewhere (see sections 3.5 and 2.1.2).

The x-ray scattering measurements on the densified samples have been performed with a double aim *i*) to check, during the preparation of the sample, the efficiency of the protocol used for the densification; *ii*) to study the relation between the changes of the microscopic structure of the glass and the transformation of its vibrational properties.

The increase of pressure during the densification process do not correspond necessarily to an increase of the density of the sample; in order then to check if the densification process takes place we need to look at the microscopic structure of the glass.

The characterization of the samples performed by Mössbauer spectroscopy allows us to get a picture of the local structure of the glass. These measurements were required because the changes of the microscopic structure of the glass associated with a rearrangement of the environment of iron atoms cannot be easily distinguished in x-ray scattering data. These data are the result of a process involving all atomic species of the system and then the contribution of Fe atoms cannot be clearly distinguished. In contrast Mössbauer spectroscopy is sensitive to the chemical environment of the Fe atoms allowing us to probe the local structure of the atoms surrounding Fe. Moreover, the use of Mössbauer spectroscopy, combined with x-ray and neutron scattering techniques, has already been applied to the study of sodium silicates allowing establishing a relationship between the Mössbauer data and the coordination state of iron atoms [84][85]. Supported by such experimental data we used the Mössbauer spectroscopy to understand the effect of densification on the local structure of the glass.

Finally combining the information on the structure of densified samples with that on their DOS we could test the reliability of models that relate the presence of the Boson Peak to a characteristic correlation length between the atoms of the system.

4.6.1 X-ray scattering measurements and results

The measurements of x-ray scattering have been performed at the ID27 beamline at the ESRF in collaboration with Dr. W. Crichton, using the same equipment and procedure discussed in section 3.6.1. The energy of the probing radiation was 61 keV; this energy allows collecting the radiation scattered from the sample in a range of Q between 5 and 150 nm^{-1}.

The sample holder used for the measurements was a needle placed at 1.5 m far from the detector. After each measurement the sample was removed and we collected the radiation scattered from air. This measurement has been subtracted from the data collected using the sample, following the same procedure described in section 3.6.1. The scattering from the air is particulary intense in the low Q region (≈ 5 nm^{-1}) and it masks the changes in the intensity of the radiation scattered from the sample. We did not estimate other contributions to the scattering from our samples (as Compton scattering) because, as we have discussed in section 3.6.1, we were interested only to observe the relative changes in the static structure factor of the samples. To proceed with a comparison between the different samples, we normalized the data to the same value of the intensity of the scattered radiation at Q=100 nm^{-1}. Figure 4.9 clearly shows significant differences in the intensity of the scattered radiation ($I(Q)$) in the region of the first diffraction peak (between 10 and 25 nm^{-1}); at higher Q values, all $Na_2FeSi_3O_8$ samples show the same $I(Q)$.

Between 12 and 25 nm^{-1} the first sharp diffraction peak (FDP) appears not as a unique well defined line but we can recognize the presence of at least two distinct contributions: at 14.5 and 21.5 nm^{-1}. These two features have been associated, by previous studies in sodium silicate glasses [101], to the correlation length of oxygen

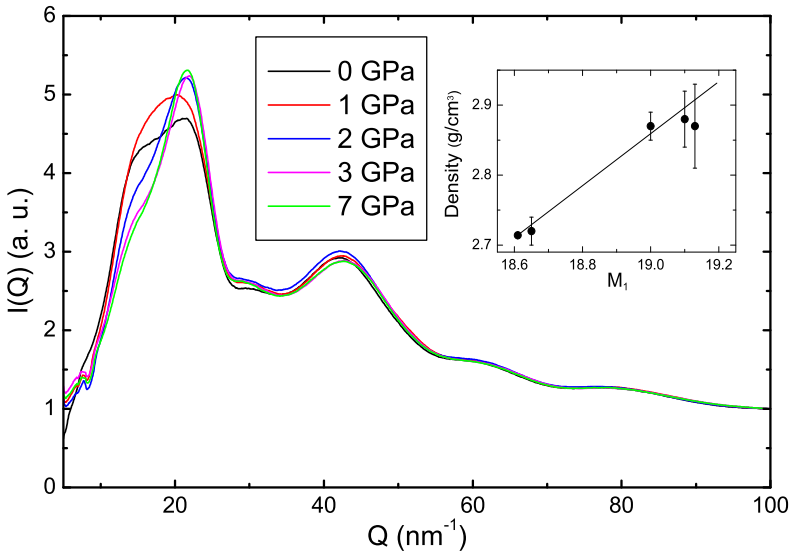

Figure 4.9: *Momentum dependence of the intensity of the scattered radiation for densified $Na_2FeSi_3O_8$ glasses, the inset shows the correlation between the density of the samples and the center-of-mass position M_1 (see text).*

atoms O-O (the peak at 14.5 nm^{-1}) and of Si-Na atoms (the maximum at 21.5 nm^{-1}). Increasing the densification we observe a progressive increase of the scattered intensity at 21.5 nm^{-1} with a correspondent decrease of that at 14.45 nm^{-1}; the change of FSDP is also accompanied by a shift of its position toward high Q values (see inset of figure 4.9). This effect has been evaluated measuring the center of mass of the FSDP M_1.

$$M_1 = \int_{Q_{min}}^{Q_{max}} dQI(Q)Q, \tag{4.1}$$

here Q_{min}=10 nm^{-1} and Q_{max}=25 nm^{-1} identify the limits of the Q region for the FSDP.

The shift of M_1 towards higher Q values reflects the increase in density of the glass. As well as for a crystal, an increase in reciprocal space of the dimension of the first pseudo-Brillouin zone (M_1 moves to higher Q values) corresponds to a decrease, in real space, of the distance between atoms and then to an increase of the density ($V \sim 1/M_1^3$, $\rho \sim M_1^3$).

The change of the first diffraction peak increasing the densification seems not to proceed continuously; passing from the 0 to the 1 GPa sample we observe a clear change of the shape of the FSDP. The structure of the FSDP of the 0 GPa sample, where one can recognize a peak and a well pronounced shoulder, appear in the 1 GPa sample as a unique maximum at 19.5 nm^{-1}. On the other hand at 2 GPa the

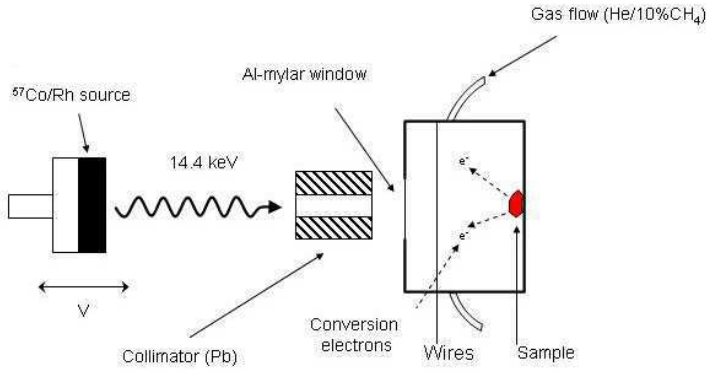

Figure 4.10: *Experimental set-up used for the Mössbauer measurements.*

FSDP presents again the structure of a peak and a shoulder and the maximum at 21.5 nm^{-1} significantly increases in intensity. At 3 GPa the glass has already reached the maximum level of densification, the 7 GPa sample in fact shows only small changes in the FSDP compared to 3 GPa. The saturation of the densification process, as seen in the microscopic changes of the glass, is also supported by the results of density measurements: beyond 3 GPa, the density does not reveal appreciable changes.

We conclude that the densification has a direct influence on the FSDP of the glass, the shape and the position of the FSDP change remarkably with densification. Such changes on the FSDP have been interpreted in the literature as a transformation of a the middle range order of the system [105, 99]. In particular, according to these models the structure of the glass can be regarded as a packing of atoms and interstitial voids, the increase of the density would produce a suppression of the void spaces present in the glass with a consequently decrease of the length associated with the structural correlations that give rise to the FSDP.

4.6.2 Mössbauer measurements

In order to study the effect of densification on the local structure of the $Na_2FeSi_3O_8$ glass, the electron conversion Mössbauer spectroscopy technique has been used. Such technique allows obtaining Mössbauer spectra via a process of internal conversion of nuclear excitation [102]. The energy corresponding to the deexcitation of Fe nuclear levels can be transferred to the electrons of the atom because of their finite probability to be at the nuclear site.

In figure 4.10 we sketched the experimental set-up used for the measurements. The electrons coming out from the sample are accelerated by the electric field produced by a difference in electric potential between a wire of tungsten and the sample. The collisions of the electrons with the molecules of the gas, present in the chamber of sample, produce a large number of ions that diffuse toward the wire producing a signal.

Measuring the absorption of γ rays by electron conversion we can obtain Mössbauer spectra also for samples in which the thickness prevents the use of the "classical" Mössbauer technique. If the thickness of the sample exceeds $\sim 200 \mu m$, using the usual transmission geometry all γ rays are absorbed by the sample itself.

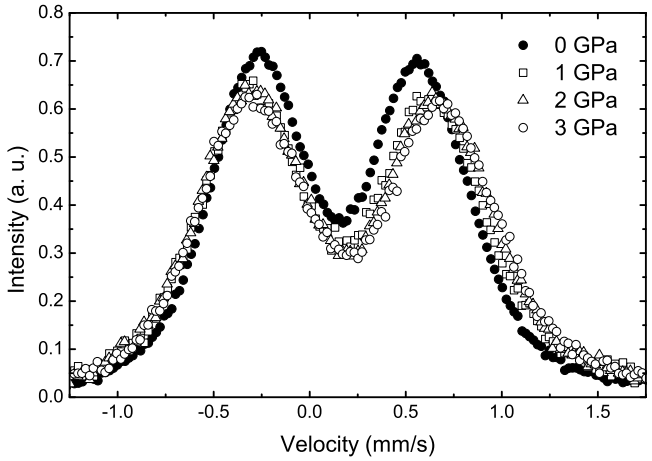

Figure 4.11: *Conversion electron Mössbauer spectra of densified $Na_2FeSi_3O_8$ glass.*

The measurements of electron conversion Mössbauer spectroscopy have been performed by Prof. J. Korecki in the Department of Physics of the University of Krakow. The data analysis of the measurements has been performed in collaboration with Dr. M. Zajac.

The data have been normalized to the same unity area: after subtracting the background we integrated for each spectrum the number of counts between -2.5 to 2.5 mm/s, then at each velocity the counts of the spectrum have been divided by the integrated value.

In figure 4.11 and 4.12 we report the measured Mössbauer spectra of 0-3 GPa $Na_2FeSi_3O_8$ samples. Because the time consuming character of this technique and the small dimensions of the 7 GPa glass we did not measure this sample. The figures clearly show the presence of a doublet in the measured signal, the quadrupole splitting allows identifying the Fe^{+3} coordination state for the iron atoms. The collected spectra do not show the presence of the characteristic Fe^{+2} doublet.

From a first glance at figure 4.11 a difference between the original glass (0 GPa sample) and the densified samples is clearly visible. The 0 GPa sample has a smaller quadrupole splitting compared to the densified samples. On the other hand the 1-2-3 GPa glasses have quite similar Mössbauer spectra and do not show significant differences. In order to extract quantitative information from Mössbauer data we proceed with an analysis of the lineshape of the spectra using a quadrupole pair. We fit the experimental data with the following model function [41]:

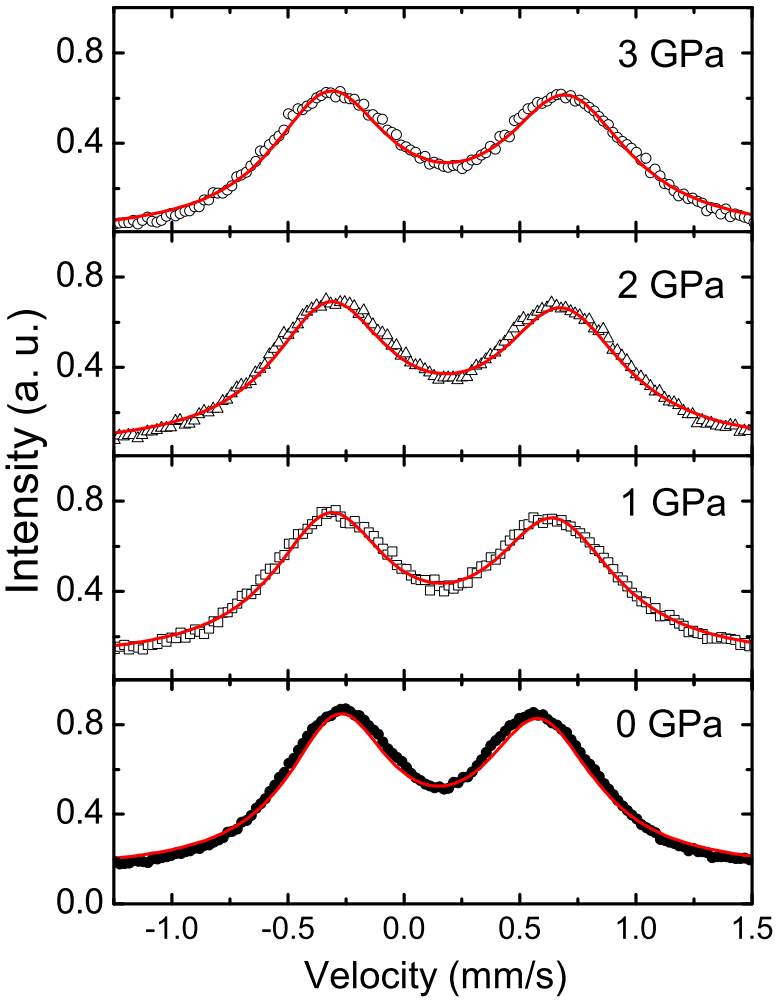

Figure 4.12: *Conversion electron Mössbauer spectra, the red lines are the results of the fit (see text).*

$$I_M = I_0 \frac{1}{2} \left(\frac{(\Gamma/2)^2}{((x-\delta-\Delta/2)^2 + (\Gamma/2)^2)} + \frac{(\Gamma/2)^2}{((x-\delta+\Delta/2)^2 + (\Gamma/2)^2)} \right). \quad (4.2)$$

The results of the fit to our data with the model function I_M are shown in figure 4.12. The function I_M includes the two parameters δ and Δ: respectively the chemical shift and the quadrupole splitting. As we have discussed in section 2.1.2 these two parameters are related to the distribution of electrical charges surrounding the iron atoms. Δ quantifies the gradient of the electric field at the nuclear site and δ the density of electric charge. Thus the hyperfine parameters allow speculating on the relative changes in position between the ions surrounding the Fe atoms of the glass. The Γ parameter presents in Eq. 4.2 has been introduced to take into account the broadening of the Mössbauer lines, due to the distribution of the local environments that is typical for glasses [103].

The value of δ, that in our samples is comprised between 0.26 and 0.30, allows us to estimate that the Fe atoms are tetrahedrally coordinated to oxygen. From the works present in the literature [84, 85] it has been found that in silicate glasses, with composition similar to our glasses, the tetrahedral coordination to oxygen corresponds to a value of δ in the range of 0.2-0.32 mm/s.

In table 4.1 we report the values of the hyperfine parameters Δ and δ for all samples. The densification proceeds increasing the isomer shift linearly, conversely the quadrupole splitting does not show any linear dependence on densification. Passing from the 0 to the 1 GPa sample the quadrupole splitting increases relatively by 12% while from 1 to 3 GPa it changes only by 5%. The behavior of Δ indicates that in the earlier stage of densification there is a relevant change in the gradient of the electric field at the nuclear site, suggesting that passing from the 0 to the 1 GPa samples there is rearrangement of the local structure of the glass around the iron atoms.

Combining this information with that coming from density and x-ray scattering measurements we can conclude that the densification process proceeds in two steps. Passing from the 0 to the 1 GPa sample, we have a rearrangement of the local structure of the glass around the iron atoms (the hyperfine parameters Δ increases by 12%), this change is not followed by a relevant modification of the density of the glass. Increasing the densification further on, passing from the 1 to 3 GPa sample, the glass does not change considerably its local structure (i.e. Δ increases by only about 5%) while the structure in the middle range region changes continuously.

4.7 Brillouin light scattering measurements

In this paragraph we present Brillouin Light Scattering measurement performed on the $Na_2FeSi_3O_8$ samples. The measurements have been performed in collaboration with Prof. D. Fioretto at the Department of Physics of Perugia, using the same experimental equipment discussed in section 3.5. Thus most of the experimental details of the measurements are in section 3.5.

Table 4.1: The hyperfine parameters of the isomer shift δ and quadrupole splitting Δ for the initial (0 GPa) and densified samples are here reported. The isomer shift is given relative to α-iron absorber.

Sample	δ (mm/s)	Δ (mm/s)
0 GPa	0.262(1)	0.862(2)
1 GPa	0.274(3)	0.963(4)
2 GPa	0.292(3)	0.999(4)
3 GPa	0.302(3)	1.018(5)

4.7.1 The measured spectra and the speed of sound

The BLS measurements have been performed collecting the scattered radiation in the two geometries: at 90° and in backscattering (180°) geometry. As we already pointed out in section 3.5, these two geometries allow us to investigate both the longitudinal and the transverse acoustic excitations of the glass.

The samples have been aligned in order to match the position, on the sample, of the incident laser beam and the focus of the lens used to collect the scattered radiation. The procedure used for the alignment is the same discussed in section 3.5. Because of the high value of the imaginary part of the refractive index (n_i) of $Na_2FeSi_3O_8$, we could not collect the radiation scattered from a point too far from the surface: the absorption of the glass limits the transmission of the radiation. We try to find a good compromise in the choice of the scattering volume between a point representative of the bulk properties of the glass (inside the sample), and a point where the absorption of the sample allows us to have an intense scattered radiation (not too far from the surface).

The typical acquisition time for a spectrum was of 12h in the 90° degree configuration and 3 h in the 180° geometry, where the intensity increases because of the higher efficiency of the collecting optics.

We collected 8 BLS spectra, one in backscattering geometry and one in the 90° for each sample (0-3 GPa sample, we exclude the 7 GPa because of its small dimensions). The spectra collected at 90° show, in addition to the presence of transverse excitations, a quite different aspect compared to the spectra in the backscattering geometry. In the 90° geometry the increase of intensity associated with the elastic scattering (i.e. when $E \approx 0$) is already important at ± 10 GHz. In backscattering geometry the intensity increases at lower frequencies. This effect is mostly associated with the scattering from the surface. In fact, in the 90° scattering geometry we collect the radiation from a wider surface position of the sample. Moreover, the increase of the uncertainty on the selected values of Q results in a broadening of the inelastic features of the spectra (see

Table 4.2: Here we report for all densified samples: the geometry used for the BLS measurement, the exchanged wave vector Q, the longitudinal ν_L and transverse ν_T frequencies, and the ratio $R = \nu_L/\nu_T$.

Sample	Geometry	Q [nm^{-1}]	ν_L [GHz]	ν_T [GHz]	ν_L/ν_T
0 GPa	90°	0.0359(2)	30.15(2)	17.54(8)	1.72(1)
1 GPa	90°	0.0360(2)	30.51(5)	17.57(8)	1.74(1)
2 GPa	90°	0.0366(2)	31.49(6)	18.1(1)	1.73(2)
3 GPa	90°	0.0345(2)	30.66(6)	17.5(2)	1.75(2)
0 GPa	180°	0.0398(2)	33.43(1)	—	—
1 GPa	180°	0.0399(1)	33.73(2)	—	—
2 GPa	180°	0.0409(1)	35.28(3)	—	—
3 GPa	180°	0.0410(1)	36.39(3)	—	—

section 3.5).

As we have discussed in section 3.5.2 in order to determine the Q corresponding to the collected spectrum, we needed an accurate estimation of the value of the refractive index of the sample. In order to measure n for the $Na_2FeSi_3O_8$ glass we followed the procedure discussed in section 3.5.2. Measuring the Brillouin shift of the longitudinal excitation at 90° and in the backscattering geometry, and assuming the same value of speed of sound we obtain the value of n. Such procedure has been applied for the 0 GPa sample where the quality of the surface allowed also for a precise measurement of the angle of scattering θ_i at 90° (see figure 3.11).

For the densified samples we derived the value of n from the 0 GPa sample taking into account the change of density according to the Clausius -Mossotti relationship [2]:

$$\frac{n-1}{n+2} = 4\pi\alpha\rho. \tag{4.3}$$

The value of n allows us to calculate the wave vector Q for the backscattering geometry measurements[1]. To determine the wave vector associated with the 90° geometry

[1]In the backscattering geometry θ_i is always equal to 180° that correspond to $Q = 2nk_0$ (see section

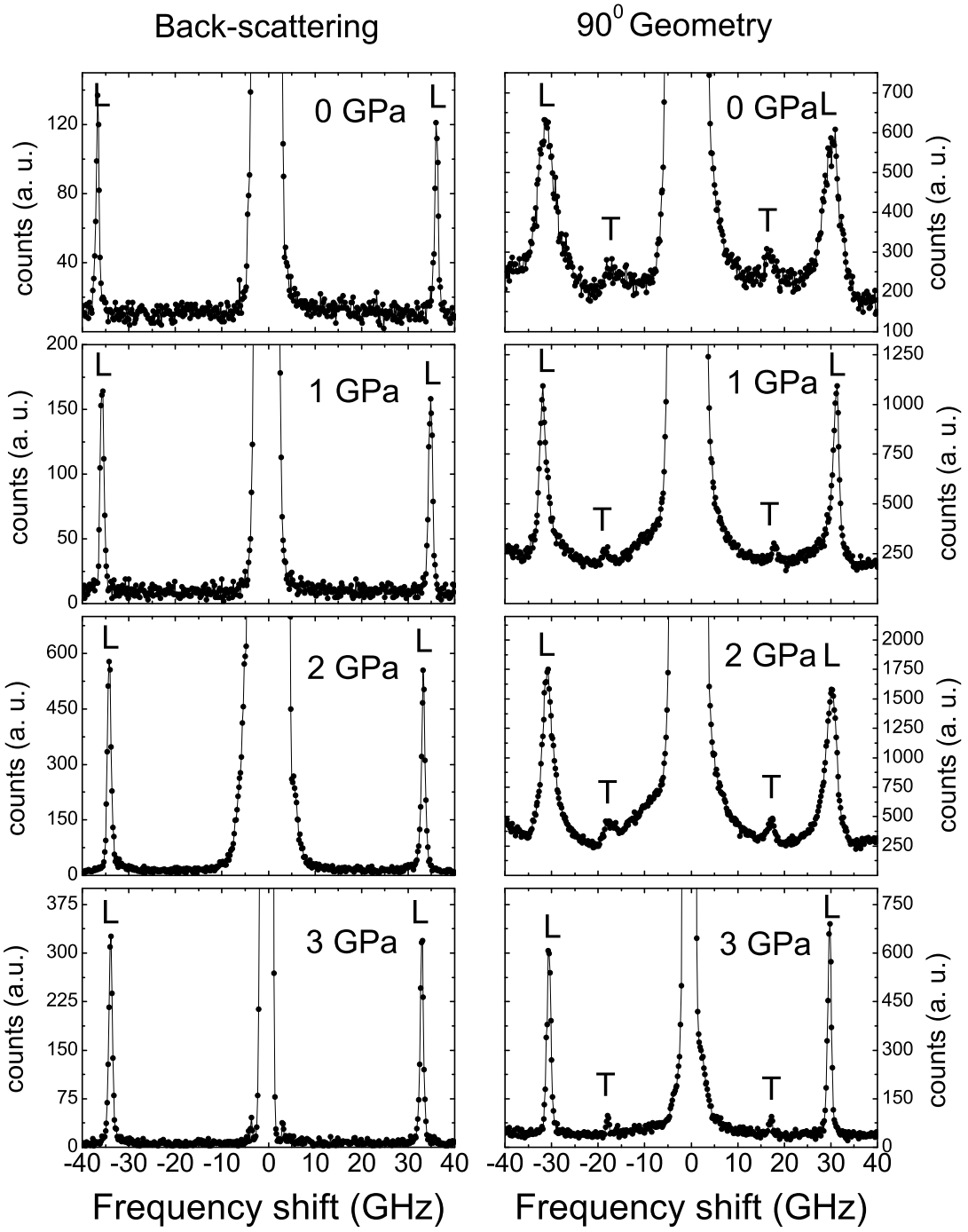

Figure 4.13: *Panel of the BLS spectra collected in backscattering and 90º geometry, the L and T indicate the longitudinal and the transverse Brillouin peaks.*

Table 4.3: We report, for all samples: the density (ρ), the refraction index n, the longitudinal (v_L) and transverse (v_T) sound velocity.

Sample	$\rho\,(\mathrm{g\,cm^{-3}})$	n	$v_L\,(\mathrm{km\,s^{-1}})$	$v_T\,(\mathrm{km\,s^{-1}})$
0 GPa	2.714(3)	1.622(1)	5.28(2)	3.07(3)
1 GPa	2.72(2)	1.624(5)	5.32(2)	3.06(3)
2 GPa	2.87(2)	1.668(6)	5.41(2)	3.12(5)
3 GPa	2.88(4)	1.671(5)	5.58(3)	3.18(5)

spectra, we could not measure directly θ_i, exploiting the radiation reflected from the sample (this radiation would allows us to know the angle between the sample surface and the incoming laser beam, see section 3.5.2). In fact, the high absorption of the glass and the roughness of the sample decrease significantly the intensity of the reflected radiation. However, previously we determined the longitudinal speed of sound v_L from the spectra measured in backscattering geometry. v_L is independent of the relative orientation of the sample (see note) while Q is defined by n_i. Then, once determined the position in frequency of the longitudinal excitation measured at 90° (ω_{90L}), we derived the value of the corresponding exchanged wave vector Q from the relation $Q = \omega_{90L}/v_L$. Here we have assumed that v_L does not depend on Q, in fact the linear relation between ω and Q is valid up to Q values of the order of ≈ 1 nm^{-1}, quite far from that probed by BLS ($\approx 10^{-2}$ nm^{-1}). In the table 4.2 we report the values of ω_L and ω_T with the relatives values of Q measured for all samples at 90° and in the backscattering geometry. From the value of Q for the spectra in the 90° geometry we could determine the value of the transverse speed of sound $v_T = \omega_T/Q$ (see table 4.3).

In figures 4.14 we show that the values of the speed of sound (the frequency of the Brillouin peak is proportional to the speed of sound of the glass $\omega_L = v_L Q$) change passing from the 1 to the 3 GPa sample, i.e., the samples which show as well an increase in the density. The 0 and the 1GPa glasses show only a small difference in the peak position of the longitudinal excitation.

The relative increase of the Brillouin frequency shift between 0 and 3 GPa is $\approx 6\%$: the same value measured for the density. Moreover, the ratio between the longitudinal and transverse speed of sound $R = \omega_L/\omega_T$ is not affected by the increase of densification and keeps almost the same value (see table 4.2). The measurements of Brillouin light scattering confirm the two step scenario for the densification process arising from the measurements of the density of samples. The compression of the initial glass at 1 GPa does not lead to notable changes of the properties of elastic media, both density and sound velocity reveal only a slight increase. In a second step the $Na_2FeSi_3O_8$ glass experiences an increase of density and speed of sound up 6%.

3.5.2).

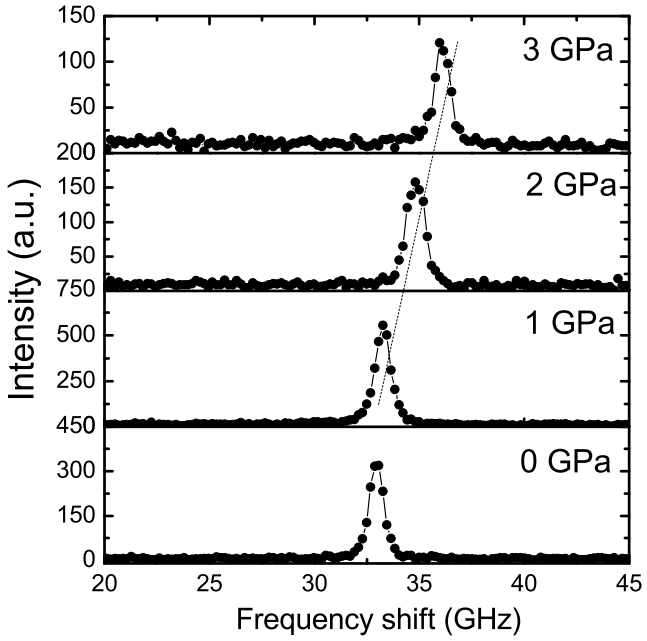

Figure 4.14: *Longitudinal peak of BLS spectra measured in backscattering geometry for all samples. The dashed line indicates the shift of the peak with densification.*

4.8 NIS measurements

In this section we present the measurements of Nuclear Inelastic Scattering (NIS) on densified glasses and the results relative to the effect of the densification on the DOS. The procedure used to derive the DOS from the NIS spectra is not discussed here, for this topic we refer to chapter 2.

4.8.1 Raw spectra

The Nuclear Inelastic Scattering measurements have been performed at the Nuclear Resonance beam-line ID18 of the European Synchrotron Radiation Facility (ESRF).

The densified samples have been placed under the beam at an angle of $\simeq 70°$ between the normal to the surface of the sample and the direction of the beam (see figure 3.20).

This geometry decreases the escape depth for the collected Fe K_α fluorescent radiation and, therefore, increases the count rate. At the same time the orientation of the sample allow the synchrotron radiation to be transmitted through the sample. This radiation is collected by an APD detector in order to measure the instrumental function of the spectrometer.

The energy resolution used during the measurements was 0.5 meV in order to have high quality data also in the low energy region. For each sample we scanned an energy range from -100 to +120 meV. In different energy ranges we used different acquisition times, in order to acquire the entire scan in a relative short time and to increase the statistics in the low energy region (from 0 to 20 meV). The average acquisition time for each energy points was between 80 and 130 s. We obtained the energy dependence of NIS adding a number of scans composed between 10 and 20.

In figure 4.15 we report the collected raw energy dependence of NIS for all densified samples. The data have been normalized to the same value of the first moment allowing for a comparison of the raw data in absolute scale (see section 3.8.1). The collected NIS data present a maximum in the energies range between 5 and 8 meV, this feature corresponds to the presence of the BP in the DOS of the glass. Moreover, increasing the densification of the samples the intensity of the maximum decreases. At 3 GPa this effect seems to saturate, the intensity of the maximum is close to that of the sample at 7 GPa. The asymmetry of the intensity of the energy dependence of NIS with respect to the zero energy, visible in figure 4.15, is associated to the different probability of creating or annihilating phonons and depends on the temperature according to Eq. (3.41).

4.8.2 DOS in densified samples

From the measured energy dependence of Nuclear Inelastic Scattering we extract the corresponding partial density of vibrational states of iron atoms, following the procedure described in section 2.1.3.

Figure 4.16 shows the measured Fe partial DOS for all samples, the data have a higher quality up to 20 meV. In this energy region the picture presents the typical

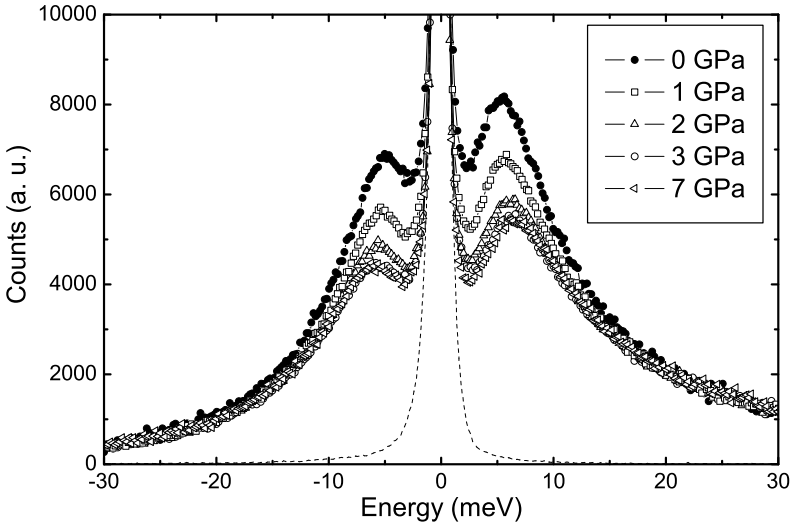

Figure 4.15: *Energy dependence of NIS normalized to the first moment, the dashed line represents the resolution function of the measurements; the legend indicate the different densified samples.*

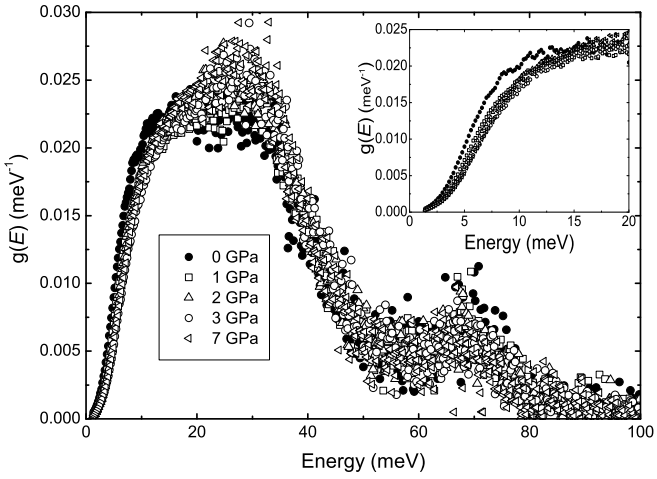

Figure 4.16: *Density of vibrational states (DOS) of the initial and densified $Na_2FeSi_3O_8$ glass, the inset shows the DOS in the low energy region.*

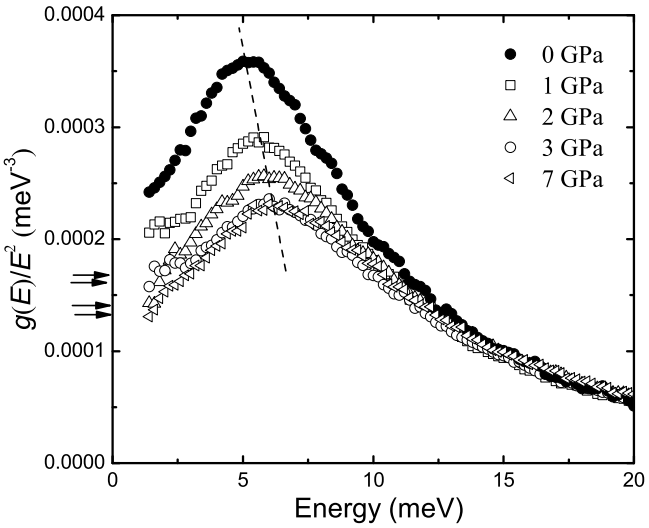

Figure 4.17: *Reduced density of vibrational states (RDOS) of the initial and densified $Na_2FeSi_3O_8$ glasses. The arrows indicate the zero energy limit predicted by the Debye model for each sample (the arrows of 0 and 1 GPa sample coincide). The dashed line emphasizes the shift of the BP with densification.*

increase of the number of vibrational states (from 0 up to 20 meV) associated with the acoustic phonon branches (see section 1.6.1). At higher energies the contribution to the DOS from optical modes is clearly visible, these appear as peaks at 30 and 70 meV.

In order to study the effect of densification on the low energy region of the DOS, we plotted the reduced density of states (RDOS) $g(E)/E^2$. Figure 4.17 shows for all samples a maximum in the RDOS located around 5 meV: the Boson Peak. Its position is in agreement with the values typical for other silicate glasses [75]. Increasing the densification, the maximum of the RDOS decreases in intensity and moves to higher energies. In particular, comparing the 0 and 3 GPa samples, the intensity of the maximum is reduced about 35% and its energy position shifts by 23.5%. Beyond 3 GPa the effect of the densification on the DOS does not proceed further on, the samples 3 and 7 GPa have the same value in the maximum of the RDOS. The differences between the measured RDOS vanish at higher energy, at 17 meV the tails merge in a unique curve.

4.8.3 RDOS in Debye energy units

Looking at figure 4.17 the question naturally arises about the mechanisms responsible for the changes in the maximum of the RDOS. We try to have insights into this issue estimating the effect of the transformation of the macroscopic properties of the glass on

the RDOS. In particular, we calculated the Debye energy E_D for each sample according to Eq. 4.4 using the values of number of atoms per unit volume n and the speed of sound v_L, v_T previously measured (see section 4.7 and 4.5).

$$E_D = (6\pi^2\hbar^3 n < v >^3)^{\frac{1}{3}}, \tag{4.4}$$

$$\frac{3}{< v >^3} = \left(\frac{1}{v_L^3} + \frac{2}{v_T^3}\right). \tag{4.5}$$

Applying the Debye model to our $Na_2FeSi_3O_8$ glass, the zero energy limit of the RDOS is defined by the value of the Debye energy according the relationship:

$$\lim_{E\to 0} \frac{g(E)}{E^2} = \frac{3}{E_D^3} \frac{m_r}{< m >} \tag{4.6}$$

Here the ratio between the average atomic mass of the glass $< m >$ and the mass of iron atoms m_r has been introduced because the model is compared to the partial density of vibrational states of iron atoms. In table 4.4 we report for each sample the calculated E_D and the relative zero energy limit of the RDOS. The zero energy limit defined by Eq. (4.6) represents also the reference level for the RDOS to evaluate the intensity of the Boson Peak.

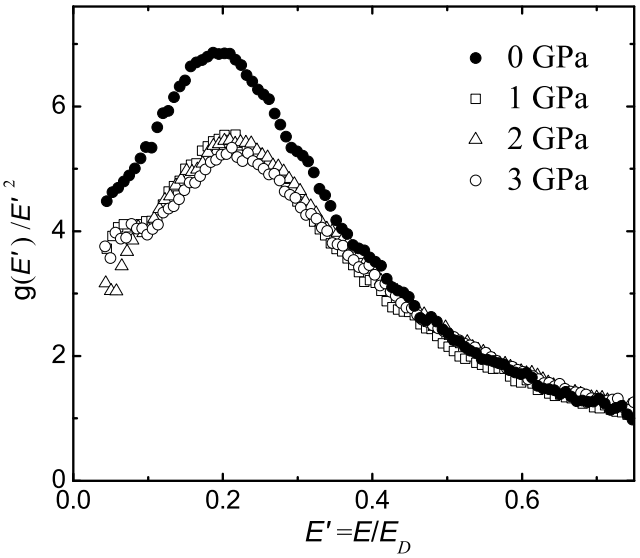

Figure 4.18: *Reduced density of vibrational states in rescaled Debye energy units E'=E/E$_D$.*

The limit at 0 energy of the RDOS predicted by the Debye model has been reported for each sample in figure 4.17 using arrows. Looking at figure 4.17 we observed that

Table 4.4: We report the Debye energy (E_D), and the zero limit energy of RDOS $\lim_{E\to 0} \frac{g(E)}{E^2}$ for the initial (0 GPa) and the densified glasses.

Sample	E_D (meV)	$\lim_{E\to 0} \frac{g(E)}{E^2}$ (10^{-4} meV^{-3})
0 GPa	15.1(2)	1.57(2)
1 GPa	15.1(2)	1.57(3)
2 GPa	15.6(4)	1.41(3)
3 GPa	16.0(5)	1.32(4)

the positions of the arrows change from the 0 to the 3 GPa samples suggesting that the evolution of the maximum of the RDOS with densification does not correspond to a change of the intensity of the BP. In fact, according to the definition of the BP, its intensity has to be evaluated with respect to the level defined by equation 4.6. To take into account the effect of the transformation of the macroscopic properties of the glass on the RDOS, we rescaled the RDOS in Debye energy units: $E' = E/E_D$.

The plot of $g(E')/E'^2$ vs E' (see figure 4.18) allows removing from figure 4.17 the changes in the density of states induced by the modification of the elastic medium. After this correction the differences between the 1 2 and 3 GPa samples disappear, on the other hand the curve corresponding to the initial glass (0 GPa) stays still different from the others.

Figure 4.18 reveals a two step scenario for the influence of densification on the DOS of the glass. In a first stage, between the 0 and 1GPa samples, the densification process changes the DOS and this modification cannot be taken into account by the relative change of the Debye energy. We recall that passing from the 0 to the 1 GPa sample the glass experiences a structural rearrangement on the short length scale (see section 4.6.2). This indicates that the BP is closely connected to the local structure of the sample. In a second step, the densification produces a decrease and a shift of the maximum of the RDOS that is compensated by the increase of the Debye energy of the glass. This further densification of the glass does not change the BP and the modification of the DOS can be completely described by the transformation of the macroscopic properties of the continuum medium.

4.9 Conclusions

The main conclusions that we can derive from our study on the $Na_2FeSi_3O_8$ glass is that the presence of the Boson Peak in glasses is intimately connected to the local structure of the system. Moreover, in absence of changes in the local structure of the effect of the densification process on the DOS of the sample, can be related to the

transformation of a continuum medium.

These conclusions have been obtained combining information on the structure and on the dynamical properties of densified glasses. Using Nuclear Inelastic Scattering we observed that increasing densification and pressure the peak of the reduced DOS decreases in height and shifts to higher energies. Brillouin light scattering, x-ray scattering and Mössbauer spectroscopy reveal two steps in the glass modification: i) the glass changes its local structure at constant density (from 0 to 1 GPa sample) ii) the glass increases density and sound velocity with a continuous modification of its middle range order but keeping the same local structure (from the 1 to the 3 GPa sample).

Rescaling the energy axes of the RDOS in Debye energy units $E' = E/E_D$ the reduced densities of states becomes almost identical for all densified samples that have the same local structure. The energy position of the Boson Peak scales with the Debye energy and the corresponding peak in the RDOS increases its height according to the change of $3/E_D^3$. Thus, with the exeption of the case where structural rearrangement takes place, the transformation of the density of vibrational states induced by densification is described entirely by the transformation of the continuous medium. Conversely if a structural modification in the short range order takes place, the dependence of the Boson Peak on density cannot any longer be taken into account by the corresponding changes in the macroscopic properties and the system behaves as a different glass.

Our results allow testing the reliability of some of the models proposed to describe the mechanisms responsible for the presence of the Boson Peak in glasses.

In the "phonon localization" model [96] the BP is related to the presence of modes localized at a characteristic correlation length R on the intermediate range scale; at such length scale the glass does not have a completely random structure but shows some structural correlation. If we consider the structure of the glass as a packing of atoms and interstitial voids, R can be regarded as the length over which the partial atom-void distribution function become featureless. According to this model the energy of the boson peak E_{BP} behaves as: $E_{BP} \sim v/R$ (v is the speed of sound of the system). Assuming that R scales as the inverse of the cubic root of the density $R \sim (1/\rho)^{1/3} = (V)^{1/3}$ (here V is the volume of the glass, the correlation length R scales with the mean distance between the atoms), it follows that $E_{BP} \sim (\rho)^{1/3}v$ exactly as the Debye energy, whereas the height of the Boson Peak in the RDOS $\sim 1/(\rho v^3)$. Such results are in agreement with our data, nevertheless our study does not confirm the relation between R and the first diffraction peak (FSDP) of the glass [96, 97, 104, 105] as claimed by the "phonon localization" model. In the literature R, referred to as the length scale for the middle range order of the glass, has been associated with the width or the position of the FSDP. The modification of the BP has been attributed to the corresponding modification of the first diffraction peak of the glass. In contrast to this interpretation our data show that despite the continuous modification of the FSDP, the BP does not change. Passing from the 1 to the 3 GPa sample, while the first diffraction peak experiences a relevant evolution in shape and position, the BP does not change.

Another model that can be directly compared against the results of our study is the "dynamical disorder" model [29]. Such model associates the origin of the BP to the distribution of the elastic constants K in the glass. Such distribution has a finite width $\sigma(K)$ around a fixed value K. Changing only the density of the glass we vary the value

of K without altering $\sigma(K)$. In this case the density dependence of RDOS is described only by a single parameter: the Debye energy. This model is thus in agreement with what we found in the $Na_2FeSi_3O_8$ glass.

Résumé du chapitre 5

Dans ce dernier chapitre une étude sur l'orto-terphenile (OTP) vitreux sera présentée. Elle sera effectuée en utilisant la Spectroscopie Inelastique de rayons-X (IXS). En particulier avec cette technique, on a étudie la dynamique du verre en mesurant le facteur de structure dynamique S(Q,ω) dans un intervalle de moments échangés (Q) entre 2 et 10 nm^{-1}. Dans le première paragraphe la thématique scientifique d'intért de cette étude est présentée: le comportement de la dynamique d'un verre dans une région d'énergie proche à celle du BP. Dans cette partie, on accentuera' sur l'utilisation de la pression et en particulier de l'évaluation du paramètre de Gruneisen, qui permet d'avoir des informations sur la nature des modes vibrationnels étudies. En suite, on est passé à illustrer la méthode expérimentale suivi pour réaliser les mesures IXS et celle pour l'analyse de donnés. Un paragraphe sera dédié à rappeler les informations qui permettent d'extraire des mesures IXS et de présenter les paramètres du modèle utilisé pour décrire les données expérimentales. Donc, om montrera les résultats de la comparaison du modèle avec ceux des données expérimentales, en discutant le comportement de Q et en pression des différents paramètres du modèle. Une attention particulière sera réservée à l'analyse du comportement en pression de la fréquence vibrationnelle caractéristique du système. Avec ce paramètre a été possible évaluer le paramètre de Gruneisen (γ) des modes vibrationnelles sondés par les mesures IXS. Les valeurs ainsi estimées de γ des mesures IXS ont été confrontés avec ceux obtenus de mesures US et BLS. Enfin on a confronté le comportement de gamma en variant l'énergie en plusieurs systèmes : OTP, Glicerol, et silica. Cette comparaison avec les données présentes en littérature nous a permit d'insérer les résultats sur l'OTP dans contexte plus vaste. Dans les derniers paragraphes on donne des conclusions sur l'interaction parmi les modes acoustiques mesure par IXS dans un verre et le modes responsables du BP.

Chapter 5

Glassy ortho-terphenyl: an Inelastic X-ray Scattering study

5.1 Scientific Background

In this section we present a study of the high frequency dynamics of glassy ortho-terphenyl (OTP) performed using Inelastic X-ray Scattering (IXS). With such technique we probed the density fluctuations of the glass in the mesoscopic length-scale region (from ≈ 0.6 up to ≈ 3 nm) in order to recover information on the acoustic modes present in the system at these wavelengths.

In our previous studies of hyperquenched and densified glasses (see chapter 3 and 4) we have observed that the density of vibrational states, at low energy, scales with the contribution of the acoustic modes of the system. Thus a detailed characterization of the acoustic excitations, up to energies across the Boson Peak (BP), appears necessary to investigate the nature of the vibrational states present in the low energy region of the DOS.

In the literature there are several studies that have speculated on the origin of the BP in glasses looking at the behavior of the high frequency acoustic modes [106, 107, 108, 109, 110, 111]. Nevertheless, these studies do not produce conclusive or unique results. For example, it has been both pointed out that the vibrational excitations responsible for the presence of the BP in glasses have a character strongly localized [106] or propagating [108]. To give new insights into this issue we used the thermodynamic parameter of pressure to investigate the connection between the acoustic dynamics and the low energy vibrations involved in the BP. In particular, we characterized the high frequency vibrations of glassy orto-therphenyl measuring the Grüneisen parameter $\gamma_L(Q)$.

Monitoring the energy shift of a vibrational excitation induced by a change of volume V of the glass, we directly estimate $\gamma_L(Q)$ ($\gamma_L(Q) = \frac{dln\Omega_L(Q)}{dlnV}$, where $\Omega_L(Q)$ is the frequency of the longitudinal excitation corresponding to the exchanged wavevector Q [112]). We measured the value of $\gamma_L(Q)$ for vibrations at an energy (in the $\approx$ meV region) across that of the BP. The value of the Grüneisen parameter allows us to give hints on the nature of the probed vibrational excitations: comparing $\gamma_L(Q)$ for different energies of the acoustic wave, we investigated whether the nature of the acoustic waves

experiences a change at energies across that of the BP.

So far, for practical reasons, most of the studies on disordered systems were dedicated to the investigation of acoustic modes as a function of temperature at ambient pressure. Nevertheless, the use of pressure allows us to recover more efficiently the value of $\gamma_L(Q)$. The primary effect of pressure in a solid is to change interatomic distances, the changes in vibrational energies can follow via the anharmonicity (in a crystal) or from the topological disorder (in a glass). In contrast the primary effect of temperature is to alter the population of vibrational states, the changes of the interatomic distances are usually a secondary effect.

In the present study we measured the density-density correlation function of glassy OTP varying the pressure from 0.001 up to 2.5 kbar (the temperature was fixed at T=233 K). We observe that OTP is able to support acoustic modes up to energies above that of the BP. Moreover, we found that the acoustic excitations are characterized by a Grüneisen parameter that does not change if evaluated at energies lower or higher than the BP. Conversely, in glycerol and SiO_2, the behavior of $\gamma_L(Q)$ changes through the energy region of the BP. These observations indicate that the nature of the interaction between acoustic and BP's modes depends on the system, and might be related to the fragility of the glass.

5.2 Glassy ortho-terphenyl

The system which we have decided to investigate by IXS is the molecular glass: ortho-terphenyl (OTP, $C_{18}H_{14}$ with a melting point T_m=330 K and a glass transition temperature T_g=243.5 K).

OTP has been extensively studied for more than 40 years [115, 116, 117, 127, 128, 129, 130] as an archetypal glass former, it is neither a polymer nor hydrogen bonded material but forms a glass simply because of the steric hindrance due to the molecular structure. The molecule is not polar and consists of a central benzene ring and two lateral phenyl rings rotated out of plane (see figure 5.1). The molecular shape allows describing the liquid phase of OTP by simple models: rigid molecular units that interact via non directional van der Waals forces [113]. Such simple picture of OTP has suggested that the dynamics of this system presents universal features representative for the entire class of glass formers and is independent of the microscopic peculiarities of the system.

OTP has an extremely non-Arrhenius behavior of the shear viscosity as function of temperature, thus its fragility index puts the system into the class of the fragile glasses (see section 1.3). An interesting characteristic of OTP, that justifies the existence of such a large number of studies, is the possibility to have the liquid, crystalline and glassy state close to room temperature. The system can be easily supercooled, however single crystals of high quality and considerable size can be grown from methanol solutions. Depending on the cooling rate the fictive temperature T_f lies between 242 K and 245 K. One can bypass T_g avoiding the nucleation of the crystal cooling the liquid with a rate relatively low.

The thermodynamic properties as the pressure-volume-temperature relations (PVT)

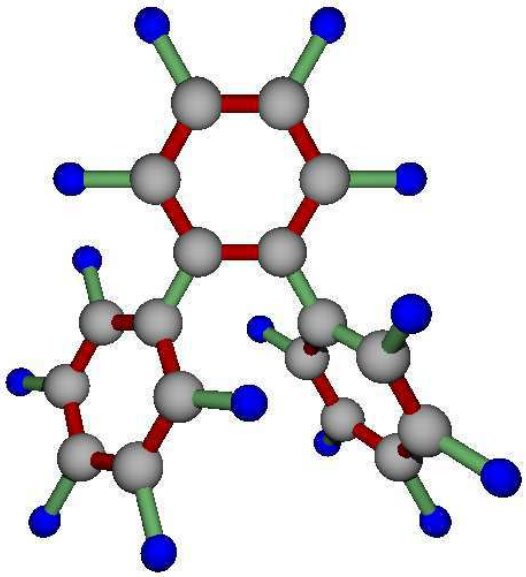

Figure 5.1: *Ortho-therphenyl molecule, the blue spheres are the hydrogen atoms and the gray ones represent carbon.*

have been investigated in a wide range of pressure and temperature [114]. Such extensive characterization of thermodynamic properties of the system has encouraged using OTP to test theories describing the density correlation function. This system was among the first simple molecular liquids in which the secondary β-relaxation process has been measured [115], and several studies have explored the structural α-relaxation process on a wide timescale [128, 129, 119]. Nevertheless, despite the large number of studies of OTP, for practical reasons, only few of them have investigated the effect of pressure on the glass dynamics [128, 131].

5.3 Information on the dynamics of a glass by IXS

In section 2.2 we have illustrated how it is possible to have access by IXS to the Fourier transform (in the $Q-\omega$ space) of density-density correlation function, i.e. to the dynamic structure factor $S(Q,\omega)$.

$$S(Q,\omega) = \frac{1}{2\pi\hbar N}\int_{-\infty}^{+\infty} e^{i\omega t}\langle e^{i\vec{Q}\cdot\vec{R}_j(t)}e^{-i\vec{Q}\cdot\vec{R}_k(0)}\rangle dt = \tag{5.1}$$
$$\frac{1}{2\pi\hbar N}\int_{-\infty}^{+\infty} dt e^{i\omega t}\langle\int_{-\infty}^{+\infty} d\vec{r}d\vec{r}' e^{i\vec{Q}(\vec{r}-\vec{r}')}\delta(\vec{r}-\vec{R}_j(t))\delta(\vec{r'}-\vec{R}_k(0))\rangle.$$

$S(Q,\omega)$ contains all the dynamical information of the system on the length-scale defined by Q. In section 2.2 we have shown that for a crystal it is possible to describe

the $S(Q,\omega)$ starting from first principles; within the hypothesis of small displacements ($u << R$) of the atoms from their equilibrium positions (R) we can write:

$$S(Q,\omega) = \frac{1}{4\pi MN} e^{-W(Q)} \sum_j e^{i\vec{Q}\cdot\vec{R}_j} \frac{(\vec{Q}\cdot\hat{\epsilon}_{s,\vec{Q}})^2}{\omega_{js}} [\delta(\omega-\omega_{js})\langle n(\omega)+1\rangle + \delta(\omega+\omega_{js})\langle n(\omega)\rangle],$$

here ϵ and ω_s represent respectively the phonon polarization and frequency, and $< n(\omega) >$ is the Bose occupation number.

Thus according to the previous equation, in a crystal where the $S(Q,\omega)$ is dominated by the Brillouin contribution, we have two inelastic lines located at $\pm\omega_{js}$. These lines have an intensity that reflects the probability of creating and annihilating phonons. The ratio between the intensity of $S(Q,\omega)$ at energies $\pm\hbar\omega_{js}$ is equal to :

$$\frac{S(Q,\omega_{js})}{S(Q,-\omega_{js})} = \frac{\langle n(\omega)+1\rangle}{\langle n(\omega)\rangle} = e^{\frac{\hbar\omega_{js}}{k_B T}}$$

Nevertheless the dynamical structure factor predicted by the theory presents some differences compared to the experimental one. In a crystal the anharmonicity and the interactions of phonons with the imperfections of the material lead to a finite lifetime of the phonon excitations. The vibrational excitations are not any longer two delta functions $\delta(\omega \pm \omega_{js})$ but they show a finite width Γ.

In a glass, the simple form that $S(Q,\omega)$ assumes in crystals is strongly modified and there are no models able to describe the dynamic structure factor from first principles. In contrast to the crystalline state a disordered system is characterized by the absence of translational invariance, thus a density fluctuation with wave-vector Q is not an "eigenstate" of the system. The dynamics of a glass is influenced by the presence of new degrees of freedom compared to a crystal: hopping, tunneling and relaxation processes.

According to the complexity of the processes that control the dynamics in a glass, its $S(Q,\omega)$ is not simply structured as in a crystal. However, the dynamic structure factor of a glass at low Q can be characterized using the quantities that have well defined meaning in the relative crystalline state as Ω, Γ, f_Q.

- Ω represents the frequency of the investigated excitation. As we have discussed in section 1.6 an amorphous system is able to support acoustic vibrational excitations. Such modes are characterized by their energy $\hbar\Omega$ and wave-length $\lambda = 2\pi/Q$. At low Q, where the system roughly behaves as a continuum, these excitations have the character of acoustic modes and define the macroscopic elastic properties of the glass. At high Q, Ω starts to be strongly modified because the typical length scale of the structure becomes comparable to the wavelength of the excitation. At even higher Q values the excitations lose their acoustic nature.

- Γ is the width of the inelastic excitations. As we have discussed in section 1.6, the mechanisms responsible for sound attenuation in glasses are still not fully

understood. Nevertheless different sources of damping have been identified: relaxation processes, scattering from defects, anharmonicity. These mechanisms lead to a decay of the density fluctuations toward different degrees of freedom and therefore to a broadening of the $S(Q,\omega)$ that now is characterized by a finite width Γ of the inelastic peaks.

- f_Q is the non-ergodicity factor defined as the fraction of the radiation elastically scattered by the sample (see figure 5.2) and represents a measure of the ergodicity of the system ($0 < f_Q < 1$). The relevance of this quantity rises from the role that it plays in a theory of the glass transition, the Mode Coupling theory [132]. f_Q in fact quantifies the arrest of density fluctuations in the non-ergodic glassy state ($f_Q = \phi_Q(t \to \infty)$ where ϕ_Q is the time correlation function of the system at fixed Q value). The theory makes precise predictions on the behavior of f_Q passing from the liquid (f_Q=0) to the glassy state. Moreover, it has been proposed that f_Q allows predicting an important property of the glass as the fragility [118] though this relationship is still highly debated.

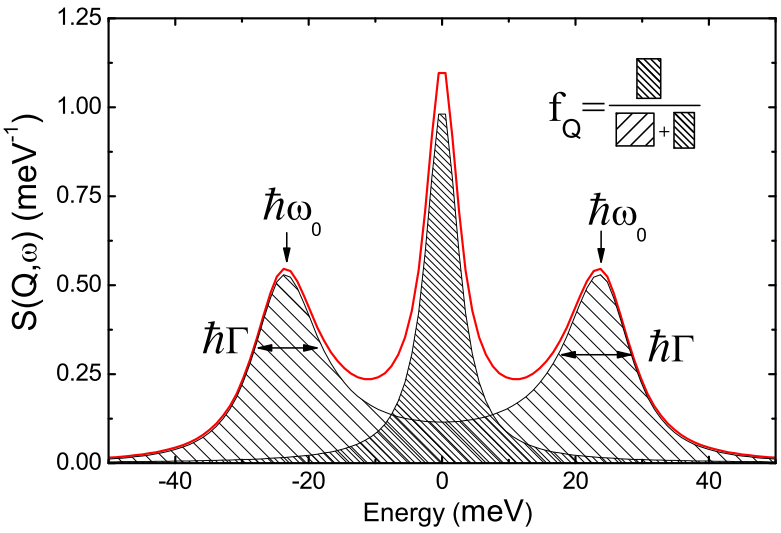

Figure 5.2: *Example of the $S(Q,\omega)$ predicted by the model function (DHO plus a Lorentian function, see text) used in the data analysis. An indication of the features associated to the parameters: Γ, $\Omega = (\omega_0^2 + 2\Gamma^2)^{1/2}$ and f_Q is also reported.*

In order to quantitatively evaluate from the collected IXS data the values of Γ, Ω and f_Q, we used a model function able to describe the measured $S(Q,\omega)$. Such model is the sum of a Lorentian function, that takes into account the elastic and quasi-elastic scattering by the sample (the peak at $\omega = 0$) and a Damped Harmonic Oscillator (DHO) able to describe the inelastic scattering (see Eq. (5.2)). In figure 5.2 we show

the typical shape of the $S(Q.\omega)$ predicted by the model and the features corresponding to the parameters Ω, Γ and f_Q. The DHO model function can be theoretically derived as the high frequency limit of the $S(Q,\omega)$ line shape obtained within the generalized hydrodynamic theory [133]. This model has been applied with success not only to the study of glasses with inelastic x-ray scattering but also with inelastic neutron scattering.

$$\frac{S(Q,\omega)}{S(Q)} = \left[(n(\omega)+1)\frac{\hbar\omega}{k_B T}\right]\left[\frac{f_Q}{\pi}\cdot\frac{\xi}{\omega^2+\xi^2} + (1-f_Q)\frac{2\Gamma(Q)\Omega^2(Q)}{(\omega^2-\Omega^2(Q))^2+\Gamma^2(Q)\omega^2}\right]. \tag{5.2}$$

In Eq.(5.2) the parameter Γ represents the full width at half maximum (FWHM) of the inelastic excitation, and Ω is the frequency of the maximum of the correlation function of the longitudinal current $J(q,\omega) = (\omega^2/q^2)S(Q,\omega)$, while the maxima of the DHO function are placed at $\omega_0 = \sqrt{\Omega^2 - 2\Gamma^2}$. Ω identifies the frequency of the acoustic mode of the system. The parameter ξ controls the width of the elastic peak.

The factor $[(n(\omega)+1)\frac{\hbar\omega}{k_b T}]$ in Eq.(5.2) has been introduced in order to take into account the asymmetry of the $S(Q,\omega)$ associated to the different probability of annihilation or creation of phonons [44].

5.4 IXS measurements

The IXS measurements have been performed at the ID-16 beam-line at the ESRF. The temperature for the measurements was fixed at $T = 233$ K and the pressure was changed in the range between 0.001 and 2.5 kbar. The spectra have been collected at values of the exchanged wave vector equal to 1, 2, 4, 7 and 10 nm^{-1}, using an energy resolution of 1.5 meV (FWHM). The total acquisition time for each thermodynamic point has been between 6 and 12 h. We have summed several spectra at each value of pressure. This strategy of data collection was assumed in order to minimize the loss of data due to the crystallization of the sample. In fact, after each spectrum we checked the state of our sample collecting the total scattering as function of wave vector Q, the crystallization is visible by the appearance of characteristic Bragg peaks in the intensity of the total scattered radiation $I(Q)$ (see figure 5.3). The samples in which we recognized the start of a crystallization process have been replaced by new ones.

In figure 5.4 we report the collected spectra at different values of Q and at different values of pressure. From a first sight at the figure we can observe the dispersion of the inelastic excitations $\Omega = \Omega(Q)$. The energy of the characteristic vibrational excitation Ω (indicated by arrows in the picture) increases at higher Q values. Moreover, the attenuation of the acoustic excitations is strongly Q dependent, we observe a broadening of the inelastic feature increasing Q.

5.4.1 Experimental apparatus

Pressure, as we pointed out in the introduction of this chapter, is the key parameter of our study allowing investigating the nature of the high frequency vibrations of OTP in a region of energy close to that of the BP.

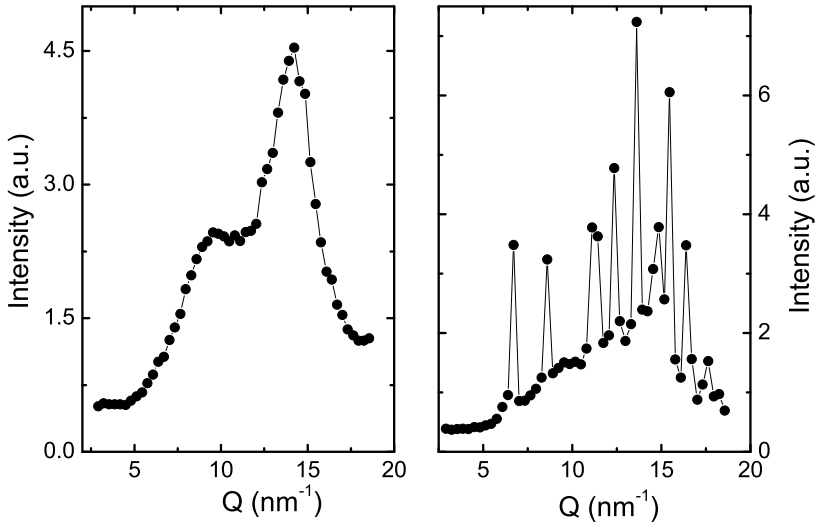

Figure 5.3: *Intensity of the radiation scattered by glassy (left panel) and partially crystallized (right panel) OTP.*

However, the two requirements of the experiment, i.e. to have a sample in the glassy state and to change its pressure, have been the source of not negligible technical difficulties during our measurements. The main problem that we had to face was to prevent the crystallization of the sample and, at the same time, guarantee hydrostatic pressure condition for the sample. Moreover, we had to ensure the stability of the thermodynamic conditions of the sample over the entire duration of each measurement, i.e. over a relative long time (6-12 h).

In order to keep our sample at low temperature and under pressure we used a large volume cell formed by a stainless steel cubic body with an interior cylindrical hole (0.8 cm^3) where the samples were loaded. A drawing of this cell is reported in fig. 5.5. Its main characteristics are the long sample length (10 mm) and the angular acceptance of 30 degrees, which at our working energy of 21.7 keV allows reaching exchanged momenta up to 50 nm^{-1}. The cell can be connected to the external pressure generator through a standard Nova Swiss HP connection.

The HP sealing of this cell is shown in fig. 5.5. The two diamond windows, through which the incident and the scattered beam passes, are single crystal diamond disks of 6 mm diameter and 1 mm thickness. Beside the resistance to mechanical solicitations, a decisive advantage in using diamond windows is their negligible contribution to the scattered intensity. Diamonds are glued on the flat internal face of the two conical supports. The diameter of the hole (2.3 mm) at the flat surface of the support, which allows the beam to go through the cell, was chosen as the best compromise between maximizing the angular opening and minimizing the pressure on the windows. The supports are screwed and tightened against the cell's body by special circular nuts.

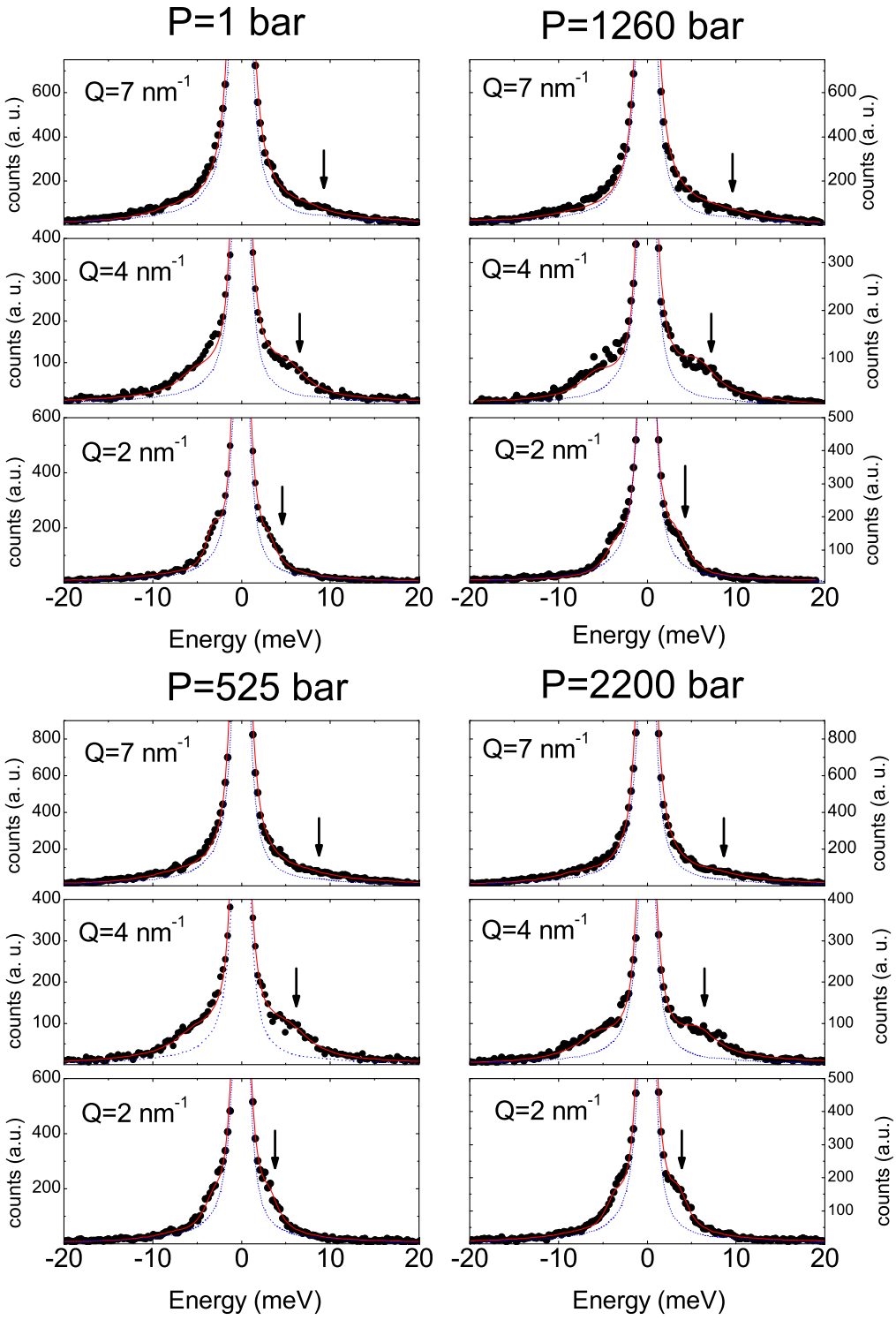

Figure 5.4: *IXS spectra collected at different pressures and exchanged wave-vectors Q, the arrows indicate the position in energy of the vibrational frequency Ω. The red lines represent the results of the fit and the dashed line the resolution function of the measuremsts.*

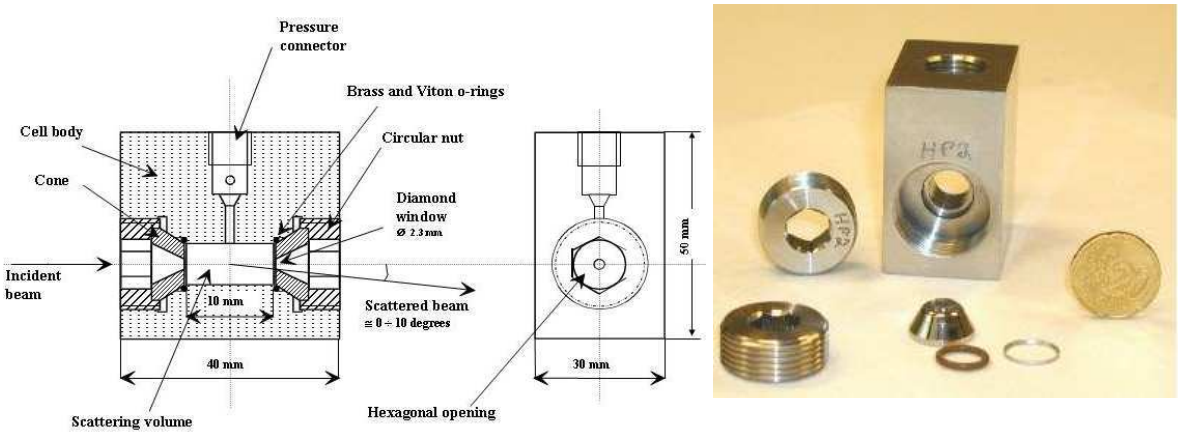

Figure 5.5: *The sketch (left panel) of the large volume cell used for the experiment (right panel).*

Two brass or copper ring gaskets with triangular section are inserted into the inner space between the conical surface of the supports and the inner wall of the internal chamber. The HP tightness is accomplished by this double metal to metal contact (conical supports and internal chamber). The two gaskets were coated with indium in order to improve the tightness. A couple of viton O-rings were used in addition to seal the cell at low pressure. In fact, while at high pressures the compression medium itself pushed the metallic gasket ensuring the tightness, the O-rings are used as a spring, which pushes the gaskets from the back, ensuring the tightness also at low pressure.

The HP generator was a Nova-Swiss hand pump, whose maximum output pressure is 7 kbar. This hand pump was located outside the experimental hutch and connected to the HP cell through a long capillary. In this way the pressure could be changed without entering in the experimental hutch. Moreover, pressure valves that allow decoupling the HP generator from the HP cell were used (see fig. 5.6). The pressure was controlled by two pressure gauges with a precision of ± 20 bar at 3 kbar.

We used the silicone oil (AP 150 Wacker) as transmitting medium for the pressure, such material has the characteristics to keep its liquid phase over all thermodynamic conditions explored in our measurements (P=0.001-2.5 kbar, T=233 K). OTP has been introduced inside the cell being previously enclosed in a cylindrical container of aluminium (diameter of 8.0 mm and height 9.0 mm). The aluminium container is formed by a short and a long cap of 0.2 mm thickness; the two parts are glued together once the longest has been filled by OTP. The container provides hydrostatic pressure conditions, the silicone oil in fact surrounds completely the cylinder. The use of aluminium for the container has been motivated by the fact that the radiation scattered by aluminium gives a negligible contribution to the total inelastic scattering signal coming from OTP, as we will observe in what follows.

In order to have OTP in the glassy state, after loading the cell with the sample we heated the entire cell up to 373 K ($\approx$40 K over the melting point of OTP, T_m=330 K)

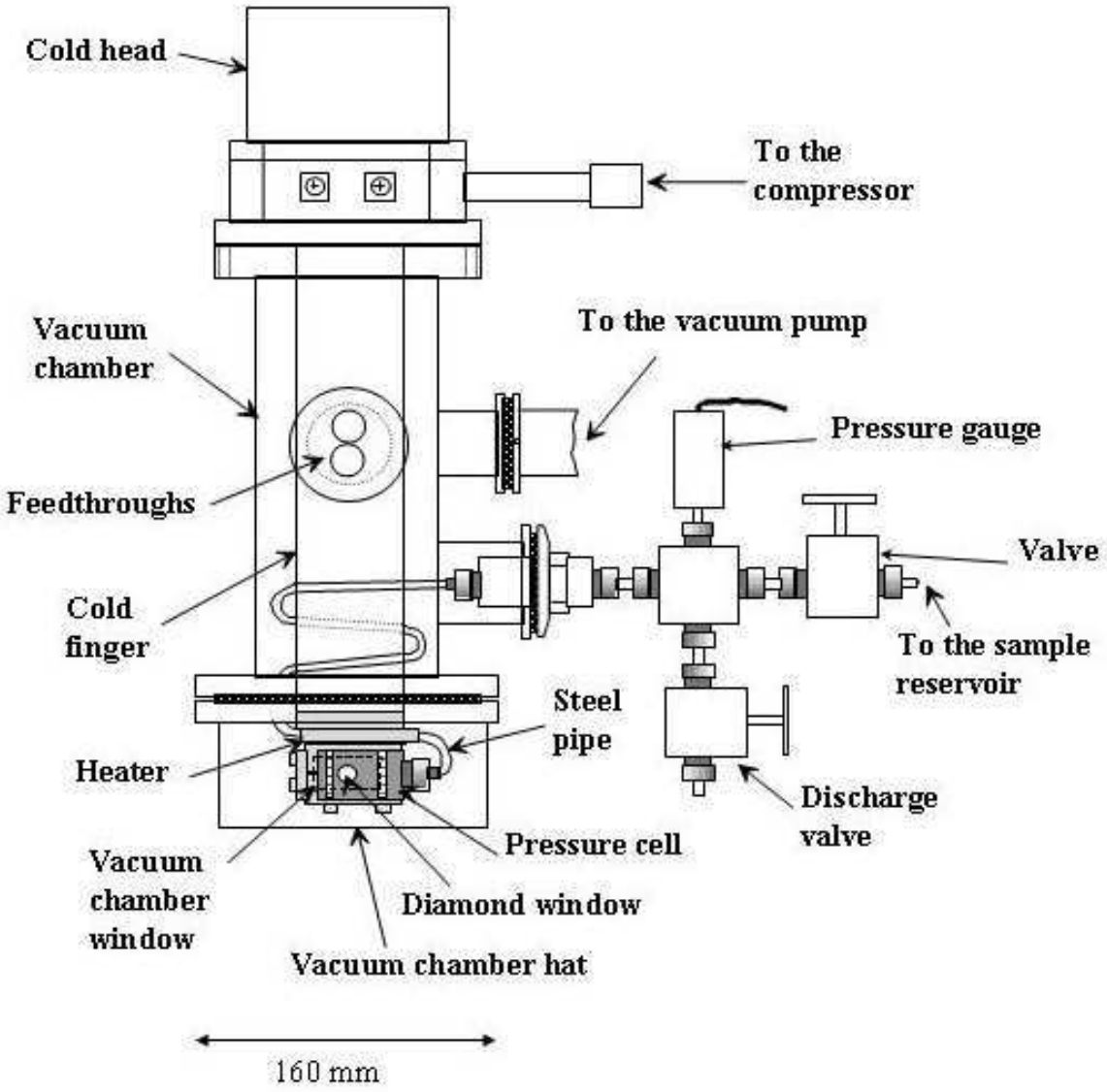

Figure 5.6: *High pressure apparatus used for the experiment.*

to get OTP in liquid phase, then we plunged the cell into liquid nitrogen. The glass was kept below T_g using the circulation of a cooling liquid around the cell at 220 K. A thermocouple inserted in the body of the cell close to the sample has been used to monitor the temperature during the sample preparation and the measurements.

5.4.2 Data analysis

In order to perform a quantitative analysis of the effect of pressure on the acoustic dynamics of the OTP, we started to collect the IXS spectrum of the empty cell. The measurements were performed with the Al cylinder closed without sample inside the cell filled with the silicon oil. Such measurement allows evaluating the contribution to the scattered radiation coming from the empty cell ($I_{0(e)}$): the aluminium container plus the two diamond windows of the cell and the silicon oil. Then we subtracted from each IXS spectrum I_{exp} the $I_{0(e)}$ weighted by the coefficient $e^{-\mu L}$ (μ is the absorption coefficient and L the length of the sample), that takes into account the fraction of the scattered radiation transmitted through the sample. The resulting scattered radiation coming only from glassy OTP I^*_{OTP} can be written as:

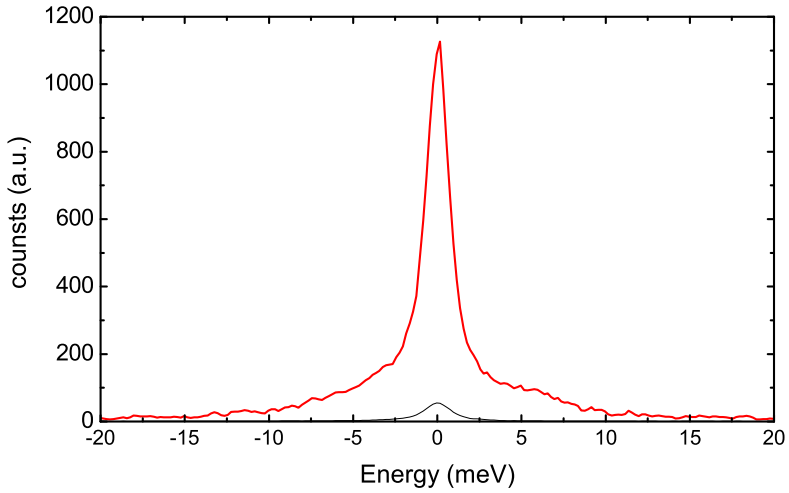

Figure 5.7: *IXS spectrum of OTP (red line) and the corresponding contribution of the empty cell (black line).*

$$I^*_{OTP} = I_{exp} - I_{0(e)}e^{-\mu L}. \tag{5.3}$$

Comparing I^*_{OTP} and I_{exp} we observe that the contribution to the total scattering due to the empty cell is negligible (see figure 5.7).[1]

[1]This is confirmed also by the results of our data analysis that lead to almost the same value of the parameters Ω, Γ, f_Q when analyzing either I^*_{OTP} or I_{exp}.

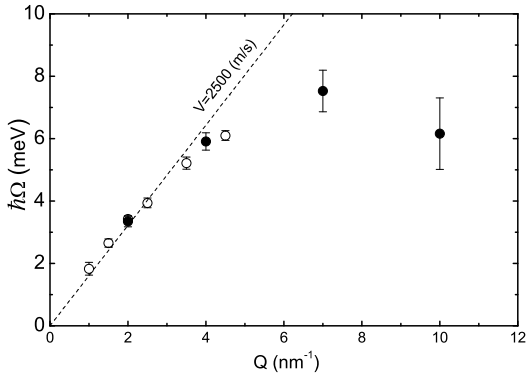

Figure 5.8: *Energy $\hbar\Omega$ of the excitations measured by IXS as function of the exchanged wave-vectors Q at ambient pressure. The empty symbols are from [119].*

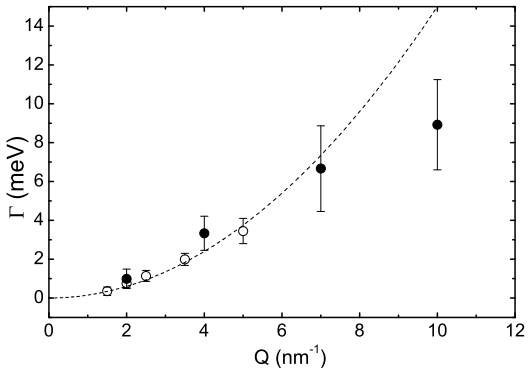

Figure 5.9: Γ *parameter measured as a function of the exchanged wave-vector Q at ambient pressure. The empty symbols are from [119].*

As we have pointed out in section 5.3 to have quantitative information from IXS data we compare I_{exp} with the model $S(Q,\omega)$ (see Eq. 5.2). The model $S(Q,\omega)$ has been convoluted to the experimental resolution function $R(\omega)$ before being compared to the experimental data.

$$\tilde{I}^*_{OTP}(Q,\omega) = \int S(Q,\omega')R(\omega-\omega')d\omega'. \tag{5.4}$$

A fitting routine looks for the best values of the free parameters f_Q, Ω, and Γ, in order to minimize the χ^2 estimated from the experimental data and the model:

$$\chi^2 = \sum_{i=1}^{N}\left(\frac{I^*_{iOTP} - \tilde{I}^*_{iOTP}}{\sigma_i}\right)^2$$

here σ_i is the error on the experimental data I^*_{iOTP}. The agreement between the model function $\tilde{I}^*_{iOTP}$ and I^*_{iOTP} evaluated minimizing the χ^2 function, is shown in figure 5.4.

The statistical quality of our IXS spectra combined with the used energy resolution ($\approx$ 1.5 meV) allowed us to extract reliable values for the fitting parameters (Ω, Γ, f_Q) in the Q wave-vector range from 2 to 10 nm^{-1}. At lower Q values the energy resolution does not allow resolving the inelastic features of the sample. In addition at Q values larger than 10 nm^{-1} the intensity of the radiation scattered inelastically is too low for the fitting routine to give a reliable estimation of the free parameters. Thus we derived the values of Ω, Γ, f_q only for the spectra collected at Q=2,4,7 and 10 nm^{-1}.

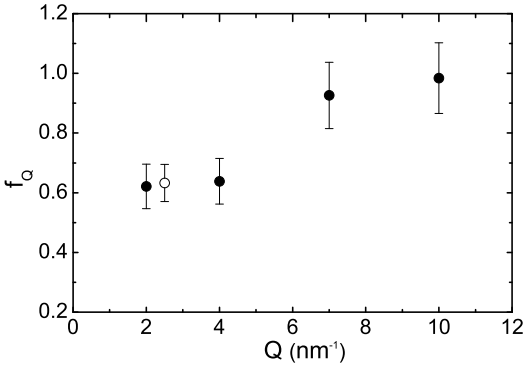

Figure 5.10: *Non-ergodicity factor f_Q measured as function of exchanged wave-vector Q at ambient pressure, the open symbol are the data from [119].*

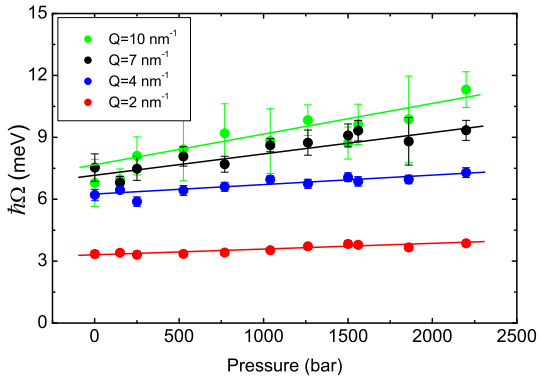

Figure 5.11: *Energy $\hbar\Omega$ of excitation measured as function of pressure at different Q as shown in the legend.*

5.5 Results

Here we report the results of our data analysis, in particular we present the behavior of the parameters discussed in the previous section (Ω, Γ, f_Q) as function of exchanged wave vector Q and pressure P. Collecting data at different exchanged wave vectors we have observed a progressive increase of the error bar for the parameters on increasing Q. This effect is essentially related to the decrease of inelastic scattering compared to elastic one that reduces, at high Q, the sensitivity of the fitting routine used to estimate the parameters of the model.

Q-dependence

Looking at figure 5.8 we observe that the characteristic energy of the inelastic excitations Ω follows the expected behavior as a function of the exchanged wave-vector Q. Up to Q=4 nm^{-1} Ω increases almost linearly, moreover such linear dependence defines a value of the speed of sound ($v_s = \Omega/Q$, $v_s \approx$2500 m/s) that is compatible with that of the pure longitudinal modes measured by Brillouin Light Scattering (BLS) and ultra sound (US) technique [117, 119]. The values of Ω at ambient pressure are in agreement with the data from previous IXS measurements [119]. Such agreement confirms the soundness of the entire procedure used to extract the values of the parameters involved in the model of the IXS data.

At high energy values, Ω loses its linear dependence on Q (see figure 5.8), the $\Omega - Q$ dispersion relation starts to bend because the wave-length of the excitation approaches the characteristic correlation length for the microscopic structure of OTP. Similarly to what happens in a crystal, the dispersion relationship $\Omega - Q$ bends because $\Omega \to 0$ at the end of the Brillouin zone where the static structure factor $S(Q)$ of the system

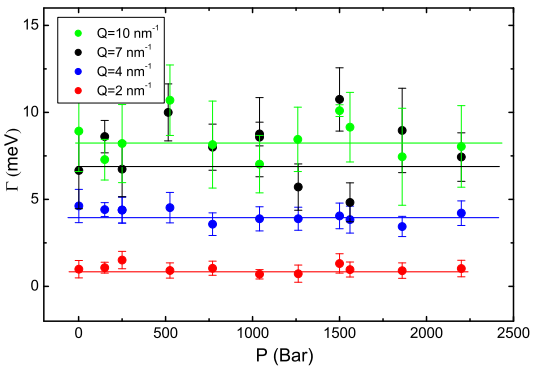

Figure 5.12: Γ *parameter measured as function of pressure for different values of exchanged wave-vectors Q (indicated in the legend).*

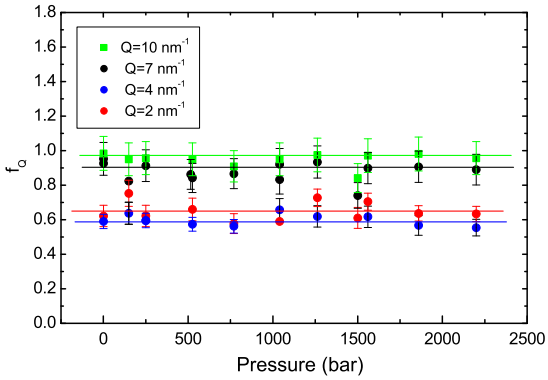

Figure 5.13: *Non-ergodicity factor f_Q measured as function of pressure for different values of exchanged wave-vectors Q (indicated in the legend).*

presents a maximum. In OTP the presence of a pre-peak in the $S(Q)$ at ≈ 8 nm^{-1} (see figure 5.3) is responsible for the bending of the vibrational frequencies already at Q=7 nm^{-1}.

From what concerns the attenuation of the probed excitations, we observe that the widths of the excitations Γ are in agreement with the Q^2 trend also found in the previous IXS measurement [119] on OTP (see figure 5.9). The same behavior of Γ has been found in other systems measured by IXS. However, the origin of this Q dependence of the sound attenuation is still highly debated [120, 106, 121, 122]. While in fact, the anharmonicity of the system predicts a Q^2 behavior of Γ, it is not clear whether such mechanism can be extrapolated in the nm^{-1} region of Q. At this values of exchange wave-vector, Γ is strongly influenced by the microscopic structure of the system; however, a clear picture of the connection between the Q^2 dependence of Γ and the topological disorder of the system is still missing.

Figure 5.10 shows the dependence of the non-ergodicity factor f_Q on the exchanged wave vector Q; at Q=2 and 4 nm^{-1} f_Q has comparable values (within the error bars), at higher Q its value increases. The change of f_Q increasing Q is related to the increase of the intensity of the radiation elastically scattered from the sample approaching the maximum of the $S(Q)$.

P-dependence

Inspecting figure 5.11 we observe that the influence of pressure on Ω is more pronounced at high Q values (i.e. at Q=7 and 10 nm^{-1}). At Q=7 and 10 nm^{-1}, the slope of the $\Omega - P$ line increases considerably, this increase will be discussed in the next section. Here it has to be stressed that the pressure dependence of Ω is linear in the whole explored pressure range allowing to derive a unique value of the Grüneisen parameter

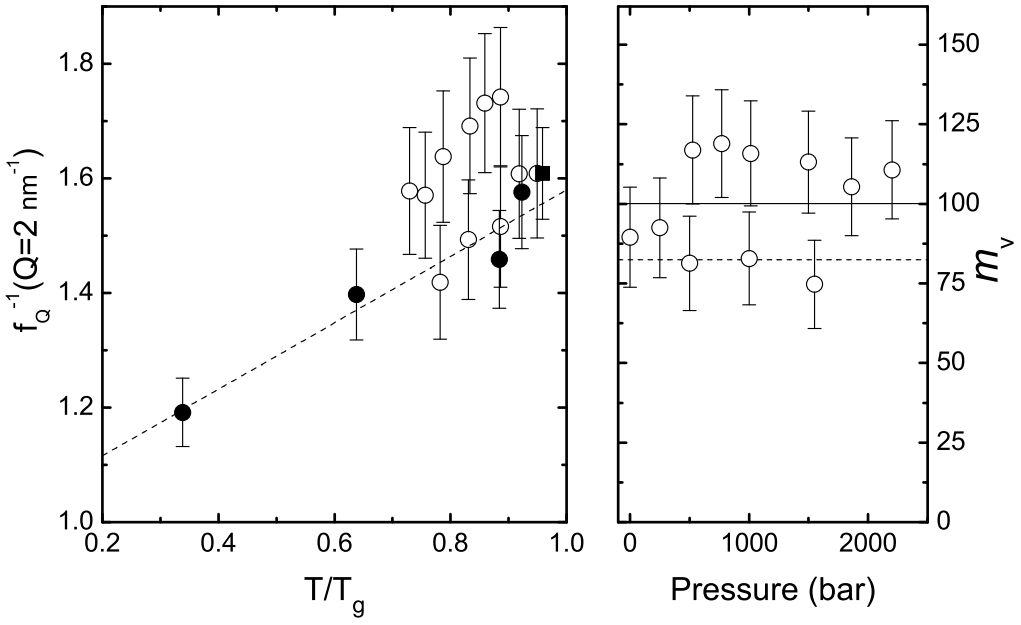

Figure 5.14: *Non-ergodicity factor f_Q measured as function of temperature by IXS at Q=2 nm^{-1} (left panel). The solid circles are the results from [118], the square is the value obtained from our IXS data at ambient pressure, the open symbols are the values of f_Q estimated at different values of pressure (see text). The dashed line is the linear fit to the full symbols. In the right panel the open symbols represent the vibrational fragility estimated from our values of f_Q (see text) measured at Q=2 nm^{-1} as a function of pressure. The dashed line corresponds to the value of m_v estimated from the fit of the full symbols in the left panel, the continuous line is the mean value of the open symbols.*

(see next section).

In figure 5.12 we report the dependence on pressure of the parameter Γ, and we observe that at fixed Q values, Γ is constant (within the error bar). Such result indicates that the main contribution to the damping of the acoustic excitations in OTP, does not change significantly in the explored pressure range.

The non-ergodicity factor f_Q as well does not experience relevant changes induced by pressure (see figure 5.13). From the measured values of f_Q, we could explore the pressure dependence of the vibrational fragility (m_v) of the glass defined from the work of Scopigno et al. [118]. Here the slope α_m of the quantity f_Q^{-1} reported as a function of T/T_g is related to the vibrational fragility according the linear relation $m_v = 135\alpha_m$.

Taking into account that varying the pressure of the glass we modify the glass transition T_g of the glass [114], we can plot each measured value of f_Q as a function of T/T_g and derive a value of m_v. In figure 5.14 we report our values of f_Q together with those from Ref. [118]. The values of m_v derived from Fig. (5.14) do not show any strong dependence on P within their (rather large) error bar and suggest a P-independent value of m_v for OTP (m_v=100± 20). This value is compatible with that observed from [118] being m_v=80± 5. The P independence of m_v is in agreement with the pressure independence of the fragility of OTP estimated by viscosities measurements in the same pressure range [123].

5.6 The frequency dependence of the Grüneisen parameter

From a first sight at the behavior of Ω vs P (see figure 5.11) we observe that the frequency of the acoustic excitations increases linearly with pressure but its slope changes for different values of Q. Such behavior can be directly related to a different behavior of the probed vibrations. An indication of the different nature of the acoustic excitations of glassy OTP from those of an ideal harmonic system can be obtained measuring the Grüneisen parameter. $\gamma_L(Q)$ can be written as a function of the pressure dependence of Ω as:

$$\gamma_L(Q) = -\frac{\partial ln\Omega_i}{\partial lnP}\frac{\partial lnP}{\partial lnV}, \tag{5.5}$$

where V is the volume of the system. Thanks to the pressure-volume-temperature (PVT) measurements present in the literature [114] we can estimate the volume corresponding to each applied pressure and then using Eq. (5.5) we determine $\gamma_L(Q)$ in a Q range from 2 up 10 nm^{-1} (see figure 5.15). The Grüneisen parameter obtained by IXS data increases increasing Q. In order to understand the reason for such behavior we estimated also the value of the Grüneisen parameter γ_{th} from thermodynamic data and that resulting from the measurements of the acoustic modes using US ($\gamma_L(Q_{US})$) and BLS ($\gamma_L(Q_{BLS})$) spectroscopy (see table 5.1). The value of γ_{th} is obtained starting from the value of the thermodynamic parameters: bulk modulus $B_T = V\partial P/\partial V|_T$, heat capacity at constant volume c_v, and thermal expansion $\alpha = \frac{1}{V}\frac{dV}{dT}\Big|_P$. γ_{th} can be

also expressed as the sum of the Grüneisen parameters $\gamma_i(Q)$ of all modes of the system weighted by the respective contribution to the heat capacity c_v:

$$\gamma_{th} = \frac{\alpha B_T}{c_v} = \frac{\sum_i \int dQ c_{vi}(Q)\gamma_i(Q)}{\sum_i \int dQ c_{vi}(Q)}. \tag{5.6}$$

In order to determine $\gamma_L(Q_{US})$ and $\gamma_L(Q_{BLS})$, we have used data present in the literature on the temperature behaviour of Ω_i measured at different frequencies by US and BLS spectroscopy. In fact $\gamma_L(Q)$ can be also written as [112]:

$$\gamma_i = -\frac{\partial ln\Omega_i}{\partial lnV} = -\frac{\partial ln\Omega_i}{\partial lnT}\Big|_V \frac{\partial lnT}{\partial lnV}\Big|_P = -\frac{\partial ln\Omega}{\partial T}\Big|_P \frac{1}{\alpha}. \tag{5.7}$$

In table 5.1 we report the value of the Grüneisen parameters obtained by the different spectroscopic techniques: $\gamma_L(Q_{US})$, $\gamma_L(Q_{BLS})$, $\gamma_L(Q_{IXS})$, corresponding to different Q values.

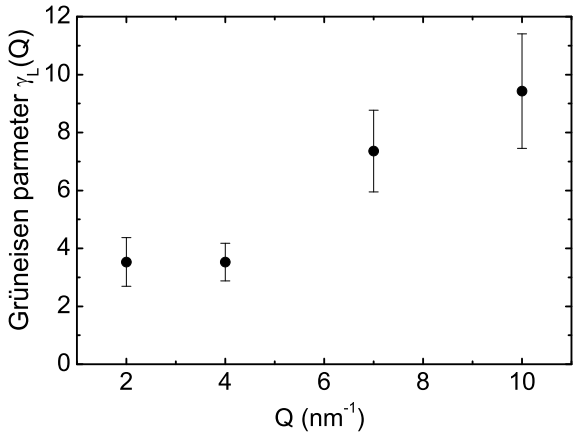

Figure 5.15: *Grüneisen parameter calculated from IXS data using the volume dependence of* Ω *at different* Q *values.*

Looking at the values of table 5.1 we observe that $\gamma_L(Q_{US})$, $\gamma_L(Q_{BLS})$, $\gamma_L(Q_{IXS})$ are higher than the thermodynamic one γ_{th}. Such difference can be understood if we recall that γ_{th} contains the contributions from all possible thermally excited vibrations weighted by the relative heat capacity (c_i) (see Eq. (5.6))[2]. Thus γ_{th} contains also contributions from non-acoustic excitations possibly characterized by a Grüneisen parameter much smaller than that of the modes probed by US, BLS or IXS spectroscopy.

From figure 5.16 we observe that the value of $\gamma_L(Q)$ is constant in a large range of energy. The Grüneisen parameter of the longitudinal modes $\gamma_L(Q_{US})$ and $\gamma_L(Q_{BLS})$,

[2]The values of the Grüneisen parameters corresponding to the transverse modes are supposed to be close to the longitudinal one reported in Table 5.1.

corresponding respectively to an energy of $\approx 10^{-6}$ meV and $\approx 10^{-1}$ meV, is comparable of that measured by IXS up to energy values of $\approx$ 7 meV. This result suggests that the acoustic excitations measured at relevantly high values of Q (i.e. Q=2 and Q=4 nm^{-1}, see figure 5.15) have a very similar nature as the lower-energy ones.

We refer to the properties evaluated by the Grüneisen parameter as the *anharmonic-like* nature of the mode. The terminology has been chosen in analogy with the case of a crystal where the Grüneisen parameter is also a measure of the anharmonicity of the system. From figure 5.16 we observe that the longitudinal acoustic vibrations in OTP are characterized by the same anharmonic-like behavior up to energies above that of the Boson Peak. This result suggests two possible scenarios: i) The Grüneisen parameter of the modes embedded in the BP is very similar to that of the acoustic modes, and therefore $\gamma_L(Q)$ is insensitive to any possible coupling between these modes and the acoustic ones; ii) There is no or marginal effect of a possible coupling among the excitations embedded in the BP and the acoustic ones.

Concerning the second scenario, we note that, e.g., in network glasses [106] an analysis of the Q-dependence of the acoustic attenuation does suggests a strong coupling between acoustic excitations and BP modes. This, however, may not necessarily be valid for the case of OTP.

Further information supporting the proposed two scenarios, can be provided analyzing the width of the inelastic excitations Γ measured at different Q values. In fact, sound waves passing through a solid can be attenuated by two processes. First, the acoustic wave produces through the dilatations and contractions of the solid a temperature wave via thermal expansion. The energy of the acoustic wave is dissipated by heat conduction between the regions of different temperature. Here we name Γ_{th}, the contribution to sound attenuation from this mechanism. A second source of sound attenuation is that called Akhiezer mechanism (Γ_{Ak}): the sound waves propagating in a system interact with other thermally excited modes (i.e. the thermal phonons). Because of anharmonicity, the strain field associated to a sound wave causes a change in the thermal phonon energies. This change in general differs for phonons with different polarization vectors and propagation directions. The equilibrium condition is re-established via phonon-phonon collisions; such process requires an increase of entropy and then leads to the absorption of sound wave at finite temperature. One can show that in OTP the Akhiezer mechanism represents the main contribution to sound attenuation $\Gamma_{th}/\Gamma_{Ak} \approx 0.03$ [122].

The Akhiezer mechanism of sound attenuation is characterized by a mean time τ_{th} that the phonon's population takes to return to equilibrium and by the Grüneisen parameter $\gamma_L(Q)$. According a simple model [140] one can relate γ to the value of the measured Γ_L, following the relationship:

$$\Gamma = \gamma_L^2 \cdot \frac{c_v T v}{2\rho v_D^3} \cdot \frac{\Omega^2 \tau_{th}}{1 + \Omega^2 \tau_{th}^2}, \tag{5.8}$$

here v is the speed of the acoustic wave, v_D is the Debye sound velocity of the system, c_v the heat capacity at constant volume, ρ the density and T the temperature.

The Q dependence of the Γ parameters obtained by BLS and IXS measurements up to Q=4 nm^{-1} can be described, according to Eq. (5.8) by the Akhiezer mechanism.

Inserting in Eq. (5.8) the values of Γ measured at different Q, and the corresponding Grüneisen parameters $\gamma_L(Q)$, we obtain in the whole probed Q range $\tau_{th} \approx 0.25$ ps[3].This results confirms that in OTP the anharmonic-like nature of the acoustic excitations of the glass stays unaltered from $\approx 10^{-1}$ up to 7 meV. The modes have almost identical Grüneisen parameter and are attenuated by the same mechanism, i.e. the Akhiezer one.

Furthermore, the fact that the attenuation of the acoustic waves, across the energy of the BP, does not differ from that predicted by the Akhiezer mechanism, indicates that there is a small or negligible interaction between the BP's modes and the acoustic one.

5.7 Comparison to literature data

In order to have a deeper understanding of the results obtained from the measurements of IXS on OTP, we proceed to compare these data with those present in literature for other two systems: glycerol and amorphous SiO_2.

These three glasses are characterized by a value of the fragility m that varies in a large range (glycerol has m=50, SiO_2 m=20 and OTP m=80) allowing to collect information representative of a wide class of systems. Moreover in all three systems the sound attenuation is dominated by the Akhiezer mechanism ($\Gamma_{th}/\Gamma_{Ak} \approx 0.03$, 0.01 and 10^{-7} respectively for OTP, glycerol and glassy SiO_2). Similarly to the case of OTP, we recover from the literature the value of the Grüneisen parameter estimated by the pressure or temperature dependence of the longitudinal mode, measured using US, BLS, and IXS techniques. In tables 5.1, 5.2, 5.3, and figure 5.16 we report the collected $\gamma_L(Q)$ values.

Looking at figure 5.16 we observe that in glycerol the energy dependence of $\gamma_L(Q)$, up to energies of 10^{-1} meV is similar to that observed in OTP. The Grüneisen parameter obtained from the longitudinal excitations probed by US and BLS techniques is almost the same. However, at high energy $\approx$ 7 meV (i.e. corresponding to Q=2 nm^{-1}) $\gamma_L(Q)$ increases. This increase of the Grüneisen parameter takes places at an energy corresponding to that of the BP (red arrow in the figure). This effect suggests that in glycerol there is an interaction of the excitations responsible for the BP with the longitudinal ones, possibly resulting in a hybridization of these excitations.

Finally we analyzed the behavior of the Grüneisen parameter in glassy SiO_2, a system that has been the object of intensive studies because of its peculiar behavior. Silica, in fact, is characterized by thermal activated relaxation processes that appear in the anomalous temperature dependence of the speed of sound v ($\partial v/\partial T < 0$ at T <70 K and $\partial v/\partial T > 0$ at T >70 K) as shown in Fig. (5.17). The effect of these relaxations is also visible in the value of the Grüneisen parameter that is quite different if evaluated varying the volume of the system by changing temperature or pressure of the glass (in the latter case γ is 20 times smaller compared to the value obtained varying the temperature) [4]. Such effect suggests that activated relaxations are not equally sensitive

[3]The value of $\tau_{th} \approx$0.25 ps is in agreement with that estimated in SiO_2 also using Eq. (5.8) [140].

[4]Here it has to be stressed that the relative changes of the volume $\Delta V/V$ of the glass obtained

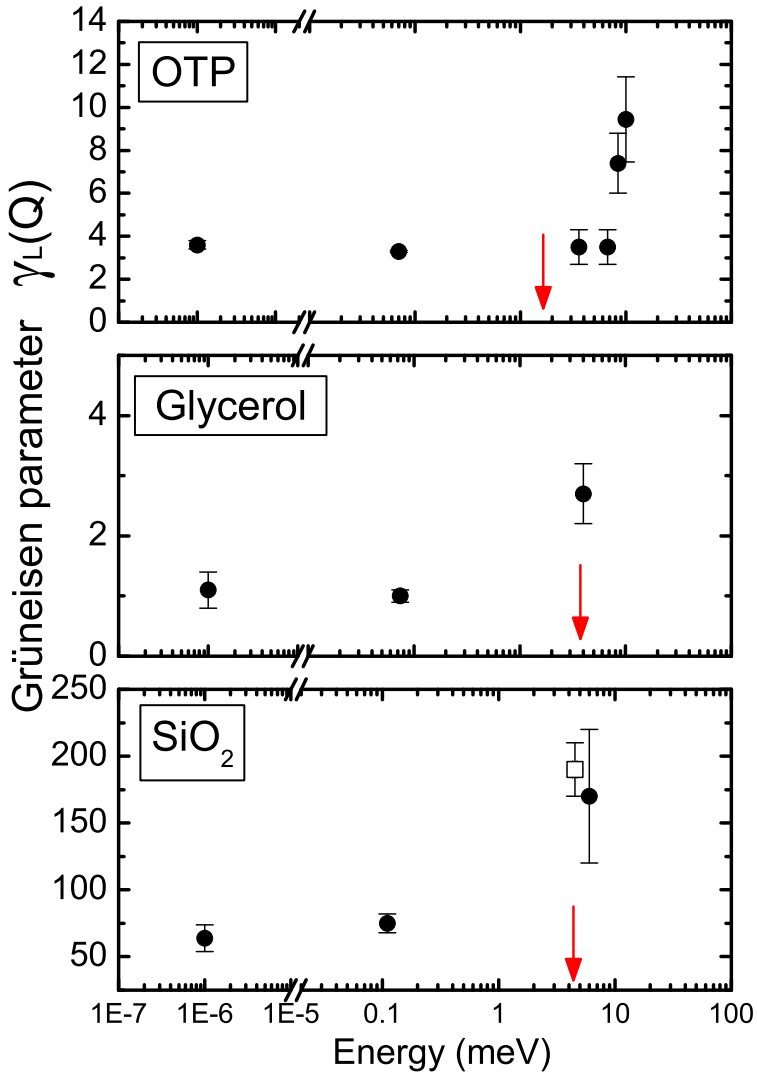

Figure 5.16: *Energy dependence of the Grüneisen parameter in OTP, glycerol and SiO_2 measured at temperature 0.95 T/T_g for glycerol and OTP and 0.25 T/T_g for silica. The points at $\approx 10^{-6}$ meV have been estimated using US data, at ≈ 0.1 meV using BLS data and in the meV region using IXS data. The arrows indicate the energy position of the BP. The open square in the SiO_2 panel indicates the Grüneisen parameter of the Boson Peak γ_{BP} (see text).*

to pressure and temperature. Here we analyzed the value of the Grüneisen parameter obtained varying the temperature of SiO_2.

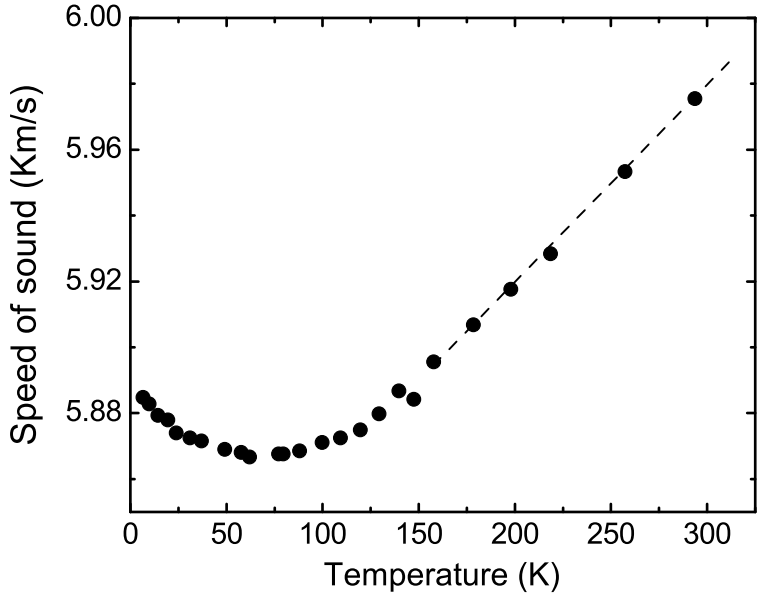

Figure 5.17: *Energy dependence of the longitudinal speed of sound in amorphous silica measured by R. Vacher at al. [126] using BLS.*

We evaluated $\gamma_L(Q)$ from measurements of the longitudinal excitations performed at T=275 K where the speed of sound of the glass shows a linear behavior. Studies available in the literature [140] predict that at such temperature the activated relaxation processes are strongly suppressed. Looking at the values of $\gamma_L(Q)$ for SiO_2 in figure 5.16 we recognize a behavior similar to that of glycerol.

In SiO_2 the values of $\gamma_L(Q_{BLS})$ and $\gamma_L(Q_{US})$ are almost the same, while at energies corresponding to that of the BP the Grüneisen parameter strongly increases. Moreover, thanks to the presence in the literature of measurements of the BP as function of temperature we could estimate the Grüneisen parameter for the modes embedded in the BP. Similarly to a single vibrational excitation it is possible to define the Grüneisen parameter also for the BP:

$$\gamma_{BP} = -\frac{\partial ln\Omega_{BP}}{\partial lnV}, \tag{5.9}$$

where Ω_{BP} is the frequency position of the BP (defined as the maximum of the RDOS).

In figure 5.16 we observe that the value of γ_{BP} is comparable to the Grüneisen parameter measured by IXS for an acoustic excitation almost at the same energy ≈6

varying temperature are much smaller than that obtained varying pressure. Applying of 1 GPa $\Delta V/V \approx 0.03$, varying the temperature of 100 K at 200 K $\Delta V/V \approx 0.001$.

Table 5.1: We report for the OTP the Grüneisen parameters $\gamma_L(Q_{US})$, $\gamma_L(Q_{BLS})$, $\gamma_L(Q_{IXS})$ and γ_{Th} with the corresponding errors $\Delta\gamma$ (see text); all data correspond to measurements at 0.95 T/T_g. We indicate also the exchanged wave-vector Q corresponding to the measured Grüneisen parameters. The [*] refers to our IXS measurements.

	γ	$\Delta\gamma$	Q (nm^{-1})	Ref.
$\gamma_L(Q_{US})$	3.6	0.2	$\approx 10^{-6}$	[141]
$\gamma_L(Q_{BLS})$	3.30	0.05	0.04	[142]
$\gamma_L(Q_{IXS})$	3.5	0.8	2	[*]
$\gamma_L(Q_{IXS})$	3.5	0.8	4	[*]
$\gamma_L(Q_{IXS})$	7.4	1.4	7	[*]
$\gamma_L(Q_{IXS})$	9.4	1.9	10	[*]
γ_{th}	1.02	0.8	–	[114, 143]

meV. Thus we conclude that in silica, approaching the energy of the BP, the vibrational excitations start to lose their purely acoustic nature being strongly hybridized with the modes of the BP.

Comparing for these three glasses the relative increase of $\gamma_L(Q)$ at energies close to that of the BP, we conclude that the coupling between the vibrational excitations responsible for the BP and the acoustic ones increases passing from OTP to glycerol and to SiO_2. Thus, it seems that the effect of the increase of $\gamma_L(Q)$ at energies typical of the BP might correlate with the increase of fragility of the glass.

Using the measurements that we have performed on the Boson Peak and on the acoustic modes in densified and hyperquenched glasses we can estimate γ_{BP} and $\gamma_L(Q_{BLS})$ also for these two systems. In this case $\gamma_{BP} \approx \gamma_L(Q_{BLS}) \approx 0.9$. In these glasses, both densified and hyperquenched, we have observed that the BP scales with the Debye energy of the glass and then with the acoustic modes measured by BLS spectroscopy (see chapter 3 and 4). Varying the density of these glasses the corresponding shift in energy of the BP is dominated by the effect of the acoustic modes. This implies that in these systems the analysis of the Grüneisen parameter does not allow discriminating between the modes responsible for the BP and the acoustic ones.

This clearly does not allow us to estimate a coupling mechanism -weak or strong- between the modes embedded in the BP and the acoustic ones for these network glasses. Maybe a detailed study of the acoustic absorption in the energy range of the BP would allow solving this issue.

Table 5.2: Grüneisen parameter in glycerol measured at $0.95T/T_g$.

	γ	$\Delta\gamma$	Q (nm^{-1})	Ref.
$\gamma_L(Q_{US})$	1.1	0.3	$\approx 10^{-6}$	[144]
$\gamma_L(Q_{BLS})$	1.0	0.1	0.037	[145]
$\gamma_L(Q_{IXS})$	2.7	0.2	2	[146]
γ_{th}	3	0.2	–	[147, 148]

Table 5.3: Grüneisen parameter in amorphous SiO_2 measured at $0.25T/T_g$.

	γ	$\Delta\gamma$	Q (nm^{-1})	Ref.
$\gamma_L(Q_{US})$	64	10	$\approx 10^{-6}$	[149]
$\gamma_L(Q_{BLS})$	75	7	0.03	[126]
$\gamma_L(Q_{IXS})$	170	50	1.6	[150]
γ_{th}	0.034	0.005	–	[152, 153]
γ_{BP}	190	20	–	[150, 151]

5.8 Conclusions

Measuring by IXS the dynamic structure factor of glassy OTP, we have characterized the high frequency dynamics of the glass, studying the influence of pressure (0.001-2.5 kbar) on the density fluctuations of the system at wave vectors between 2 and 10 nm^{-1}.

Here we briefly summarize the main results of our study.

- Concerning the effect of pressure on the $S(Q,\omega)$ of glassy OTP, we have observed that the width of the inelastic excitations Γ, and the non-ergodicity factor f_Q do not change varying the pressure. Conversely, the characteristic frequency Ω has a linear dependence on pressure allowing to obtain a unique value of the Grüneisen parameter in the all probed pressure range.

- Exploiting the connection between the measured non-ergodicity factor f_Q and the vibrational fragility (m_v) of the glass we have been able to evaluate the effect of pressure on m_v. No sensible variation of m_v has been observed increasing

pressure. The same effect of pressure has been reported in the literature concerning the kinetic fragility m [123]. These observations indicate that the increase of pressure does not alter the correlation between m_v and m valid at ambient pressure, at least within the (rather large) error bars of the present experiment.

- Analyzing the values of the Γ measured at different Q values, using BLS and IXS, we have observed that the same Akhiezer mechanism dominates the attenuation of the acoustic excitations from $Q \approx 0.04$ nm up to 4 nm^{-1}. The values of Γ can be properly described by a simple model of the Akhiezer mechanism using as characteristic phonon relaxation time $\tau_{th} \approx 0.25$ ps.

- In OTP the Grüneisen parameter keeps a constant value ≈ 3 from $Q = 10^{-6} nm^{-1}$ up to $Q = 4 nm^{-1}$, corresponding to energies across the BP's energy. This observation suggests that in OTP the measured acoustic excitations do not or weakly interact with those responsible for the BP. At energies higher than ≈ 7 meV the Grüneisen parameter shows a clear increase. This effect can be associated to different causes, e.g. hybridization of the sound wave with non-acoustic modes.

- Finally we studied the interaction between the acoustic vibrations and those embedded in the BP recovering from the literature the Grüneisen parameter in a wide range of energies also for glycerol and amorphous SiO_2. In glycerol, at the energy of the BP, the acoustic excitations do not have the same Grüneisen parameter as in the MHz frequency region. In silica, the acoustic waves in the nm^{-1} range are completely hybridized with the excitations embedded in the BP. The variation of the Grüneisen parameter across the BP for glycerol and SiO_2, together with the previously recalled results obtained for OTP, suggest a possible relation between the fragility of the glass and hybridization of the BP's excitations with the acoustic ones.

Conclusions and Perspectives

In this section we summarize the main results of the present Thesis work and we trace some perspectives for future experimental investigations on this topic.

The object of our studies was to investigate the vibrational dynamics of the glassy phase with a particular interest on the low frequency "anomaly" in the density of vibrational states: the Boson Peak. The research project presented in this manuscript has been developed in three years and it has involved the investigation of the vibrational dynamics of four classes of samples: hyperquenched glasses, the silicate glass $Na_2FeSi_3O_8$ both under pressure and densified, the fragile glass OTP under pressure. Our studies have been supported by various experimental techniques: Nuclear Inelastic Scattering, Inelastic X-ray Scattering, Brillouin Light Scattering, X-ray diffraction, Differential Calorimetric scans, Mössbauer spectroscopy and density measurements. Such variety of experimental methods allowed us to have information on the dynamics and on the structure of the probed glassy systems over a wide range of length and times scales, from the macroscopic limit to the mesoscopic region of nm and ps.

We can summarize the main conclusions of our study, for each specific class of samples, as follows:

- In the hyperquenched glass we have observed that the variation of the fictive temperature T_f of the glass corresponds to a modification of the DOS in the low energy region where the BP is present. Such change is entirely associated with the corresponding transformations of the macroscopic properties of the glass.

- From the study on the silicate glass $Na_2FeSi_3O_8$, we have observed that the effect of "densification" on the the maximum of the RDOS is associated with the change of the macroscopic properties of the glass. Moreover, in the $Na_2FeSi_3O_8$ glass we could clarify that a rearrangement of the local structure of the glass leads to a modification of the BP. Conversely, a change of the structure of the sample in the middle range length scale, as it appears from the modification of the first diffraction peak of the glass, does not have any strict correlation with the evolution of the low energy region of the DOS.

- From the study of glassy OTP, we have observed that the acoustic modes propagate at energies beyond that of the BP. These excitations, that are clearly not plane waves, are characterized by a value of the Grüneisen parameter γ that does not change passing from the MHz up to the THz frequency region. Moreover, a unique mechanism, the Akhiezer one, can describe the acoustic attenuation over this entire frequency range. These two observations suggests that in OTP there is

no or marginal interaction between the acoustic waves and the modes responsible for the BP. An analysis of literature data shows in addition that in both glycerol and SiO_2 there is a clear hybridization between the BP modes and the acoustic one, suggesting that the strength of the coupling might be simply related to the fragility of the glass.

These conclusions allowed us to have new insights on fundamental questions on the vibrational dynamics of glasses, for instance: What is the nature of the modes involved in the BP, how it depends on external parameters as pressure or thermal history. However, several and new questions naturally arise from our conclusions.

In order to answer some of them, a further experimental effort on the same class of samples is required. We could imagine to plan a new set of experiments to complete those presented on this Thesis work. For instance, in the case of hyperquenched glasses, a study with molecular dynamics simulations could be helpful to understand if the established correlation between T_f, DOS and macroscopic properties of the glass, can be predicted also within the energy landscape approach.

In fact, according to the experience of this Thesis work, in order to plan decisive experimental studies on this subject, one has to elaborate a new strategy of investigation. The complexity of the subject and the number of theoretical models proposed to describe the BP demand for a closer integration between theoretical and experimental studies. In particular the final task of the experimental studies should be to perform a more accurate analysis of the BP on a quantitative basis.

In this perspective it would be helpful to use, at the same time, on the same sample, different techniques able to probe both the structure and the dynamics of the system. Moreover, one would more easily trace general conclusions on the investigated phenomenology using samples for which the physical properties, even the most peculiar ones, are well characterized.

A possible experiment, decisive for the study of the BP, could be realized on a system in which one can easily control its DOS by an external parameter. Monitoring, at the same time, the evolution of the DOS and that of the dynamic structure factor $S(Q, \omega)$ in the range of energy of the BP, one could clarify the role of the possible coupling between the modes of the BP and the acoustic one.

Finally, it would be an interesting approach the study of the BP from another point of view: looking at the crystalline phase. It should be interesting to investigate the dynamics and the microscopic structure of a system when it experiences the transition between the glass to the crystalline phase. In fact, a description of the BP starting from the analysis of the corresponding crystalline phase could be helpful for an explanation of this vibrational "anomaly" which is consistent with the knowledge of the dynamics at the microscopic scale.

Conclusions

Dans cette section on cherchera de faire un résume des résultats de notre étude de thèse et nous tracerons les prospectives pour les futures études expérimentales dans ce domaine.

L'objet de notre étudie a été l'investigation de la dynamique vibrationelle de la phase vitreuse avec un intérêt particulier pour l'anomalie de basse fréquence dans la densité d'états vibrationelle: le "Boson Peak". Le projet de recherché présenté dans ce manuscrit a été développé in trios années avec l'etude de la dynamique vibrationelle de quatre classes de échantillons: verres "hyperquenched", verres silicates $Na_2FeSi_3O_8$ sois sous pression sois densifiés, et un verre d'orto-therphenil sous pression. Ntres études ont été supportées de différentes techniques expérimentales: Nuclear Inelastic Scattering, Inelastic X-ray Scattering, Brillouin Light Scattering, X-ray diffraction, Differential Calorimetric scans, Mössbauer spectroscopy et mesures de densité. Cette variété de méthodes expérimentales ont permis d'avoir informations sur la dynamique et sur la structure des systèmes vitreux a différents echelles de longheurs et temps, de la limite macroscopique jusqu a la région mesoscopique de nm et ps.

Nous pouvons faire un résumé des conclusions principales de notre étude, pour chaque classe de échantillon, dans la manière suivant:

- Dans le verre "hyperquenched" nous avons observé que la variation de température fictive T_f du verre corresponde a une modification de la DOS dans la région de basse énergie ou est présente le BP. Ce changement est directement associé avec la transformation de les propriétés macroscopiques du verre.

- Avec l'étude du verre silicate $Na_2FeSi_3O_8$, nous avons observé que l'affect de densification sur le maximum de la RDOS est associé avec un changement des propriétés macroscopiques du verre. Dans le $Na_2FeSi_3O_8$ le réarrangèrent de la structure locale du verre conduit a la modification du BP. Contrairement, a changement de la structure de l'échantillon a une echelle de longheurs du nanometer, qui modifie le premier pic de diffraction du verre, n'as aucune corrélation avec l'évolution de la DOS a basse énergie

- De l'étude du verre OTP, nous avons observé que un mode acoustique propagate a énergies plus élevés du BP. Ces excitations, que ne sont pas des ondes planes, sont caractérisés par un valeur du paramètre de Grüneisen γ que ne change pas en passant de MHz jusqu'à a la région de fréquence du THz. En plus, un seul mécanisme, celui d'Akhiezer, peut décrire l'atténuation acoustique sur dans cette region de fréquences. Ces deux observations suggèrent que dans l'OTP il n'y a

pas interaction entre le modes acoustiques et le modes responsables du BP. Une analyse des donnes présente en littérature montre en plus que dans le glycerol et le SiO_2 il y a une hybridization entre le mode du BP et celles acoustiques, ce résultat nous suggère que l'intensité de l'interaction peut être simplement associé a la fragilité du verre.

Ces conclusions permet d'avoir des nouveaux point de vu sur des questions fondamentales de la dynamique vibrationelle des verres, pour exemple: Quelle est la nature des modes du BP, comme ils dépendent par un paramètre extérieure. Pourtant, beaucoup et nouvelles questions naturellement sortent par notre conclusions.

Au fin de répondre a ces questions, il faut an effort expérimental plus profond sur la même classe d' échantillons. Nous pouvons penser de planifier des nouvelles expériences au fin de compléter celles présente dans ce travaille de thèse. Pour exemple, dans le cas des verres "hyperquenched", un étude avec simulations numérique de la dynamique pourra être utile pour comprendre si la corrélation entre T_f, DOS, et propriétés macroscopiques du verre peut être prévu aussi en utilisant la méthode de "l'energy landscape".

En fait, a partir de ce travaille de thèse, au fin d'avoir expériences décisives dans ce domaine, il faut élaborer une nouvelle stratégie d'investigation. La complexité du sujet et le nombre des modelés proposés pour décrire le BP ont besoin d'une intégration plus proche entre études théoriques et expérimentales. En particulier le but final des expériences expérimentales dois être d'avoir une plus fin analyse du BP sur de bases quantitatives.

Dans ce perspective est utile avoir, au même temps, sur le même échantillon, différents techniques qui peuvent étudier la structure et la dynamique du système. En plus, on pourrait plus facilement avoir des conclusions générales sur la phénoménologie étudié en utilisant des échantillons dans le quel aussi le propriétés plus spécifiques au système sont bien caractérisé.

Une expérience décisive pour l'étude du BP peut être réalisé sur un système dans le quel on peut facilement contrler la DOS avec en paramètre extérieur. En contrlent, au même temps, l'évolution de la DOS et celle du facteur de structure dynamique $S(Q,\omega)$ dans la region d'énergie du BP, on pourrait clarifier le rle d'un possible connexion entre le mode du BP et celles acoustiques.

Enfin, serait intéressant affronter l'étude du BP avec en autre point de vu: en regardant a la phase cristalline. En fait, une description du BP en partant de l'analyse de la phase cristalline correspondent pourrait être utile pour une explication de cette anomalie vibrationelle consistent avec la connaissance de la dynamique du cristal.

Appendix A

Elasticity of a solid

Under the action of applied forces, solid bodies exhibit a behavior that on the macroscopic scale can be considered elastic: the system returns to its initial state after the external force is removed. The characterization of the elasticity in a solid can be regarded as a first look at the dynamical behavior of the system on a macroscopic length scale.

A natural way to define the elasticity of a solid is to monitor its reaction to an applied deformation. When a body is deformed the distance between its points changes. Considering a particular point we can define its position vector before the deformation as $\vec{r}$, and after the deformation as $\vec{r}'$ (with components x_i'). The displacement of the point because of deformation is given by $\vec{r}' - \vec{r}$, which we denote as u with components: $u_i = x_i' - x_i$.

If we consider now two points very close together and the radius vector joining them before the deformation has components dx_i, after the deformation of the solid, the new radius vector will be $dx_i' = dx_i + du_i$, where du is the displacement of these two points. The distance between the points will change from $dl = (dx_1^2 + dx_2^2 + dx_3^2)^{\frac{1}{2}}$ to $dl^{2'} = (dx_1'^2 + dx_2'^2 + dx_3'^2)^{\frac{1}{2}}$; using $du_i = (\frac{\partial u_i}{\partial x_k})dx_k$ we can write [77]:

$$dl'^2 = dl^2 + 2\frac{\partial u_i}{\partial x_k}dx_i dx_k + \frac{\partial u_i}{\partial x_k}\frac{\partial u_i}{\partial x_l}dx_k dx_l. \tag{A.1}$$

Eq. (A.1) can be also expressed in the form:

$$dl'^2 = dl^2 + 2u_{ik}\ dx_i dx_k, \tag{A.2}$$

introducing the strain tensor u_{ik}:

$$u_{ik} = \frac{1}{2}\left(\frac{\partial u_i}{\partial x_k} + \frac{\partial u_k}{\partial x_i} + \frac{\partial u_l}{\partial x_i}\frac{\partial u_l}{\partial x_k}\right), \tag{A.3}$$

u_{ik} gives a measure of the change in length of an element of the body deformed by du_i (here i is the index of the component of the direction of deformation). When a deformation occurs the arrangement of the atoms is altered and the body ceases to be in its original state of equilibrium. Therefore, forces arise which tend to return the body to equilibrium. These internal forces are called internal stresses. The total force

acting on a part of the body along the ith direction F_{Ti}, as reaction to a deformation, can be written as the volume integral: $F_{Ti} = \int F_i dV$, where the F_i is the force per unit volume. F_{Ti} is regarded as the force exerted on a given portion of the body by the portion surrounding it and can be written as the sum of forces acting on all surfaces elements df:

$$\int F_i dV = \int \frac{\partial \sigma_{ik}}{\partial x_k} dV = \oint \sigma_{ik} df_k, \tag{A.4}$$

with

$$F_i = \partial \sigma_{ik} / \partial x_k. \tag{A.5}$$

Here we have defined the stress tensor σ_{ik} as the i^{th} component of the force on a unit area perpendicular to the x_k axis. Using the strain tensor u_{ik} and the stress tensor σ_{ik} we can fully characterize the elasticity of a solid introducing the elastic constants C_{ijkl}. The elastic behavior of a solid (the system returns to its initial state after external forces are removed) can be expressed formally by the proportionality between the stress and the strain tensor:

$$\sigma_{ij} = C_{ijkl}\ u_{kl}. \tag{A.6}$$

The fourth rank tensor C_{ijkl} is called elastic constant and because of the symmetrical properties of the strain and the stress tensor it has 36 independent components. Nevertheless it can be shown that for an isotropic medium the number of independent elastic constants is reduced to two components: ξ and μ [77]. A possible way to measure ξ and μ is to observe the reaction of the solid to an induced deformation.

An isotropic solid in fact can support two types of elastic waves: longitudinal and transverse waves. The longitudinal waves are characterized by a displacement of the medium parallel to the direction of propagation of the wave i.e. a polarization parallel to its wave vector $\vec{q}$ ($|q| = 2\pi/\lambda$ where λ is the wavelength of the wave). Conversely in transverse waves the medium is displaced perpendicularly to the wave vector. The existence of elastic waves in solids can be derived starting from the fundamental law of dynamics $\vec{F} = m\vec{a}$. The force per unit volume of a stressed material $F_i = \partial \sigma_{ij} / \partial x_j$, gives rise to an acceleration $\partial^2 u_i / \partial t^2$ of the unit volume along the i^{th} axis that can be written as:

$$\rho \frac{\partial^2 u_i}{\partial t^2} = \frac{\partial \sigma_{ij}}{\partial x_j}. \tag{A.7}$$

Using of Eq.(A.6) the equation of the motion A.7 becomes:

$$\rho \frac{\partial^2 u_i}{\partial t^2} = C_{ijkl} \frac{\partial^2 u_l}{\partial x_j \partial x_k}. \tag{A.8}$$

A general solution of this equation for an isotropic solid has the form: $u_i = u_0^{i\vec{q}(x_i - vt)}$, that represents a propagating wave. To calculate the phase velocity v and the wave vector $\vec{q}$ (i.e. the displacement direction) we insert $u_i = u_0^{i\vec{q}(x_i - vt)}$ into Eq.(A.8) obtaining:

$$\rho v^2 u_i = C_{ijkl} q_j q_k u_l. \tag{A.9}$$

Alternatively Eq. (A.9) can be expressed as:

$$\Gamma_{il} u_l = \rho v^2 u_i, \tag{A.10}$$

introducing the second rank tensor Γ_{il}:

$$\Gamma_{il} = C_{ijkl} q_j q_k. \tag{A.11}$$

The eigenvalues and the eigenvectors of the tensor Γ_{il} give the velocities and the polarizations of the plane waves that propagate along the direction $\vec{q}$. In an isotropic medium the Eq. $(A.11)$ can be replaced by:

$$\Gamma_{il} = (\xi + \mu)\ q_i q_l + \mu\ q_i q_l \delta_{il}. \tag{A.12}$$

This equation has two solutions [77]:

- When $\vec{q} \perp \vec{u}$, which corresponds to a shear wave propagating with velocity $v_T = \sqrt{\mu/\rho}$.
- When $\vec{q} // \vec{u}$, which corresponds to a longitudinal wave propagating with a velocity $v_L = \sqrt{(4/3\mu + \xi/)\rho}$.

Thus, an isotropic solid supports the propagation of longitudinal or transverse plane waves in which the velocities: v_L and v_T, do not depend on the propagation directions. Moreover, the solid has two independent elastic constants ξ and μ, that can be directly evaluated by measurements of density and speed of sound ($\mu = \rho v_T^2$ and $\xi = \rho v_L^2$-$4/3\rho v_T^2$).

Bibliography

[1] R.C. Zeller and R. O. Pohl, *Phys. Rev. B* **4**, 2029 (1971).

[2] N. W. Ashcroft N. D. Mermin, "*Solid State Physics*", Harcourt College Publishers (1976).

[3] W. A. Philips, "*Amorphous solids Low-Temperature Properties*", Springer-Verlag Berlin Heidelberg New York (1981).

[4] R. J. Palmer and D.C. Stein, "*Relaxation in Complex Systems*", K. Ngai and G.B. Wright (1985).

[5] S. S. Chang and A.B. Bestul, *J. Chem. Phys.* **56**, 503 (1972).

[6] C. A. Angell, K. L. Ngai, G. B. McKenna, P. F. McMillan, S. W. Martin, *J. Appl. Phys.* **88**, 3113-3157 (2000).

[7] G. Adam and J.H. Gibbs, *J. Chem. Phys.* **43**, 139 (1965).

[8] I. Prigogine and R. Defay, "*Chemical Thermodynamics*" edited by Longman Greens (1985).

[9] W. Kauzmann, *Chem. Rev.* **43**, 219 (1948).

[10] T. G. Fox and P.J. Flory, *J. App. Phys.* **21**, 581 (1950).

[11] C. A. Angell and W. Sichina, *Ann. N.Y. Acad. Sci.* **279** 53 (1976).

[12] H. Vogel, *Phys. Z.* **22**, 645 (1921).

[13] G. Tamman and W. Hesse, *Z. Anorg. Allg. Chem.* **156**, 245 (1926).

[14] G. S. Fulcher, *J. Am. Ceram. Soc.* **8**, 339 (1925).

[15] C. A. Angell, *J. Non-Cryst. Solids* **131-133**, 13 (1991).

[16] R. Böhmer and C. A. Angell, *Phys. Rev. B* **45**, 10091 (1992).

[17] C. A. Angell, *J. of Non-Cryst. Solids* **73**, 1 (1985).

[18] D. Huang and G.B. Mckenna, *J. Chem. Phys.* **114**, 5621 (2001). C. A. Angell, *J. of Non-Cryst. Solids* 73, 1 (1985)

[19] T.H.K. Barron J.G. Collins and G.K. White, *Adv. Phys.* **29**, 609-730 (1980).

[20] P. Debye, *Ann. Phys.* **39** 689 (1912).

[21] M. Born and T. von Karman, *Physik. Z.* **13**, 297 (1912).

[22] S. Takeno and M. Goda, *Prog. Theor. Phys.* **45**, 331 (1971).

[23] T. Scopigno, J.-B. Suck, R. Angelini, F. Albergamo, G. Ruocco, *Phys. Rev. Lett.*, **96**, 135501 (2006).

[24] A. Akhieser, *J. Theor. Phys.* **1**, 277 (1939).

[25] J.W.S. Rayleigh, "*The Theory of Sound*", MacMillan and Company Ltd.,London, (1894).

[26] W. A. Philips, *J. Low Temp. Phys.* **7**,351 (1972).

[27] T. Tohei, A. Kuwabara, F. Oba, and I. Tanaka *Phys. Rev. B* **73**, 064304 (2006).

[28] S. N. Taraskin, Y. L. Loh, G. Natarajan, and S. R. Elliott, *Phys. Rev. Lett.* **86**, 1255-1258 (2001).

[29] W. Schirmacher, *Europhysics. Lett.* **73**, 892 (2006).

[30] M. I. Klinger, *J. Non-Cryst. Solids* **293-295**, 345 (2001).

[31] V. L Gurevich, D. A. Parshin, and H. R. Schober, Phys. Rev. B **71**, 014209 (2005).

[32] V. N. Novikov and A. P. Sokolov,*Solid State Commun.* **77**, 243 (1991).

[33] A. P. Sokolov, A. Kisliuk, M. Soltwisch, and D. Quitmann, *Phys. Rev. Lett.* **69**, 1540 (1992).

[34] T. S. Grigera, V. Martin-Mayor, G. Parisi, and P. Verrocchio, *Nature* **422**, 289 (2003).

[35] G. Parisi, *J. Phys.: Condens. Matter* **15**, S765 (2003).

[36] R. L. Mössbauer, *Z. Phys.* **151**, 124 (1958).

[37] W. Potzel, G. M. Kalvius, J. Gal, in "*Handbook on the Physics and Chemistry of rare Earths*", Vol 17, K.A. Gschneider, Jr., L. Eyring (Eds.),Elsevier, 1993.

[38] G. Schatz, A. Weidinger, "*Nukleare Festkörperphysik*", Teubner, 1997, p. 44.

[39] D. Barb, *Grundlagen und Anwendungen der Mössbauerspektroskopie*, Akademie-Verlag, Berlin, 1980, p.11

[40] F. J. van Steenwijk, PhD Thesis, University of Leiden, (1976).

[41] P. Gütlich, R. Link, A. Trautwein *Mössbauer Spectroscopy and Transition Metal Chemistry*, Springer-Verlag, (1978) p. 13.

[42] J. P. Sanchez, J.M. Friedt, G. K. Shenoy, A. Percherton, J. C. Achard, *J. Phys. C: Solid State Phys.* **9**, 2207 (1976).

[43] G. V. Smirnov, *Hyperfine Interact.* **97/98**, 551 (1996).

[44] S. W. Lovesey, *Theory of neutron scattering from condensed matter. Vol. 1 Nuclear scattering* published by Oxford University Press (1986)

[45] M. Seto, Y. Yoda, S. Kikuta, X.W. Zhang, M. Ando, *Phys. Rev. Lett.* **74**, 3828 (1995).

[46] V.G. Kohn and A.I. Chumakov, *Hyperfine Interactions* **125**, 205 (2000).

[47] W. Heitler, *The quantum theory of radiation* Oxford University Press, New York (1944).

[48] L.V. Hove, *Phys. Rev.* **95**, 249 (1954).

[49] K.S. Singwi and A. Sjölander *Phys. Rev.* **120**, 1093 (1960).

[50] A. I. Chumakov, R. Rüffer, *Hyp. Int.* **113**, 59 (1998).

[51] E. Burkel, "*Inelastic Scattering of X-Rays with Very High Energy Resolution*", Springer-Verlag, (1991).

[52] E. Burkel, *Rep. Prog. Phys.*, **63**, 171 (2000)

[53] P.A.M. Dirac, "*The principles of quantum mechanics*", Oxford University Press, Oxford (1958).

[54] E.R. Pike and S. Sarkar, "*The quantum theory of radiation*", Oxford University Press, Oxford (1995).

[55] J.J. Sakurai, "*Modern Quantum Mechanics. Revised Edition*", Addison-Wesley Publishing Company (1994).

[56] W. Marshall and S. W. Lovesey, "*Theory of Thermal Neutron Scattering*", Clarendon Press, Oxford (1971).

[57] S. Takeno and M. Gôda, *Prog. Theor. Phys.*, **45**, 331 (1971).

[58] S. Takeno and M. Gôda, *Prog. Theor. Phys.*, **47**, 790 (1972).

[59] M. Gôda, *J. Phys. C*, **6**, 3047 (1973).

[60] M. Krisch, *J. Raman Spectrosc.*, **34**, 628 (2003).

[61] R. Verbeni, F. Sette, M. Krisch, U. Bergmann, B. Gorges, C. Halcoussis, K. Martel, C. Masciovecchio, J.F. Ribois, G. Ruocco, H. Sinn, *J. Synchrotron Radiat.*, **3**, 62 (1996).

[62] C. Masciovecchio, U. Bergmann, M. Krisch, G. Ruocco, F. Sette, R. Verbeni, *Nucl. Instrum. Methods. B*, **111**, 181 (1996).

[63] C. Masciovecchio, U. Bergmann, M. Krisch, G. Ruocco, F. Sette, R. Verbeni, *Nucl. Instrum. Methods. B*, **117**, 339 (1996).

[64] A. Bergamini, G. Cavagnero and G. Mana, *J. Appl. Phys.*, **82**, 5396 (1997).

[65] F.H. Stillinger, *Science* **267**, 1935 (1995).

[66] L. Angelani, R. Di Leonatso, G. Ruocco, A. Scala, F. Sciortino, *Phys. Rev. Lett.* **85**, 5356 (2000).

[67] C. A. Angell *et al.*, *J. Phys.: Condens. Matter* **15**, S1051 (2003).

[68] C. A. Angell, J. Phys.: Condens. Matter **16**, S5153 (2004).

[69] T. S. Grigera, V. Martin-Mayor, G. Parisi, and P. Verrocchio, *Nature* **422**, 289 (2003).

[70] G. Parisi, *J. Phys.: Condens. Matter* **15**, S765 (2003).

[71] C. A. Angell, K. L. Ngai, G. B. McKenna, P. F. McMillan, S. W. Martin, *J. Appl. Phys.* **88**, 3113 (2000).

[72] W. Gotze and L. Sjogren, *Rep. Prog. Phys.* **55** 241 (1992).

[73] P. Bordat, F. Affouard, M. Descamps, and K. L. Ngai, *Phys. Rev. Lett.* **93**, 105502 (2004).

[74] T. Scopigno, G. Ruocco, F. Sette, and G. Monaco, *Science* **302**, 849 (2003).

[75] R. Böhmer, K. L. Ngai, C. A. Angell, and D. J. Plazek, J. Chem. Phys. **99**, 4201 (1993).

[76] Y. Z. Yue, R. von der Ohe, and S. L. Jensen, J. Chem. Phys. **120**, 8053 (2004).

[77] A.I. Bletzer, "*Acoustic of Solids*", Springer-Verlag, Berlin (1988).

[78] C.V. Raman, K.S. Krishnan, *Nature*, **121**, 501 (1928).

[79] J.D. Jackson, "*Classical electrodynamics*" John Wiley, (1999).

[80] B.J. Berne, R. Pecora "*Dynamic light scattering with applications to chemistry. biology, and physics*" John Wiley, (1976).

[81] A. Authier "*Dynamical theory of X-ray diffraction*" Oxford University Press, Oxford (2005).

[82] Y. Ding, T. Nanba, and Y. Miura, *Phys. Rev. B* **58**, 14279-14287 (1998).

[83] M. Mezouar *et al.*, *J, Synchrotron Rad.* **12**, 659 (2005).

[84] L. A. Johnson *et al.*, *J. Non-Cryst. Solids* **246**, 104 (1999).

[85] M. D. Dyar, *Am. Mineral* **70**, 304 (1985).

[86] H. J. Lipkin, *Annals of Physics* **9**, 332 (1960).

[87] A. I. Chumakov, I. Sergueev, U. van Brck, W. Schirmacher, T. Asthalter, R. Rffer, O. Leupold, and W. Petry *Phys. Rev. Lett.* **92**, 245508 (2004).

[88] W. Jones and N.H. Marsh "*Theoretical Solid State Physiscs*" Vol.1, Dover New York (1985).

[89] M. Y. Hu *et al.*, *Phys. Rev. B* **67**, 94304 (2003).

[90] A. I. Chumakov, I. Sergueev, U. van Brck, W. Schirmacher, T. Asthalter, R. Rffer, O. Leupold, and W. Petry, *Phys. Rev. Lett.* **92**, 245508 (2004).

[91] J. D. Boyer, J. C. Lasjaunias, R. A. Fisher, and N. E. Phillips, *J. Non-Cryst. Solids* **55**, 413 (1983).

[92] R. Geilenkeuser, Th. Porschberg, M. Jäckel, A. Gladun, *Physica B* **263-264**, 276 (1999).

[93] B. Frick, C. Alba-Simionesco, *Appl. Phys. A* **74**, S549 (2002).

[94] V. L Gurevich, D. A. Parshin, and H. R. Schober, *Phys. Rev. B* **71**, 014209 (2005).

[95] T. Arai, H. Kataura, H. Yasouka, and S. Onari, *J. Non-Cryst. Solids* **77&78**, 1149 (1985).

[96] S. Sugai and A. Onodera, *Phys. Rev. Lett.* **77**, 4210 (1996).

[97] R. J. Hemley, C. Meade, and H. K. Mao, *Phys. Rev. Lett.* **79**, 1420 (1997).

[98] Y. Inamura, M. Arai, N. Kitamura, S. M. Bennington, and A. C. Hannon, *Physica B* **241-243**, 903 (1998).

[99] Y. Inamura, M. Arai, M. Nakamura, T. Otomo, N. Kitamura, S. M. Bennington, A. C. Hannon, and U. Buchenau, *J. Non-Crystal. Solids* **293-295**, 389 (2001).

[100] H.K. Mao, P.M. Bell, J.W. Shaner and D.J. Steinberg, *J. App. Phys.*,**49**, 3276 (1978).

[101] A. Meyer, J. Horbach, W. Kob, F. Kargl, H. Schober, *Phys. Rev. Lett.*,**93**, 027801 (2004).

[102] M. Przybylski1, J. Korecki1 and U. Gradmann *Hyper. Int.*,**57**, 2053 (1990).

[103] G. J. Long, "*Mössbauer Spectroscopy Applied to inorganic Chemistry*",**Vol. 1**, Plenum Press N.Y., (1984).

[104] V. N. Novikov and A. P. Sokolov, Solid State Commun. **77**, 243 (1991).

[105] A. P. Sokolov, A. Kisliuk, M. Soltwisch, and D. Quitmann, Phys. Rev. Lett. **69**, 1540 (1992).

[106] B. Ruffle', M. Foret, E. Courtens, R. Vacher, and G. Monaco, *Phys. Rev. Lett.* **90**, 095502 (2003).

[107] M. Foret, R. Vacher, E. Courtens, and G. Monaco, *Phys. Rev. B* **66**, 024204 (2002).

[108] P. Benassi, M. Krisch, C. Masciovecchio, V. Mazzacurati, G. Monaco, G. Ruocco, F. Sette, and R. Verbeni, *Phys. Rev. Lett.* **77**, 3835-3838 (1996).

[109] B. Guillot and Y. Guissani, *Phys. Rev. Lett.* **78**, 2401-2404 (1997).

[110] O. Pilla, A. Cunsolo, A. Fontana, C. Masciovecchio, G. Monaco, M. Montagna, G. Ruocco, T. Scopigno, and F. Sette, *Phys. Rev. Lett.* **85**, 2136-2139 (2000).

[111] T. Scopigno, J.-B. Suck, R. Angelini, F. Albergamo, and G. Ruocco, *Phys. Rev. Lett.* **96**, 135501 (2006).

[112] T.H.K. Barron, J.G. Collins, G.K. White *Adv. Phys.* **4**, 609 (1980).

[113] S. Mossa, R. Di Leonardo, G. Ruocco, and M. Sampoli *Phys. Rev. E* **62**, 612-630 (2000).

[114] M. Naoki and S. Koeda, *J. Phys. Chem.* **93**, 948 (1989).

[115] G.P. Johary, M. Goldstein, *J. Phys. C.* **74**, 2034 (1970).

[116] M. Kuchierman, J.W. Lane, D.R. Uhlmann, *J. Chem. Phys.* **59**, 3639 (1973).

[117] G. D'Arrigo, *J. Chem. Phys.* **61**, 63 (1975).

[118] T. Scopigno, G. Ruocco, F. Sette, and G. Monaco, *Science* **302**, 849 (2003).

[119] G. Monaco, C. Masciovecchio, G. Ruocco, and F. Sette *Phys. Rev. Lett.* **80**, 2161-2164 (1998).

[120] G. Ruocco, F. Sette, R. Di Leonardo, D. Fioretto, M. Krisch, M. Lorenzen, C. Masciovecchio, G. Monaco, F. Pignon, and T. Scopigno *Phys. Rev. Lett.* **83**, 5583-5586 (1999).

[121] C. Masciovecchio, G. Baldi, S. Caponi, L. Comez, S. Di Fonzo, D. Fioretto, A. Fontana, A. Gessini, S. C. Santucci, F. Sette, G. Viliani, P. Vilmercati, and G. Ruocco *Phys. Rev. Lett.* **97**, 035501 (2006).

[122] J. Fabian and P. B. Allen *Phys. Rev. Lett.* **82**, 1478-1481 (1999)

[123] K. U. Schug, H. E. King, R. Böhmer, *J. Chem. Phys.* **109**, 1472 (1998).

[124] F.J. Bermejo, G.J. Cuello, E. Courtens, R. Vacher and M.A. Ramos, *Phys. Rev. Lett.*, **81**, 3801 (1998).

[125] A. Tölle, *Rep. Prog. Phys*, **64**, 1473 (2001).

[126] R. Vacher, J. Pelous *Phys. Rev. B*, **14**, 823 (1975).

[127] A. Tölle, H. Schober, J. Wuttke, O. G. Randl, and F. Fujara, *Phys. Rev. Lett.*, **80**, 2374-2377 (1998).

[128] A. Tölle, *Rep. Prog. Phys.*, **64**, 1473 (2001).

[129] G. Monaco, D. Fioretto, L. Comez, and G. Ruocco, *Phys. Rev. E*, **63**, 061502 (2001).

[130] S. Mossa, G. Ruocco, and M. Sampoli, *Phys. Rev. E*, **64**, 021511 (2001).

[131] C. Dreyfus, A. Aouadi, J. Gapinski, M. Matos-Lopes, W. Steffen, A. Patkowski, and R. M. Pick, *Phys. Rev. E* **68**, 011204 (2003).

[132] W. Gotze and L Sjogren, *Rep. Prog. Phys.* **55** 241 (1992).

[133] U. Balucani, M. Zoppi, *Dynamics of the liquid state*, Oxford University Press (1994).

[134] R. Piccirilli, T. Litovitz, *J. Acoust. Soc. Am.* **29**, 1009 (1957).

[135] L. Comez, D. Fioretto, F. Scarponi, G. Monaco, *J. Chem. Phys.* **119**, 6032 (2003).

[136] C. Masciovecchio, G. Monaco, G. Ruocco, F. Sette, A. Cunsolo, M. Krisch, A. Mermet, M. Soltwisch, and R. Verbeni *Phys. Rev. Lett.* **80**, 544 (1998).

[137] J. Wuttke, W. Petry, G. Coddens, and F. Fujara, *Phys. Rev. E* **52**, 4026 (1995).

[138] R. Vacher and J. Pelous, *Phys. Rev. B* **14**, 823 (1975).

[139] A. Wischnewski, U. Buchenau, A. J. Dianoux, W. A. Kamitakahara, and J. L. Zarestky, *Phys. Rev. B* **57**, 2663 (1998).

[140] E. Rat, M. Foret, G. Massiera, R. Vialla, M. Arai, R. Vacher, and E. Courtens, *Phys. Rev. B* **72**, 214204 (2005).

[141] G. Monaco, B. Balschun, D. Fioretto, G. Ruocco, and M. Soltwisch (unpublished)

[142] G. Monaco, D. Fioretto, L. Comez, and G. Ruocco, *Phys. Rev. E* **63**, 061502 (2001).

[143] S.S. Chang and A.B. Bestul, *J. Chem. Phys.* textbf56, 503 (1972).

[144] K.F. Herzfeld and T.A. Litovitz, "*Absorption and Dispersion of ultrasonic waves*" Academic Press N.Y., (1959).

[145] L. Comez, D. Fioretto, F. Scarponi, G. Monaco, *J. Chem. Phys.***119**, 6032 (2003).

[146] C. Masciovecchio, G. Monaco, G. Ruocco, F. Sette, A. Cunsolo, M. Krisch, A. Mermet, M. Soltwisch, and R. Verbeni, *Phys. Rev. Lett.* **80**, 544-547 (1998).

[147] M. Rajeswari and A. K. Raychaudhuri, *Phys. Rev. B* **47**, 3036 (1993).

[148] F. Scarponi, L. Comez, D. Fioretto, and L. Palmieri, *Phys. Rev. B* 70, 054203 (2004).

[149] R. Vacher, E. Courtens, and M. Foret, *Phys. Rev. B* **72**, 214205 (2005).

[150] C. Masciovecchio, V. Mazzacurati, G. Monaco, G. Ruocco, T. Scopigno, F. Sette, P. Benassi, A. Cunsolo, A. Fontana, M. Krisch, A. Mermet, M. Montagna, F. Rossi, M. Sampoli, G. Signorelli, R. Verbeni, *Phil. Mag. B* **79**, 2013 (1999).

[151] A. Wischnewski, U. Buchenau, A. J. Dianoux, W. A. Kamitakahara, and J. L. Zarestky, *Phys. Rev. B* **57**, 2663-2666 (1998).

[152] G.K. White, *J. Phys. D.: App. Phys.* **6**, 2070 (1973).

[153] R.C. Lord and J.C. Morrow, *J. Chem. Phys.* **26**, 230 (1957).

$\sim \cdot \sim \cdot \sim$

Résumé

Le travail actuel de thèse est consacrè l'étude de la dynamique vibrationnelle du verre et en particulier à la recherche sur l'anomalie de basse fréquence: le " Boson Peak " (BP). Dans le premier chapitre, les aspects généraux de l'état vitreux sont présentés. Ici nous discutons comment le comportement thermodynamique anormal des verres peut tre associé à la présence du Boson Peak dans la densité vibrationnelle (DOS) du verre. Dans le deuxième chapitre, nous discutons les techniques spectroscopiques principales utilisées dans cette étude: Diffusion non élastique nucleaire et la diffusion non élastique de rayons X. Dans le troisième chapitre, nous présentons l'étude du verre " hyperquenched ". Les effets de l'histoire thermique sur les propriétés dynamique et structurales des verres sont étudies. Le quatrième chapitre est consacrée à l'étude de l'effet de la pression et de la densité sur le DOS d'un verre. Les changements de la DOS sont corrélées une fois de plus avec les changements macroscopiques à moins qu'une transformation structurale ait lieu. En conclusion, nous présentons une étude sur la dynamique à haute fréquence (dans la région de fréquence de THz) d'ortho-terphenyl vitreux, et l'effet de la pression sur cette dynamique est discute. En comparant nos résultats à d'autres données disponibles dans la littérature, il à été possible de déduire quelques conclusions sur la nature des modes acoustique aux énergies identiques à celle du BP.

Mots clés: Boson Peak, densité des états vibrationelles, verres densifiés, hyperquenched, Diffusion non élastique nucléaire, diffusion non élastique de rayons x.

Summary

The present thesis work is devoted to the study of the vibrational dynamics in glasses, in particular we investigated the low frequency anomaly: the Boson Peak. In the first chapter the general aspects of the glassy state are. Here we discuss how the anomalous thermodynamic behavior of glasses can be associated to the presence of the Boson Peak in the density of vibrational state of the glass. In the second chapter we discuss the main spectroscopic techniques used in this study: Nuclear Inelastic Scattering (NIS) and the Inelastic X-ray Scattering (IXS). In the third chapter we present the study of hyperquenched glass. In this chapter the effects of the thermal history on the dynamical and structural properties of glasses are investigated. The fourth chapter is dedicated to the study of the effect of pressure and density on the DOS of glass. The changes that the DOS experiences are correlated once more to the macroscopic changes, unless structural transformation takes place. Finally we present study on the high frequency dynamics (in the THz frequency region) of glassy ortho-terphenyl, and the effect of pressure on this dynamics is discussed. From the comparison of our results to others data available in the literature it has been possible to deduce some conclusions on the nature of the acoustic modes at energies comparable to that of the BP.

Key words: Boson Peak, vibrational density of states, densified glasses, hyperquenched, nuclear inelastic scattering, inelastic x-ray scattering.